



## 저작자표시-비영리-변경금지 2.0 대한민국

이용자는 아래의 조건을 따르는 경우에 한하여 자유롭게

- 이 저작물을 복제, 배포, 전송, 전시, 공연 및 방송할 수 있습니다.

다음과 같은 조건을 따라야 합니다:



저작자표시. 귀하는 원저작자를 표시하여야 합니다.



비영리. 귀하는 이 저작물을 영리 목적으로 이용할 수 없습니다.



변경금지. 귀하는 이 저작물을 개작, 변형 또는 가공할 수 없습니다.

- 귀하는, 이 저작물의 재이용이나 배포의 경우, 이 저작물에 적용된 이용허락조건을 명확하게 나타내어야 합니다.
- 저작권자로부터 별도의 허가를 받으면 이러한 조건들은 적용되지 않습니다.

저작권법에 따른 이용자의 권리는 위의 내용에 의하여 영향을 받지 않습니다.

이것은 [이용허락규약\(Legal Code\)](#)을 이해하기 쉽게 요약한 것입니다.

[Disclaimer](#)

공학박사 학위논문

산화물 고체 전해질 기반  
리튬금속전지에 관한 연구

A study on lithium metal batteries  
using oxide solid electrolyte

2023 년 2 월

서울대학교 대학원

재료공학부

김 세 원

# 산화물 고체 전해질 기반 리튬금속전지에 관한 연구

A study on lithium metal batteries  
using oxide solid electrolyte

지도 교수 강 기 석

이 논문을 공학박사 학위논문으로 제출함

2023 년 2 월

서울대학교 대학원

재료공학부

김 세 원

김세원의 공학박사 학위논문을 인준함

2022 년 12 월

위 원 장	장 호 원	(인)
부위원장	강 기 석	(인)
위 원	이 규 태	(인)
위 원	유 태 환	(인)
위 원	임 동 민	(인)

# **Abstract**

## **A study on lithium metal batteries using oxide solid electrolytes**

Kim, Sewon

Department of Materials Science and Engineering

College of Engineering

The Graduate School

Seoul National University

Ever-growing demand for the sustainable energy resources due to the environmental concerns has attracted the worldwide interest for energy storage systems, in order to efficiently store and re-distribute the energy generated from renewable resources. Lithium ion batteries (LIBs) have been regarded as one of the most powerful system due to their high energy density, power capability and long-term cyclability. However, the demand for high energy density is surging beyond the limitation of conventional LIBs. Although the Li-metal batteries (LMBs) utilizing a lithium metal as an anode have shown great potential, their practical implement has been retarded. When a lithium metal electrode is introduced to a battery cell paired with liquid electrolyte, a short-circuit is formed due to lithium metal penetration through the cell, jeopardizing the safety of battery. In regard this, solid-state Li-metal batteries (SLMBs) using solid electrolytes are considered promising solution to implement safe lithium batteries with high energy density. However, the interfacial instability occurring between lithium metal anode and solid electrolyte and the



consequent lithium penetration through the electrolyte have been obstacles in developing SLMBs. Thus, in order to achieve the acceptable electrochemical performances for practical applications of SLMBs, interfacial stability should be ensured. In this thesis, I present the systematic investigation of the interface between lithium metal electrode and solid electrolyte, using garnet-type  $\text{Li}_7\text{La}_3\text{Zr}_2\text{O}_{12}$  (LLZO) electrolytes as a model system, and provide a strategy to design a stable interface from both perspectives of the solid electrolyte and the lithium metal electrode for the implementation of high performance SLMBs.

In chapter 2, I focus on revealing the possible origins for the degradation of the interface between LLZO electrolytes and lithium metal LLZO electrolytes, and present the feasible way to stabilize by tailoring the electrolyte surface. I explore the stabilities of bulk LLZOs doped with various dopants with Li-metal considering the potential by-product formation due to the electrolyte decomposition through the grain boundaries. It is theoretically and experimentally revealed that the composition of LLZO can significantly alter its stability against lithium metal, indicating the importance of selecting suitable dopants. Supported by the additional theoretical calculation, it is suggested that the compositional optimization along the grain boundaries and surface by secondary dopant introduction, protonation, can effectively improve the compatibility with lithium metal by suppressing the formation of conductive by-products, while preserving the high bulk ionic conductivity of doped-LLZO. Simultaneously, I discover that the method used to protonate LLZOs, solution-based acid treatment, can also tailor the other properties of the LLZO surface, which aids in enhancing the interfacial stability. It is revealed that the acid treatment effectively releases the residual stress in LLZO and improve

the maintenance of an intact contact at the interface through the removal of surface contamination and enlargement of the contact area. The efficacy of this approach is verified by showing a significant enhancement in the performance of a practical full cell consisting of a conventional cathode at a commercially applicable loading capacity with a thin Li-metal anode and LLZO electrolyte. These findings highlight that a coupled approach to designing the bulk and grain boundaries of the solid electrolyte plays a key role in achieving the long-term stability of solid-state batteries.

On the one hand, understanding the interfacial instability from the perspective of lithium metal is critical to ensure the stable performance of SLMBs, as the lithium metal electrode keep changing its status through the repetitive lithium plating and stripping. In chapter 3, I elucidate the dynamic changes of the LLZO/Li-metal interface during electrochemical reaction by direct probing the lithium deposition behavior in real time. It is revealed that the lithium plating is strongly affected by the geometry of the LLZO surface, where non-uniform/filamentary growth is triggered particularly at morphological defects. More importantly, when the LLZO surface is modified with an artificial interlayer intentionally introduced on the electrolyte surface, lithium-growth behavior significantly changes depending on the nature of the interlayer species. That is, I show that the uniformity and morphologies of lithium plating/stripping vary greatly according to the reaction characteristics with lithium in the interlayer. Subsequently, the dynamic role of the interlayer in battery operation is discussed as a buffer and seed layer for lithium redistribution and precipitation, respectively, in tailoring lithium deposition. These findings broaden the understanding of the electrochemical lithium-plating process at the solid-electrolyte/Li-metal interface, highlight the importance of exploring various

interlayers as a new avenue for regulating the lithium-metal anode, and also offer insight into the nature of lithium growth in anode-free solid-state batteries.

In chapter 4, I propose a design strategy of interlayer to achieve the long-term stability of interface between the lithium metal and LLZO electrolyte for the repeated lithium deposition/stripping and finally demonstrate the SLMBs that can deliver the commercial available battery performance. I introduce an optimal interlayer, which employs (i) crystalline-direction-controlled carbon material, which provides isotropic lithium transports, with (ii) pre-lithium deposits that guides the lithium nucleation direction toward the current collector. This combination ensures that the morphology of the interlayer is mechanically robust while regulating the preferred lithium growth underneath the interlayer without disrupting the initial interlayer/electrolyte interface, thereby remarkably enhancing the durability of the interface. I illustrate how these material/geometric optimizations are conducted from the thermodynamic considerations, and its applicability is demonstrated for surface tailored LLZO solid electrolytes which are achieved through the study described in chapter 2, paired with the high-capacity cathode, by showing a remarkable battery performance under room temperature and high-current operation conditions. These findings demonstrate that ensuring the stable interface considering from both the electrolyte side and lithium metal electrode side and designing the optimal interlayer are ultimately critical factors for practical implementation of SLMBs.

**Keyword :** Energy storage, Lithium metal batteries, Solid-state batteries, Garnet-type solid electrolytes, Operando analysis, Interlayers

**Student Number :** 2017-38966

# Table of Contents

<b>Abstract .....</b>	<b>i</b>
<b>List of Figures .....</b>	<b>viii</b>
<b>List of Tables .....</b>	<b>xxiv</b>
<b>Chapter 1. Introduction .....</b>	<b>1</b>
1.1. Motivation and outline.....	1
1.2. References .....	7
<b>Chapter 2. High-energy and durable lithium metal batteries using garnet-type solid electrolytes with tailored lithium-metal compatibility .....</b>	<b>15</b>
2.1. Introduction .....	15
2.2. Experimental and computational details .....	19
2.2.1. Material synthesis .....	19
2.2.2. Coloration test.....	24
2.2.3. Characterizations of the solid electrolytes .....	24
2.2.4. Electrochemical characterization .....	26
2.2.5. Calculation details.....	30
2.3. Results and Discussion .....	32
2.3.1. Chemical stabilities of doped-LLZOs against Li metal.....	32
2.3.2. Selective passivation of doped-LLZOs along the grain-boundaries and interface .....	53
2.3.3. Additional effects of acid treatment on interfacial stabilization	61
2.3.4. Electrochemical performance of solid-state Li full cell with protonated Ta-LLZO .....	81
2.4. Conclusion.....	107
2.5. References .....	108
<b>Chapter 3. The role of interlayer chemistry in Li-metal growth through a garnet-type solid electrolyte .....</b>	<b>121</b>

<b>3.1. Introduction .....</b>	<b>121</b>
<b>3.2. Experimental and computational details .....</b>	<b>125</b>
3.2.1. Material synthesis .....	125
3.2.2. In operando observation and electrochemical test .....	127
3.2.3. Material characterization .....	128
3.2.4. Simulation method .....	129
<b>3.3. Results and Discussion .....</b>	<b>130</b>
3.3.1. Surface-morphology-dependent lithium plating .....	130
3.3.2. Lithium redistribution by diffusion through the metal layer ..	138
3.3.3. Interlayer chemistry impacts on lithium plating/stripping behavior .....	142
3.3.4. Possible explanations for different lithium nucleation kinetics depending on interlayer .....	157
<b>3.4. Conclusion.....</b>	<b>163</b>
<b>3.5. References .....</b>	<b>164</b>
 <b>Chapter 4. High-power solid-state batteries enabled by preferred directional lithium growth mechanism .....</b>	 <b>174</b>
<b>4.1. Introduction .....</b>	<b>174</b>
<b>4.2. Experimental and computational details .....</b>	<b>179</b>
4.2.1. Material synthesis .....	179
4.2.2. Cell assembly and electrochemical test .....	181
4.2.3. Material characterization .....	185
4.2.4. Simulation methods .....	185
<b>4.3. Results and Discussion .....</b>	<b>191</b>
4.2.1. Material selection through thermodynamic calculations .....	191
4.2.2. Kinetics of lithium precipitation and the strategy to guide lithium plating.....	195
4.2.3. Influence of the carbon interlayer on cell performance .....	202
4.2.4. Lithium stripping through the interlayer and the orientation of lithium transport pathways.....	209
4.2.5. Optimization of amorphous carbon interlayer for LLZO electrolyte.....	224
<b>4.4. Conclusion.....</b>	<b>229</b>
<b>4.5. References .....</b>	<b>231</b>

<b>Chapter 5. Summary .....</b>	<b>243</b>
<b>Abstract in Korean.....</b>	<b>246</b>

## List of Figures

**Figure 2.1.** XRD patterns and Rietveld refinement results of the as-made LLZO powders doped with various metals such as Ta, Al, Nb, and Ga,W.

**Figure 2.2.** Particle size distribution of the LLZO powders with various dopants, Ta, Al, Nb and Ga,W.

**Figure 2.3.** Optical images of LLZO pellets in contact with Li metal at 200 °C over time after assembly under a cold isostatic pressure of 250 MPa.

**Figure 2.4.** X-ray diffraction (XRD) patterns of the doped-LLZO pellets with various dopants.

**Figure 2.5.** Cross-sectional scanning electron microscopy (SEM) images of the fractured LLZO pellets with various dopants (Ta, Al, Nb, Ga,W).

**Figure 2.6.** (a) EIS profiles of Au/LLZO/Au symmetric cells at 25 °C and (b) Arrhenius plot of the total ionic conductivities of the LLZO pellets doped with various metals (Ta, Al, Nb, and Ga,W).

**Figure 2.7.** (a) Optical images of Ga,W-LLZO pellets in contact with Li metal (recorded over time at 200 °C) and the corresponding SEM images of the surface exhibiting numerous cracks and the pulverization of the pellet and (b) Comparison between the images of a Ga,W-LLZO pellet in contact with Li metal and the images of another pellet where Li metal contact at 200 °C was absent.

**Figure 2.8.** SEM images and energy-dispersive X-ray spectroscopy (EDS) images

recorded for the LLZO surfaces that were in contact with Li metal during the coloration test.

**Figure 2.9.** Comparison of the cross-sectional SIMS images of (a) Ta-LLZO, (b) Nb-LLZO, and (c) Ga,W-LLZO. The images were recorded after the coloration test had been conducted (Scale bars: 100  $\mu\text{m}$ ).

**Figure 2.10.** Comparison of XRD patterns of LLZO pellets with reference XRD pattern (ICSD 01-080-6142) (left) before and (right) after contact with Li-metal.

**Figure 2.11.** X-ray photoelectron spectroscopy (XPS) profiles recorded for the cross-section of Ga,W-doped LLZO pellet before and after coloration tests. Zr 3*d* core-level spectra before (left) and after (right) the reaction. Fitted curves obtained using fixed spin splits ( $3d_{3/2} - 3d_{5/2} = 2.40$  eV) are presented.

**Figure 2.12.** XRD patterns and Rietveld refinement results obtained for the Nb-LLZO pellets. The patterns and data were recorded before and after the coloration test.

**Figure 2.13.** EDS images of the cross-section of Nb-LLZO pellet recorded after the coloration test. Lithium metal propagation through the grain boundaries is observed.

**Figure 2.14.** (a) Evolution of the electrochemical impedance spectra over time for the Li/LLZO/Au cells measured at 60 °C. (b) Galvanostatic cycling of Li/LLZO/Li symmetric cells at 60 °C with a 0.2 mA cm<sup>-2</sup> current density.

**Figure 2.15.** (a) Calculated Arrhenius relations of lithium ion diffusivities for  $\text{Li}_{6.5}\text{La}_3\text{Zr}_{1.5}\text{Nb}_{0.5}\text{O}_{12}$ ,  $\text{Li}_{6.75}\text{La}_3\text{Zr}_{1.5}\text{Nb}_{0.5}\text{O}_{12}$ , and  $\text{Li}_7\text{La}_3\text{Zr}_{1.5}\text{Nb}_{0.5}\text{O}_{12}$  and (b) Calculated lithium ionic probability densities in  $\text{Li}_{6.5}\text{La}_3\text{Zr}_{1.5}\text{Nb}_{0.5}\text{O}_{12}$  and



$\text{Li}_7\text{La}_3\text{Zr}_{1.5}\text{Nb}_{0.5}\text{O}_{12}$ .

**Figure 2.16.** EIS profiles and the results obtained from experiments conducted (before and after galvanostatic cycling) with Li/LLZO/Li symmetric cells at 60 °C (Figure 2.14b).

**Figure 2.17.** Electrochemical stability window of all the samples under study, evaluated by DFT calculations. The color scheme indicates the electrical properties of the decomposed products; red: metallic and electronically conductive, orange: electronically and ionically conductive, blue: ionically conductive but electronically insulating, and green: stable and does not decompose.

**Figure 2.18.** Electrochemical stability windows for pristine and protonated Ta- and Nb-LLZOs calculated using the DFT.

**Figure 2.19.** Thermogravimetric analysis (TGA) curves of (a) pristine and (b) protonated Ta-LLZO pellets, revealing the partial substitution of  $\text{Li}^+$  ions in LLZO with  $\text{H}^+$ . Data were recorded under an atmosphere of  $\text{N}_2$ .

**Figure 2.20.** (a) Optical images (recorded over time) of protonated LLZO pellets in contact with Li-metal at 200 °C, after the system was assembled under a cold isostatic pressure of 250 MPa. (b) Comparison of XRD patterns of protonated LLZO pellets before (left) and after (right) coloration test. The reference XRD pattern is also indicated (ICSD 01-080-6142). (c) Variation of the EIS profiles with time (Li/LLZO/Au cells measured at 60 °C), and (d) Results of galvanostatic cycling experiments conducted with Li/LLZO/Li symmetric cells at 60 °C (current density:  $0.2 \text{ mA cm}^{-2}$ ).

**Figure 2.21.** Electronic conductivities of Ta– and Nb–LLZO pellets before and after protonation measured by DC polarization with an applied voltage of 0.5 V at 60 °C.

**Figure 2.22.** Electrochemical impedance spectroscopy (EIS) results for (a) Li/Ta–LLZO/Li and (b) Li/Al–LLZO/Li symmetric cell before and after surface tailoring, showing decrease in the interfacial resistance after the surface tailoring.

**Figure 2.23.** XPS spectra of C 1s and O 1s region of Ta–LLZO pellets before and after surface tailoring along the sputtering depth, showing the elimination of  $\text{Li}_2\text{CO}_3$  below the surface.

**Figure 2.24.** SEM images of the polished and tailored Ta–LLZO pellet surfaces and cross-sections in contact with Li-metal.

**Figure 2.25.** The time-load curve of (left) the pristine and (right) the protonated Ta–LLZO (right) pellets exhibiting the maximum load that the pellet can endure during the ring-on-ring test. The tests were conducted by measuring the maximum value while applying a load at the same rates to the pellet placed between the two rings, as shown in the inset figure. The tensile strength of each pellet was calculated from the maximum load at which the pellet was broken, and the vertical displacement of the bent pellet.

**Figure 2.26.** XRD patterns of Ta–LLZO before and after surface tailoring. (Details of the Rietveld refinement are provided in Figure 2.27-2.30.)

**Figure 2.27.** XRD patterns and Rietveld refinement results of the pristine LLZO pellets doped with various metals such as Ta, Al, Nb, and Ga,W. (The chemical composition of the corresponding pellets examined by the ICP-AES (Inductively

Coupled Plasma-Atomic Emission Spectroscopy) is tabulated in Table 2.2)

**Figure 2.28.** XRD patterns and Rietveld refinement results of the crushed/ground LLZO pellets in powder state, doped with various metals such as Ta, Al, Nb, and Ga,W.

**Figure 2.29.** XRD patterns recorded for a pristine pellet (blue line) and the corresponding crushed/ground pellet in the powder state (grey line) of Ta–LLZO. We simply compared the XRD peaks of the pellet sample with those from the powder sample obtained by crushing/grinding the pellet for the Ta–LLZO.

**Figure 2.30.** XRD patterns and Rietveld refinement results of the protonated LLZO pellets doped with various metals such as Ta, Al, Nb, and Ga,W.

**Figure 2.31.** Size–strain plots for LLZO pellets before and after surface tailoring. The graphs were plotted based on the Williamson–Hall analysis and Rietveld refinement results presented in Figure 2.25 and 2.28. Williamson–Hall plots were obtained using the equation,  $\beta_{hkl} \cdot \cos\theta = \frac{K\lambda}{D} + 4\varepsilon \cdot \sin\theta$  with the integral breadth that was calculated from the U, X, and Y values from the Rietveld refinement process.

**Figure 2.32.** (a) Bright-field transmission electron microscopy (TEM) images of the surface of Ta–LLZO pellets before and after surface tailoring. The wave pattern in the pristine pellet indicates the existence of a strain field. (b) SAD patterns of Ta–LLZO pellets before and after surface stabilization.

**Figure 2.33.** Critical current densities of pristine (light blue and green lines) and surface-tailored (dark blue and green lines) Ta– or Al–LLZO (a) at 60 °C and (b) 25 °C

as determined by galvanostatic cycle tests on the symmetrical cells with increasing current densities ranging from 0.1 to 1 mA cm<sup>-2</sup> at a step size of 0.1 mA cm<sup>-2</sup> and from 1.0 to 3.0 mA cm<sup>-2</sup> at a step size of 0.2 mA cm<sup>-2</sup>. At each current density, the cells were cycled twice with 30 min of Li plating/stripping.

**Figure 2.34.** Voltage profiles of Li/LLZO/NCM111 cells at 60 °C with doped, surface-tailored (a) Ta- and (b) Al-LLZO electrolytes.

**Figure 2.35.** Electrochemical performances of hybrid solid-state full cells measured at 60 °C, employing a Li-metal anode and a pristine LLZO with various dopants. The extent of operating current density increase was more in the case when Ta- and Al-LLZO were used than the case when Nb- and Ga,W-LLZO were used.

**Figure 2.36.** Electrochemical performances of hybrid solid-state full cells measured at 60 °C. The cells were fabricated using a Li-metal anode and a protonated Nb- and Ga,W-LLZO.

**Figure 2.37.** Rate capability of hybrid solid-state full cells with surface-tailored LLZOs and Li-metal anodes for various dopants.

**Figure 2.38.** Voltage profiles and cyclability of the hybrid solid-state full cell using surface-tailored Ta-LLZO and an NCM811 cathode with a high capacity of 6.4 mAh cm<sup>-2</sup> at 60 °C. A capacity of 6.0 mAh cm<sup>-2</sup> corresponds to a Li-metal thickness above 30 μm.

**Figure 2.39.** (a) Rate capability of the hybrid solid-state full cells with surface-tailored LLZOs and Li-metal anodes for various dopants. For the rate capability test at 100 °C, the cells were operated with increasing current densities (indicated with

numbers in parentheses). (b) Cyclability of the hybrid solid-state full cell using surface-tailored Ta–LLZO at 100 °C.

**Figure 2.40.** (a–b) Voltage profiles of Li/protonated Al–LLZO/NCM111 cells at 100 °C under the current densities of (a) 0.5, 1.0, 2.0, and 3.0 mA cm<sup>-2</sup> and (b) 0.3 mA cm<sup>-2</sup> before and after the tests (shown in (a)). (c) Initial EIS profiles recorded with NCM111/protonated Ta– or Al–LLZO/Li cells at 100 °C before the electrochemical tests were conducted (Figure 2.39).

**Figure 2.41.** Crystal structures of lithium aluminium oxide ( $\gamma$ -LiAlO<sub>2</sub>) and lithium orthotantalate ( $\beta$ -Li<sub>3</sub>TaO<sub>4</sub>). The lithium sites are marked with numbers in each structure.

**Figure 2.42.** Long-term cycling performance of NCM111/protonated Ta–LLZO/Li hybrid cells.

**Figure 2.43.** EIS profiles of NCM111/protonated Ta–LLZO/Li hybrid cells at 60 °C before and after cycling, as shown in Figure 2.42.

**Figure 2.44.** Electrochemical performance of hybrid solid-state full cells at 60 °C, fabricated using a Li-metal anode and thin 110- $\mu$ m-thick surface-stabilized Ta–LLZO. (a) Voltage profiles of the Li/LLZO/NCM111 cell and (b) Cyclability at 60 °C. The cells could be operated for a prolonged time (600 cycles) without short-circuiting under a high current density of 2 mA cm<sup>-2</sup>.

**Figure 2.45.** The comparisons of physical properties of hot press-sintered and tape cast Ta–LLZO electrolytes. (a) XRD patterns of the hot-pressed and sintered Ta–LLZO (thickness: 350  $\mu$ m) and tape-cast Ta–LLZO (thickness:110  $\mu$ m) electrolyte

surfaces after protonation. (b) Raman spectral profiles of the hot-pressed and sintered Ta-LLZO (thickness: 350  $\mu\text{m}$ ) and tape-cast Ta-LLZO (thickness: 110  $\mu\text{m}$ ) electrolyte surface after protonation. (c) Cross-sectional SEM images of surface tailored pellet and tape-cast electrolyte in contact with the lithium metal.

**Figure 2.46.** Voltage profiles and long-term cycling performance of all-solid-state battery using a composite of NCM811 and  $\text{Li}_6\text{PS}_5\text{Cl}$  electrolyte as the cathode, showing a capacity of 5  $\text{mAh cm}^{-2}$  at 60  $^\circ\text{C}$  with doped, surface-tailored electrolytes.

**Figure 2.47.** Performance comparison of solid-state batteries using garnet-type solid electrolytes and Li-metal anodes. The left graph shows the cathode capacity of full cells studied previously in comparison with the cells of the surface-stabilized Ta-LLZO electrolyte. The right plot summarizes the current density and cumulative areal plating capacity at several temperatures based on the previous reports (see Table 2.5 for detailed references, Ref. S1-S20 as indicated on the figure) The values corresponding to full cells are distinguished from those of the symmetric cells by red asterisks; the dashed lines indicate the minimum requirement for industrial applications.

**Figure 3.1.** (a) Side-view schematic and (b) actual images of the *in operando* optical system with a coin-type half-cell.

**Figure 3.2.** *In operando* optical microscopy images of lithium deposition on a pre-coated thick ( $\sim 1 \mu\text{m}$ ) lithium layer during the galvanostatic deposition of lithium.

**Figure 3.3.** *In operando* optical microscopy images of lithium deposition on a polished LLZO with a sputtered thin ( $\sim 5 \text{ nm}$ ) gold layer during the galvanostatic deposition of lithium.

**Figure 3.4.** Schematic descriptions of uneven lithium-ion flux induced by surface morphological fluctuations and the corresponding inhomogeneous lithium deposition.

**Figure 3.5.** Demonstrating the local lithium-ion flux dependence on surface geometry (a) Reference model used for simulations. (b) Simulation result. In panel (b), the green lines are equipotential lines, and the red arrows show the intensity and direction of the lithium-ion current density.

**Figure 3.6.** In operando optical microscopy images of polished LLZO with a sputtered ( $\sim 30$  nm) gold layer during the  $0.1\text{-mA cm}^{-2}$  galvanostatic deposition of lithium metal, which shows the lithium-gold alloying reaction, followed by lithium precipitation.

**Figure 3.7.** Schematic description of lithium redistribution through the gold layer and lithium nucleation.

**Figure 3.8.** *In operando* optical microscopy images of sputtered ( $\sim 100$  nm) a silicon layer on polished LLZO surfaces during lithium deposition with stepwise increases in current density (from  $0.1$  to  $0.4\text{ mA cm}^{-2}$ ).

**Figure 3.9.** *In operando* optical microscopy images of sputtered ( $\sim 100$  nm) a silver layer on polished LLZO surfaces during lithium deposition with stepwise increases in current density (from  $0.1$  to  $0.4\text{ mA cm}^{-2}$ ).

**Figure 3.10.** In operando optical microscopy images of sputtered  $100\text{-nm-thick}$  (a) silver and (b) gold layers on polished LLZO surfaces during the  $0.1\text{-mA cm}^{-2}$  galvanostatic deposition of lithium on/through the layer.

**Figure 3.11.** SIMS analyses of interlayers on polished LLZO surfaces after the galvanostatic deposition of lithium at  $0.1 \text{ mA cm}^{-2}$  for 15 min ( $0.025 \text{ mAh cm}^{-2}$ ) on/through 100-nm-thick (a) silver and (b) gold layers (Scale bars:  $10 \text{ }\mu\text{m}$ ).

**Figure 3.12.** AFM images of the surface of (a) silver and (b) gold interlayers at various charge/discharge states after  $0.2 \text{ mA cm}^{-2}$  galvanostatic deposition and  $0.1 \text{ mA cm}^{-2}$  galvanostatic stripping of lithium. ( $R_{\text{rms}}$  = root mean square roughness, and the scale bar in each the image =  $10 \text{ }\mu\text{m}$ . The maximum amounts of lithium stripped from each interlayer at  $0.47 \text{ mAh cm}^{-2}$  for silver and  $0.38 \text{ mAh cm}^{-2}$  for gold case differ due to their distinct reversibilities.)

**Figure 3.13.** Electrochemical performance of solid-state batteries employing 100-nm-thick interlayers under the same test conditions of  $0.2 \text{ mA cm}^{-2}$  galvanostatic deposition and stripping of lithium at  $60^\circ\text{C}$ , showing distinct coulombic efficiencies.

**Figure 3.14.** Electrochemical performance of anode-free hybrid-solid-state batteries. The hybrid full cells, using ionic liquid wetted NCM111 electrode as a hybrid cathode and 100-nm-thick (a) silver and (b) silicon metal layer as an interlayer at solid electrolyte/anode current collector interface, were tested under the galvanostatic charge/discharge condition with the current densities of  $0.1$  and  $0.2 \text{ mA cm}^{-2}$  for silver interlayer and  $0.1 \text{ mA cm}^{-2}$  for silicon interlayer at  $60^\circ\text{C}$ .

**Figure 3.15.** *In operando* optical microscopy images of the sputtered 100-nm-thick (a) silicon, (b) gold and (c) silver layers on polished LLZO surfaces during  $0.1 \text{ mA cm}^{-2}$  galvano-static deposition and stripping of lithium through the layer.

**Figure 3.16.** Cross-sectional SEM image of silver layer at different charge/discharge state after  $0.1 \text{ mA cm}^{-2}$  galvano-static deposition and stripping of lithium.



**Figure 3.17.** Classical picture of nucleation and growth, showing the free energy change associated with the surface energy for nucleation.

**Figure 3.18.** Voltage profiles of silicon, gold and silver interlayer during lithium deposition at a current density of  $0.1 \text{ mA cm}^{-2}$  showing the differences of the overpotential for precipitation in each interlayer. For the ease of comparison, the curves are shifted horizontally according to the onset of lithium precipitation and the magnitudes of vertical axis are set to 12 mV.

**Figure 4.1.** Schematic illustrations of the degradation mechanism at the interface of a solid electrolyte and a lithium-metal anode during repetitive lithium plating and stripping. (a) The failure of the cell on using bare lithium metal anode. (b) The failure of the cell on using conventional interlayers at the interface of LLZO electrolyte/lithium metal anode due to the (electro)chemical/physical instability of the interlayer.

**Figure 4.2.** Carbon interlayers coated on copper foil. SEM images of (left) surface and (right) cross-section of as-prepared (a) graphite and (b) amorphous carbon interlayer.

**Figure 4.3.** Schematic of cells used for lithium plating experiments. Cell #1 uses lithium metal as a counter electrode and a carbon layer as a working electrode. Cell#2 uses lithium metal as a counter electrode and a carbon layer with lithium metal as a working electrode.

**Figure 4.4.** Schematic of lithium plating positions and the corresponding interfaces used for interfacial energy calculations. Case #1 describes lithium plating at the interlayer/solid-electrolyte interface. Lithium-metal plating between the solid

electrolyte and the interlayer, which are in direct contact, does not prevent lithium-metal penetration into the electrolyte. In contrast, when lithium is plated between the current collector and the interlayer, as shown in Case #2, the interlayer effectively prevents direct contact of the lithium metal and the solid electrolyte.

**Figure 4.5.** The geometry of the model structure mimicking the experimental cell configuration.

**Figure 4.6.** Cross-sectional SEM and EDS images of anode/LLZO electrolyte interfaces showing the instability of metal interlayers. (a) Volume expansion of gold interlayer after the lithium plating with alloying reaction. Initially 100 nm-thick gold layer was deposited by RF sputtering on the one side of LLZO electrolyte, and lithium of  $0.5 \text{ mAh cm}^{-2}$  was electrochemically deposited to gold layer. (b) Dissolution of silver interlayer into lithium metal. The images show the cross section of LLZO electrolyte/lithium metal interface of a hybrid solid-state lithium cell employing NCA111 cathode ( $3.2 \text{ mAh cm}^{-2}$ ), which initially included a 30 nm-thick silver interlayer at the interface, after 20 cycles at  $0.6 \text{ mA cm}^{-2}$  at  $25^\circ\text{C}$ .

**Figure 4.7.** Cross-sectional SEM and EDS images of the LLZO solid electrolyte/anode interfaces after electrodeposition of lithium at various magnification scales to the (top) graphite layer and (bottom) amorphous carbon layer at  $100^\circ\text{C}$ .

**Figure 4.8.** Cross-sectional SEM and EDS images of the LLZO solid electrolyte/anode interfaces after electrodeposition of lithium at various magnification scales to the (top) graphite layer and (bottom) amorphous carbon layer at  $25^\circ\text{C}$ .

**Figure 4.9.** Cross-sectional SEM and EDS images of the LLZO solid electrolyte/anode interfaces after electrodeposition of lithium at various magnification scales to the (top) graphite layer and (bottom) amorphous carbon layer at 60 °C.

**Figure 4.10.** Cross-sectional SEM and EDS images of the LLZO solid electrolyte/anode interfaces after electrodeposition of lithium at various magnification scales through the (top) graphite interlayer or (bottom) amorphous carbon interlayer with the pre-existing lithium metal at 25 °C.

**Figure 4.11.** Electrochemical performance of hybrid solid-state battery cells using garnet-type solid electrolytes and lithium-metal anodes (a) without and (b) with carbon interlayers, showing the significant differences in results due to the presence of the interlayer and the type of carbon.

**Figure 4.12.** Rate and cycle performances of hybrid solid-state battery cells using garnet-type solid electrolytes and lithium-metal anodes without and with carbon interlayers, showing the significant differences in results due to the presence of the interlayer and the type of carbon.

**Figure 4.13.** Cross-sectional SEM and EDS images recorded after the failure of a cell with a graphite interlayer.

**Figure 4.14.** Cross-sectional SEM and EDS images recorded after the failure of the cell with a graphite interlayer shown in Figure 4.13c.

**Figure 4.15.** Voltage responses to the pulse currents as a function of the capacity during lithium stripping from the cell with (top) the graphite interlayer and (bottom)

the amorphous carbon interlayer, and the EIS result of each cell before and after stripping.

**Figure 4.16. Fitting results of EIS featured in Figure 4.15.** (a) Equivalent circuit used for fitting the EIS results shown in Figure 4.15.  $R_1$  at high frequency represents the resistance of LLZO solid electrolyte.  $R_2$ -CPE<sub>2</sub> and  $R_3$ -CPE<sub>3</sub>-W<sub>s</sub> circuits can be attributed to the interfacial responses. Meanwhile, as Li metal counter electrode was attached by a high pressure of 250 MPa, the interfacial resistance at LLZO/Li metal interface was considered negligible as reported. (b-c) Enlarged Nyquist plots of Figure 4.15 and the fitting results (the resistance and capacitance data in table) of cells using (b) the graphite interlayer and (c) the amorphous carbon interlayer before and after lithium stripping.

**Figure 4.17.** Nyquist representations of the impedance-spectra evolutions on lithium stripping from the lithium metal anode with (a) the graphite interlayer and (b) the amorphous carbon interlayer.

**Figure 4.18.** Detailed results of GEIS measurements using cells with graphite and amorphous-carbon interlayers. (a) Voltage profile of the cell with the graphite interlayer during lithium plating at  $0.3 \text{ mA cm}^{-2}$  and (inset graph) the evolution of EIS according to the amount of plated lithium amount (b) Voltage profile of the cell with the graphite interlayer during lithium stripping at  $0.3 \text{ mA cm}^{-2}$  and comparison of EIS (section-wise) according to the voltage change. (c) Voltage profile of the cell with the amorphous carbon interlayer during (upper) lithium plating and (lower) stripping at  $0.3 \text{ mA cm}^{-2}$ .

**Figure 4.19.** Cross-sectional SEM images of the LLZO solid electrolyte/lithium metal anode interface with (a) the graphite interlayer and (b) the amorphous carbon interlayer after lithium stripping and subsequent lithium plating.

**Figure 4.20.** Crystallinities and morphologies of graphite and amorphous carbon. (a) Raman spectra. Raman spectra were collected using a Renishaw inVia™ Raman microscope with a 514 nm laser. (b) Cross-sectional SEM images of the graphite and amorphous layers.

**Figure 4.21.** SEM images of the particles in each interlayer indicating the dependence of the local lithium transport pathway on the orientation of particle alignment and crystallites of carbon (top: graphite, bottom: amorphous carbon).

**Figure 4.22.** Apparent lithium diffusivities of the graphite and amorphous-carbon interlayers. (a) GITT profiles and (b) Calculated diffusion coefficients. (a) GITT profiles during de-lithiation of the lithiated graphite and amorphous carbon, along with their lithium contents. The cells with configuration of Cell#1 described in Figure 4.3 were prepared using graphite and amorphous carbon interlayer, and fully lithiated at 0.1 C-rate considering the amount and the capacity of each carbon interlayer. Then, GITT measurements with a de-lithiation current pulse at 0.3 mA cm<sup>-2</sup> for 3 minutes and the rest period for 177 minutes were conducted. (b) The calculated lithium diffusivities from the graphite and amorphous-carbon layers.

**Figure 4.23.** Simulation of the consequent lithium concentration distribution with the lithium diffusion pathways (white arrows) in the anode with (top) the graphite interlayer and (bottom) the amorphous carbon interlayer during lithium stripping

(*e.g.*, discharging of the full cell with the configuration at the left side) at  $2 \text{ mA cm}^{-2}$ .

**Figure 4.24.** Simulation results of the lithium-concentration distribution in the lithium metal anode with graphite or amorphous carbon interlayer of cell with different state of (top) charging and (bottom) discharging.

**Figure 4.25.** XRD patterns and TEM images of the amorphous carbon powder used for the optimal interlayer. The second carbon exhibits small crystallites ( $\sim 0.7 \text{ nm}$ ) and particle size ( $10\text{--}20 \text{ nm}$ ), facilitating more isotropic lithium transport through the interlayer.

**Figure 4.26.** Long-term cycling performance of the NCA811/LLZO/amorphous carbon interlayer/lithium-metal cell. Initial 13 pre-cycles were conducted at  $0.5$ ,  $0.8$ ,  $1.0$ ,  $1.6$  and  $2 \text{ mAcm}^{-2}$ , respectively, before cycling at  $2.5 \text{ mAcm}^{-2}$ .

**Figure 4.27.** A performance comparison of solid-state batteries using garnet-type solid electrolytes and lithium-metal anodes. The plot summarizes the current densities ( $x$ -axis) and areal plating capacities of cathodes ( $y$ -axis) reported previously. The inset graph compares the cumulative areal capacities of lithium plating (the number at the top of each bar) of full cells.

## List of Tables

**Table 2.1.** Phase equilibria of (top) pristine and (bottom) protonated LLZO doped with various metals at the potential for the first reduction.

**Table 2.2.** Chemical composition of LLZO pellets from ICP-AES results. Atomic ratio of Li:La:Zr:dopant is normalized by the La content in the formula  $\text{Li}_{7-x}\text{La}_3\text{Zr}_{2-y}(\text{Dopant})_a\text{O}_{12}$ .

**Table 2.3.** Lithium-ion diffusion energy barrier in lithium aluminium oxide ( $\gamma$ -LiAlO<sub>2</sub>) and lithium orthotantalate ( $\beta$ -Li<sub>3</sub>TaO<sub>4</sub>) calculated using the nudged elastic band (NEB) method implemented in VASP. All possible pathways of lithium vacancy migration in the crystal structure were considered, corresponding to the sites shown in **Figure 2.41**.

**Table 2.4.** Parameters considered for estimating the energy densities of the full cells.

**Table 2.5.** Summary of the electrochemical plating/stripping performances of the cells (garnet electrolyte and Li-metal) reported in the literature.

**Table 4.1.** Parameters related to the electrochemical reaction simulation

**Table 4.2.** Calculated interfacial energies according to the lithium plating position and interlayer materials (see section 4.2.4 and Figure 4.4 for details).

# Chapter 1. Introduction

## 1.1. Motivation and outline

In recent decades, the demand for energy has been surging rapidly with the industrialization and technological development. However, such enormous use of energy has not only exhausted the main resource of energy, but also caused severe environmental problems, including global warming. As a solution for this issue, sustainable energy has attracted worldwide interest and the demand for this energy has been increasing. Along with this trend, the energy storage systems, like high-energy batteries, have been attracting great attention since the energy generated from such renewable resources should be stored once generated to properly balance the difference between energy supply and demand. Lithium ion batteries (LIBs) have been one of the most useful and effective means to meet their requirements since they were developed.<sup>1-4</sup> Especially, with the increased energy consumption of mobile devices and to extend the driving range of electric vehicles, the demand for higher energy density LIBs is ever-growing. However, conventional LIBs have reached the limitation of energy density.

Li-metal batteries (LMBs) that utilize the lithium metal as an anode have shown huge potential to meet the requirements for higher energy density<sup>5</sup>, as lithium metal provides the highest theoretical capacity ( $3860 \text{ mAh g}^{-1}$  or  $2061 \text{ mAh cm}^{-3}$ ) with lowest negative electrochemical potential ( $-3.04\text{V}$  vs standard hydrogen electrode)<sup>6,7</sup>. Unfortunately, they have not been commercialized yet due to their inherent and fatal problem, safety issue.<sup>8,9</sup> It has been reported that lithium dendrites can grow during



charge process of LMBs and they can penetrate the separator and reach the cathode, causing short circuit formation.<sup>10</sup> This short circuit leads a cell thermal runaway, finally resulting in cell explosion. To address the safety issue of LMBs<sup>9,11-16</sup>, replacing liquid electrolytes to solid-state electrolytes, especially inorganic solid electrolytes (ISEs), is regarded as one of the most promising solution to secure the safety of LMBs due to their mechanical strength to block the lithium dendrite penetration and non-flammability to prevent the cell explosion.<sup>17-23</sup> Nevertheless, attempts to use ISEs in LMBs have been failed due to unexpectedly premature short circuiting during the cell operation at high current density. It was found that lithium-metal still grows penetrating through the ISEs, causing the short circuit formation.<sup>24-</sup>  
<sup>28</sup> Various mechanisms underlying this phenomenon have been proposed, such as i) decomposition of electrolyte<sup>29-31</sup>, ii) non-zero electronic conductivity of solid electrolyte<sup>32-35</sup>, iii) non-uniform current distribution<sup>26,36-41</sup>, and iv) crack propagation.<sup>26,36-38</sup> Accordingly, numerous attempts to solve the short circuit formation problem have been suggested.<sup>39,42-49</sup> However, none of them have succeeded in realizing practical SLMBs. It can be attributed to the limited efficacy of the approaches, which were designed in consideration of only some or each of the different causes for the short circuit. More importantly, there was a lack of awareness that the interface where the short circuit formation initiates is the interface between the solid electrolyte and lithium metal, that is, the interface between solid and solid. Since the interface between solid electrolyte and the lithium metal is different from the interfaces between liquid electrolyte and electrodes in conventional LIBs, mechanistic understanding of origin of the short circuit formation regarding the interface between solid electrolyte and lithium metal should be preceded to

implement SLMBs. Further, it should not be overlooked that the lithium metal changes its morphology during electrochemical reaction when investigating the interface.

Therefore, I try to present the comprehensive understanding of short-circuit formation focusing on the interface between solid electrolyte and lithium metal anode and their possible interactions. Further, based on that understanding, I suggest viable solutions to implement the practical SLMBs. For efficient and practical research, I choose Garnet-type oxide electrolytes, *e.g.*  $\text{Li}_7\text{La}_3\text{Zr}_2\text{O}_{12}$  (LLZO), as a model system because they are some of the leading candidates for Li-metal solid-state batteries. LLZOs provide enough mechanical strength to suppress the lithium dendrite growth and also benefits from relatively high ionic conductivity at room temperature ( $\sim 1$  mS/cm), with a lithium-ion transference number close to unity.<sup>23,50-54</sup> Moreover, the material stabilities of oxides in ambient air facilitate the practical synthesis of solid electrolytes and the fabrication of solid-state batteries using LLZOs, enhancing the possibility of implementing SLMBs.

In Chapter 2, I investigate the origins of short-circuit formation related to the intrinsic properties of the electrolyte and their effects on the stability of the interface with lithium metal anode. The interfacial stabilities of LLZOs doped with various dopants against lithium metal and their impacts on short-circuit formation, in consideration of decomposition of the electrolyte and the related electronic conductivity, are studied. I show the presence of metallic by-products caused by the reaction between lithium metal and doped-LLZO depending on the composition of the electrolyte can induce the substantial electronic conductivity with rapid

propagation of the reductive decomposition throughout the LLZO electrolyte, eventually leading the fracture of the electrolyte and lithium metal penetration. Based on it, I suggest the rational selection of dopants each for bulk electrolyte and for stabilization of interfaces such as surface and grain boundaries. It was demonstrated that the protonation of LLZO with the appropriate primary dopant, Ta, can effectively suppress the metallic by-product formation and retard the formation of electron-conducting paths in electrolyte. In addition, it is revealed that this interfacial treatment/protonation method not only effectively aid in the maintenance of an intact contact at the interface by the removal of surface contamination and the increase in electrolyte surface area, but also releases the residual stress in LLZO, increasing the mechanical strength that is beneficial to block the electrolyte fracture or crack propagation upon lithium propagation. Finally, it is demonstrated that this strategy can lead to a significant enhancement in the performance of a practical full cell consisting of a conventional cathode at a commercially applicable loading capacity with a thin lithium metal anode (20  $\mu\text{m}$ ) and LLZO electrolyte.

However, the interpretation of short circuit only from the viewpoint of electrolyte properties is not sufficient to fully comprehend the mechanism and provide the overall solution. As the short-circuit formation stems from the “lithium metal” penetration or growth through the electrolyte, it must also be unveiled how the lithium metal behaves during battery operation and affects the short-circuit formation. In particular, since lithium metal continuously alters its status during battery operation due to the repetitive lithium metal plating and stripping, real-time probing should be accompanied to explicate the exact mechanism of lithium metal propagation. In Chapter 3, I elucidate the underlying mechanisms of lithium

plating/stripping behaviors on the LLZO electrolyte surface and at the interface between the electrolyte and lithium metal electrode through the *in operando* observations, which uses newly designed in-house cell and optical microscope system. It is verified that lithium metal penetration can be triggered by the non-uniform lithium plating due to pre-existing surface flaws that act as preferred sites for the electrodeposition of lithium, and the poor contact at the interface generated by localized lithium stripping can further aggravate the lithium penetration. More importantly, I describe how the chemistry at the interface alters the deposition mechanism during electrochemical reactions by carefully examining the interface with artificial interlayers exploiting various types of metal as model materials. It is revealed that lithium plating is strongly dominated by the kinetics of alloying and precipitation through the metal interlayer; the unevenness of the lithium plating due to the geometry of the surface can either be exacerbated or mitigated by the interlayer metal species. Finally, I provide useful guidance for engineering the interface to secure the stable lithium plating/stripping by suggesting the dynamic roles of the interlayer during battery operation.

Based on these understandings and insights in Chapter 2 and 3, I recognize that engineering of the solid electrolyte surface/interface considering lithium metal compatibility and ensuring the stable lithium plating/stripping at the interface are key factors to achieve the acceptable performance of SLMBs for practical applications. Thus, in Chapter 4, I focus on how to design an optimal interlayer rationally. Supported by the thermodynamic properties of the candidate materials estimated by density functional theory (DFT) calculations, I select a carbon-based material as the core component of interlayer as it is predicted to induce lithium

plating preferentially between the current collector (copper) and the interlayer. In this consideration, I also point out that the crystalline orientations of the carbon domains are important in homogenizing the lithium distribution through the interlayer, indicating the necessity in the crystalline engineering of carbon. In addition, I suggest that the pre-lithium deposits can further facilitate the preferred lithium growth without destructing the original interlayer/electrolyte interface by facilitating lithium nucleation. Through the series of in-depth characterizations, I demonstrate that this rational selection allows the long-term stability of the interlayer and reversible lithium stripping/deposition. Finally, I manufacture a SLMB cell with a high-capacity of  $5 \text{ mAh cm}^{-2}$  by employing the optimized carbon interlayer between a surface tailored LLZO electrolyte and lithium metal anode, and validate its remarkable room-temperature cycling performance even at high current densities. I believe this successful long-term operation of SLMB paves a new pathway toward the development of practical all-solid-state lithium metal batteries.

## 1.2. References

- 1      Whittingham, M. S. Electrical Energy Storage and Intercalation Chemistry. *Science* **192**, 1126-1127, doi:doi:10.1126/science.192.4244.1126 (1976).
- 2      Deng, D. Li-ion batteries: basics, progress, and challenges. *Energy Science & Engineering* **3**, 385-418, doi:https://doi.org/10.1002/ese3.95 (2015).
- 3      Li, M., Lu, J., Chen, Z. & Amine, K. 30 Years of Lithium-Ion Batteries. *Advanced Materials* **30**, 1800561, doi:https://doi.org/10.1002/adma.201800561 (2018).
- 4      Yoshino, A. The Birth of the Lithium-Ion Battery. *Angewandte Chemie International Edition* **51**, 5798-5800, doi:https://doi.org/10.1002/anie.201105006 (2012).
- 5      Thackeray, M. M., Wolverton, C. & Isaacs, E. D. Electrical energy storage for transportation—approaching the limits of, and going beyond, lithium-ion batteries. *Energy & Environmental Science* **5**, 7854-7863, doi:10.1039/C2EE21892E (2012).
- 6      Cheng, X.-B., Zhang, R., Zhao, C.-Z. & Zhang, Q. Toward Safe Lithium Metal Anode in Rechargeable Batteries: A Review. *Chemical Reviews* **117**, 10403-10473, doi:10.1021/acs.chemrev.7b00115 (2017).
- 7      Schmuck, R., Wagner, R., Hörpel, G., Placke, T. & Winter, M. Performance and cost of materials for lithium-based rechargeable automotive batteries. *Nature Energy* **3**, 267-278, doi:10.1038/s41560-018-0107-2 (2018).
- 8      Liu, B., Zhang, J.-G. & Xu, W. Advancing Lithium Metal Batteries. *Joule* **2**, 833-845, doi:https://doi.org/10.1016/j.joule.2018.03.008 (2018).

- 9 Hu, Z., Li, J., Zhang, X. & Zhu, Y. Strategies to Improve the Performance of Li Metal Anode for Rechargeable Batteries. *Frontiers in Chemistry* **8**, doi:10.3389/fchem.2020.00409 (2020).
- 10 Dornbusch, D. A., Hilton, R., Lohman, S. D. & Suppes, G. J. Experimental Validation of the Elimination of Dendrite Short-Circuit Failure in Secondary Lithium-Metal Convection Cell Batteries. *Journal of The Electrochemical Society* **162**, A262-A268, doi:10.1149/2.0021503jes (2014).
- 11 Li, B., Wang, Y. & Yang, S. A Material Perspective of Rechargeable Metallic Lithium Anodes. *Advanced Energy Materials* **8**, 1702296, doi:https://doi.org/10.1002/aenm.201702296 (2018).
- 12 Wang, Q. *et al.* Confronting the Challenges in Lithium Anodes for Lithium Metal Batteries. *Advanced Science* **8**, 2101111, doi:https://doi.org/10.1002/advs.202101111 (2021).
- 13 Lin, D., Liu, Y. & Cui, Y. Reviving the lithium metal anode for high-energy batteries. *Nature Nanotechnology* **12**, 194-206, doi:10.1038/nnano.2017.16 (2017).
- 14 Ghazi, Z. A. *et al.* Key Aspects of Lithium Metal Anodes for Lithium Metal Batteries. *Small* **15**, 1900687, doi:https://doi.org/10.1002/smll.201900687 (2019).
- 15 Liu, J. *et al.* Pathways for practical high-energy long-cycling lithium metal batteries. *Nature Energy* **4**, 180-186, doi:10.1038/s41560-019-0338-x (2019).
- 16 Varzi, A. *et al.* Current status and future perspectives of lithium metal

- batteries. *Journal of Power Sources* **480**, 228803,  
doi:<https://doi.org/10.1016/j.jpowsour.2020.228803> (2020).
- 17 Janek, J. & Zeier, W. G. A solid future for battery development. *Nature Energy* **1**, 16141, doi:10.1038/nenergy.2016.141 (2016).
  - 18 Randau, S. *et al.* Benchmarking the performance of all-solid-state lithium batteries. *Nature Energy* **5**, 259-270, doi:10.1038/s41560-020-0565-1 (2020).
  - 19 Zhao, Q., Stalin, S., Zhao, C.-Z. & Archer, L. A. Designing solid-state electrolytes for safe, energy-dense batteries. *Nature Reviews Materials* **5**, 229-252, doi:10.1038/s41578-019-0165-5 (2020).
  - 20 Manthiram, A., Yu, X. & Wang, S. Lithium battery chemistries enabled by solid-state electrolytes. *Nature Reviews Materials* **2**, 16103, doi:10.1038/natrevmats.2016.103 (2017).
  - 21 Zheng, F., Kotobuki, M., Song, S., Lai, M. O. & Lu, L. Review on solid electrolytes for all-solid-state lithium-ion batteries. *Journal of Power Sources* **389**, 198-213, doi:<https://doi.org/10.1016/j.jpowsour.2018.04.022> (2018).
  - 22 Sun, C., Liu, J., Gong, Y., Wilkinson, D. P. & Zhang, J. Recent advances in all-solid-state rechargeable lithium batteries. *Nano Energy* **33**, 363-386, doi:<https://doi.org/10.1016/j.nanoen.2017.01.028> (2017).
  - 23 Deng, Z., Wang, Z., Chu, I.-H., Luo, J. & Ong, S. P. Elastic Properties of Alkali Superionic Conductor Electrolytes from First Principles Calculations. *Journal of The Electrochemical Society* **163**, A67-A74, doi:10.1149/2.0061602jes (2015).



- 24 Yuan, C. *et al.* Coupled crack propagation and dendrite growth in solid electrolyte of all-solid-state battery. *Nano Energy* **86**, 106057, doi:<https://doi.org/10.1016/j.nanoen.2021.106057> (2021).
- 25 Hao, S. *et al.* 3D Imaging of Lithium Protrusions in Solid-State Lithium Batteries using X-Ray Computed Tomography. *Advanced Functional Materials* **31**, 2007564, doi:<https://doi.org/10.1002/adfm.202007564> (2021).
- 26 Porz, L. *et al.* Mechanism of lithium metal penetration through inorganic solid electrolytes. *Advanced Energy Materials* **7**, 1701003 (2017).
- 27 Li, C. *et al.* An advance review of solid-state battery: Challenges, progress and prospects. *Sustainable Materials and Technologies* **29**, e00297, doi:<https://doi.org/10.1016/j.susmat.2021.e00297> (2021).
- 28 Cheng, E. J., Sharafi, A. & Sakamoto, J. Intergranular Li metal propagation through polycrystalline  $\text{Li}_{6.25}\text{Al}_{0.25}\text{La}_3\text{Zr}_2\text{O}_{12}$  ceramic electrolyte. *Electrochimica Acta* **223**, 85-91, doi:<https://doi.org/10.1016/j.electacta.2016.12.018> (2017).
- 29 Wenzel, S., Leichtweiss, T., Krüger, D., Sann, J. & Janek, J. Interphase formation on lithium solid electrolytes—An in situ approach to study interfacial reactions by photoelectron spectroscopy. *Solid State Ionics* **278**, 98-105, doi:<https://doi.org/10.1016/j.ssi.2015.06.001> (2015).
- 30 Wenzel, S. *et al.* Direct Observation of the Interfacial Instability of the Fast Ionic Conductor  $\text{Li}_{10}\text{GeP}_2\text{S}_{12}$  at the Lithium Metal Anode. *Chemistry of Materials* **28**, 2400-2407, doi:10.1021/acs.chemmater.6b00610 (2016).
- 31 Hartmann, P. *et al.* Degradation of NASICON-Type Materials in Contact

- with Lithium Metal: Formation of Mixed Conducting Interphases (MCI) on Solid Electrolytes. *The Journal of Physical Chemistry C* **117**, 21064-21074, doi:10.1021/jp4051275 (2013).
- 32 Han, F. *et al.* High electronic conductivity as the origin of lithium dendrite formation within solid electrolytes. *Nature Energy* **4**, 187-196, doi:10.1038/s41560-018-0312-z (2019).
- 33 Tian, H.-K., Xu, B. & Qi, Y. Computational study of lithium nucleation tendency in Li<sub>7</sub>La<sub>3</sub>Zr<sub>2</sub>O<sub>12</sub> (LLZO) and rational design of interlayer materials to prevent lithium dendrites. *Journal of Power Sources* **392**, 79-86, doi:https://doi.org/10.1016/j.jpowsour.2018.04.098 (2018).
- 34 Ping, W. *et al.* Reversible Short-Circuit Behaviors in Garnet-Based Solid-State Batteries. *n/a*, 2000702, doi:10.1002/aenm.202000702.
- 35 Aguesse, F. *et al.* Investigating the Dendritic Growth during Full Cell Cycling of Garnet Electrolyte in Direct Contact with Li Metal. *ACS Applied Materials & Interfaces* **9**, 3808-3816, doi:10.1021/acsami.6b13925 (2017).
- 36 Kim, S. *et al.* The Role of Interlayer Chemistry in Li-Metal Growth through a Garnet-Type Solid Electrolyte. **10**, 1903993, doi:https://doi.org/10.1002/aenm.201903993 (2020).
- 37 Manalastas, W. *et al.* Mechanical failure of garnet electrolytes during Li electrodeposition observed by in-operando microscopy. *Journal of Power Sources* **412**, 287-293, doi:https://doi.org/10.1016/j.jpowsour.2018.11.041 (2019).
- 38 Swamy, T. *et al.* Lithium Metal Penetration Induced by Electrodeposition

- through Solid Electrolytes: Example in Single-Crystal  $\text{Li}_6\text{La}_3\text{ZrTaO}_{12}$  Garnet. *Journal of The Electrochemical Society* **165**, A3648-A3655, doi:10.1149/2.1391814jes (2018).
- 39 Tsai, C.-L. *et al.*  $\text{Li}_7\text{La}_3\text{Zr}_2\text{O}_{12}$  Interface Modification for Li Dendrite Prevention. *ACS Applied Materials & Interfaces* **8**, 10617-10626, doi:10.1021/acsami.6b00831 (2016).
- 40 Hofstetter, K., Samson, A. J., Narayanan, S. & Thangadurai, V. Present understanding of the stability of Li-stuffed garnets with moisture, carbon dioxide, and metallic lithium. *Journal of Power Sources* **390**, 297-312, doi:https://doi.org/10.1016/j.jpowsour.2018.04.016 (2018).
- 41 Sharafi, A. *et al.* Surface Chemistry Mechanism of Ultra-Low Interfacial Resistance in the Solid-State Electrolyte  $\text{Li}_7\text{La}_3\text{Zr}_2\text{O}_{12}$ . *Chemistry of Materials* **29**, 7961-7968, doi:10.1021/acs.chemmater.7b03002 (2017).
- 42 Han, X. *et al.* Negating interfacial impedance in garnet-based solid-state Li metal batteries. *Nature Materials* **16**, 572, doi:10.1038/nmat4821 (2016).
- 43 Luo, W. *et al.* Reducing Interfacial Resistance between Garnet-Structured Solid-State Electrolyte and Li-Metal Anode by a Germanium Layer. *Advanced Materials* **29**, 1606042, doi:doi:10.1002/adma.201606042 (2017).
- 44 Shao, Y. *et al.* Drawing a Soft Interface: An Effective Interfacial Modification Strategy for Garnet-Type Solid-State Li Batteries. *ACS Energy Letters* **3**, 1212-1218, doi:10.1021/acsenrgylett.8b00453 (2018).
- 45 Krauskopf, T., Richter, F. H., Zeier, W. G. & Janek, J. Physicochemical Concepts of the Lithium Metal Anode in Solid-State Batteries. *Chemical*

- Reviews* **120**, 7745-7794, doi:10.1021/acs.chemrev.0c00431 (2020).
- 46 Luo, W. *et al.* Transition from Superlithiophobicity to Superlithiophilicity of Garnet Solid-State Electrolyte. *Journal of the American Chemical Society* **138**, 12258-12262, doi:10.1021/jacs.6b06777 (2016).
- 47 Huo, H. *et al.* In-situ formed  $\text{Li}_2\text{CO}_3$ -free garnet/Li interface by rapid acid treatment for dendrite-free solid-state batteries. *Nano Energy* **61**, 119-125, doi:https://doi.org/10.1016/j.nanoen.2019.04.058 (2019).
- 48 Ferraresi, G., Uhlenbruck, S., Tsai, C.-L., Novák, P. & Villevieille, C. Engineering of Sn and Pre-Lithiated Sn as Negative Electrode Materials Coupled to Garnet Ta-LLZO Solid Electrolyte for All-Solid-State Li Batteries. *Batteries & Supercaps* **3**, 557-565, doi:https://doi.org/10.1002/batt.201900173 (2020).
- 49 Li, Y. *et al.* Garnet Electrolyte with an Ultralow Interfacial Resistance for Li-Metal Batteries. *Journal of the American Chemical Society* **140**, 6448-6455, doi:10.1021/jacs.8b03106 (2018).
- 50 Murugan, R., Thangadurai, V. & Weppner, W. Fast Lithium Ion Conduction in Garnet-Type  $\text{Li}_7\text{La}_3\text{Zr}_2\text{O}_{12}$ . **46**, 7778-7781, doi:10.1002/anie.200701144 (2007).
- 51 Murugan, R., Ramakumar, S. & Janani, N. High conductive yttrium doped  $\text{Li}_7\text{La}_3\text{Zr}_2\text{O}_{12}$  cubic lithium garnet. *Electrochemistry Communications* **13**, 1373-1375, doi:https://doi.org/10.1016/j.elecom.2011.08.014 (2011).
- 52 Buschmann, H., Berendts, S., Mogwitz, B. & Janek, J. Lithium metal electrode kinetics and ionic conductivity of the solid lithium ion conductors “ $\text{Li}_7\text{La}_3\text{Zr}_2\text{O}_{12}$ ” and  $\text{Li}_{7-x}\text{La}_3\text{Zr}_{2-x}\text{Ta}_x\text{O}_{12}$  with garnet-type

- structure. *Journal of Power Sources* **206**, 236-244,  
doi:<https://doi.org/10.1016/j.jpowsour.2012.01.094> (2012).
- 53 Lee, J.-M. *et al.* High lithium ion conductivity of  $\text{Li}_7\text{La}_3\text{Zr}_2\text{O}_{12}$  synthesized by solid state reaction. *Solid State Ionics* **258**, 13-17,  
doi:<https://doi.org/10.1016/j.ssi.2014.01.043> (2014).
- 54 Samson, A. J., Hofstetter, K., Bag, S. & Thangadurai, V. A bird's-eye view of Li-stuffed garnet-type  $\text{Li}_7\text{La}_3\text{Zr}_2\text{O}_{12}$  ceramic electrolytes for advanced all-solid-state Li batteries. *Energy & Environmental Science* **12**, 2957-2975, doi:[10.1039/C9EE01548E](https://doi.org/10.1039/C9EE01548E) (2019).

## Chapter 2. High-energy and durable lithium metal batteries using garnet-type solid electrolytes with tailored lithium-metal compatibility

(The content of this chapter has been published in *Nature communication*. Reprinted with permission from [Kim, S., Kim, JS., Miara, L. *et al.*, *Nat Commun.*, **2022**, 13, 1883. <https://doi.org/10.1038/s41467-022-29531-x>]. Copyright 2022 Nature Publishing Group.)

### 2.1. Introduction

One of the viable options to increase the energy densities of lithium-ion batteries (LIBs), taking full advantage of the state-of-the-art LIB technology, is to adopt Li-metal anode in the cell, which affords the highest theoretical capacity ( $3,860 \text{ mAh g}^{-1}$ ) among the anode materials<sup>1,2</sup>. However, practical limitations such as dendrite growth, low Coulombic efficiency, and safety issues remain unresolved despite extensive efforts to apply Li-metal anode in LIBs<sup>3-5</sup>. Recent progress in the development of solid-state electrolytes has provided a promising new opportunity for using Li-metal anodes, whose mechanical rigidity can effectively suppress lithium dendrite short-circuiting, which together with the non-flammable characteristics can secure the safety of a battery<sup>6,7</sup>. Garnet-type oxide electrolytes, *e.g.*  $\text{Li}_7\text{La}_3\text{Zr}_2\text{O}_{12}$  (LLZO), are some of the leading candidates for Li-metal solid-state batteries, and show high ionic conductivities at room temperature ( $\sim 1 \text{ mS cm}^{-1}$ ), along with excellent chemical stability with lithium metal<sup>8-10</sup>. Owing to the stability of LLZO in ambient air, which is beneficial in the fabrication of solid-state

batteries, it is widely considered as a promising and feasible solid electrolyte. Nevertheless, no prior study to date has reported that the LLZO-based Li-metal batteries with acceptable electrochemical performances for practical applications. This is primarily attributed to the unexpected short-circuiting caused by lithium metal piercing through the LLZO at practical current densities<sup>11,12</sup>. Various mechanisms underlying this phenomenon have been proposed, including crack propagation induced by stress concentration on the LLZO surface<sup>13-16</sup> and non-uniform current distribution caused by poor contact between the Li metal and LLZO<sup>17-19</sup>.

Recent studies of lithium penetration suggested that the electronic conductivity of LLZO can contribute to substantial lithium formation inside LLZO, causing premature short-circuiting<sup>12,20</sup>. Although the underlying mechanism is debatable, studies have begun to reveal that the non-zero electronic conductivity of solid electrolyte can promote lithium nucleation both in the bulk and at the grain boundary of the electrolyte<sup>12,21-23</sup>. In particular, presumably higher electronic conductivity along the grain boundary may facilitate nucleation and growth of the lithium metal throughout the electrolyte, expediting the short-circuiting between the two electrodes<sup>23,24</sup>. In addition, previous literature reports have suggested that the doped-LLZOs can yield electronically conductive by-products via chemical/electrochemical reduction upon contact with Li-metal at the interface<sup>10,25,26</sup>. If lithium metal precipitates along the grain boundaries, the subsequent by-products with high electronic conductivity cannot passivate the decomposition reaction and therefore would more critically accelerate the short-circuiting along the grain boundaries in the doped-LLZO solid-state electrolytes. As various dopants have been

used to optimise the ionic conductivity of LLZOs<sup>26-28</sup>, these possibilities should not be overlooked.

In this study, we particularly pay attention to the potential by-product formation along grain boundaries by tailoring the LLZO-based solid electrolyte for stability and passivation against lithium penetration. The original idea is to adjust the by-products of LLZO by selecting suitable dopants for the grain boundary and bulk, considering the compatibility between doped-LLZO and lithium, without compromising the overall ionic conductivity. To achieve this goal, we investigate the stabilities of bulk LLZOs doped with various dopants with Li-metal. A subsequent process to selectively alter the grain boundaries by solution-based etching that permeates LLZO solid-electrolyte pellets is implemented. It is envisioned that such treatment would accompany a substantial compositional change specifically at the grain boundary, *e.g.* lithium substitution by protons during acid etching<sup>29,30</sup>. This is expected to suppress the formation of conductive by-products, while preserving the high bulk ionic conductivity of doped-LLZO. Besides, we reveals our interfacial treatment method effectively releases the residual stress in LLZO and aid in the maintenance of an intact contact at the interface.

In the following discussion, it is demonstrated that the rational selection of dopants and etching agents can lead to a significant enhancement in the performance of a practical full cell consisting of a conventional cathode (*i.e.*  $\text{LiNi}_{1/3}\text{Co}_{1/3}\text{Mn}_{1/3}\text{O}_2$  (NCM111)) at a commercially applicable loading capacity with a thin Li-metal anode (20  $\mu\text{m}$ ) and LLZO electrolyte. The cell delivers an areal capacity of 3.2  $\text{mAh cm}^{-2}$  for 1,000 cycles at C/2 rate with a capacity retention of 95.0%. The feasibility of the



new cell with 110- $\mu\text{m}$ -thick Ta-LLZO solid electrolyte further indicates its potential in delivering a remarkable energy density of  $470 \text{ Wh L}^{-1}$ . More importantly, an all-solid-state cell using  $5 \text{ mAh cm}^{-2}$  composite cathode also delivers  $4000 \text{ mAh cm}^{-2}$  at  $3 \text{ mA cm}^{-2}$ . This is the first report that describes solid-state cells with a Li-metal anode that can meet the lifespan requirements of general commercial applications: (i) 500 cycles without Li-metal shorting; (ii) at an operating current density of  $1.5 \text{ mA cm}^{-2}$  (0.5 C rate); (iii) with Li-metal utilisation per cycle of over  $3 \text{ mAh cm}^{-2}$ .<sup>31,32</sup> These findings are expected to advance the development of solid-state batteries with garnet solid electrolytes by highlighting that a coupled approach to designing the bulk and grain boundaries of the solid electrolyte plays a key role in achieving the long-term stability of solid-state batteries.

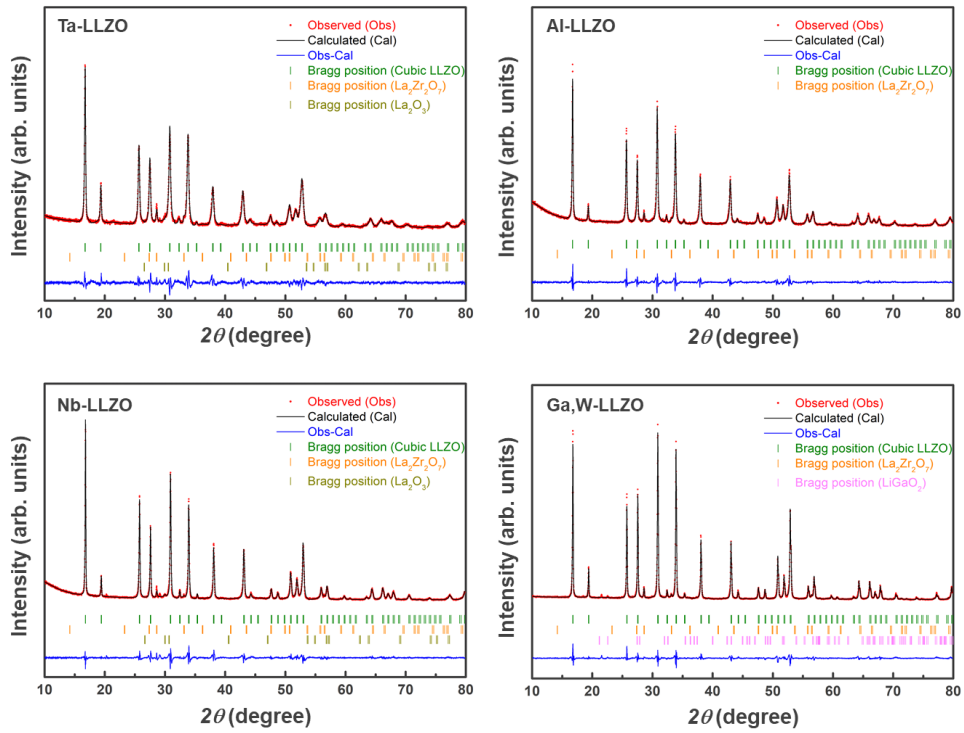
## 2.2. Experimental and computational details

### 2.2.1. Material synthesis

We prepared Ta-, Al-, Nb-, and Ga,W-LLZO using a solid-state synthesis technique with  $\text{Li}_2\text{CO}_3$  (>99.0%, ChemPoint),  $\text{La}_2\text{O}_3$  (98.6%, MolyCorp), and  $\text{ZrO}_2$  (98%, Zircoa Inc.) as the starting precursors. As dopants, we used  $\text{Ta}_2\text{O}_5$  (99.99%, Sigma Aldrich),  $\text{Al}_2\text{O}_3$  (99.99%, Sigma Aldrich),  $\text{Nb}_2\text{O}_5$  (99.9%, Sigma Aldrich),  $\text{Ga}_2\text{O}_3$  (99.99%, Sigma Aldrich), and  $\text{WO}_2$  (99.9%, Alfa Aesar).  $\text{La}_2\text{O}_3$  was heat treated in  $\text{N}_2$  at 1,000 °C for 5 h before use. We mixed the powders at stoichiometry and calcined them in air at 950 °C for 5 h followed by 1,200 °C for 5 h with a heating rate of 150 °C h<sup>-1</sup>. After calcining, the powder was ball milled for 10 min at 300 rpm at the ball-to-powder ratio of 400 wt% by planetary milling (Pulverisette 7, Fritsch, Germany). Ball milling was repeated 12 times with a 5 min interval. The as-prepared powder was mainly a cubic garnet phase along with small amounts of impurity phases,  $\text{La}_2\text{Zr}_2\text{O}_7$  and  $\text{La}_2\text{O}_3$ . However, the tetragonal phase was not detected (Figure 2.1). The particle size distribution was measured by using the particle size analyser (Bluewave, Microtrac). All samples had similar bimodal particle size distributions with peaks at 0.4 and 4 µm, showing approximately the same average particle sizes of 0.7-0.8 µm (Figure 2.2). We hot-pressed 100 g of calcined powder in a graphite die at 1,100 °C for 2 h and 20 MPa in Ar gas with a heating rate of 300°C min<sup>-1</sup>. The relative density of the obtained pellet was >98% with respect to the theoretical density of LLZO calculated from the XRD data. The pellet was cut using a wire saw into 360-µm-thick slices, which were then laser cut into 14-mm-diameter discs, followed by ultrasonic cleaning in hexane for 10 min and heat treatment at 800 °C

for 1 h in an air-controlled box furnace filled with dry air. For the heat treatment, we placed the garnet discs in a Pt container lined with  $\sim 100$   $\mu\text{m}$  thick sintered garnet tape of the same composition. The surface of the obtained pellet was polished to a thickness of about 350  $\mu\text{m}$  using polishing machines (LaboForce-3, Struers).

We carried out acid treatment for modifying the LLZO surface by simply immersing the discs into a 1 M HCl solution (in distilled water) at a weight ratio of 1:10 (pellet:acid solution) at room temperature. To prevent local variations in concentration of the acid solution due to the released lithium and/or prevent close contact between the electrolyte and the container, the container was rolled at about 60 rpm during protonation. We then removed the solution, washed the discs with ethanol, and dried them in a dry room.



Sample	Phase	Lattice parameter (a, Å)	Cell volume (Å <sup>3</sup> )	Phase fraction (wt.%)	R <sub>i</sub> (%)	R <sub>f</sub> (%)
Li <sub>6.5</sub> La <sub>3</sub> Zr <sub>1.5</sub> Ta <sub>0.5</sub> O <sub>12</sub> (R <sub>p</sub> : 5.21 %, R <sub>wp</sub> : 6.58 %)	Cubic	12.9816 (4)	2187.7 (1)	96.3 (7)	2.30	1.83
	La <sub>2</sub> Zr <sub>2</sub> O <sub>7</sub>	10.80732	1262.275	2.88 (7)		
	La <sub>2</sub> O <sub>3</sub>	3.9337 (6.1387)	82.263	0.82 (3)		
Li <sub>6.25</sub> Al <sub>0.25</sub> La <sub>3</sub> Zr <sub>2</sub> O <sub>12</sub> (R <sub>p</sub> : 3.37 %, R <sub>wp</sub> : 4.47 %)	Cubic	12.9894 (2)	2191.63 (5)	97.6 (6)	1.63	1.64
	La <sub>2</sub> Zr <sub>2</sub> O <sub>7</sub>	10.80732	1262.275	2.42 (6)		
	La <sub>2</sub> O <sub>3</sub>					
Li <sub>6.5</sub> La <sub>3</sub> Zr <sub>1.5</sub> Nb <sub>0.5</sub> O <sub>12</sub> (R <sub>p</sub> : 4.38 %, R <sub>wp</sub> : 6.11 %)	Cubic	12.9344 (2)	2163.92 (6)	97.7 (6)	2.32	1.76
	La <sub>2</sub> Zr <sub>2</sub> O <sub>7</sub>	10.80732	1262.275	1.98(7)		
	La <sub>2</sub> O <sub>3</sub>	3.9337 (6.1387)	82.263	0.33(4)		
Li <sub>4.9</sub> Ga <sub>0.5</sub> La <sub>3</sub> Zr <sub>1.7</sub> W <sub>0.3</sub> O <sub>12</sub> (R <sub>p</sub> : 5.09 %, R <sub>wp</sub> : 6.59 %)	Cubic	12.9447 (1)	2169.10 (4)	97.0 (5)	2.20	3.00
	La <sub>2</sub> Zr <sub>2</sub> O <sub>7</sub>	10.80732	1262.275	2.49 (6)		
	LiGaO <sub>2</sub>	3.9337 (6.1387)	82.263	0.5 (1)		

\* For the reliability of the data, only scale factor was set as a refinement parameter for the impurity phases.

**Figure 2.1.** XRD patterns and Rietveld refinement results of the as-made LLZO powders doped with various metals such as Ta, Al, Nb, and Ga,W. Each powder sample shows a cubic garnet phase as a main phase with a small amount of impure phases, such as  $\text{La}_2\text{Zr}_2\text{O}_7$  (about 2~3 % for all compositions),  $\text{La}_2\text{O}_3$  (less than 1% for Ta-LLZO and Nb-LLZO) and  $\text{LiGaO}_2$  (about 0.5% for Ga,W-LLZO).

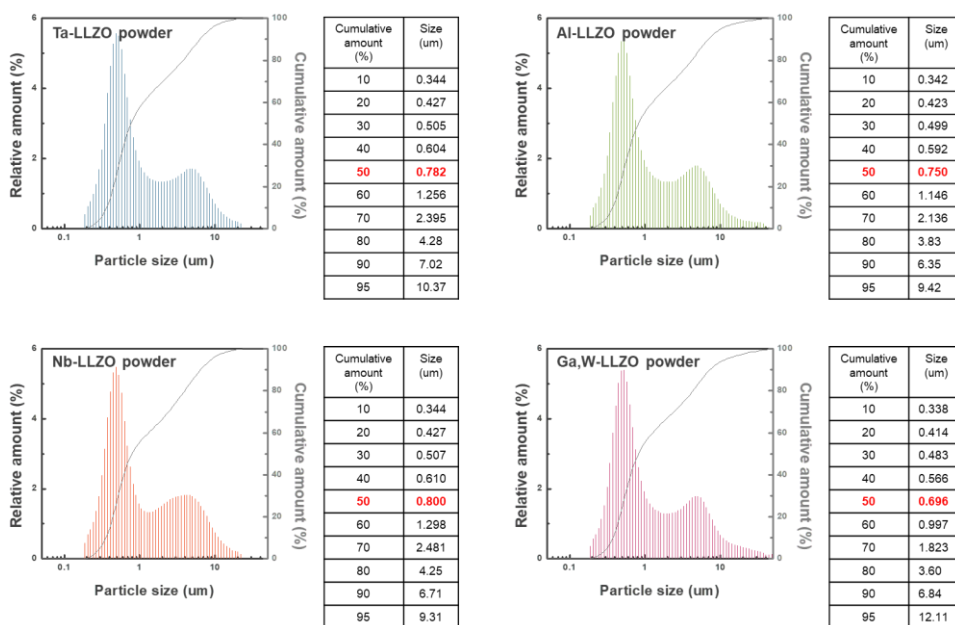


**Figure 2.2.** Particle size distribution of the LLZO powders with various dopants, Ta, Al, Nb and Ga,W. All the samples exhibit similar bimodal particle size distribution with peaks at 0.4 and 4  $\mu\text{m}$ , showing roughly the same average particle sizes with  $D_{50} \sim 0.7\sim 0.8 \mu\text{m}$ .

### 2.2.2. Coloration test

To prepare a flat, smooth surface, we carefully polished the surface of a prepared pellet with P800-, 1200-, 2400-, and 4000-grit SiC abrasive paper to a thickness of  $\sim 300\text{ }\mu\text{m}$ . The last two steps were performed in an Ar glove box to minimize surface contamination from exposure to air. Then, we attached the Li-metal electrode, scratched using a brush to expose the fresh Li-metal surface, to the prepared LLZO, and applied a pressure of 250 MPa to the assemblies using a cold isostatic press to effectively adhere the Li-metal foil to the LLZO. After assembly, we placed each pellet on a part of a 2032-coin cell and heated them up to  $200\text{ }^{\circ}\text{C}$  over a period of 10 min on a hot plate. (Molten metal is commonly applied directly to a ceramic pellet for chemical coloration tests. However, this can crack the pellet owing to thermal shock, and the contact of the molten lithium with LLZO can vary depending on the surface condition of LLZO<sup>19</sup>.)

### 2.2.3. Characterizations of the solid electrolytes

We characterized the crystal structures of the LLZO electrolytes using XRD. Diffraction patterns of the LLZO pellets before and after the coloration test, the as-made powder and the tape-cast LLZO electrolyte were collected using a PANalytical (Empyrean) diffractometer with Cu K $\alpha$  radiation ( $\lambda = 1.5406\text{ }\text{\AA}$ ). The data were recorded in the  $2\theta$  range of  $10^{\circ}$ – $90^{\circ}$ , with a step size of  $0.02^{\circ}$  and a step time of 4.5 s. X-ray diffraction patterns for the original pristine pellets, protonated pellets and the crushed pellets, which were subjected to Rietveld refinement, were collected on another PANalytical (Empyrean) diffractometer equipped with a monochromator and Cu K $\alpha$  radiation ( $\lambda = 1.5406\text{ }\text{\AA}$ ) to obtain the high resolution to precisely

deconvolute the overlapped patterns arising from the coexistence of the two LLZO phases (cubic vs. tetragonal phases). The data were recorded in the  $2\theta$  range of  $10^\circ$ – $120^\circ$ , with a step size of  $0.01313^\circ$  and a step time of 1.6 seconds. In order to prevent the exposure of the electrolytes to the ambient atmosphere, all pellet samples were examined in an air-tight holder.

We conducted XPS with a Quantum 2000 Scanning ESCA Microprobe (Physical Electronics, Inc.) spectrometer using focused monochromatised Al  $K\alpha$  radiation (1,486.6 eV). The residual pressure inside the XPS analysis chamber was  $9.3 \times 10^{-10}$  Pa. To avoid any contamination, we transferred the LLZO pellets from the Ar-filled glove box to the XPS chamber using a specially designed air-proof chamber.

We examined the surface morphology and cross-sectional microstructure of the acid-treated LLZO electrolytes using an SU-8030 FE-SEM (Hitachi) coupled with an EDS spectrometer with a 5 kV accelerating voltage and an 8 mm working distance. We evaluated the mechanical strength according to the ring-on-ring test using an MTS 10D Load Frame, with a 1.9 cm diameter support ring and 0.635 cm diameter load ring, both available from Sintech Corporation.

We prepared cross-sectional samples for TEM at the LLZO surfaces using a focused ion beam (FIB, FEI-Helios 450-F1) and finally milled them with Ga ions at a 5 kV acceleration voltage. We acquired bright-field (BF) TEM images and SAD patterns to identify the phase and crystallinity of LLZO near the surface using double Cs-corrected TEM (FEI Titan cubed 60-300). We conducted TEM with minimum e-beam exposure conditions because LLZO is prone to transform into its amorphous phase under strong e-beam irradiation.



Phase fraction of each compound was obtained by Rietveld refinement using the crystallographic information file. The Thompson-Cox-Hastings pseudo-Voigt function was applied to determine the shape of the diffraction peak. Rietveld refinement was conducted for the phase fraction analysis of the XRD patterns of the pellet samples using the Fullprof program.<sup>33,34</sup>

#### **2.2.4. Electrochemical characterization**

We prepared asymmetric cells and symmetric cells with 14-mm diameter pellets that were polished to remove the surface contamination to the maximum extent possible, using P800-, 1200-, and 2000-grit SiC abrasive paper, or protonated as demonstrated in the previous section in a dry room, where the dew point was maintained under  $-50\text{ }^{\circ}\text{C}$ . In either case, prepared pellets were rinsed with ethanol and dried in a dry room, and any remaining dust was blown using high pressure  $\text{N}_2$  gas gun. For symmetric cells, Li-metal electrodes, 100- $\mu\text{m}$ -thick Li-metal on 10- $\mu\text{m}$ -thick Cu foil (Honjo Metal Co., Ltd.) with a diameter of 8 or 11 mm, were placed onto both side of the pellet, and the assembly was vacuum sealed inside a polymer-coated aluminum pouch, which is commonly used for battery fabrication. Then, Li-metal anodes were attached by applying a pressure of 250 MPa for 3 min using a cold isostatic press to improve the physical contact between the LLZO pellet and Li-metal anode. We also prepared asymmetric cells with a blocking gold electrode sputtered onto one side of the LLZO pellet and a non-blocking Li-metal electrode on the opposite side, which was attached in the same manner as the symmetric cell electrodes. Finally, we assembled the cells applying our modified 2032-type coin cell configuration. The cells were constructed as a conventionally structured coin

cell, except for the spring used to apply the pressure. Instead, we vacuum-sealed the cells in an aluminum pouch, with extended lines for electrical connection. With this configuration, we could prevent air exposure and apply a constant atmospheric pressure by maintaining the vacuum state. Using these cells, we performed the EIS measurements, galvanostatic cycling tests, and critical current density measurements.

EIS measurements were conducted at 60 and 25 °C at an open-circuit voltage in the galvanostatic mode over a frequency range of 0.1–10 kHz using an alternating current (AC) perturbation of 10 mV, using a frequency response analyser (Solartron, SI 1255 FRA) in conjunction with a potentiostat (Solartron, SI 1287 ECI). We recorded the spectra at various time intervals and compared the spectra recorded for each LLZO pellet to understand how the reactivity of LLZO with lithium varies with composition. The intercept on the real impedance axis in the high-frequency region corresponds to the resistance of the bulk LLZO electrolyte. The low-frequency semi-circle with a tail results from the interfacial resistance at the LLZO/Li electrode interface and the capacitance at the LLZO/Au electrode interface.<sup>35</sup> Note that the interfacial impedance estimated from the EIS spectra solely represents the chemical reactions at the interface over time because we applied a small potential perturbation (10 mV) at the open-circuit voltage. This implies that significant lithium plating (or stripping), which affects the physical contact conditions, did not occur when EIS experiments were conducted.

Galvanostatic cycling tests were conducted on the symmetric cells at 60 and 25 °C at a current density of 0.2 mA cm<sup>-2</sup> with 1 h of Li plating/stripping. The critical current density measurements were performed for pristine and protonated Ta–LLZO

and Al–LLZO solid electrolytes at 60 and 25 °C. The cells employed 100- $\mu\text{m}$ -thick Li metal on 10- $\mu\text{m}$ -thick Cu foil with a diameter of 11 mm ( $0.95\text{ cm}^2$ ) for the tests at 60 °C or 8 mm ( $0.50\text{ cm}^2$ ) for the tests at 25 °C, and they were cycled twice with 30 min of lithium plating/stripping at each current density. The current density was increased from 0.1 to  $1\text{ mA cm}^{-2}$  at a step size of  $0.1\text{ mA cm}^{-2}$  and from 1.0 to  $3.0\text{ mA cm}^{-2}$  at a step size of  $0.2\text{ mA cm}^{-2}$ .

To evaluate the electrochemical performance of the LLZO solid electrolyte in a battery full cell using a Li-metal anode, we introduced a hybrid electrolyte cell in which an ionic liquid electrolyte was used as the cathode electrolyte (catholyte) and a solid oxide electrolyte was used as the Li-metal anode electrolyte (anolyte). For the dual-structured electrolytes, a full cell with a high-loading cathode (active material  $\geq 93\text{ wt}\%$ ) was fabricated via infiltration with the liquid catholyte, and microscale short circuits were clearly detected by monitoring the potential transient curves under galvanostatic charging mode. We used coin cells (20 mm diameter) in all full-cell measurements. We fabricated the hybrid electrolyte cells in a dry-room using an ionic liquid as the catholyte and an LLZO solid electrolyte as the anolyte. First, 20- $\mu\text{m}$ -thick Li metal on 10- $\mu\text{m}$ -thick Cu foil (Honjo Metal Co., Ltd.) was attached to the protonated surface of the LLZO pellet by cold-isostatic pressing at 250 MPa. We used a commercially available NCM111 electrode (loading capacity:  $3.2\text{ g cm}^{-3}$ , active material: 93 wt%; Samsung SDI) coated onto Al foil as the cathode. The ionic liquid Pyr13FSI (Kanto Chemical Co. Inc.) was mixed with LiFSI salt (2 M) to prepare the catholyte. We dropped the mixed solution onto the cathode and then infiltrated it into the cathode under a vacuum for 2 h. The infiltrated amount of ionic liquid was 20 wt% relative to the cathode weight. We placed the infiltrated

cathode on the other side of the LLZO pellet in a 2032 coin cell. To eliminate the possibility of direct contact between the ionic liquid and Li-metal, we used a relatively small cathode (0.4 cm in diameter) for the hybrid electrolyte cell. Finally, we sealed the cell under vacuum using a pouch cell. The charge/discharge characteristics of the hybrid electrolyte cells were examined at 60 and 100 °C using a battery cycler (TOSCAT-3100, Toyo System). The cells were charged using a conventional constant current (CC)–constant voltage (CV) protocol and discharged in CC mode in the potential range of 2.85–4.2 V (vs. Li<sup>+</sup>/Li). The electrochemical profiles at 60 °C were obtained by increasing the current density stepwise; *i.e.*, the cells were charged/discharged with current densities of 0.3 mA cm<sup>-2</sup> for the first cycle, 0.5 mA cm<sup>-2</sup> for the next five cycles, 1 mA cm<sup>-2</sup> for the subsequent five cycles, 1.6 mA cm<sup>-2</sup> for the 12<sup>th</sup> to the 21<sup>st</sup> cycle, 2 mA cm<sup>-2</sup> for the 22<sup>nd</sup> to the 31<sup>st</sup> cycle, and 3 mA cm<sup>-2</sup> for the 32<sup>nd</sup> to the 41<sup>st</sup> cycle. For the rate capability test at 100 °C, the cells were operated with increasing current densities. The cells were cycled at 0.3 mA cm<sup>-2</sup> for the first cycle and then the current densities are increased from 0.5 and 1 mA cm<sup>-2</sup> to 1.6 mA cm<sup>-2</sup> and then increased from 2.0 to 10.0 mA cm<sup>-2</sup> at a step size of 1.0 mA cm<sup>-2</sup>. The cells were cycled for five times at each current density. For data reliability, we evaluated five cells for each electrolyte. To further confirm the interface stabilization effect on the cell performance, we conducted long-term cycling tests on the NCM111/protonated Ta-LLZO/Li hybrid cells using two NCM111 cathodes with capacities of 2 and 3.2 mAh cm<sup>-2</sup>. With 2 mAh cm<sup>-2</sup> cathode, the cells were charged/discharged with current densities of 0.3 mA cm<sup>-2</sup> for the first cycle, 0.5 mA cm<sup>-2</sup> for the next two cycles, 1 mA cm<sup>-2</sup> for the subsequent two cycles, and cycled at current densities 3 mA cm<sup>-2</sup> for 2000 times. With 3.2 mAh cm<sup>-2</sup> cathode,

the cells were charged/discharged with current densities of 0.3 mA cm<sup>-2</sup> for the first cycle, 0.5 mA cm<sup>-2</sup> for the next five cycles, 1 mA cm<sup>-2</sup> for the subsequent five cycles, and cycled at current densities 3 mA cm<sup>-2</sup> for 1000 times.

### 2.2.5. Calculation details

The structures of the doped garnets (Ta, Al, Nb, Ga, W, and H) were determined from the original experimentally determined structure of Li<sub>7</sub>La<sub>3</sub>Zr<sub>2</sub>O<sub>12</sub>. Metal dopants were introduced at appropriate sites (i.e., Ta, Nb, and W in Zr sites; Al and Ga in Li sites). The lithium ions were removed as vacancies from the highest energy sites to maintain charge neutrality. In the protonated structures, lithium ions were partially substituted by hydrogen ions. The electrostatic energy criterion was considered for the analysis performed using the Python Materials Genomics (pymatgen) package<sup>36</sup> to pre-screen structures with Li<sup>+</sup>/Al<sup>3+</sup>(Ga<sup>3+</sup>)/vacancy and Ta<sup>5+</sup>(Nb<sup>5+</sup>, W<sup>5+</sup>)/Zr<sup>4+</sup> orderings to obtain the lowest-energy structure. We then performed structural optimization experiments and total energy calculations using the DFT method with the Perdew–Burke–Ernzerhof (PBE) generalised-gradient approximation (GGA),<sup>37</sup> implemented in the Vienna Ab initio Simulation Package (VASP).<sup>38</sup> We used the projector augmented wave potentials with a kinetic energy cut-off of 520 eV and a k-point grid of  $\geq 500/n_{\text{atoms}}$  for all the calculations.

We evaluated the electrochemical stability from grand canonical phase diagrams following reported protocols.<sup>39,40</sup> The oxidation and reduction limits of the stability window were defined as the voltage limits at which the material begins to get oxidised via the process of lithium extraction or reduced via the method of lithium insertion, respectively. To determine the relevant phase diagrams, we obtained the

DFT total energies of all the related compounds in the given quinary system of Li-La-Zr-O-M (where M = dopant) from the Materials Project database [[www.materialsproject.org](http://www.materialsproject.org)]. The data presented in the database were computed using the same DFT method that we had followed.

## 2.3. Results and Discussion

### 2.3.1. Chemical stabilities of doped-LLZOs against Li metal

Doping the LLZOs is important to attain a high ionic conductivity of the LLZO solid electrolyte<sup>41-43</sup>; however, the stability of doped LLZO with Li metal may substantially differ depending on the dopants<sup>28,44-46</sup>. To compare the effect of the dopant on the stability, chemical colouration<sup>47</sup> tests were performed, which visually showed the reactivity between the Li-metal and LLZO pellets (Figure 2.3). The test was performed using LLZOs with four representative dopants:  $\text{Li}_{6.5}\text{La}_3\text{Zr}_{1.5}\text{Ta}_{0.5}\text{O}_{12}$  (Ta-LLZO),  $\text{Li}_{6.25}\text{Al}_{0.25}\text{La}_3\text{Zr}_2\text{O}_{12}$  (Al-LLZO),  $\text{Li}_{6.5}\text{La}_3\text{Zr}_{1.5}\text{Nb}_{0.5}\text{O}_{12}$  (Nb-LLZO) and  $\text{Li}_{4.9}\text{Ga}_{0.5}\text{La}_3\text{Zr}_{1.7}\text{W}_{0.3}\text{O}_{12}$  (Ga,W-LLZO); these dopants have been most commonly used to increase the Li-ion conductivity or density of the LLZO pellet<sup>41-43</sup>. The physical properties of doped LLZO electrolyte pellets such as their crystal structures, morphology with relative density, and ionic conductivity are presented in Figure 2.4-2.6. To accelerate the potential reaction between Li metal and LLZO, the pellets were heated to 200 °C, which was close to the melting point of Li metal, over the observation period. Figure 2.3 shows the difference in the stabilities of the LLZOs against Li metal depending on the dopants. Initially, the Li was plainly visible beneath the thin LLZO pellet for all the samples without an apparent side reaction. In the case of Ta- and Al-LLZOs, the contact area slightly darkened over time; however, no significant change in color was observed even after 8 h. Meanwhile, Nb- and Ga,W-LLZOs showed pronounced degradation under same experimental conditions. The contact area of Nb-LLZO began to darken from the contact area within only 10 min, subsequently becoming black and fracturing into

pieces after 1 h. This observation was consistent with those reported in prior studies, where Nb-containing garnet-type solid electrolytes discolored after the electrochemical test, suggesting that  $\text{Nb}^{5+}$  could have been reduced to  $\text{Nb}^{4+}$  <sup>46,48</sup>. Ga,W-LLZO showed more severe changes in a few minutes. In addition to the color change, the Li metal penetrated the pellet (Figure 2.7). The reaction proceeded until the Li was completely consumed, and the entire pellet turned black with significant pulverization. Considering that LLZOs with four different compositions did not show noticeable differences in the crystal structures, relative phase amounts, and microstructures, but only differed in the dopant characteristics, the rapid color change and/or Li metal penetration in these experiments suggested that the LLZO with certain dopants could substantially react with Li during long-term cycling of the batteries.

The doped-LLZO samples were carefully analyzed after the coloration tests (Figure 2.8-2.12). Energy-dispersive X-ray spectroscopy (EDS) data (Figure 2.8) revealed a significant segregation of La and Zr with extensive micro-crack formation in the case of Nb- and Ga,W-LLZO, indicating instability upon prolonged exposure to Li-metal, while Ta- and Al-LLZO remained intact. The cross-sectional lithium distribution examined by secondary ion mass spectrometry (SIMS; Figure 2.9) also indicated that the entire Nb- and Ga,W-LLZO pellets reacted with Li-metal blurring the initial boundary between the Li and LLZO, while Ta-LLZO was less affected. Consistent with the chemical coloration results, the X-ray diffraction (XRD) patterns (Figure 2.10) showed substantially broadened peaks for Ga,W-LLZO, indicating the loss of crystallinity owing to the side reaction with Li-metal, accompanied by reduction of the electrolyte (Figure 2.11) and pellet pulverization.



The peaks for Nb–LLZO were also altered due to the changes of the lattice parameters and the relative phase amounts of the cubic and tetragonal phases (Figure 2.12), accompanied by Li insertion into the garnet structure with Nb<sup>5+</sup> reduction<sup>49</sup>. Notably, when the cross-section of the reacted Nb–LLZO pellet was examined, Li had propagated through the grain boundary region<sup>50</sup> (Figure 2.13). This indicated that, even without electrochemical bias, the chemical instability of doped-LLZO against Li could lead to high Li metal penetration through the solid-state electrolyte along the grain boundaries. In addition, Ta– and Al–LLZOs, which appeared stable during the chemical colouration test, partially reacted with Li, resulting in new sets of XRD peaks at approximately 20.4° and 31.6°. These peaks could be assigned to Li<sub>2</sub>ZrO<sub>3</sub> and ZrO<sub>2</sub>, respectively, implying that Ta- and Al-LLZOs underwent side reactions even though they appeared stable at the macroscale, which presumably occurred locally, unlike in the case of Nb– and Ga,W–LLZO.

The observed chemical stability of the doped LLZOs was proportionally correlated to the electrochemical performance of Li/LLZO solid-state cells. Figure 2.14a shows the electrochemical impedance spectroscopy (EIS) results for Li/doped-LLZO/Au half-cells as a function of time. The EIS spectra of Ta– and Al–LLZO showed minor changes in the low-frequency semi-circle tail over time, indicating a slight increase in the interfacial impedance. In contrast, the spectra of Nb– and Ga,W–LLZOs were significantly altered with respect to both the low-frequency interfacial impedance and high-frequency region corresponding to the resistance of the bulk LLZO electrolyte. Nb–LLZO showed an additional interfacial impedance, which can be attributed to the substantial formation of by-products at the interface<sup>48</sup>, together with an increase in the bulk resistance due to the degradation of the garnet

structure<sup>51</sup>. (See Figure 2.15 for more details.) For Ga,W–LLZO, the impedance decreased over time; however, this was due to substantial lithium propagation into the pellet, which decreased the geometric distance between the electrodes. The relative stability of the EIS spectra for Ta- and Al-doped LLZOs compared to those of Nb- and Ga,W-doped LLZOs is consistent with the tendency observed through the chemical reaction with Li-metal. This is also critical in the galvanostatic cycling performances of Li/LLZO/Li symmetric cells. Figure 2.14b shows the time-dependent voltage profile of each symmetric cell for electrochemical lithium deposition/stripping at a current density of  $0.2 \text{ mA cm}^{-2}$  at  $60^\circ\text{C}$ . The cells with Ta- or Al–LLZO showed relatively stable voltage profiles during 160 h of cycling. In contrast, the cell with Nb–LLZO showed a continuous increase in polarisation over repeated cycles, which is in agreement with the EIS result showing increasing bulk and interfacial resistances over time. Comparing the EIS results before and after cycling, both the bulk and interfacial resistances changed significantly (Figure 2.16). Ga,W–LLZO showed an unstable profile with large perturbations in voltage, suggesting that dynamic short circuits were formed inside the solid electrolyte<sup>52,53</sup>.

To elucidate the observed distinct stabilities of the LLZOs, even with small dopant concentrations, theoretical calculations to determine the thermodynamic stability of the doped-LLZOs were performed using the density functional theory (DFT). Grand potential phase diagrams were constructed<sup>39,54</sup>, and the stabilities of the doped-LLZOs were examined against a reservoir of lithium (Figure 2.17). These results show that LLZOs become highly susceptible to reduction by Li-metal in the presence of dopants, yielding metallic by-products, which is consistent with previous reports describing that very few metal dopants in oxide systems are stable against lithium<sup>26,27</sup>.

All dopants, including Ta and Al, tend to diminish the reduction stability of the LLZOs compared to that of the undoped LLZO in the order of Ga, W-, Nb-, Ta-, and Al. Upon exposure to lithium, the reduction of the LLZOs leads to the formation of electronically conductive by-products such as Ta,  $\text{Al}_3\text{Zr}$ , W/Ga,  $\text{LiNbO}_2$  (followed by complete reduction to Nb), and  $\text{Zr}_3\text{O}$ , as indicated by the red and orange bars in Figure 2.17. The presence of metallic by-products can lead to a failure in passivating the reaction between Li-metal and doped-LLZO, rapidly propagating the reductive decomposition throughout the LLZO electrolyte.

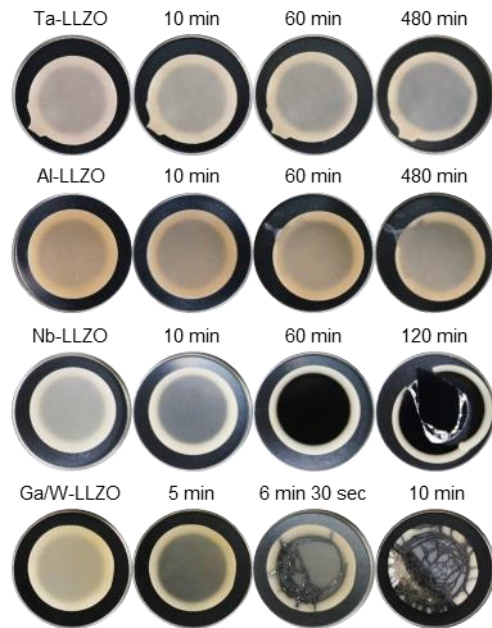


**Figure 2.3.** Optical images of LLZO pellets in contact with Li metal at 200 °C over time after assembly under a cold isostatic pressure of 250 MPa.

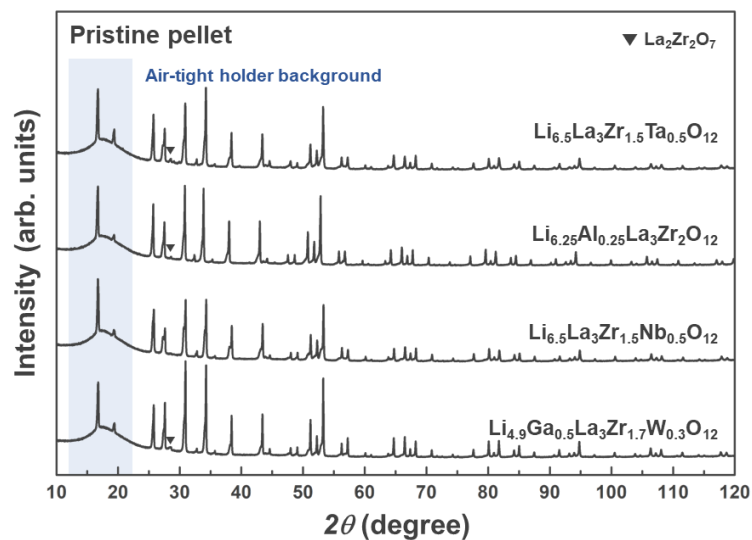


**Figure 2.4.** X-ray diffraction (XRD) patterns of the doped-LLZO pellets with various dopants. All pellets consist of cubic and tetragonal LLZO phases. Regardless of the form of LLZOs, trace amounts of impurity phases, such as  $\text{La}_2\text{Zr}_2\text{O}_7$  and  $\text{La}_2\text{O}_3$  are detected.

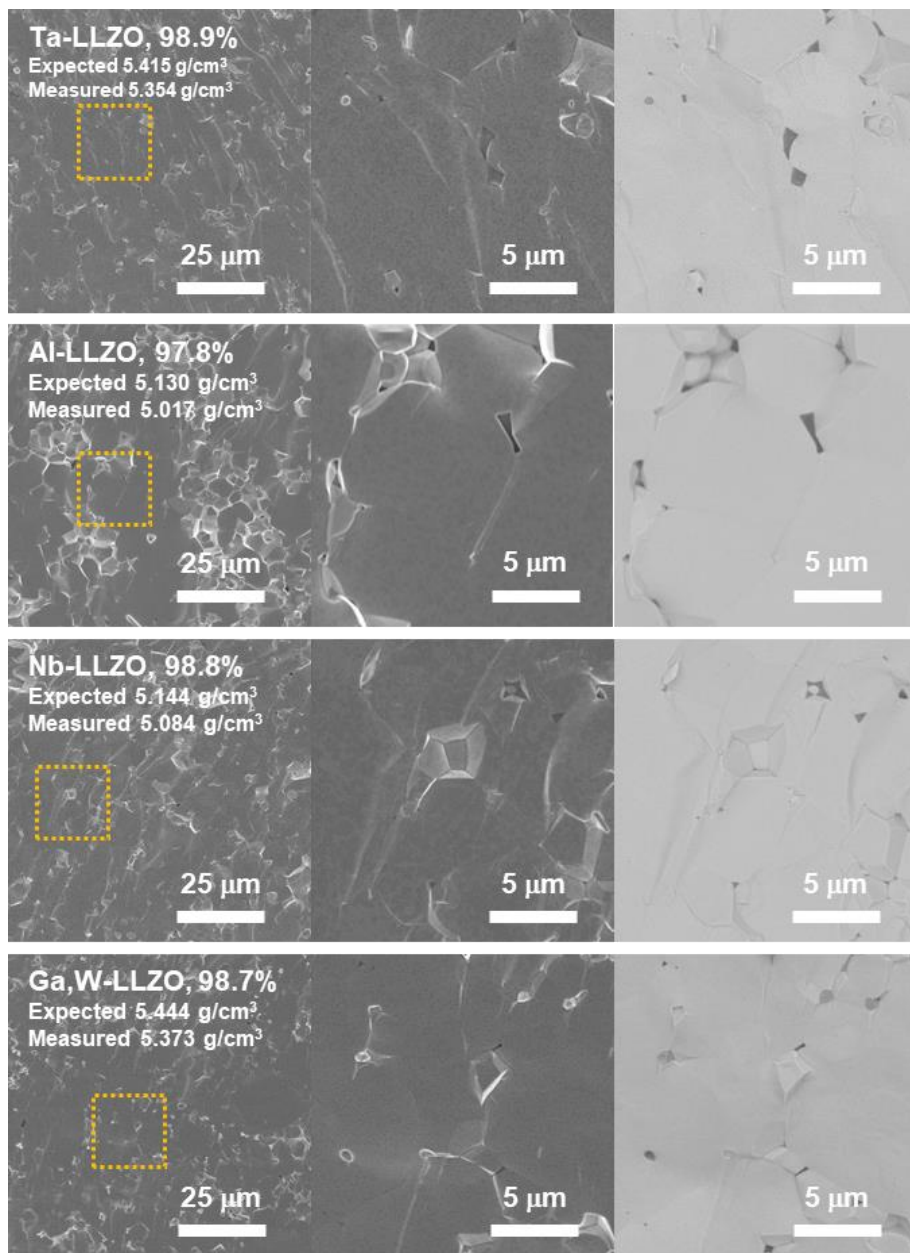


**Figure 2.5.** Cross-sectional scanning electron microscopy (SEM) images of the fractured LLZO pellets with various dopants (Ta, Al, Nb, Ga,W). The SEM technique was used to analyze the fractured surface of each pellet, and the microstructures were characterized. All samples exhibited dense microstructures consistent with the relative densities (shown in the images) calculated from the

measured densities using Archimedes' principle in anhydrous isopropanol and the expected densities estimated based on the XRD refinement results. Al-doped LLZO exhibited a partial intergranular fracture with an average grain size of 5  $\mu\text{m}$ . The other doped LLZOs exhibited similar microstructural features. The average grain sizes (approximately 3  $\mu\text{m}$ ) were comparable. A major fracture mode (primarily the transgranular mode) was observed, indicating a high grain boundary strength.

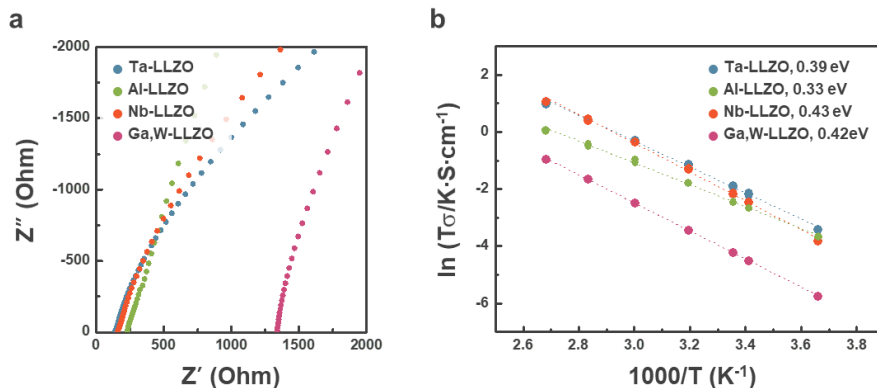


**Figure 2.6.** (a) EIS profiles of Au/LLZO/Au symmetric cells at 25 °C and (b) Arrhenius plot of the total ionic conductivities of the LLZO pellets doped with various metals (Ta, Al, Nb, and Ga,W). AC-impedance measurements using Au (blocking) electrodes were performed on polished pellets (~14 mm in diameter and 300–350  $\mu m$  in thickness) to determine the total ionic conductivities. The ionic conductivities was calculated using the intercept values of the real axis of the Nyquist plots. The calculated ionic conductivities of Ta-, Al-, Nb- and Ga,W-LLZO at 25 °C were 0.51, 0.29, 0.39, and 0.05  $mS \cdot cm^{-1}$ , respectively. The corresponding activation energies are presented in the figure. These values agree well with the reported values.<sup>9</sup>



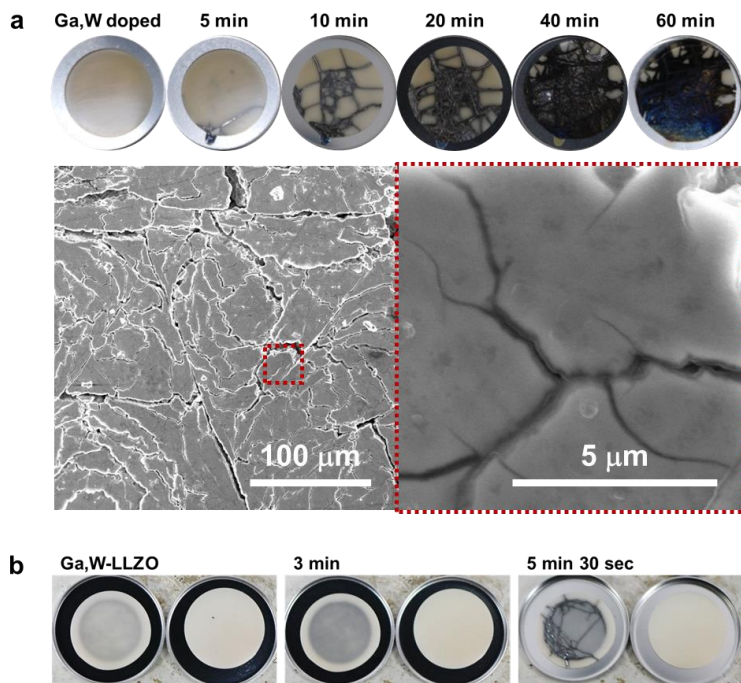


**Figure 2.7.** (a) Optical images of Ga,W-LLZO pellets in contact with Li metal (recorded over time at 200 °C) and the corresponding SEM images of the surface exhibiting numerous cracks and the pulverization of the pellet and (b) Comparison between the images of a Ga,W-LLZO pellet in contact with Li metal and the images of another pellet where Li metal contact at 200 °C was absent. The results indicated that the origin of pulverization could be attributed to the chemical reaction occurring between LLZO and Li metal, not simply to the thermal shock. The volume change and the corresponding strain induced by the chemical reactions between the electrolyte and Li metal can cause the fracture of these pellets, as reported.<sup>55</sup> It was reported that the growth of an interphase (the  $\text{Li}_{1+x}\text{Al}_x\text{Ge}_{2-x}(\text{PO}_4)_3$  (LAGP) and Li metal interface) during the electrochemical cycling process results in the formation of fracture in the material.

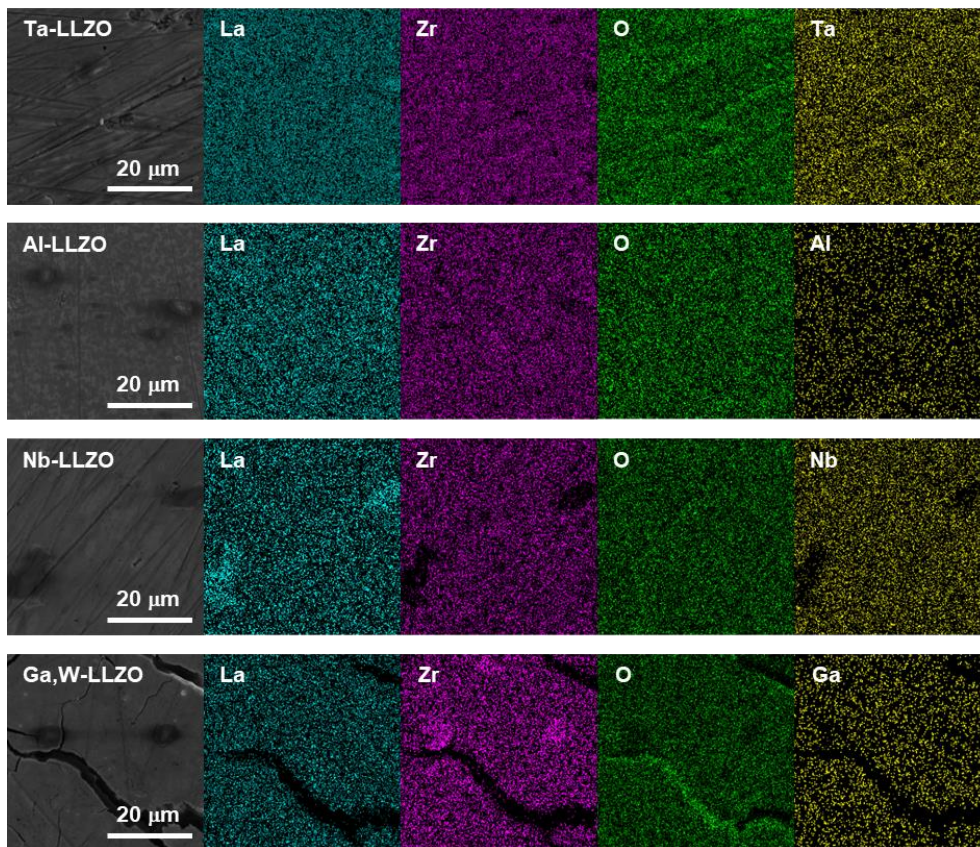


**Figure 2.8.** SEM images and energy-dispersive X-ray spectroscopy (EDS) images recorded for the LLZO surfaces that were in contact with Li metal during the coloration test. Cation segregation on the surface of Nb- and Ga,W-LLZO pellets were observed. Transition metals did not noticeably segregate from the Ta- and Al-LLZO surfaces, whereas a non-uniform distribution of La or Zr was observed in the case of Nb- and Ga,W-LLZO, indicating that it rapidly reacted with Li-metal during the coloration test.

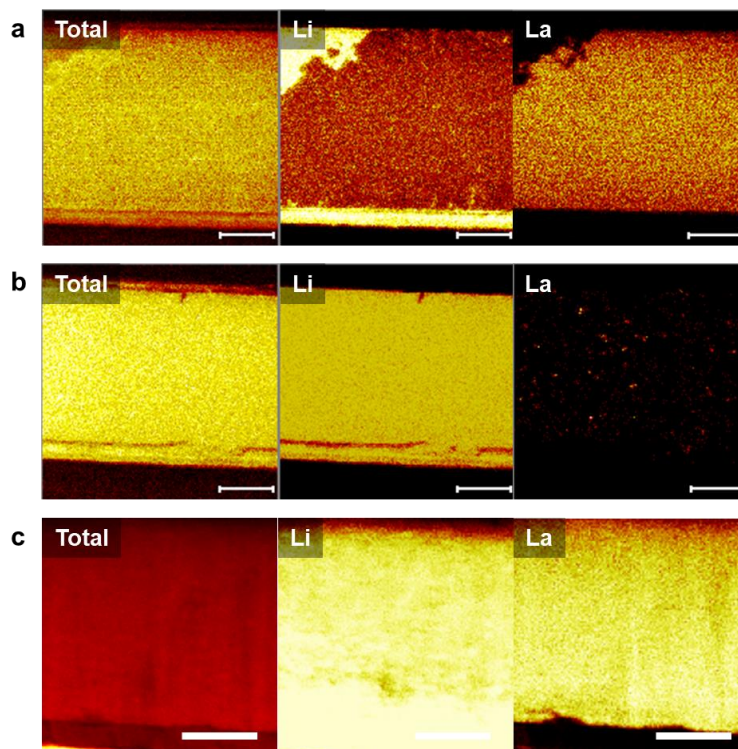


**Figure 2.9.** Comparison of the cross-sectional SIMS images of (a) Ta-LLZO, (b) Nb-LLZO, and (c) Ga,W-LLZO. The images were recorded after the coloration test had been conducted (Scale bars: 100  $\mu\text{m}$ ). The amount of lithium present in Ta-LLZO was significantly less than that present in Li-metal (100% lithium content). The lithium contents in Nb-LLZO and Ga,W-LLZO were as high as the lithium content in the Li-metal over the entire area, making it difficult to distinguish the electrolyte from Li-metal. This implies a favorable reaction between Nb-LLZO (and Ga,W-LLZO) and the Li-metal.

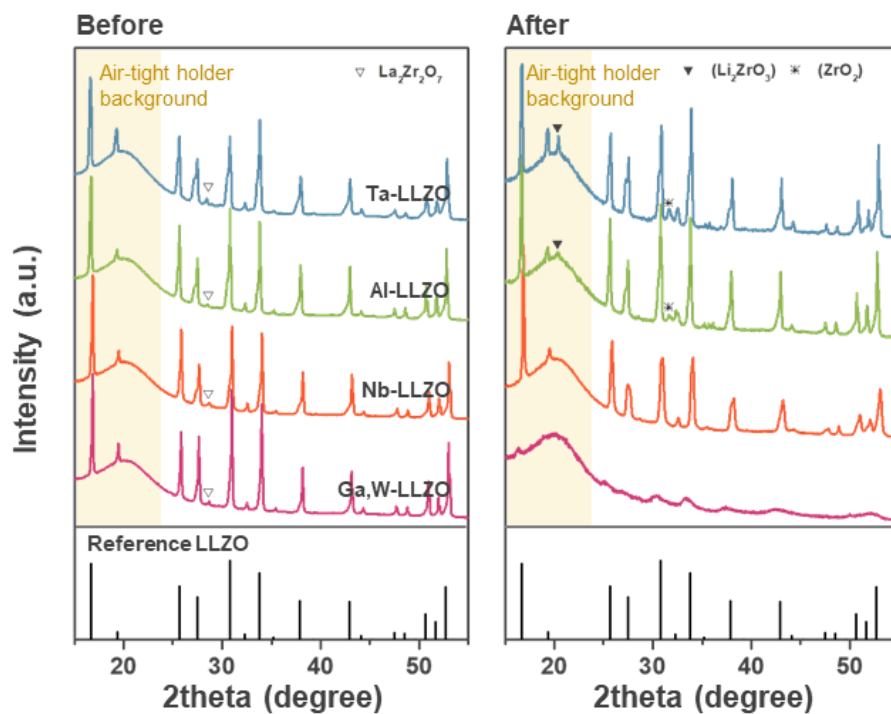


**Figure 2.10.** Comparison of XRD patterns of LLZO pellets with reference XRD pattern (ICSD 01-080-6142) (left) before and (right) after contact with Li-metal.

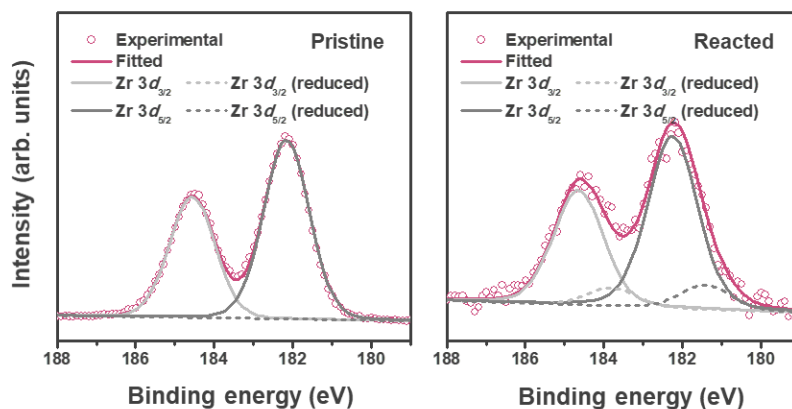


**Figure 2.11.** X-ray photoelectron spectroscopy (XPS) profiles recorded for the cross-section of Ga,W-doped LLZO pellet before and after coloration tests. Zr  $3d$  core-level spectra before (left) and after (right) the reaction. Fitted curves obtained using fixed spin splits ( $3d_{3/2} - 3d_{5/2} = 2.40$  eV) are presented. Two different chemical environments around Zr were observed in the pristine pellet. A doublet signal arising from those two peaks (separated by 2.40 eV) was observed in the profile of the reacted pellet, indicating the reduction of Zr.



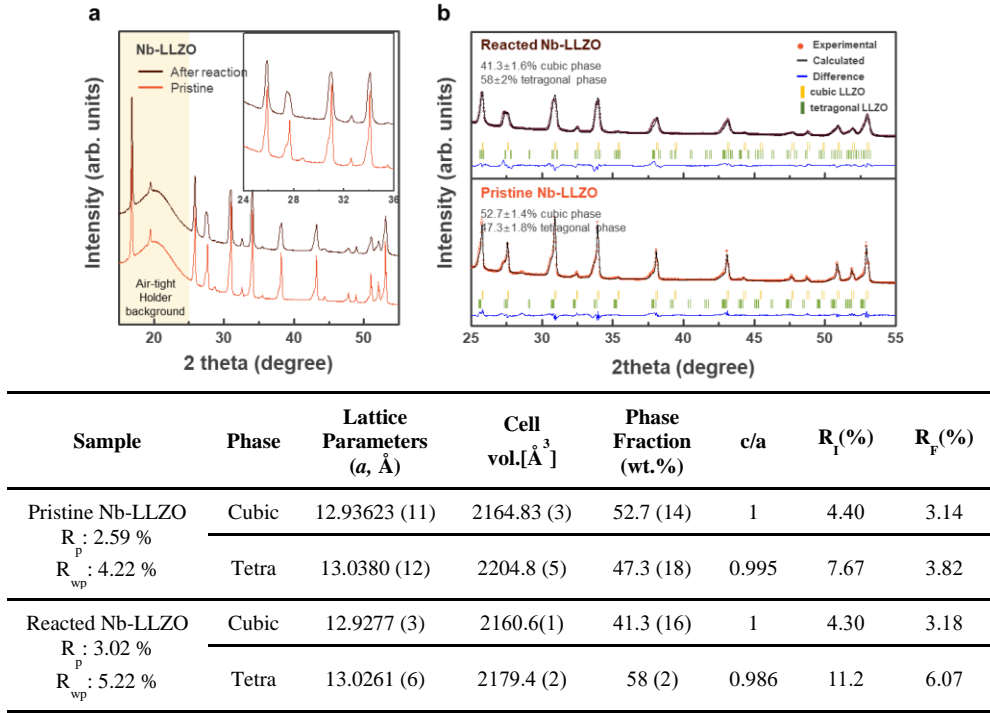


**Figure 2.12.** XRD patterns and Rietveld refinement results obtained for the Nb-LLZO pellets. The patterns and data were recorded before and after the coloration test. The relative amount of tetragonal phase increased and the  $c/a$  ratio decreased after the reaction, indicating that Nb-LLZO exhibited more tetragonal-like phase. We believe that this result provides insight into the reaction between Li metal and Nb-LLZO. Lithium is introduced into the Nb-LLZO system via an  $\text{Nb}^{5+}$  reduction process. Thompson, T. *et al.*<sup>49</sup> reported that Ta-doped LLZO exhibited the tetragonal phase under conditions of low lithium vacancy. We hypothesized that lithium insertion, accompanied by  $\text{Nb}^{5+}$  reduction, can potentially induce the structural change of Nb-LLZO, which appeared as a change in the XRD pattern (after the reaction with Li metal).

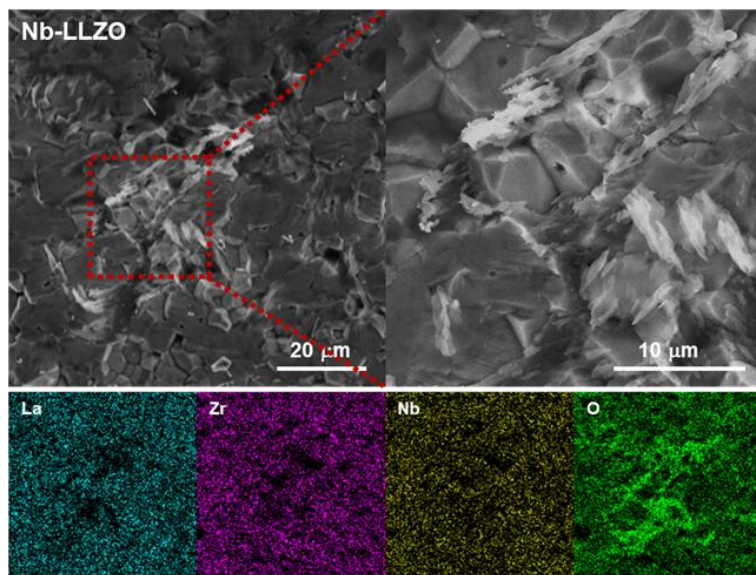


**Figure 2.13.** EDS images of the cross-section of Nb-LLZO pellet recorded after the coloration test. Lithium metal propagation through the grain boundaries is observed.

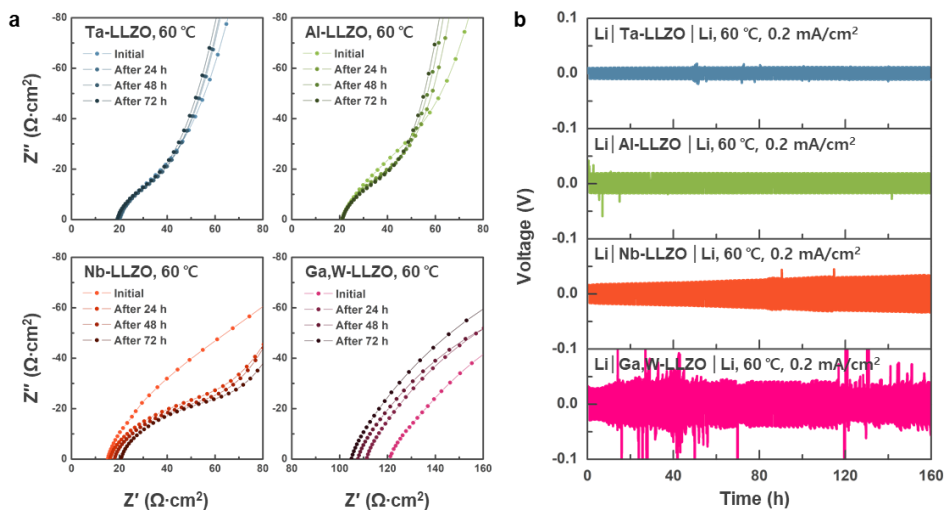


**Figure 2.14.** (a) Evolution of the electrochemical impedance spectra over time for the Li/LLZO/Au cells measured at 60 °C. (b) Galvanostatic cycling of Li/LLZO/Li symmetric cells at 60 °C with a 0.2 mA cm<sup>-2</sup> current density.



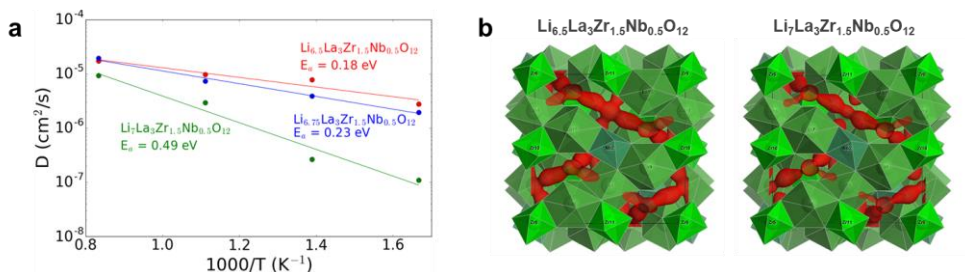


**Figure 2.15.** (a) Calculated Arrhenius relations of lithium ion diffusivities for  $\text{Li}_{6.5}\text{La}_3\text{Zr}_{1.5}\text{Nb}_{0.5}\text{O}_{12}$ ,  $\text{Li}_{6.75}\text{La}_3\text{Zr}_{1.5}\text{Nb}_{0.5}\text{O}_{12}$ , and  $\text{Li}_7\text{La}_3\text{Zr}_{1.5}\text{Nb}_{0.5}\text{O}_{12}$  and (b) Calculated lithium ionic probability densities in  $\text{Li}_{6.5}\text{La}_3\text{Zr}_{1.5}\text{Nb}_{0.5}\text{O}_{12}$  and  $\text{Li}_7\text{La}_3\text{Zr}_{1.5}\text{Nb}_{0.5}\text{O}_{12}$ . The ionic conductivities in Li-excess garnets doped with  $\text{Nb}^{4+}$  ( $\text{Li}_{6.75}\text{La}_3\text{Zr}_{1.5}\text{Nb}_{0.5}\text{O}_{12}$  and  $\text{Li}_7\text{La}_3\text{Zr}_{1.5}\text{Nb}_{0.5}\text{O}_{12}$ ) are much lower than the ionic conductivities in  $\text{Li}_{6.5}\text{La}_3\text{Zr}_{1.5}\text{Nb}_{0.5}\text{O}_{12}$  doped with  $\text{Nb}^{5+}$ . The  $\text{Li}^+$  migration channels are well connected in  $\text{Li}_{6.5}\text{La}_3\text{Zr}_{1.5}\text{Nb}_{0.5}\text{O}_{12}$ , but the channels are disrupted in  $\text{Li}_7\text{La}_3\text{Zr}_{1.5}\text{Nb}_{0.5}\text{O}_{12}$  near the  $\text{Nb}^{4+}$  sites. It was speculated that the bulk resistance of Nb-doped LLZO increases with time in Figure 2.14a because the lithium vacancy concentration decreases with an increase in  $\text{Li}^+$  in the Nb-doped LLZO due to the reduction of  $\text{Nb}^{5+}$ . It is supported by the *ab initio* Molecular Dynamics (AIMD) results here, which show that the ionic conductivities of  $\text{Li}_{6.75}$ - or  $\text{Li}_7$ - garnet compositions with  $\text{Nb}^{4+}$  are significantly lower than that of  $\text{Li}_{6.5}\text{La}_3\text{Zr}_{1.5}\text{Nb}_{0.5}\text{O}_{12}$  with only  $\text{Nb}^{5+}$  due to the disrupted  $\text{Li}^+$  migration channels near  $\text{Nb}^{4+}$ .

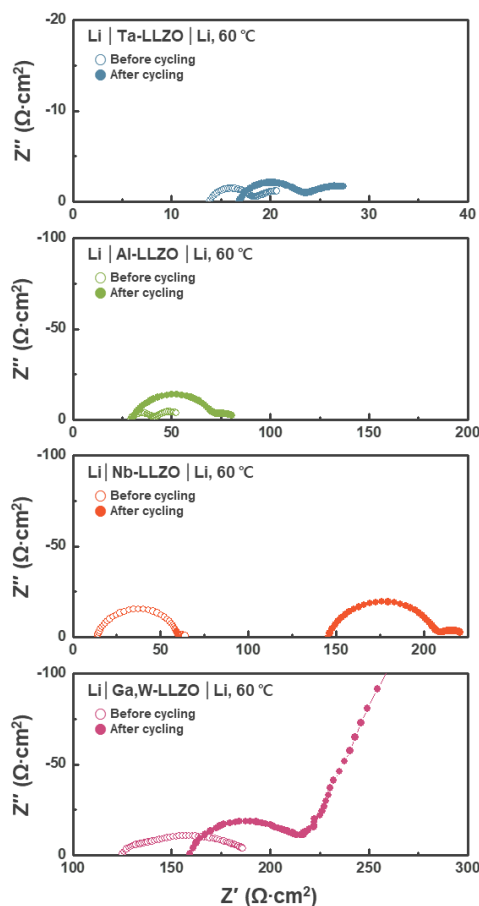


**Figure 2.16.** EIS profiles and the results obtained from experiments conducted (before and after galvanostatic cycling) with Li/LLZO/Li symmetric cells at 60 °C (Figure 2.14b). Analysis of the EIS profiles revealed slight changes in the bulk or interfacial resistance (before and after cycling) in the cells fabricated using Ta- or Al-LLZO (that exhibited stable cycling performance). The results agreed well with the results obtained from the galvanostatic cycling experiments. Significant changes in both bulk and interfacial resistance were observed in cells fabricated using Nb- or Ga,W-LLZO (that exhibited unstable cycling behavior).

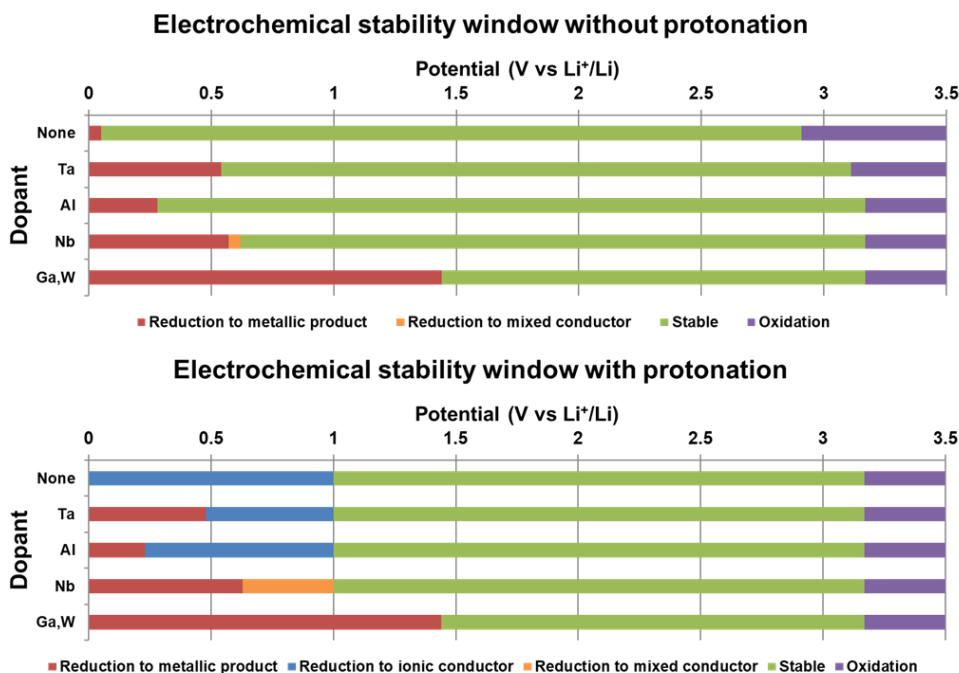


**Figure 2.17.** Electrochemical stability window of all the samples under study, evaluated by DFT calculations. The color scheme indicates the electrical properties of the decomposed products; red: metallic and electronically conductive, orange: electronically and ionically conductive, blue: ionically conductive but electronically insulating, and green: stable and does not decompose. When lithium ions are exchanged with protons for Ta- or Al-LLZO, electronically insulating products at the LLZO/Li-metal interface are produced.

### **2.3.2. Selective passivation of doped-LLZOs along the grain boundaries and interface**

As chemical/electrochemical reduction by lithium is rarely avoidable, even for relatively stable dopants such as Ta or Al, attempts to further tailor the compositions of the doped LLZOs with secondary dopants were made such that the by-products from any decomposition were electronically insulating but ionically conducting. Moreover, to minimize the effect of secondary doping on the overall ionic conductivities of LLZOs, the compositional tailoring was limited to the interface of LLZO, including the grain boundaries. Considering the practical feasibility of the selective doping of the interface, a possible solution-based process was considered, which could permeate through the grain boundaries of the LLZOs. Additionally, inspired by the conventional etching technique to visualize the grain boundaries of pellet samples by scanning electron microscopy (SEM)<sup>56</sup>, the acid etching process was employed to exclusively alter the grain boundaries and interface. It was speculated that acid etching could be a feasible method to dope protons, because the ion exchange between lithium and proton could occur when LLZO is immersed in an acid solution, which could also be reversed using  $\text{LiNO}_3$ -containing solutions<sup>57</sup>. Therefore, the degree of protonation could be empirically modified to balance the potential increase in stability with the expected decrease in ionic conductivity. The DFT thermodynamic assessment supported the hypothesis that exchanging lithium with proton in the LLZOs aided the production of passivating by-products during reduction at the Li/LLZO interface (Table 2.1). The calculations predicted that insulating by-products such as hydroxides ( $\text{La}(\text{OH})_3$  and  $\text{LiOH}$ ) could form during the reduction of Ta- and Al-doped systems, which could passivate further

decomposition. Interestingly, as shown in Figure 2.18 and Table 2.1, the co-doping of Ta and proton in LLZO leads to the formation of the insulating  $\text{Li}_3\text{TaO}_4$  phase in addition to hydroxides at approximately 1.0 V (vs.  $\text{Li}/\text{Li}^+$ ), while the doping of only Ta in LLZO yields a metallic Ta phase as the by-product. This implies that when reductive decomposition is initiated for the proton-doped Ta–LLZO, the reaction route would first produce these electronically insulating (and ionically conducting) phases that passivate further reduction to metallic phases. A similar phenomenon was observed for the co-doping of Nb and proton, which produced  $\text{Li}_8\text{Nb}_2\text{O}_9$  as an intermediate by-product during the decomposition reaction. However, the  $\text{Li}_8\text{Nb}_2\text{O}_9$  phase is considered a mixed electronic ionic conductor due to its small band gap energy<sup>58</sup>, and is therefore expected to be unsuccessful in passivating the decomposition. The difference between Ta and Nb doping indicates that the secondary dopant should be rationally selected specifically considering the primary dopant of LLZO.

Inspired by these results, we protonated the grain boundaries and interfaces of doped LLZOs by a secondary doping process via the acid treatment of 350- $\mu\text{m}$  doped-LLZO pellets. The protonation of the samples was confirmed by thermal gravimetric analysis (TGA) performed under  $\text{N}_2$  atmosphere (Figure 2.19). An apparent weight loss was observed for the protonated LLZO pellet at approximately 450 °C, which was attributed to the release of hydrogen from the pellet, whereas pristine LLZO did not show any change up to 1000 °C<sup>30</sup>. For the co-doped LLZOs, the stability against Li-metal was comparatively evaluated (Figure 2.20). Protonated Ta– and Al–LLZO showed higher stability with Li-metal than the pristine Ta– and Al–LLZO pellets, whereas protonated Nb– and Ga,W–LLZO pellets still showed

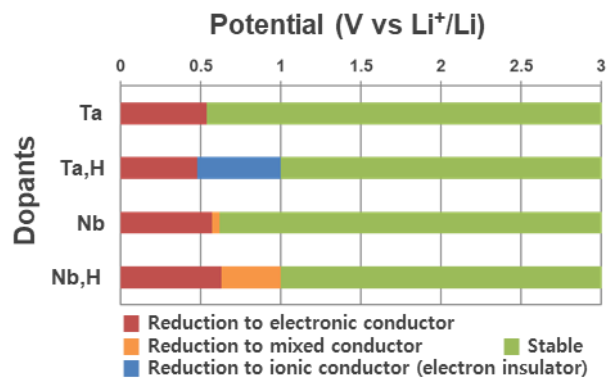
significant degradation. These results were consistent with those of the DFT calculations, which indicated the production of insulating by-products only for Ta- and Al-doped cases. The chemical coloration test also verified that protonated Ta- and Al-LLZO were stable without apparent degradation over time. Notably, the additional XRD peaks observed for pristine Ta- and Al-LLZO were not observed for their protonated counterparts, confirming the enhanced stability against Li-metal. In contrast, Nb- and Ga,W-LLZO remained unstable even after protonation, showing pellet fracture and pulverization, which indicated the inefficacy of secondary proton doping. Nevertheless, a slight enhancement was observed for protonated Nb- and Ga,W-LLZO via EIS and cell cycling, which showed smaller impedance/polarization at the initial cycles. Although degradation was observed in later cycles, the enhancement shown at the initial cycles was attributed to the improved interface morphology between the Li-metal and LLZOs<sup>59</sup> (discussed later in detail). Figure 2.21 shows a comparison of the electronic conductivity of Ta- and Nb-LLZO pellets in an Au/LLZO/Li cell before and after protonation, as measured by the direct-current (DC) polarization using the Hebb-Wagner method<sup>60,61</sup> at 60 °C. Substantial electronic conductivity was measured for both pristine Ta- and Nb-LLZO pellets, probably due to the presence of conducting by-products. However, the electronic conductivity of the protonated Ta-LLZO decreases from  $1.5 \times 10^{-9} \text{ S cm}^{-1}$  to  $5 \times 10^{-10} \text{ S cm}^{-1}$ , whereas Nb-LLZO did not show any significant change after protonation. This suggests that the suppression of the metallic by-products through the protonation of Ta-LLZO can retard the formation of electron-conducting paths in the LLZO pellet in contact with Li-metal.

Composition	Potential (V vs Li <sup>+</sup> /Li)	Phase equilibria
Li <sub>7</sub> La <sub>3</sub> Zr <sub>2</sub> O <sub>12</sub>	0.05	Li <sub>2</sub> O, Zr <sub>3</sub> O, La <sub>2</sub> O <sub>3</sub>
Li <sub>6.5</sub> La <sub>3</sub> Zr <sub>1.5</sub> Ta <sub>0.5</sub> O <sub>12</sub>	0.54	Li <sub>6</sub> Zr <sub>2</sub> O <sub>7</sub> , La <sub>2</sub> O <sub>3</sub> , Li <sub>5</sub> TaO <sub>5</sub> , Ta
Li <sub>6.25</sub> Al <sub>0.25</sub> La <sub>3</sub> Zr <sub>2</sub> O <sub>12</sub>	0.28	Li <sub>6</sub> Zr <sub>2</sub> O <sub>7</sub> , La <sub>2</sub> O <sub>3</sub> , Li <sub>5</sub> AlO <sub>2</sub> , ZrAl <sub>2</sub>
Li <sub>6.5</sub> La <sub>3</sub> Zr <sub>1.5</sub> Nb <sub>0.5</sub> O <sub>12</sub>	0.62	Li <sub>6</sub> Zr <sub>2</sub> O <sub>7</sub> , La <sub>2</sub> O <sub>3</sub> , Li <sub>2</sub> O, LiNbO <sub>2</sub>
Li <sub>4.9</sub> Ga <sub>0.5</sub> La <sub>3</sub> Zr <sub>1.7</sub> W <sub>0.3</sub> O <sub>12</sub>	1.44	Li <sub>6</sub> Zr <sub>2</sub> O <sub>7</sub> , La <sub>2</sub> O <sub>3</sub> , LiGaO <sub>2</sub> , Li <sub>4</sub> WO <sub>5</sub> , W

Composition	Potential (V vs Li <sup>+</sup> /Li)	Phase equilibria
Li <sub>6</sub> HLa <sub>3</sub> Zr <sub>2</sub> O <sub>12</sub>	1.00	LiOH, Li <sub>6</sub> Zr <sub>2</sub> O <sub>7</sub> , La(OH) <sub>3</sub> , La <sub>2</sub> O <sub>3</sub>
Li <sub>4.5</sub> H <sub>2</sub> La <sub>3</sub> Zr <sub>1.5</sub> Ta <sub>0.5</sub> O <sub>12</sub>	1.00	Li <sub>6</sub> Zr <sub>2</sub> O <sub>7</sub> , La <sub>2</sub> O <sub>3</sub> , La(OH) <sub>3</sub> , LiOH, Li <sub>3</sub> TaO <sub>4</sub>
Li <sub>4.25</sub> H <sub>2</sub> Al <sub>0.25</sub> La <sub>3</sub> Zr <sub>2</sub> O <sub>12</sub>	1.00	Li <sub>6</sub> Zr <sub>2</sub> O <sub>7</sub> , La <sub>2</sub> Zr <sub>2</sub> O <sub>7</sub> , La <sub>2</sub> O <sub>3</sub> , LiOH, LiAlO <sub>2</sub>
Li <sub>4.5</sub> H <sub>2</sub> La <sub>3</sub> Zr <sub>1.5</sub> Nb <sub>0.5</sub> O <sub>12</sub>	1.00	Li <sub>6</sub> Zr <sub>2</sub> O <sub>7</sub> , La <sub>2</sub> O <sub>3</sub> , La(OH) <sub>3</sub> , LiOH, Li <sub>8</sub> Nb <sub>2</sub> O <sub>9</sub>
Li <sub>4</sub> Ga <sub>0.5</sub> HLa <sub>3</sub> Zr <sub>1.7</sub> W <sub>0.3</sub> O <sub>12</sub>	1.44	Li <sub>6</sub> Zr <sub>2</sub> O <sub>7</sub> , La <sub>2</sub> Zr <sub>2</sub> O <sub>7</sub> , La <sub>2</sub> O <sub>3</sub> , LiOH, LiGaO <sub>2</sub> , W

**Table 2.1.** Phase equilibria of (top) pristine and (bottom) protonated LLZO doped with various metals at the potential for the first reduction.



**Figure 2.18.** Electrochemical stability windows for pristine and protonated Ta– and Nb–LLZOs calculated using the DFT.



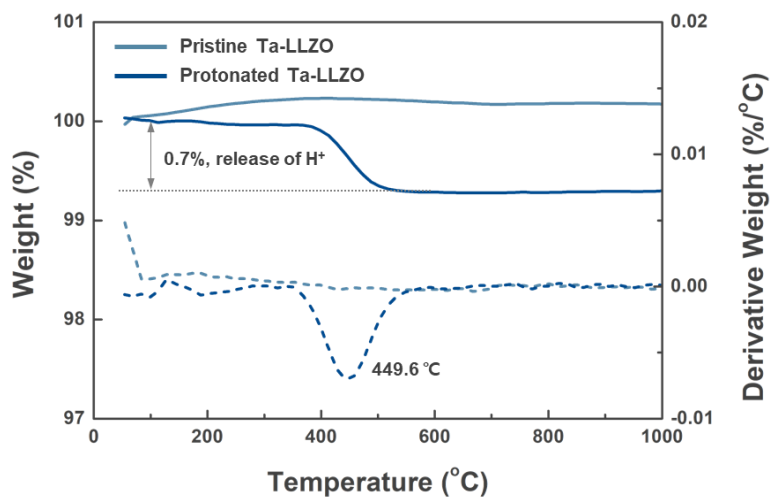


**Figure 2.19.** Thermogravimetric analysis (TGA) curves of (a) pristine and (b) protonated Ta-LLZO pellets, revealing the partial substitution of  $\text{Li}^+$  ions in LLZO with  $\text{H}^+$ . Data were recorded under an atmosphere of  $\text{N}_2$ .

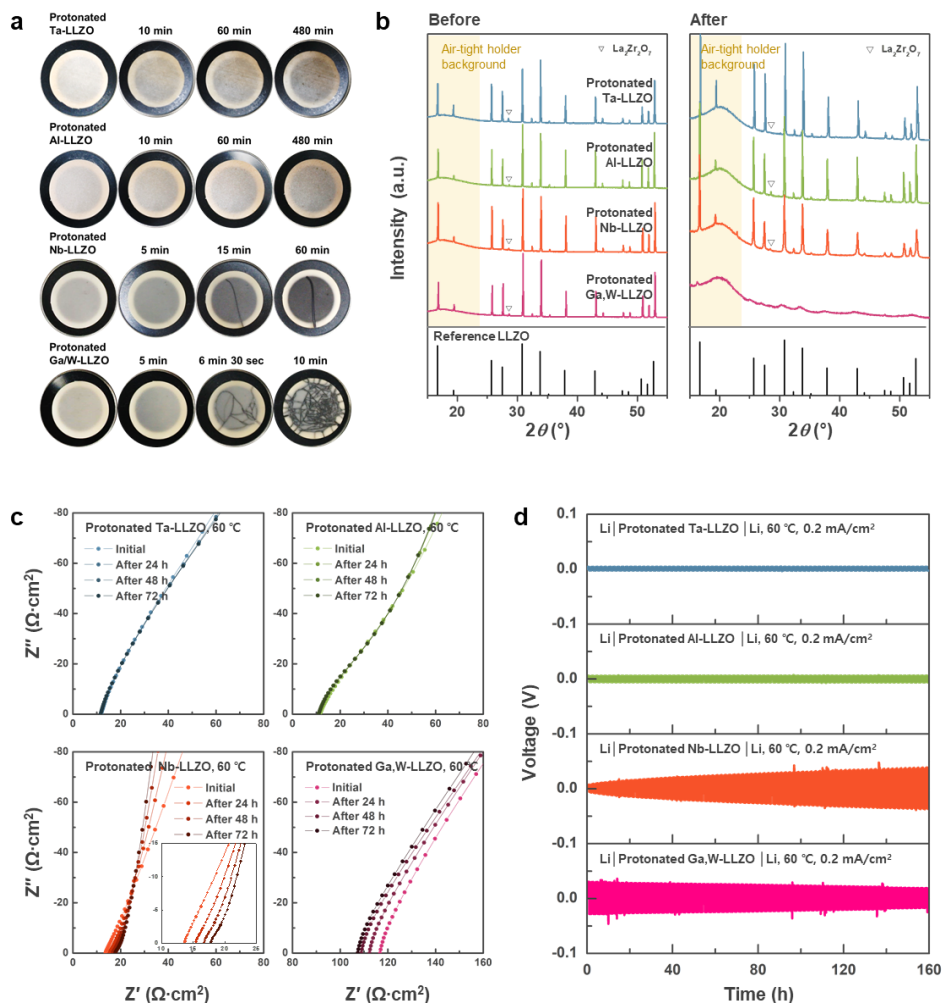


**Figure 2.20.** (a) Optical images (recorded over time) of protonated LLZO pellets in contact with Li-metal at 200 °C, after the system was assembled under a cold isostatic pressure of 250 MPa. (b) Comparison of XRD patterns of protonated LLZO pellets before (left) and after (right) coloration test. The reference XRD pattern is also indicated (ICSD 01-080-6142). (c) Variation of the EIS profiles with time (Li/LLZO/Au cells measured at 60 °C), and (d) Results of galvanostatic cycling experiments conducted with Li/LLZO/Li symmetric cells at 60 °C (current density: 0.2 mA cm<sup>-2</sup>).

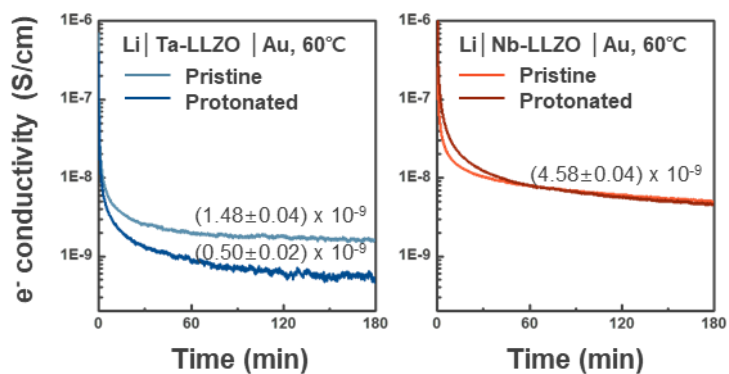


**Figure 2.21.** Electronic conductivities of Ta– and Nb–LLZO pellets before and after protonation measured by DC polarization with an applied voltage of 0.5 V at 60 °C.

### 2.3.3. Additional effects of acid treatment on interfacial stabilization

After demonstrating that doped-LLZO can be chemically stabilized by protonation, attempts to understand the possible effects of surface tailoring via acid treatment were made, and protonated Ta-LLZO was carefully investigated. Previous studies reported that acid treatment could remove the  $\text{Li}_2\text{CO}_3$  layer on the LLZO surface and decrease the interfacial resistance<sup>19,59</sup>. In accordance, the interfacial resistance noticeably decreased from  $35 \text{ } \Omega \cdot \text{cm}^2$  for the pristine pellet to  $0.9 \text{ } \Omega \cdot \text{cm}^2$  for that subjected to acid treatment at  $25 \text{ } ^\circ\text{C}$  (Figure 2.22a). A decrease in the interfacial resistance was also consistently observed for Al-LLZO (Figure 2.22b). Additionally, X-ray photoelectron spectroscopy (XPS) data (Figure 2.23) confirmed that the residual  $\text{Li}_2\text{CO}_3$  on the Ta-LLZO surface was substantially reduced after protonation. The characteristic peaks of  $\text{Li}_2\text{CO}_3$  at 289.5 eV and 531.5 eV in the C 1s and the O 1s spectra, respectively, (red dotted line in Figure 2.23) indicated that a significant amount of  $\text{Li}_2\text{CO}_3$  was present on the surface of pristine LLZO, which was detected even with prolonged XPS depth profiling. In contrast,  $\text{Li}_2\text{CO}_3$  peaks were observed only at the outermost surface of the protonated pellet (less than a few nanometres thick), supporting that acid treatment successfully removes the surface  $\text{Li}_2\text{CO}_3$  layer. Figure 2.24 shows a comparison of the SEM images of the pristine and protonated Ta-LLZO pellets assembled with Li-metal. The protonated Ta-LLZO pellet was rough and porous at the surface, owing to the corrosion along the grain boundaries, in contrast to the flat surface of the pristine pellet containing only scratches. As the presence of locally distributed defects with narrow and deep profiles (such as scratches) on the electrolyte surface can initiate the Li-metal propagation through the electrolyte and cause short-circuiting<sup>13,15,62</sup>, the removal of

local flaws and formation of a uniform rough surface by appropriate etching is thought to mitigate Li-metal penetration and improve cell performance. In addition, it indicates that the reduction of the interfacial resistance is partly attributable to the increase in the effective contact area. The increase in the effective area between LLZO and Li-metal is expected to decrease the actual areal current density<sup>63</sup>, contributing to a reduction in interfacial impedance, as observed for all protonated LLZO pellets (Figure 2.20).

Interestingly, during the handling of LLZO pellets in the experiments, it was observed that the mechanical properties could also be significantly enhanced by protonation. The ring-on-ring test, which is commonly used to measure the ceramic strength<sup>64,65</sup>, revealed that the tensile strength of the LLZO pellet increased from  $86 \pm 14$  to  $134 \pm 7$  MPa after acid treatment (Figure 2.25). While the origin of this strengthening is not clear, it is speculated that it is partly due to the strain release that accompanies acid treatment, which effectively removes the secondary garnet phase in the pellet. The careful analysis of Figure 2.26 and 2.27 shows that the pristine Ta-LLZO pellet contained a tetragonal secondary phase, accounting for ~58% based on the refinement<sup>66,67</sup>, as indicated by the pronounced asymmetry of the XRD peaks. Although the relative amount of the tetragonal phase is higher than that of the cubic phase, this represents a surface-limited property rather than a bulk property, as the interaction volume for XRD is near the pellet surface, owing to the limited penetration depth of X-rays in ceramics containing transition metals<sup>68,69</sup>. As shown in Figure 2.28 and 2.29, the tetragonal phase is barely detected in the powder from the crushed/ground pellet (considered representative of the overall properties), confirming that the coexistence of tetragonal and cubic phase LLZO was limited to

near the surface. It has been previously reported that a significant amount of tetragonal phase can be formed when a material is insufficiently doped to stabilize the cubic polymorph<sup>49</sup> or during sintering with applied pressure, and the existence of the secondary phase can result in lattice strain in the garnet structure<sup>50</sup>. The mechanical process including sintering, cutting, polishing, etc. to fabricate the electrolyte pellets can also induce the strain field on the surface.<sup>70</sup> Notably, this asymmetry was not observed after surface tailoring, indicating the removal of the secondary phase, which is consistent with the refinement results shown in Figure 2.30. It has not been confirmed if acid treatment chemically etches the secondary phase<sup>70</sup> and/or the phase transformation occurs from the tetragonal to cubic phase due to lithium redistribution during the protonation process<sup>71-73</sup>, which warrants further investigation. Nevertheless, it was confirmed that the lattice strain in the pellet was significantly reduced by the removal of the tetragonal phase). Williamson–Hall analysis and size–strain plots<sup>74</sup> in Figure 2.31 revealed that the lattice strain on the surface decreased from 0.509%, owing to the presence of the tetragonal phase in the pristine pellet, to 0.076 % in the protonated pellet. Transmission electron microscopy (TEM) analysis further confirmed the removal of the tetragonal phase and the corresponding mechanical strain. The selected-area diffraction (SAD) pattern and TEM image of the surface of the pristine pellet in Figure 2.32 clearly show that the top surface grain was composed of the tetragonal phase with a strain field, observed as fringes near the surface and double diffraction (indicated by red arrows) in the SAD pattern. In contrast, only a single pattern of the cubic phase was identified for the protonated pellet, which is in good agreement with the XRD results. Notably, the residual lattice strain in ceramics can serve as a critical

driving force for crack propagation under external pressure<sup>75</sup>. To date, the need to enhance the mechanical properties of inorganic solid electrolytes has been relatively overlooked because the fracture toughness of most inorganic solid electrolytes is significantly higher than the elastic modulus of Li-metal. However, in the presence of significant strain in the LLZO pellets, it is speculated that the accumulated stress induced by Li-metal filling in the LLZOs can more easily trigger crack propagation, leading to the mechanical failure of LLZO electrolytes<sup>15</sup>.

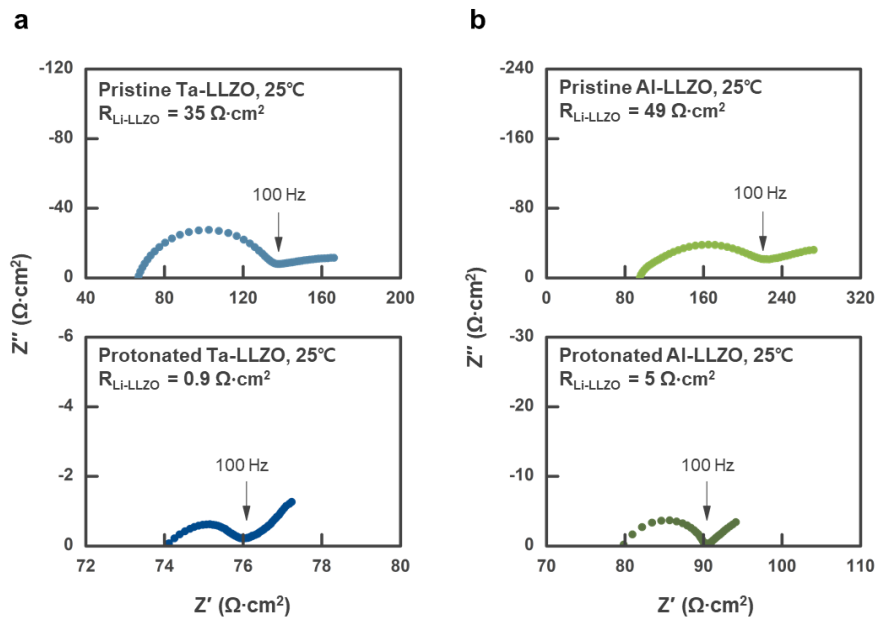


**Figure 2.22.** Electrochemical impedance spectroscopy (EIS) results for (a) Li/Ta-LLZO/Li and (b) Li/Al-LLZO/Li symmetric cell before and after surface tailoring, showing decrease in the interfacial resistance after the surface tailoring.



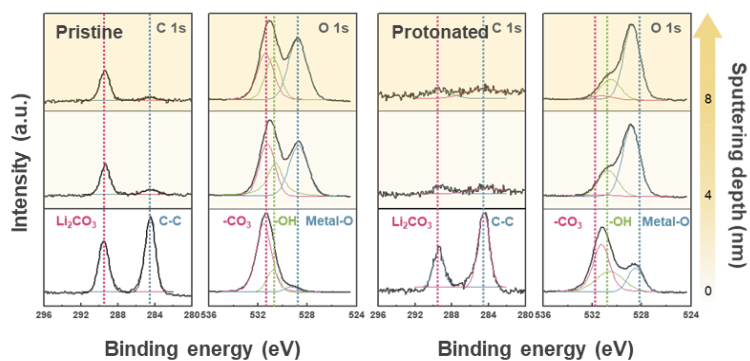


**Figure 2.23.** XPS spectra of C 1s and O 1s region of Ta-LLZO pellets before and after surface tailoring along the sputtering depth, showing the elimination of  $\text{Li}_2\text{CO}_3$  below the surface.

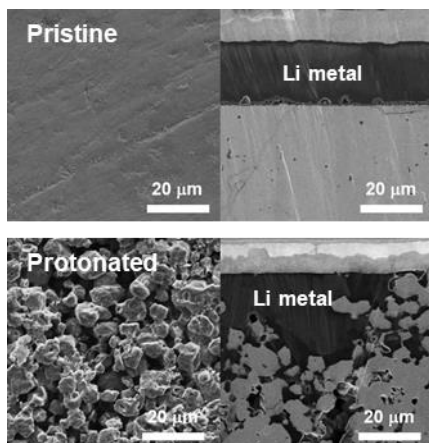


**Figure 2.24.** SEM images of the polished and tailored Ta–LLZO pellet surfaces and cross-sections in contact with Li-metal. The protonated pellet shows pronounced rough and porous surface morphology.

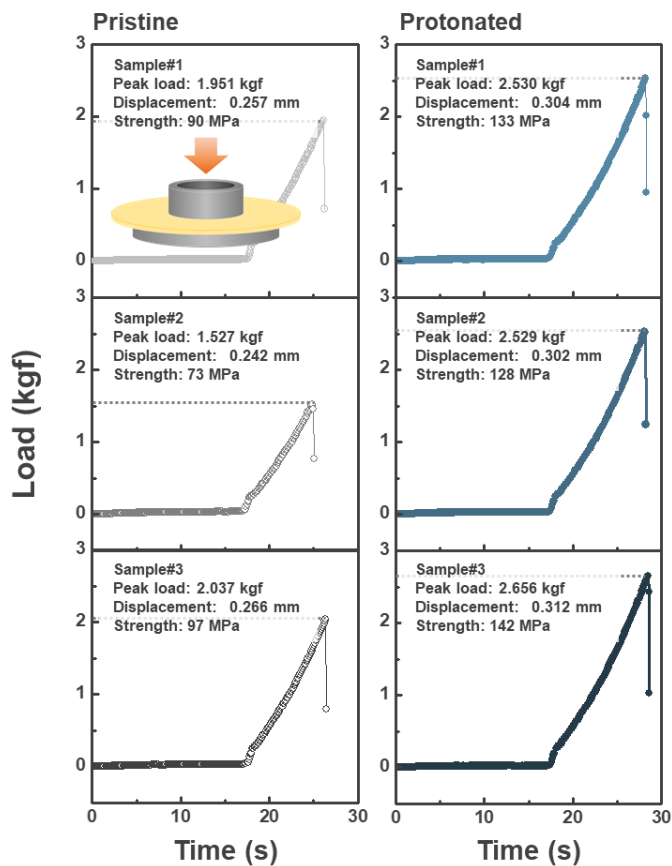


**Figure 2.25.** The time-load curve of (left) the pristine and (right) the protonated Ta-LLZO (right) pellets exhibiting the maximum load that the pellet can endure during the ring-on-ring test. The tests were conducted by measuring the maximum value while applying a load at the same rates to the pellet placed between the two rings, as shown in the inset figure. The tensile strength of each pellet was calculated from the maximum load at which the pellet was broken, and the vertical displacement of the bent pellet. The protonated pellets present the larger maximum load value compared to the pristine pellets.

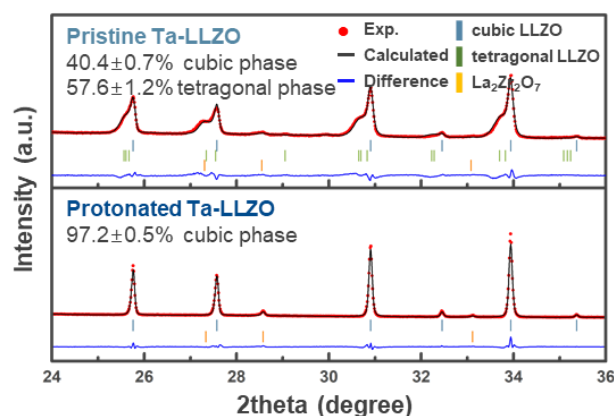
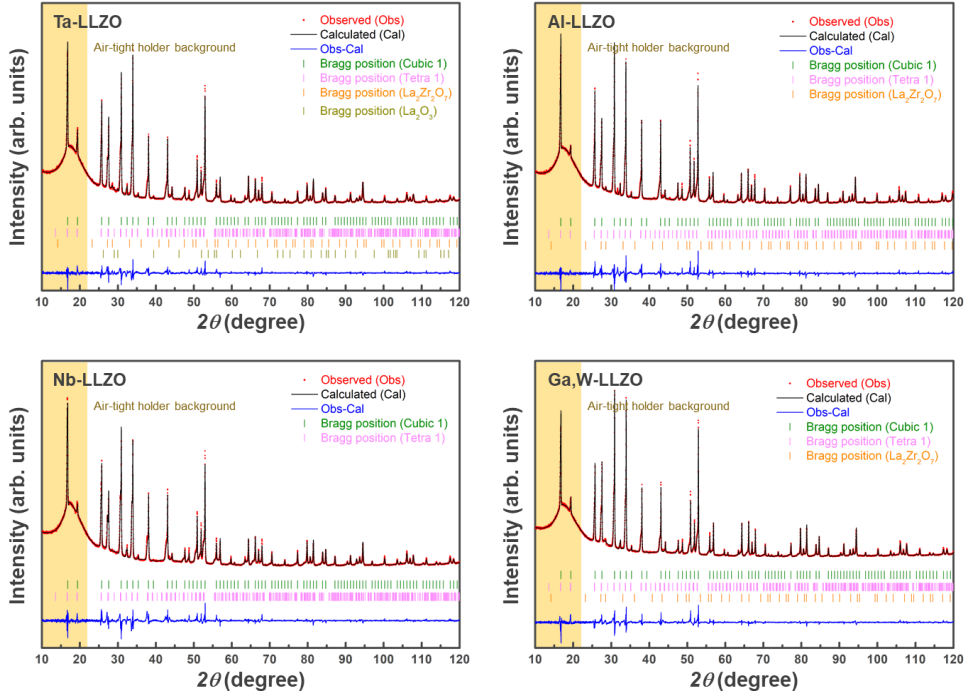


**Figure 2.26.** XRD patterns of Ta-LLZO before and after surface tailoring. It is indicated that pristine Ta-LLZO includes  $40.4 \pm 0.7$  wt% of cubic phase ( $Ia\bar{3}d$ ,  $a = 12.93$  Å) and  $57.6 \pm 1.2$  wt% of the tetragonal phase ( $I4_1/acd$ ,  $a = 13.03$  Å,  $c = 12.94$  Å,  $c/a=0.9928$ ), whereas protonated Ta-LLZO consists of  $97.2 \pm 0.5$  wt% of cubic phase ( $Ia\bar{3}d$ ) with a lattice parameter of  $12.93$  Å. The peak of the pristine pellet is clearly asymmetric due to the presence of the tetragonal phase. (Details of the Rietveld refinement are provided in Figure 2.27-2.30.)



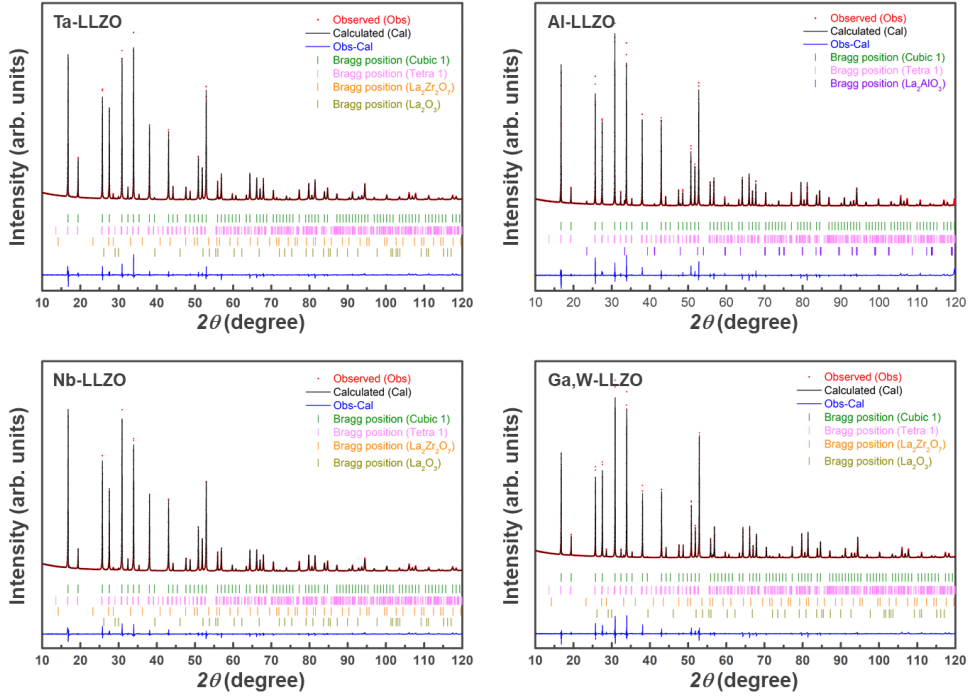
Sample	Phase	Lattice Parameters ( <i>a</i> , Å)	<i>c/a</i>	Cell vol. [Å <sup>3</sup> ]	Phase fraction (wt.%)	R <sub>I</sub> (%)	R <sub>F</sub> (%)
Li <sub>6.5</sub> La <sub>3</sub> Zr <sub>1.5</sub> Ta <sub>0.5</sub> O <sub>12</sub> R <sub>p</sub> : 3.73 % R <sub>wp</sub> : 5.42 %	Cubic	12.92980 (6)	1	2161.60 (2)	40.4 (7)	4.41	3.53
	Tetra	13.0347 (5)	0.9928	2198.8 (2)	57.6 (12)	6.69	3.96
	La <sub>2</sub> Zr <sub>2</sub> O <sub>7</sub>	10.8231 (6)	-	1267.8 (1)	1.62 (11)	-	-
	La <sub>2</sub> O <sub>3</sub>	3.9330 (7)	1.5629	82.34 (5)	0.36 (5)	-	-
Li <sub>6.25</sub> Al <sub>0.25</sub> La <sub>3</sub> Zr <sub>2</sub> O <sub>12</sub> R <sub>p</sub> : 4.40 % R <sub>wp</sub> : 6.54 %	Cubic	12.96374 (5)	1	2178.67 (14)	42.0 (7)	4.72	3.26
	Tetra	13.0483 (9)	0.9975	2216.0 (4)	57.1 (11)	6.94	4.56
	La <sub>2</sub> Zr <sub>2</sub> O <sub>7</sub>	10.8035 (5)	-	1260.9 (1)	0.89 (9)	-	-
	La <sub>2</sub> O <sub>3</sub>	-	-	-	-	-	-
Li <sub>6.5</sub> La <sub>3</sub> Zr <sub>1.5</sub> Nb <sub>0.5</sub> O <sub>12</sub> R <sub>p</sub> : 4.28 % R <sub>wp</sub> : 6.38 %	Cubic	12.93028 (6)	1	2161.84 (2)	34.7 (6)	6.24	3.91
	Tetra	13.0420 (3)	0.9927	2202.1 (2)	65.3 (9)	7.75	4.27
	La <sub>2</sub> Zr <sub>2</sub> O <sub>7</sub>	-	-	-	-	-	-
	La <sub>2</sub> O <sub>3</sub>	-	-	-	-	-	-
Li <sub>4.9</sub> Ga <sub>0.5</sub> La <sub>3</sub> Zr <sub>1.7</sub> W <sub>0.3</sub> O <sub>12</sub> R <sub>p</sub> : 3.91 % R <sub>wp</sub> : 5.70 %	Cubic	12.93939 (4)	1	2166.413 (11)	36.9 (5)	4.20	2.96
	Tetra	13.0267 (5)	0.9956	2200.8 (2)	62.6 (9)	8.10	5.37
	La <sub>2</sub> Zr <sub>2</sub> O <sub>7</sub>	10.83158	-	1270.8	0.55 (6)	-	-

**Figure 2.27.** XRD patterns and Rietveld refinement results of the pristine LLZO pellets doped with various metals such as Ta, Al, Nb, and Ga,W. The refinement of the pellet specimen indicates that a significant amount of a tetragonal phase appears with small amounts of impurities such as La<sub>2</sub>Zr<sub>2</sub>O<sub>7</sub> and La<sub>2</sub>O<sub>3</sub>. The impurity phases present in the doped-LLZO samples are not critically specific to the composition of the LLZO, *i.e.* the dopant. Most importantly, the analysis revealed that the relative amount between the tetragonal phase and the cubic phase is comparable (Ta-LLZO: cubic  $40.4 \pm 0.7$  %, tetragonal  $57.6 \pm 1.2$  %, Al-LLZO: cubic  $42.0 \pm 0.7$  %, tetragonal  $57.1 \pm 1.1$  %, Nb-LLZO: cubic  $34.7 \pm 0.6$  %, tetragonal  $65.3 \pm 0.9$  %, Ga,W-LLZO: cubic  $36.9 \pm 0.5$  %, tetragonal  $62.6 \pm 0.9$  %). This ratio between the two phases in the pellet samples significantly differs from the results from the as-made powder XRD measurements (Figure 2.1), which indicated the major cubic phase over 97%. It implies that the pressure-induced sintering process caused a partial phase transition from the cubic to the tetragonal phase. We highlight that the significant portion of the tetragonal phase is surface specific of the pellet sample and is attributed to the pellet geometry used in the XRD measurement. As shown in Figure 2.28 and 2.29, we crushed and reground the pellet into the powder, and re-measured the powder XRD, which better represent the overall properties of the materials in the pellet samples. (The chemical composition of the corresponding pellets examined by the ICP-AES (Inductively Coupled Plasma-Atomic Emission Spectroscopy) is tabulated in Table 2.2)

Elements	Nominal composition	ICP-AES result	
		Pristine	Protonated
Li : La : Zr : Ta	6.5 : 3 : 1.5 : 0.5	6.58 : 3 : 1.50 : 0.52	6.54 : 3 : 1.49 : 0.52
Li : La : Zr : Al	6.25 : 3 : 2 : 0.25	6.35 : 3 : 2.05 : 0.34	6.31 : 3 : 2.02 : 0.34
Li : La : Zr : Nb	6.5 : 3 : 1.5 : 0.5	6.66 : 3 : 1.48 : 0.52	6.54 : 3 : 1.46 : 0.53
Li : La : Zr : Ga : W	4.9 : 3 : 1.7 : 0.5 : 0.3	5.08 : 3 : 1.74 : 0.47 : 0.32	4.99 : 3 : 1.72 : 0.46 : 0.31

\*0.01 g of each crushed pellet was dissolved in a 3/0.4/100 (v/v/v) mixture of 37 wt% hydrochloric acid, 70 wt% nitric acid, and deionized water at 170 °C. As prepared solution was used for the element analysis, except for Li and Zr analysis that used further diluted solution to 1/20 of the original concentration by a 2/100 (v/v) dilution of nitric acid. ICPS-8100 (Shimadzu, Japan) was used for the measurement and the software provided by the manufacturer of the instrument was used for data acquisition

**Table 2.2.** Chemical composition of LLZO pellets from ICP-AES results. Atomic ratio of Li:La:Zr:dopant is normalized by the La content in the formula  $\text{Li}_{7-x}\text{La}_3\text{Zr}_{2-y}(\text{Dopant})_a\text{O}_{12}$ . It indicates that the final compositions of the pellets well matched with the target compositions. Along with the fact that the R factors of the refinement (Figure 2.28 and 2.29) are relatively low when applied to the nominal composition, it supports that the stoichiometry of each composition does not deviate from the designed target compositions.



Sample	Phase	Lattice Parameters ( <i>a</i> , Å)	<i>c/a</i>	Cell vol. [Å <sup>3</sup> ]	Phase fraction (wt.%)	R <sub>I</sub> (%)	R <sub>F</sub> (%)
$\text{Li}_{6.5}\text{La}_3\text{Zr}_{1.5}\text{Ta}_{0.5}\text{O}_{12}$ R <sub>p</sub> : 5.20 % R <sub>wp</sub> : 7.19 %	Cubic	12.93446 (5)	1	2163.94 (2)	94.8 (4)	3.05	3.30
	Tetra	13.03466	0.9928	2198.784	3.48 (15)		
	$\text{La}_2\text{Zr}_2\text{O}_7$	10.80732		1262.275	1.38 (3)	-	-
	$\text{La}_2\text{O}_3$	3.93367	1.5682	82.263	0.38 (2)	-	-
$\text{Li}_{6.25}\text{Al}_{0.25}\text{La}_3\text{Zr}_2\text{O}_{12}$ R <sub>p</sub> : 5.88 % R <sub>wp</sub> : 8.09 %	Cubic	12.96765 (4)	1	2160.64 (1)	91.8 (4)	4.29	3.65
	Tetra	13.03466	0.9928	2198.784	6.2 (2)		
	$\text{LaAlO}_3$	5.36569	2.4442	326.991	2.00 (5)		
	$\text{La}_2\text{O}_3$						
$\text{Li}_{6.5}\text{La}_3\text{Zr}_{1.5}\text{Nb}_{0.5}\text{O}_{12}$ R <sub>p</sub> : 4.88 % R <sub>wp</sub> : 6.72 %	Cubic	12.93433 (6)	1	2163.87 (2)	92.4 (4)	3.26	3.40
	Tetra	13.03466	0.9928	2198.784	6.66 (14)		
	$\text{La}_2\text{Zr}_2\text{O}_7$	10.80732		1262.275	0.68 (3)		
	$\text{La}_2\text{O}_3$	3.93367	1.5682	82.263	0.27 (2)		
$\text{Li}_{4.9}\text{Ga}_{0.5}\text{La}_3\text{Zr}_{1.7}\text{W}_{0.3}\text{O}_{12}$ R <sub>p</sub> : 6.03 % R <sub>wp</sub> : 8.20 %	Cubic	12.94025 (4)	1	2166.85 (1)	92.7 (4)	3.86	3.83
	Tetra	13.03466	0.9928	2198.784	4.9 (2)		
	$\text{La}_2\text{Zr}_2\text{O}_7$	10.80732		1262.275	2.48 (5)		
	$\text{La}_2\text{O}_3$						



**Figure 2.28.** XRD patterns and Rietveld refinement results of the crushed/ground LLZO pellets in powder state, doped with various metals such as Ta, Al, Nb, and Ga,W. As shown in the Rietveld refinement results, each composition consists primarily of the cubic garnet phase and includes a small amount of the tetragonal phase and impure phases, such as  $\text{La}_2\text{Zr}_2\text{O}_7$  (about 0.7~2.5% for all compositions) and  $\text{La}_2\text{O}_3$  (less than 1% for Ta-LLZO and Nb-LLZO). We highlight again that the significant portion of the tetragonal phase is surface-specific of the pellet sample and is attributed to the pellet geometry (thick pellet) used in the XRD measurement. The detailed structural information of LLZOs and the relative phase fractions are similarly tabulated along with the original XRD patterns for the four doped-LLZO powder samples crushed from the pellets here. It indicates substantially higher contents of the cubic phase are indeed present in the pellets. As shown in the Rietveld refinement results, the cubic phase accounts for 94.8 wt% for Ta-LLZO, 91.8 wt% for Al-LLZO, 92.4 wt% for Nb-LLZO and 92.7 wt % for Ga,W-LLZO, respectively, which are significantly greater than the values determined from the pellet XRD data. It supports that the pelletized LLZOs are mainly composed of the cubic phase, however, the amount of the tetragonal phase was overestimated in the pellet XRD. Small amounts of the impure phases, such as  $\text{La}_2\text{Zr}_2\text{O}_7$  (about 0.7~2.5% for all compositions) and  $\text{La}_2\text{O}_3$  (less than 1% for Ta-LLZO and Nb-LLZO) were consistently observed in the powder samples.

\* For the reliability of the data, only scale factor was set as a refinement parameter for the tetragonal phase and impurity phases.

\*\* It should be noted that we did not apply the holder for the crushed pellet XRD measurement due to the empirical/practical reasons and for more accurate analysis.

The main reason for using the air-tight holder was to protect the pellets, which were reused for another analysis or subsequent chemical/electrochemical tests, from the air exposure. Therefore, it was not critically necessary to apply the air-tight holder for powder samples that were not subjected to the further analysis or experiments. Although there might be potential effects from air exposure of powder with increased surface area, it can be considered negligible in interpreting the results. The primary phenomenon that occurs when LLZO is exposed to air is the formation of  $\text{Li}_2\text{CO}_3$  on the surface as reported by Cheng *et al.*<sup>76</sup> If there had been a significant reaction during the XRD measurement to cause the change in the LLZO structure, the peaks arising from  $\text{Li}_2\text{CO}_3$  formation should have been observed. However, it was not observed in our results of the crushed pellets. Thus, the possibility of the massive  $\text{Li}_2\text{CO}_3$  formation during XRD measurement as much as to affect the LLZO phase analysis can be excluded. For these reasons, we have concluded that the displayed results (obtained from XRD measurement without air-tight holder) were still reliable when considering the original purpose of the XRD analysis on the crushed pellets, the proof of the tetragonal LLZO phase that exists only locally on the pellet surface.

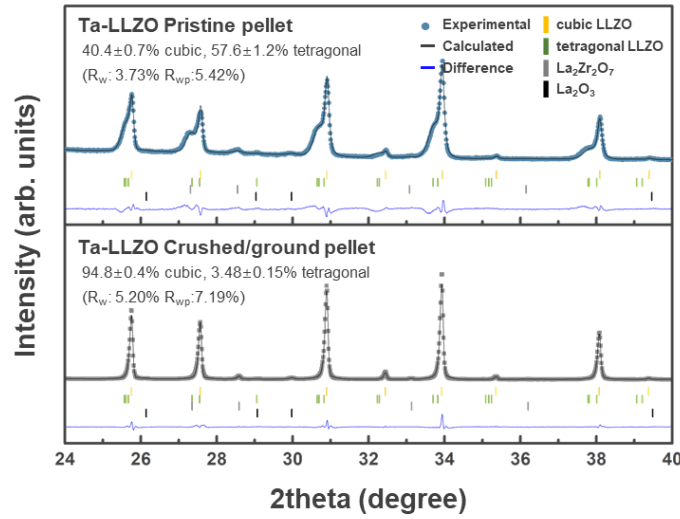
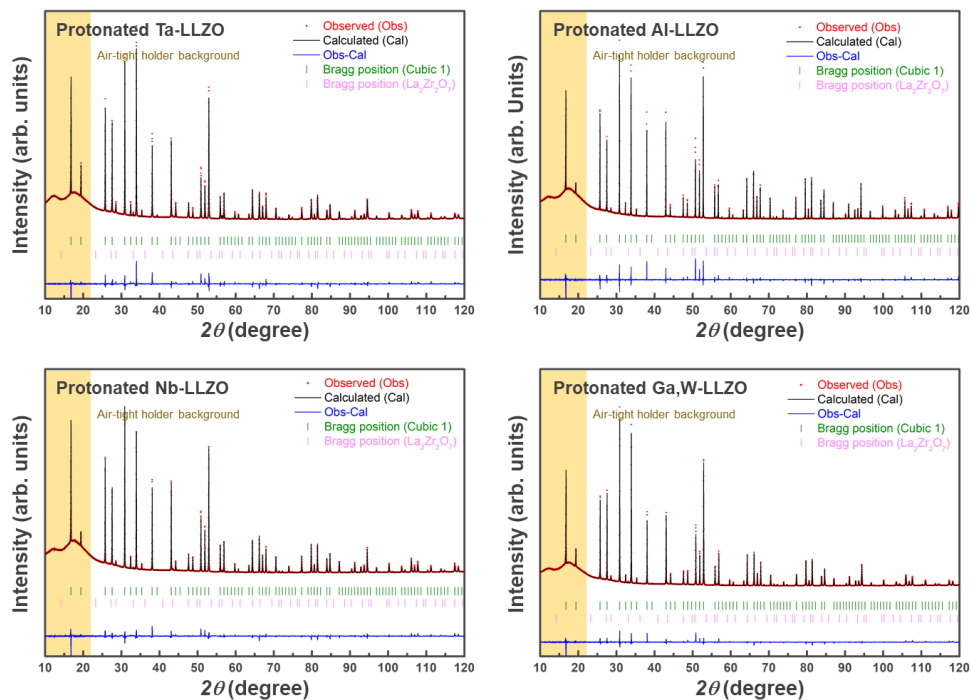


**Figure 2.29.** XRD patterns recorded for a pristine pellet (blue line) and the corresponding crushed/ground pellet in the powder state (grey line) of Ta-LLZO. We simply compared the XRD peaks of the pellet sample with those from the powder sample obtained by crushing/grinding the pellet for the Ta-LLZO. It evidently presents that the peaks from the tetragonal phase are hardly detected in the powder sample crushed from the pellet. We note that this discrepancy arises because the surface of the pellets contains relatively more tetragonal phase than the bulk, which is derived from the pellet preparation process. It is widely known that the formation of the tetragonal phase can be locally promoted during the manufacturing process of the pellets, which involves the application of pressure (during the sintering process) and polishing to remove the surface contamination such as  $\text{Li}_2\text{CO}_3$  or  $\text{LiOH}$ <sup>9,50,72</sup>. During the preparation of our thick LLZO pellet, the surface of the pellet gets exposed to this condition more vulnerably, inducing the preferred formation of the tetragonal phase at the surface. When considering an X-ray penetration depth of ~10–50  $\mu\text{m}$ <sup>68,69</sup>, the XRD results on the 300–350- $\mu\text{m}$ -thick pristine pellets would

preferably represent the surface region of the thick samples and cannot be regarded as showing the overall bulk property of the pellet. Thus, it is reasonable to consider that the coexistence of the two phases with the significant portion of the tetragonal phase is a characteristic that is limited to the surface.



Sample	Phase	Lattice parameter ( $a$ , Å)	Cell vol.[Å <sup>3</sup> ]	Phase fraction (wt.%)	$R_I$ (%)	$R_F$ (%)
H-Li <sub>6.5</sub> La <sub>3</sub> Zr <sub>1.5</sub> Ta <sub>0.5</sub> O <sub>12</sub> $R_p$ : 4.42 % $R_{wp}$ : 6.99 %	Cubic	12.92955 (3)	2161.473 (9)	97.2 (5)	5.22	4.17
	La <sub>2</sub> Zr <sub>2</sub> O <sub>7</sub>	10.81167 (17)	1263.80 (3)	2.81 (6)	-	-
H-Li <sub>6.25</sub> Al <sub>0.25</sub> La <sub>3</sub> Zr <sub>2</sub> O <sub>12</sub> $R_p$ : 3.75 % $R_{wp}$ : 6.08 %	Cubic	12.96768 (2)	2180.656 (7)	98.1 (4)	6.19	3.91
	La <sub>2</sub> Zr <sub>2</sub> O <sub>7</sub>	10.8119 (3)	1263.89 (7)	1.88 (8)	-	-
H-Li <sub>6.5</sub> La <sub>3</sub> Zr <sub>1.5</sub> Nb <sub>0.5</sub> O <sub>12</sub> $R_p$ : 3.85 % $R_{wp}$ : 6.15 %	Cubic	12.93253 (3)	2162.971 (9)	98.7 (4)	5.08	4.14
	La <sub>2</sub> Zr <sub>2</sub> O <sub>7</sub>	10.8110 (3)	1263.56 (7)	1.26 (8)	-	-
H-Li <sub>4.9</sub> Ga <sub>0.5</sub> La <sub>3</sub> Zr <sub>1.7</sub> W <sub>0.3</sub> O <sub>12</sub> $R_p$ : 3.42 % $R_{wp}$ : 5.15 %	Cubic	12.94367 (2)	2168.562 (7)	98.0 (3)	4.49	3.42
	La <sub>2</sub> Zr <sub>2</sub> O <sub>7</sub>	10.8095 (3)	1263.05 (5)	1.97 (8)	-	-

**Figure 2.30.** XRD patterns and Rietveld refinement results of the protonated LLZO pellets doped with various metals such as Ta, Al, Nb, and Ga, W. Each pellet exhibited a cubic garnet phase containing an impurity phase (La<sub>2</sub>Zr<sub>2</sub>O<sub>7</sub>).

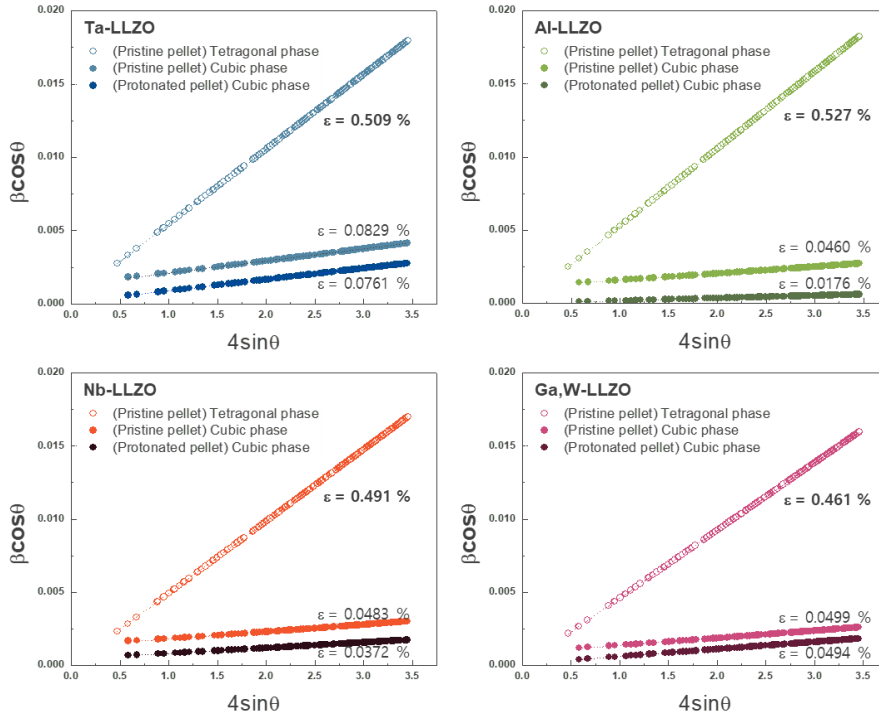


**Figure 2.31.** Size–strain plots for LLZO pellets before and after surface tailoring.

The graphs were plotted based on the Williamson–Hall analysis and Rietveld refinement results presented in Figure 2.25 and 2.28. Williamson–Hall plots were obtained using the equation,  $\beta_{hkl} \cdot \cos\theta = \frac{k\lambda}{D} + 4\varepsilon \cdot \sin\theta$  with the integral breadth that was calculated from the U, X, and Y values from the Rietveld refinement process. The micro-strain values were derived from the slope of the linear fit. Tetragonal phases in the pristine garnet samples exhibited micro-strain values (0.46 – 0.53 %) that were higher than the micro-strain values exhibited by the cubic phase (0.046 – 0.083 %). After the protonation, the micro-strain was released accompanied by the disappearance of the tetragonal phase. Protonated cubic phase also showed decrease of the micro-strain compared to the pristine cubic phase.

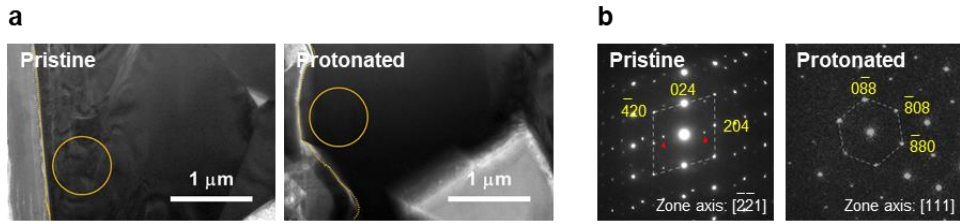


**Figure 2.32.** (a) Bright-field transmission electron microscopy (TEM) images of the surface of Ta–LLZO pellets before and after surface tailoring. The wave pattern in the pristine pellet indicates the existence of a strain field. (b) SAD patterns of Ta–LLZO pellets before and after surface stabilization. SAD pattern from the surface region of the pristine Ta–LLZO along the  $[2\bar{2}1]$  zone-axis shows the spots corresponding to the tetragonal phase. The extra spots indicated by the red arrows represent the existence of an additional phase with a similar crystal structure that might be attributed to the strain field, causing double diffraction. In contrast, protonated Ta–LLZO clearly shows a diffraction pattern corresponding to a single cubic phase.

### 2.3.4. Electrochemical performance of solid-state Li full cell with protonated Ta–LLZO

To validate the effect of the enhanced stability of the tailored LLZO electrolyte on electrochemical performance, comparative electrochemical tests in lithium cell were performed. Figure 2.33 shows the critical current densities measured for symmetric Li/LLZO/Li cells at 60 °C and 25 °C, respectively, with Ta–LLZO or Al–LLZO solid electrolytes. The critical current density represents the highest current density before the apparent short circuiting of a symmetric cell<sup>77,78</sup>, and thus, it is widely accepted as a valid criterion for determining the reliability of a solid-electrolyte–Li-metal system. The figures show that the critical current density of lithium symmetric cells can be significantly improved by employing the co-doped LLZO solid electrolytes. The cells with protonated Ta– and Al–LLZO delivered critical current densities of approximately 2.6 and 2.0 mA cm<sup>-2</sup>, respectively, at 60 °C, and 1.6 mA cm<sup>-2</sup> at 25 °C, which are remarkably higher than those obtained for the pristine equivalents. Inspired by the considerably improved stability, the tailored LLZO solid electrolyte/Li-metal anode was employed in a hybrid solid-state battery using a conventional NCM111 (LiNi<sub>1/3</sub>Co<sub>1/3</sub>Mn<sub>1/3</sub>O<sub>2</sub>) cathode with a loading capacity of 3.2 mAh cm<sup>-2</sup>, which corresponded to the cathode requirements for the commercial high-energy-density Li-ion cells<sup>79</sup>. To ensure stable contact between the thick cathode and solid electrolyte, the cathode side was slightly wetted with an ionic liquid (*i.e.* 2 M lithium bis(fluorosulfonyl)imide (LiFSI) in N-methyl-N-propyl pyrrolidinium bis(fluorosulfonyl)imide (Pyr13FSI)) in a hybrid solid-state battery. Figure 2.34 shows the charge–discharge curves and rate capability of the hybrid full cells measured at 60 °C, the temperature at which the batteries for electric vehicles are



commonly tested<sup>80,81</sup>. The electrochemical profiles were obtained by increasing the current density stepwise; *i.e.*, the cells were charged/discharged with current densities of 0.3 mA cm<sup>-2</sup> for the first cycle, 0.5 mA cm<sup>-2</sup> for the next five cycles, 1 mA cm<sup>-2</sup> for the subsequent five cycles, 1.6 mA cm<sup>-2</sup> for the 12<sup>th</sup> to the 21<sup>st</sup> cycle, 2 mA cm<sup>-2</sup> for the 22<sup>nd</sup> to the 31<sup>st</sup> cycle, and 3 mA cm<sup>-2</sup> for the 32<sup>nd</sup> to the 41<sup>st</sup> cycle. The cells delivered characteristic charge–discharge curves of the NCM111 cathode, which were sustained without any short-circuit signals (*i.e.* voltage noise and/or sudden drop), even at a high current density of 3 mA cm<sup>-2</sup>. Comparing these results with those for the cells composed of the pristine doped-LLZO electrolytes in Figure 2.35, strongly supports the hypothesis that lithium penetration in the protonated Ta– and Al–LLZO electrolytes is significantly suppressed, which allows operation at a practically high current density. In contrast, the cells with protonated Nb– and Ga,W–LLZO electrolytes short circuited at current densities below 1 mA cm<sup>-2</sup>, while the typical charge–discharge behavior of the NCM111 was observed only at low current density (Figure 2.36). This result was consistent with our findings that the secondary doping of proton in Nb– and Ga,W–LLZO did not yield insulating by-products, and thus, could not passivate the interface.

Figure 2.37 exemplifies that the protonated LLZO cells are capable of delivering a high rate capability without significant degradation. Approximately 93% and 63% of the capacity relative to the initial capacity at 0.5 mA cm<sup>-2</sup> was delivered at 3 mA cm<sup>-2</sup> for the protonated Ta–LLZO and Al–LLZO cells, respectively. Moreover, we fabricated a higher capacity cathode designed for 6.4 mAh cm<sup>-2</sup>, using high-nickel NCM811 (LiNi<sub>0.8</sub>Co<sub>0.1</sub>Mn<sub>0.1</sub>O<sub>2</sub>) and cycled the cell at 1.6 mA cm<sup>-2</sup> (Figure 2.38). It is noteworthy that the cell with the high-capacity cathode in a protonated Ta–

LLZO electrolyte provided 87% of the capacity at  $1.6 \text{ mA cm}^{-2}$  with 99.7% Coulombic efficiency after 100 cycles. The high capacity of this cathode also implies that Li-metal as thick as  $32 \text{ }\mu\text{m}$  could be reversibly deposited and stripped through the tailored Ta-LLZO solid electrolyte over 100 times without any notable degradation. The cells were also tested under harsher conditions, such as a high temperature of  $100 \text{ }^{\circ}\text{C}$  (Figure 2.39). The limiting current density could further increase over  $10 \text{ mA cm}^{-2}$  for the cell with protonated Ta-LLZO, which could not be attained for the protonated Al- or Nb- LLZO system. The cell was also successfully cycled over 100 times delivering 96% of the nominal capacity (*i.e.*,  $3.2 \text{ mAh cm}^{-2}$ ) at a current density of  $6 \text{ mA cm}^{-2}$  with a Coulombic efficiency of 99.6%. This indicates that the cell can be stably operated at  $100 \text{ }^{\circ}\text{C}$  without short-circuiting, a temperature at which most LIBs using conventional liquid electrolytes are irreversibly damaged<sup>80</sup>. The cell using protonated Nb-LLZO failed to cycle at  $100 \text{ }^{\circ}\text{C}$  owing to short-circuits, even when operated at a low current density. This is attributed to the accelerated reaction of Nb-LLZO with Li at a higher temperature, leading to premature short-circuiting. Although the cell with protonated Al-LLZO did not show any short-circuiting, its capacity notably decreased at high current densities, showing an inferior rate capability than the case of protonated Ta-LLZO cell. Further details regarding the rate capabilities are discussed in Figure 2.40-2.41 and Table 2.3.

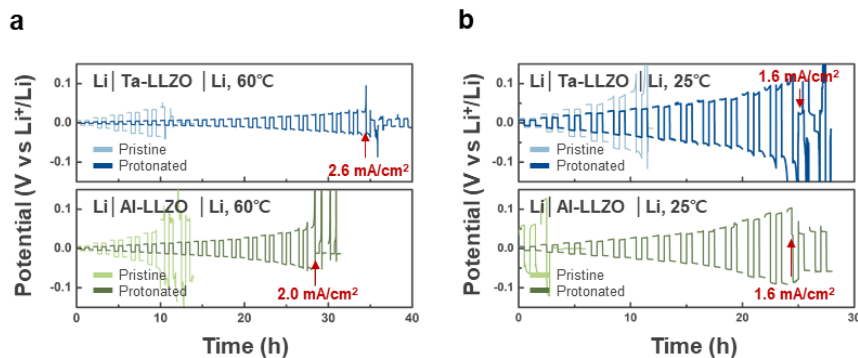
To further confirm that interface stabilization plays an important role in cell stability, we performed long-term cycling tests on the NCM111/protonated Ta-LLZO/Li hybrid cells. Two NCM111 cathodes with capacities of 2 and  $3.2 \text{ mAh cm}^{-2}$  were used in the cell and cycled at current densities of 3 and  $1.6 \text{ mA cm}^{-2}$ ,

respectively. Figure 2.42 suggests that these cells maintained remarkable cycling performance over 2,000 and 1,000 cycles, respectively, without significant capacity degradation or short-circuit failure for each capacity cell (Figure 2.32). This corresponds to a cumulative thickness of 19.4 and 15.5 mm, respectively, of plated Li-metal during cell operation. Even after 1,000 cycles, the cell had excellent coulombic efficiency (99.92% at the 1,000<sup>th</sup> cycle). We further examined the long-term performance of the cell using a thinner electrolyte (~110  $\mu\text{m}$ ) fabricated via the tape-casting method or by applying a composite cathode with a capacity of 5 mAh  $\text{cm}^{-2}$  that consisted of  $\text{Li}_6\text{PS}_5\text{Cl}$  electrolyte and high-nickel NCM811 ( $\text{LiNi}_{0.8}\text{Co}_{0.1}\text{Mn}_{0.1}\text{O}_2$ ). Figure 2.44 shows that protonated Ta-LLZO with a thickness of 110  $\mu\text{m}$  was capable of delivering long-term cycle stability over 600 cycles without short-circuiting at a high current density of 2 mA  $\text{cm}^{-2}$ , although it retained slightly less capacity than the thicker pellet due to the different surface properties (Figure 2.45). In addition, an all-solid-state-battery, excluding the ionic liquid electrolyte, was successfully demonstrated using the composite cathode, which could cycle over 1,000 times at a high current density of 3 mA  $\text{cm}^{-2}$  without short-circuiting (Figure 2.46). To the best of our knowledge, this is the first all-solid-state battery that can operate over 1,000 cycles, enabled by the garnet-type electrolytes and cathode with a commercially acceptable capacity.

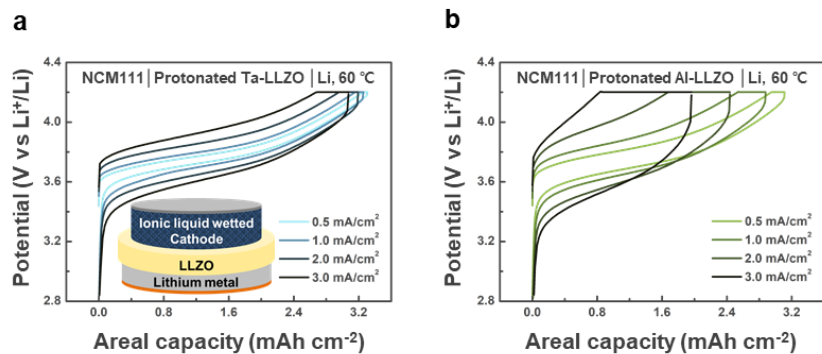
Figure 2.47 compares the performance of our Li-metal cells with results from the literature for the areal cathode capacity (*i.e.*, equivalent to the amount of Li metal utilized per cycle in a Li-metal cell), cumulative capacity of the deposited lithium, and the operating current density, which are regarded as the important practical parameters for assessing the performance of solid-state Li-metal batteries.<sup>31</sup> The left

figure shows that compared with the previously reported studies on garnet-based oxides as a solid-electrolyte, the cell with protonated Ta-LLZO utilized significantly higher cathode capacity (up to 6 mAh cm<sup>-2</sup>) in full cells. The state-of-the-art cells reported to date used cathodes with an areal capacity less than 0.5 mAh cm<sup>-2</sup>, which is hardly applicable to practical battery systems. If we assume our hybrid solid-state battery configuration as a one-unit cell in a pack, the utilization of the high-capacity-cathode (NCM811) of 6 mAh cm<sup>-2</sup> would presumably result in a volumetric energy density of 428 Wh L<sup>-1</sup>. Moreover, since we demonstrated the feasibility of the 110- $\mu$ m-thick Ta-LLZO solid electrolyte with a cathode (NCM111) of 3 mAh cm<sup>-2</sup> capacity, a new cell would be expected to deliver a remarkable energy density of 470 Wh L<sup>-1</sup>, making it promising for practical applications (see Table 2.4 for the details). The cumulative lithium capacities were calculated and plotted considering the capacity deposited on the Li-metal anode in the full cells (Figure 2.47, right). Except for the symmetric cell reported by Yang<sup>82</sup> and Taylor<sup>83</sup>, all the previous studies were conducted at current densities below 1 mA cm<sup>-2</sup>, with capacities less than 1 mAh cm<sup>-2</sup>. The cells with the tailored co-doped LLZO electrolyte showed outstanding performance, particularly in terms of the cumulative capacities, which were 4,000 mAh cm<sup>-2</sup> (3,200 mAh cm<sup>-2</sup>) when the hybrid cell with a capacity of 2 mAh cm<sup>-2</sup> (3.2 mAh cm<sup>-2</sup>) was cycled at 3 mA cm<sup>-2</sup> (1.6 mA cm<sup>-2</sup>). More importantly, the all-solid-state-battery cell with the co-doped LLZO electrolyte and 5 mAh cm<sup>-2</sup> composite cathode (without any liquid) also delivered 4,000 mAh cm<sup>-2</sup> at 3 mA cm<sup>-2</sup>. To the best of our knowledge, these are the highest long-term cycling parameters reported thus far for cells with garnet-oxide electrolytes and Li-metal anodes. This is the first time that a secondary battery of this kind could satisfy the lifespan requirements of

energy storage in vehicles and stationary applications.<sup>31</sup> The successful demonstration of the potential applicability of the garnet electrolyte and Li-metal is expected to spur the development of practical all-solid-state batteries with high-energy density and long-lasting cycling stability.



**Figure 2.33.** Critical current densities of pristine (light blue and green lines) and surface-tailored (dark blue and green lines) Ta– or Al–LLZO (a) at 60 °C and (b) 25 °C as determined by galvanostatic cycle tests on the symmetrical cells with increasing current densities ranging from 0.1 to 1  $\text{mA cm}^{-2}$  at a step size of 0.1  $\text{mA cm}^{-2}$  and from 1.0 to 3.0  $\text{mA cm}^{-2}$  at a step size of 0.2  $\text{mA cm}^{-2}$ . At each current density, the cells were cycled twice with 30 min of Li plating/stripping.



**Figure 2.34.** Voltage profiles of Li/LLZO/NCM111 cells at 60 °C with doped, surface-tailored (a) Ta- and (b) Al-LLZO electrolytes.

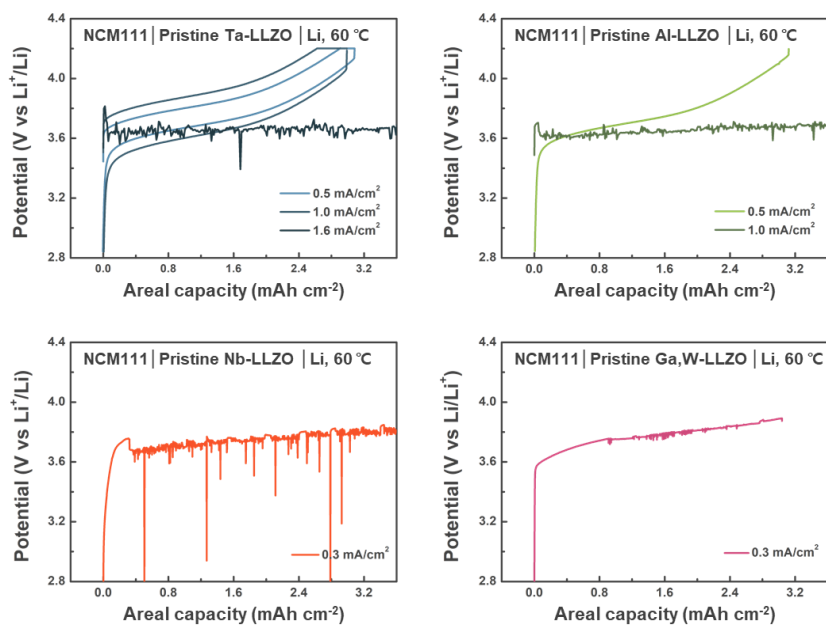


**Figure 2.35.** Electrochemical performances of hybrid solid-state full cells measured at 60 °C, employing a Li-metal anode and a pristine LLZO with various dopants. The extent of operating current density increase was more in the case when Ta– and Al–LLZO were used than the case when Nb– and Ga,W–LLZO were used. The maximum increase in the operating current density was observed when the surface-tailored Ta– and Al–LLZO were used (Figure 2.34).



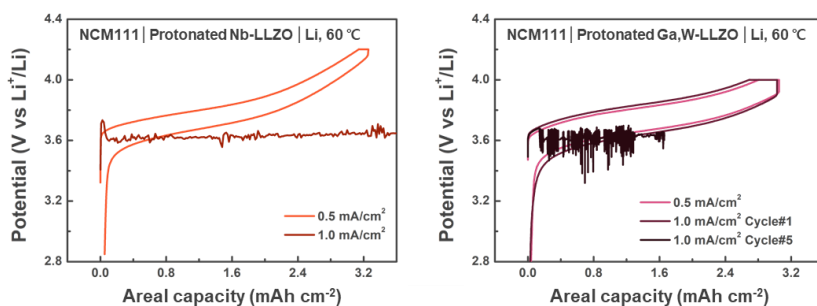


**Figure 2.36.** Electrochemical performances of hybrid solid-state full cells measured at 60 °C. The cells were fabricated using a Li-metal anode and a protonated Nb– and Ga,W–LLZO. It should be noted that the acid treatment process did not substantially mitigate lithium propagation through the Nb– and Ga,W–LLZO electrolytes. The results revealed the importance of controlling the nature of the by-products at the interface.

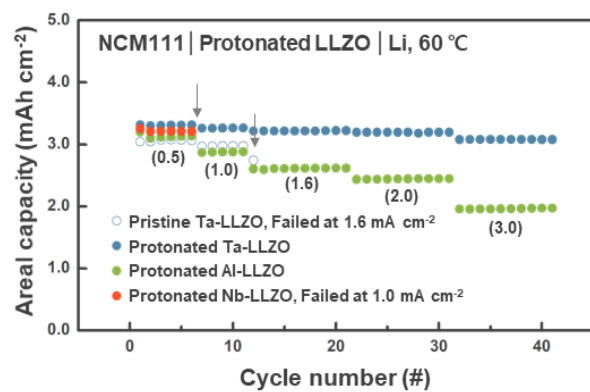


**Figure 2.37.** Rate capability of hybrid solid-state full cells with surface-tailored LLZOs and Li-metal anodes for various dopants.

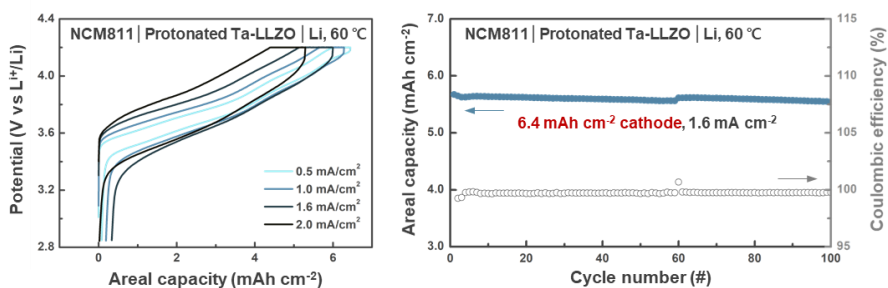


**Figure 2.38.** Voltage profiles and cyclability of the hybrid solid-state full cell using surface-tailored Ta-LLZO and an NCM811 cathode with a high capacity of 6.4 mAh cm<sup>-2</sup> at 60 °C. A capacity of 6.0 mAh cm<sup>-2</sup> corresponds to a Li-metal thickness above 30  $\mu$ m.

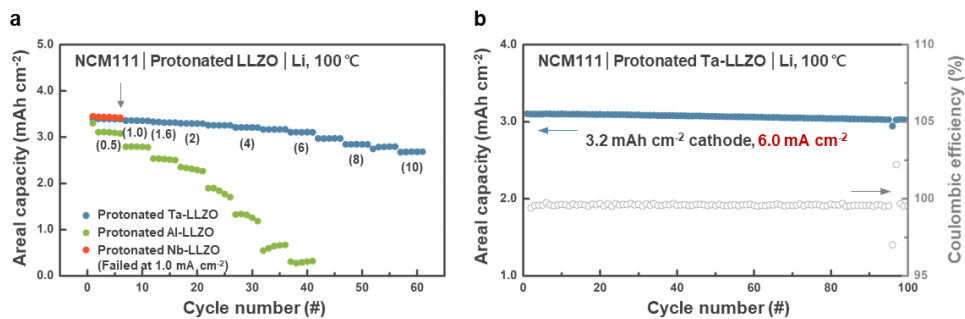


**Figure 2.39.** (a) Rate capability of the hybrid solid-state full cells with surface-tailored LLZOs and Li-metal anodes for various dopants. For the rate capability test at 100 °C, the cells were operated with increasing current densities (indicated with numbers in parentheses). (b) Cyclability of the hybrid solid-state full cell using surface-tailored Ta-LLZO at 100 °C.

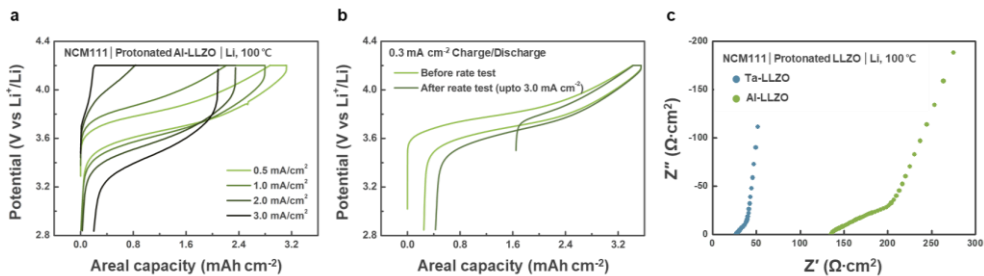


**Figure 2.40.** (a–b) Voltage profiles of Li/protonated Al–LLZO/NCM111 cells at 100 °C under the current densities of (a) 0.5, 1.0, 2.0, and 3.0 mA cm<sup>-2</sup> and (b) 0.3 mA cm<sup>-2</sup> before and after the tests (shown in (a)). (c) Initial EIS profiles recorded with NCM111/protonated Ta– or Al–LLZO/Li cells at 100 °C before the electrochemical tests were conducted (Figure 2.39). At the current densities greater than 4 mA cm<sup>-2</sup>, the Al–LLZO cell delivers far smaller capacity than Ta–LLZO cells. It is believed that the primary reason for the inferior rate capability of the Al–LLZO is the comparatively slower migration of Li in the Al–LLZO than that of the Ta–LLZO. When we performed EIS on the cells at 100 °C before cycling, it was found that Al–LLZO cell showed a larger impedance than that of the Ta–LLZO. The intrinsically large impedance of the cell would be consequently accompanied by a large overpotential at higher current densities and the capacity reduction. It is also noteworthy that the capacity decrease at high current densities is not ascribed to an irreversible degradation of the cell such as deterioration of the Al–LLZO. It is evident here that, even after the cycling at high current densities, the capacity could be recovered when the cell is cycled again at a low current density of 0.3 mA cm<sup>-2</sup>.

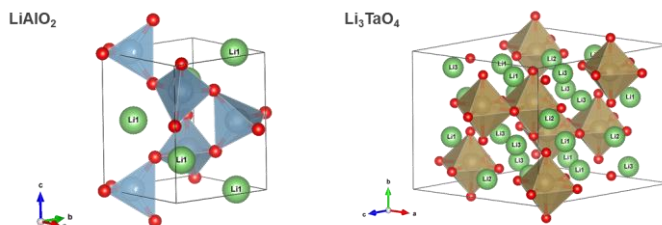


**Figure 2.41.** Crystal structures of lithium aluminium oxide ( $\gamma$ -LiAlO<sub>2</sub>) and lithium orthotantalate ( $\beta$ -Li<sub>3</sub>TaO<sub>4</sub>). The lithium sites are marked with numbers in each structure. We acknowledge that the reaction products of protonated Ta– or Al–LLZO with Li-metal may affect the rate capability of the cells. In this respect, we further investigated the ionic conductivities of Li<sub>3</sub>TaO<sub>4</sub> and LiAlO<sub>2</sub>, which are the reactant products of protonated Ta– and Al–LLZO with Li-metal. Li-ion diffusion barriers were calculated using the nudged elastic band (NEB) method and implemented in the Vienna ab initio simulation package (VASP), by considering all possible pathways of the Li vacancy migration in the crystal structure. In LiAlO<sub>2</sub>, there is only one diffusion path between the Li1 sites. In Li<sub>3</sub>TaO<sub>4</sub>, there are, in total, 14 paths for Li diffusion to occur (three different sites: Li1, Li2, and Li3). The energy barriers for Li migration through Li1–Li2 (0.17–0.29 eV) and Li2–Li3 (0.29–0.39 eV) were extremely low. These energy barriers were significantly lower than the barrier observed in LiAlO<sub>2</sub> (0.52 eV, Table 2.3). The energy barrier values refer to the barrier in its reverse direction, owing to the asymmetric diffusion path from one site to the other. A large Li-ion migration barrier in LiAlO<sub>2</sub> was also reported by Wiedemann, D. *et al.*<sup>84</sup> The results revealed that the interfacial decomposition product produced from protonated Al–LLZO exhibited lower ionic conductivity than protonated Ta–LLZO). It also implies that the different nature of the reaction products with respect to the Li migration would contribute to the difference in the overall rate performance.

	Ionic migration path		Migration energy barrier (eV)
<b>LiAlO<sub>2</sub></b>	Li1 ↔ Li1		0.52
<b>Li<sub>3</sub>TaO<sub>4</sub></b>	Li1 ↔ Li1	Path1	0.58
		Path2	0.60
	Li2 ↔ Li2	Path1	0.41
		Path2	0.47
	Li3 ↔ Li3	Path1	0.17
		Path2	1.15
	Li1 ↔ Li2	Path1	0.29 (0.17)
		Path2	0.43 (0.32)
		Path3	0.54 (0.42)
	Li2 ↔ Li3	Path1	0.39 (0.29)
		Path2	0.50 (0.40)
		Path3	0.55 (0.45)
	Li3 ↔ Li1	Path1	0.37 (0.40)
		Path2	0.78 (0.81)

**Table 2.3.** Lithium-ion diffusion energy barrier in lithium aluminium oxide ( $\gamma$ -LiAlO<sub>2</sub>) and lithium orthotantalate ( $\beta$ -Li<sub>3</sub>TaO<sub>4</sub>) calculated using the nudged elastic band (NEB) method implemented in VASP. All possible pathways of lithium vacancy migration in the crystal structure were considered, corresponding to the sites shown in Figure 2.41.

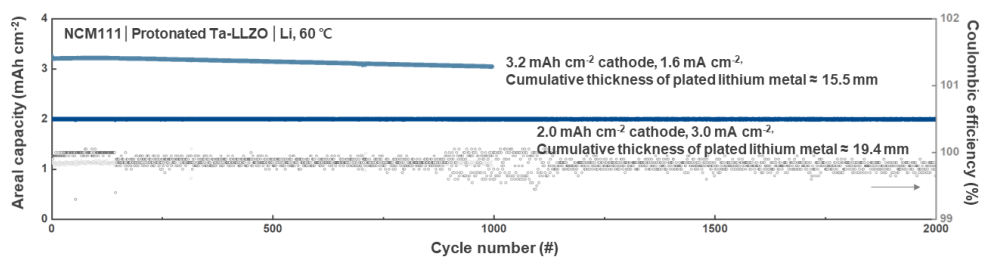


**Figure 2.42.** Long-term cycling performance of NCM111/protonated Ta-LLZO/Li hybrid cells. The cells maintained remarkable cycling performance over 1,000 and 2,000 cycles, delivering 3.2 and 2.0 mAh cm<sup>-2</sup>, respectively, at an average Coulombic efficiency over 99.83%, without significant capacity degradation or short-circuit failure.



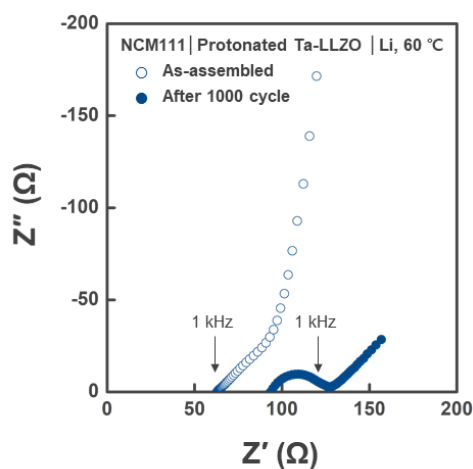


**Figure 2.43.** EIS profiles of NCM111/protonated Ta-LLZO/Li hybrid cells at 60 °C before and after cycling, as shown in Figure 2.42. The change in the cell impedance after 1000 cycles is remarkably small, considering the EIS spectrum exhibits signals corresponding to all the components and interfaces of the cell. It is noted that numerous physical or (electro) chemical reactions can potentially influence the EIS spectra (such as Solid Electrolyte Interphase (SEI) growth/decomposition, active material degradation/exfoliation, or loss of electric contact<sup>85-88</sup>).

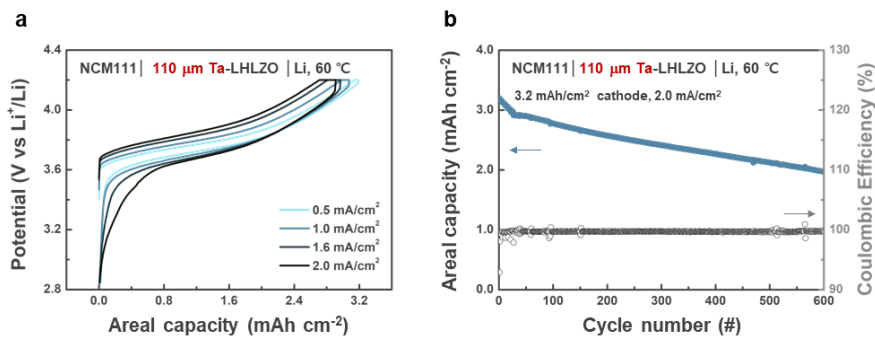


**Figure 2.44.** Electrochemical performance of hybrid solid-state full cells at 60  $^{\circ}\text{C}$ , fabricated using a Li-metal anode and thin 110- $\mu\text{m}$ -thick surface-stabilized Ta-LLZO. (a) Voltage profiles of the Li/LLZO/NCM111 cell and (b) Cyclability at 60  $^{\circ}\text{C}$ . The cells could be operated for a prolonged time (600 cycles) without short-circuiting under a high current density of 2  $\text{mA cm}^{-2}$ . A high capacity of 3.2  $\text{mAh cm}^{-2}$  was recorded. Long-term cycle stability ( $> 600$  cycles) was exhibited by the protonated 110- $\mu\text{m}$ -thick Ta-LLZO. Although this cell exhibited less capacity than the cell fabricated using a thicker pellet, Li-metal was plated/stripped during the long-term cycling process in a stable manner, owing to the enhanced interfacial stability achieved through surface tailoring. The discrepancy in the capacity retentions between the tape-cast and hot-pressed pellet cells can be potentially attributed to the degradation of the Li/LLZO interface. The degradation can be attributed to the differences in their surface properties (such as the composition and microstructure), as described in Figure 2.45.

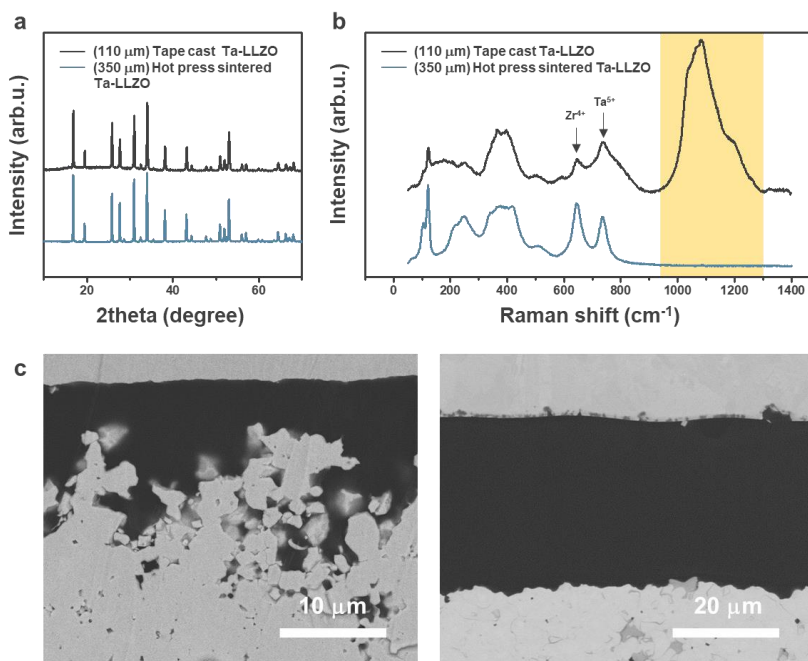


**Figure 2.45.** The comparisons of physical properties of hot press-sintered and tape cast Ta-LLZO electrolytes. (a) XRD patterns of the hot-pressed and sintered Ta-LLZO (thickness: 350  $\mu\text{m}$ ) and tape-cast Ta-LLZO (thickness: 110  $\mu\text{m}$ ) electrolyte surfaces after protonation. The electrolytes exhibited cubic-garnet-like structures containing 1–2% of  $\text{La}_2\text{Zr}_2\text{O}_7$ . The results implied that the crystal structure of the electrolytes did not significantly differ from each other. (b) Raman spectral profiles of the hot-pressed and sintered Ta-LLZO (thickness: 350  $\mu\text{m}$ ) and tape-cast Ta-LLZO (thickness: 110  $\mu\text{m}$ ) electrolyte surface after protonation. Several bands were observed in the spectral profile of the tape-cast electrolyte in the range of 950 to 1300  $\text{cm}^{-1}$  (indicated by yellow range). These bands were absent in the spectral profiles of the 350  $\mu\text{m}$ -thick pellet. While the origin of these bands is not clear, we hypothesized that these could be attributed to an amorphous phase or the residual carbon compounds present on the electrolyte surface. The residual carbon compounds originated from the organic binders used in the tape-cast process

conducted under different sintering conditions. Raman spectra were collected using a Renishaw inVia<sup>TM</sup> Raman microscope with a 514 nm laser, 2400 lines/mm holographic grating, and 50× magnification. In order to prevent the exposure of the electrolytes to the ambient atmosphere, all the samples were analysed in the sealed state using ketone tape. (c) Cross-sectional SEM images of surface tailored pellet and tape-cast electrolyte in contact with the lithium metal. The tape-cast electrolyte exhibited a less rough and porous surface morphology. The time for surface tailoring was shortened to 10 minutes, taking into account that the thickness of tape-cast electrolyte is about 1/3 of pellets and the average grain size of tape-cast electrolyte is smaller than that of the pellet. This could lead to the difference in the corrosion effect, forming a less rough and porous surface.

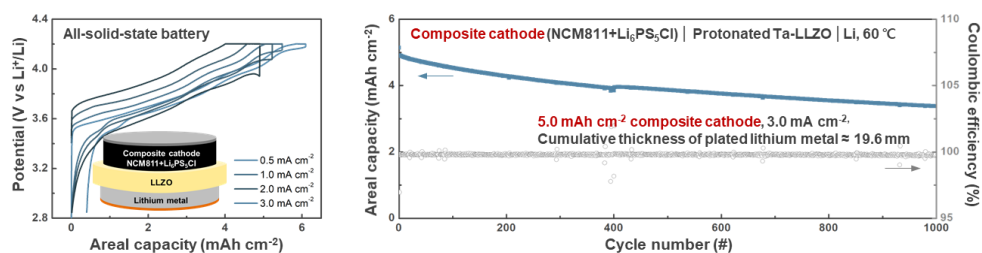


**Figure 2.46.** Voltage profiles and long-term cycling performance of all-solid-state battery using a composite of NCM811 and  $\text{Li}_6\text{PS}_5\text{Cl}$  electrolyte as the cathode, showing a capacity of  $5 \text{ mAh cm}^{-2}$  at  $60^\circ\text{C}$  with doped, surface-tailored electrolytes. The cell successfully operated over 1,000 times at a high current density of  $3 \text{ mA cm}^{-2}$  without short-circuiting.

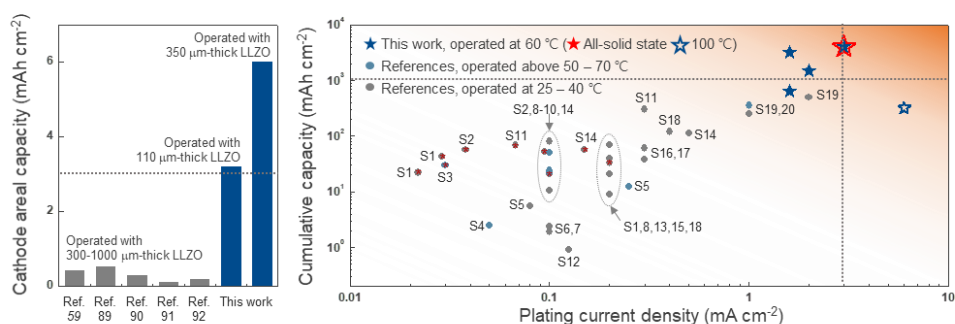


**Figure 2.47.** Performance comparison of solid-state batteries using garnet-type solid electrolytes and Li-metal anodes. The left graph shows the cathode capacity of full cells studied previously<sup>59,89-92</sup> in comparison with the cells of the surface-stabilized Ta-LLZO electrolyte. The right plot summarizes the current density and cumulative areal plating capacity at several temperatures based on the previous reports (see Table 2.5 for detailed references, Ref. S1-S20 as indicated on the figure) The values corresponding to full cells are distinguished from those of the symmetric cells by red asterisks; the dashed lines indicate the minimum requirement for industrial applications<sup>31</sup>.

	<b>Composition</b>	<b>NCM111</b>	<b>NCM811</b>
<b>Cathode</b>	Areal capacity (mAh cm <sup>-2</sup> )	3.2	6.0
	Thickness (mm)	66	81
<b>Solid electrolyte</b>	Thickness (mm)	110	330
<b>Anode</b>	Initial Li thickness (mm)	20	20
	Plated Li thickness (mm)	16	31
<b>Current collector</b>	Al for cathode (mm)	12	12
	Cu for anode (mm)	10	10
<b>Total thickness (mm)</b>		234	484
<b>Cell area (cm<sup>2</sup>)</b>		30.2	30.2
<b>Cell volume including package film (L)</b>		0.780	1.609
<b>Discharge V<sub>ave</sub> (V)</b>		3.79	3.8
<b>Energy density (Wh L<sup>-1</sup>)</b>		470	428

**Table 2.4.** Parameters considered for estimating the energy densities of the full cells.

Ref. No.	Cell configuration	Plating current density (mA/cm <sup>2</sup> )	Per-cycle plating capacity (mAh/cm <sup>2</sup> )	No. of cycles	Cumulative Li-metal capacity (mAh/cm <sup>2</sup> )	References
S1	Li LLZT-RAT LCO	0.022	0.220	100	22.0	Nano Energy 61, 119 (2019)
	Li LLZT-RAT LFP	0.029	0.286	150	42.9	
	Li LLZT-RAT Li	0.200	0.100	700	70.0	
S2	Li LLZT LCO	0.038	0.192	300	57.6	Energy & Environmental Science 13, 127 (2020)
	Li LLZT Li	0.100	0.050	1000	50.0	
S3	Li Al-LLZO+PEO NCM composite	0.030	0.300	100	30.0	J. Industrial and Engineering Chemistry, 71, 445 (2019)
S4	Li-Sn Ca,Nb-LLZO Li-Sn	0.050	0.025	100	2.5	Adv. Energy Mater. 8, 1701963 (2017)
S5	Li LLZT Li	0.080	0.160	35	5.6	ACS Appl. Mater. Interfaces 8, 10617 (2016)
	Li LLZT Li	0.250	0.500	25	12.5	
S6	Li (Mg coated)Ca,Nb-LLZO Li	0.100	0.008	225	1.9	Angew. Chem. Int. Ed. 56, 14942 (2017)
S7	Li Ca,Nb-LLZO Li	0.100	0.017	141	2.4	Nano Lett. 17, 565 (2017)
S8	Li LLZT Li	0.100	0.200	102	20.4	ACS Applied Energy Materials 2, 6720 (2019)
	Li LLZT Li	0.200	0.200	104	20.8	
S9	Li LLZT Li	0.100	0.008	1260	10.5	Nano Lett. 18, 7414 (2018)
	Li LLZT LFP	0.100	0.120	200	24.0	
S10	Li LLZT-C Li	0.100	0.100	500	50.0	Journal of the American Chemical Society 140, 6448 (2018)
	Li LLZT-C LFP	0.100	0.429	50	21.5	
S11	Li Graphite coated W-LLZO Li	0.300	0.300	1000	300.0	ACS Energy Lett. 3, 1212 (2018)
	Li Graphited coated W-LLZO NCM523	0.068	0.135	500	67.5	
S12	Li Gel LLZO gel Li	0.125	0.010	90	0.9	ACS Appl. Mater. Interfaces 9, 18809 (2017)
S13	Li LLZO Li	0.200	0.400	100	40.0	Chem. Mater. 29, 7961 (2017)
S14	Li LLZT Li	0.100	0.050	1600	80.0	Journal of Materials Chemistry A 7, 14565 (2019)
	Li LLZT Li	0.500	0.250	450	112.5	
	Li LLZT LFP	0.095	0.516	100	51.6	
	Li LLZT NCM523	0.150	0.480	120	57.6	



S15	Li LLZO Li	0.200	0.100	90	9.0	Nature Materials 16, 572-579 (2017)
S16	Li+Graphite LLZT  Li+Graphite	0.300	0.150	250	37.5	Advanced Materials 31, 1807243 (2019)
S17	Li (Graphite LLZT  NCM622)Integrated Composite Membrane	0.300	0.300	200	60.0	ACS Appl. Mater. Interfaces 12, 15120 (2020)
S18	Li Ga-LLZO Li	0.400	0.200	600	120	Ceramics International, 45, 14991 (2019)
	Li Ga-LLZO LFP	0.200	0.600	55	33	
S19	LiMg LLZO LiMg	1.000	1.000	250	250.0	Adv. Mater. 31, 1804815 (2019)
	LiMg LLZO LiMg	2.000	2.000	250	500.0	
S20	Li LLZO Li	1.000	3.000	117	351.0	Journal of Power Sources 396, 314-318 (2018)

**Table 2.5.** Summary of the electrochemical plating/stripping performances of the cells (garnet electrolyte and Li-metal) reported in the literature.

## 2.4. Conclusion

We introduced the high energy density-Li-metal battery that was stable over 2000 cycles, employing tailored garnet-type electrolytes. The compatibility between LLZO and Li-metal was suggested to be critical for the long-term stability and could be accomplished by the co-doping of bulk dopants and surface-specific secondary dopants. Given the chemical/ electrochemical instability of the doped-LLZO against Li metal, proton was rationally selected as the secondary dopant based on the DFT predictions of the reductive by-products, which could be feasibly applied for the selective doping of the interface/grain boundary by solution-based etching process. The spatially co-doped system could aid in (i) the formation of a stable passivation layer at the interface with Li-metal, (ii) the effective release of residual stress in LLZO, and (iii) maintaining the intact contact at the interface. This approach led to considerable enhancement of performance in a full cell comprising the protonated Ta-LLZO electrolyte, Li-metal, and conventional NCM111 cathode, and it exhibited an impressive cumulative Li-metal capacity of  $4000 \text{ mAh cm}^{-2}$  at  $3 \text{ mA cm}^{-2}$ . This is the first successful example of a Li-metal battery that meets the lifespan requirements of electrical energy storage in both vehicles and stationary applications. Considering the ease and broad potential applicability of our approach, the findings presented here are expected to open a new pathway for the development of solid-state batteries employing garnet electrolytes.

## 2.5. References

- 1 Tarascon, J. M. & Armand, M. Issues and challenges facing rechargeable lithium batteries. *Nature* **414**, 359-367, doi:10.1038/35104644 (2001).
- 2 Lin, D., Liu, Y. & Cui, Y. Reviving the lithium metal anode for high-energy batteries. *Nature Nanotechnology* **12**, 194-206, doi:10.1038/nnano.2017.16 (2017).
- 3 Guo, Y., Li, H. & Zhai, T. Reviving Lithium-Metal Anodes for Next-Generation High-Energy Batteries. *Adv. Mater.* **29**, 1700007 (2017).
- 4 Qian, J. *et al.* High rate and stable cycling of lithium metal anode. *Nat. Commun.* **6**, 6362 (2015).
- 5 Cheng, X.-B., Zhang, R., Zhao, C.-Z. & Zhang, Q. Toward Safe Lithium Metal Anode in Rechargeable Batteries: A Review. *Chemical Reviews* **117**, 10403-10473, doi:10.1021/acs.chemrev.7b00115 (2017).
- 6 Janek, J. & Zeier, W. G. A solid future for battery development. *Nature Energy* **1**, 16141, doi:10.1038/nenergy.2016.141 (2016).
- 7 Manthiram, A., Yu, X. & Wang, S. Lithium battery chemistries enabled by solid-state electrolytes. *Nature Reviews Materials* **2**, 16103, doi:10.1038/natrevmats.2016.103 (2017).
- 8 Miara, L. J. *et al.* Effect of Rb and Ta Doping on the Ionic Conductivity and Stability of the Garnet  $\text{Li}_{7+2x-y}(\text{La}_{3-x}\text{Rb}_x)(\text{Zr}_{2-y}\text{Ta}_y)\text{O}_{12}$  ( $0 \leq x \leq 0.375$ ,  $0 \leq y \leq 1$ ) Superionic Conductor: A First Principles Investigation. *Chemistry of Materials* **25**, 3048-3055, doi:10.1021/cm401232r (2013).
- 9 Samson, A. J., Hofstetter, K., Bag, S. & Thangadurai, V. A bird's-eye view of Li-stuffed garnet-type  $\text{Li}_7\text{La}_3\text{Zr}_2\text{O}_{12}$  ceramic electrolytes for advanced

- all-solid-state Li batteries. *Energy & Environmental Science* **12**, 2957-2975, doi:10.1039/C9EE01548E (2019).
- 10 Zhu, Y., He, X. & Mo, Y. Origin of Outstanding Stability in the Lithium Solid Electrolyte Materials: Insights from Thermodynamic Analyses Based on First-Principles Calculations. *ACS Applied Materials & Interfaces* **7**, 23685-23693, doi:10.1021/acsami.5b07517 (2015).
  - 11 Cheng, E. J., Sharafi, A. & Sakamoto, J. Intergranular Li metal propagation through polycrystalline  $\text{Li}_{6.25}\text{Al}_{0.25}\text{La}_3\text{Zr}_2\text{O}_{12}$  ceramic electrolyte. *Electrochimica Acta* **223**, 85-91, doi:https://doi.org/10.1016/j.electacta.2016.12.018 (2017).
  - 12 Aguesse, F. *et al.* Investigating the Dendritic Growth during Full Cell Cycling of Garnet Electrolyte in Direct Contact with Li Metal. *ACS Applied Materials & Interfaces* **9**, 3808-3816, doi:10.1021/acsami.6b13925 (2017).
  - 13 Kim, S. *et al.* The Role of Interlayer Chemistry in Li-Metal Growth through a Garnet-Type Solid Electrolyte. **10**, 1903993, doi:https://doi.org/10.1002/aenm.201903993 (2020).
  - 14 Manalastas, W. *et al.* Mechanical failure of garnet electrolytes during Li electrodeposition observed by in-operando microscopy. *Journal of Power Sources* **412**, 287-293, doi:https://doi.org/10.1016/j.jpowsour.2018.11.041 (2019).
  - 15 Porz, L. *et al.* Mechanism of lithium metal penetration through inorganic solid electrolytes. *Advanced Energy Materials* **7**, 1701003 (2017).
  - 16 Swamy, T. *et al.* Lithium Metal Penetration Induced by Electrodeposition

- through Solid Electrolytes: Example in Single-Crystal  $\text{Li}_6\text{La}_3\text{ZrTaO}_{12}$  Garnet. *Journal of The Electrochemical Society* **165**, A3648-A3655, doi:10.1149/2.1391814jes (2018).
- 17 Tsai, C.-L. *et al.*  $\text{Li}_7\text{La}_3\text{Zr}_2\text{O}_{12}$  Interface Modification for Li Dendrite Prevention. *ACS Applied Materials & Interfaces* **8**, 10617-10626, doi:10.1021/acsami.6b00831 (2016).
  - 18 Hofstetter, K., Samson, A. J., Narayanan, S. & Thangadurai, V. Present understanding of the stability of Li-stuffed garnets with moisture, carbon dioxide, and metallic lithium. *Journal of Power Sources* **390**, 297-312, doi:https://doi.org/10.1016/j.jpowsour.2018.04.016 (2018).
  - 19 Sharafi, A. *et al.* Surface Chemistry Mechanism of Ultra-Low Interfacial Resistance in the Solid-State Electrolyte  $\text{Li}_7\text{La}_3\text{Zr}_2\text{O}_{12}$ . *Chemistry of Materials* **29**, 7961-7968, doi:10.1021/acs.chemmater.7b03002 (2017).
  - 20 Song, Y. *et al.* Probing into the origin of an electronic conductivity surge in a garnet solid-state electrolyte. *Journal of Materials Chemistry A* **7**, 22898-22902, doi:10.1039/C9TA10269H (2019).
  - 21 Han, F. *et al.* High electronic conductivity as the origin of lithium dendrite formation within solid electrolytes. *Nature Energy* **4**, 187-196, doi:10.1038/s41560-018-0312-z (2019).
  - 22 Tian, H.-K., Xu, B. & Qi, Y. Computational study of lithium nucleation tendency in  $\text{Li}_7\text{La}_3\text{Zr}_2\text{O}_{12}$  (LLZO) and rational design of interlayer materials to prevent lithium dendrites. *Journal of Power Sources* **392**, 79-86, doi:https://doi.org/10.1016/j.jpowsour.2018.04.098 (2018).
  - 23 Ping, W. *et al.* Reversible Short-Circuit Behaviors in Garnet-Based Solid-

- State Batteries. **n/a**, 2000702, doi:10.1002/aenm.202000702.
- 24 Song, Y. *et al.* Revealing the Short-Circuiting Mechanism of Garnet-Based Solid-State Electrolyte. *Advanced Energy Materials* **9**, 1900671, doi:10.1002/aenm.201900671 (2019).
  - 25 Han, X. *et al.* Negating interfacial impedance in garnet-based solid-state Li metal batteries. *Nature Materials* **16**, 572, doi:10.1038/nmat4821 (2016).
  - 26 Han, F., Zhu, Y., He, X., Mo, Y. & Wang, C. Electrochemical Stability of Li<sub>10</sub>GeP<sub>2</sub>S<sub>12</sub> and Li<sub>7</sub>La<sub>3</sub>Zr<sub>2</sub>O<sub>12</sub> Solid Electrolytes. *Advanced Energy Materials* **6**, 1501590, doi:doi:10.1002/aenm.201501590 (2016).
  - 27 Xiao, Y. *et al.* Understanding interface stability in solid-state batteries. *Nature Reviews Materials* **5**, 105-126, doi:10.1038/s41578-019-0157-5 (2020).
  - 28 Zhu, Y. *et al.* Dopant-Dependent Stability of Garnet Solid Electrolyte Interfaces with Lithium Metal. **9**, 1803440, doi:10.1002/aenm.201803440 (2019).
  - 29 Ma, C. *et al.* Excellent Stability of a Lithium-Ion-Conducting Solid Electrolyte upon Reversible Li<sup>+</sup>/H<sup>+</sup> Exchange in Aqueous Solutions. *Angewandte Chemie International Edition* **54**, 129-133, doi:10.1002/anie.201408124 (2015).
  - 30 Yow, Z. F., Oh, Y. L., Gu, W., Rao, R. P. & Adams, S. Effect of Li<sup>+</sup>/H<sup>+</sup> exchange in water treated Ta-doped Li<sub>7</sub>La<sub>3</sub>Zr<sub>2</sub>O<sub>12</sub>. *Solid State Ionics* **292**, 122-129, doi:https://doi.org/10.1016/j.ssi.2016.05.016 (2016).
  - 31 Albertus, P., Babinec, S., Litzelman, S. & Newman, A. Status and challenges in enabling the lithium metal electrode for high-energy and low-

- cost rechargeable batteries. *Nature Energy* **3**, 16-21, doi:10.1038/s41560-017-0047-2 (2018).
- 32 Albertus, P. Integration and Optimization of Novel Ion-Conducting Solids (IONICS) Funding Opportunity Announcement (2016).
- 33 Rodriguez-Carvajal, J. Fullprof: A Program for Rietveld Refinement and Pattern Matching Analysis. *Abstract of the Satellite Meeting on Powder Diffraction of the XV Congress of the IUCr, Toulouse, France*, 127 (1990).
- 34 Rodríguez-Carvajal, J. Recent advances in magnetic structure determination by neutron powder diffraction. *Physica B: Condensed Matter* **192**, 55-69, doi:https://doi.org/10.1016/0921-4526(93)90108-I (1993).
- 35 Yang, X., Kong, D., Chen, Z., Sun, Y. & Liu, Y. Low-temperature fabrication for transparency Mg doping  $\text{Li}_7\text{La}_3\text{Zr}_2\text{O}_{12}$  solid state electrolyte. *Journal of Materials Science: Materials in Electronics* **29**, 1523-1529, doi:10.1007/s10854-017-8062-4 (2018).
- 36 Ong, S. P. *et al.* Python Materials Genomics (pymatgen): A robust, open-source python library for materials analysis. *Computational Materials Science* **68**, 314-319, doi:https://doi.org/10.1016/j.commatsci.2012.10.028 (2013).
- 37 Perdew, J. P., Burke, K. & Ernzerhof, M. Generalized Gradient Approximation Made Simple. *Physical Review Letters* **77**, 3865-3868, doi:10.1103/PhysRevLett.77.3865 (1996).
- 38 Kresse, G. & Furthmüller, J. Efficient iterative schemes for ab initio total-energy calculations using a plane-wave basis set. *Physical Review B* **54**,

- 11169-11186, doi:10.1103/PhysRevB.54.11169 (1996).
- 39 Miara, L. J., Richards, W. D., Wang, Y. E. & Ceder, G. First-Principles Studies on Cation Dopants and Electrolyte|Cathode Interphases for Lithium Garnets. *Chemistry of Materials* **27**, 4040-4047, doi:10.1021/acs.chemmater.5b01023 (2015).
- 40 Richards, W. D., Miara, L. J., Wang, Y., Kim, J. C. & Ceder, G. Interface Stability in Solid-State Batteries. *Chemistry of Materials* **28**, 266-273, doi:10.1021/acs.chemmater.5b04082 (2016).
- 41 Li, Y. *et al.* W-Doped  $\text{Li}_7\text{La}_3\text{Zr}_2\text{O}_{12}$  Ceramic Electrolytes for Solid State Li-ion Batteries. *Electrochimica Acta* **180**, 37-42, doi:https://doi.org/10.1016/j.electacta.2015.08.046 (2015).
- 42 Xia, W. *et al.* Ionic Conductivity and Air Stability of Al-Doped  $\text{Li}_7\text{La}_3\text{Zr}_2\text{O}_{12}$  Sintered in Alumina and Pt Crucibles. *ACS Applied Materials & Interfaces* **8**, 5335-5342, doi:10.1021/acsami.5b12186 (2016).
- 43 Buschmann, H., Berendts, S., Mogwitz, B. & Janek, J. Lithium metal electrode kinetics and ionic conductivity of the solid lithium ion conductors “ $\text{Li}_7\text{La}_3\text{Zr}_2\text{O}_{12}$ ” and  $\text{Li}_{7-x}\text{La}_3\text{Zr}_{2-x}\text{Ta}_x\text{O}_{12}$  with garnet-type structure. *Journal of Power Sources* **206**, 236-244, doi:https://doi.org/10.1016/j.jpowsour.2012.01.094 (2012).
- 44 Ma, C. *et al.* Interfacial Stability of Li Metal–Solid Electrolyte Elucidated via in Situ Electron Microscopy. *Nano Letters* **16**, 7030-7036, doi:10.1021/acs.nanolett.6b03223 (2016).
- 45 Rettenwander, D. *et al.* Interface Instability of Fe-Stabilized  $\text{Li}_7\text{La}_3\text{Zr}_2\text{O}_{12}$  versus Li Metal. *The Journal of Physical Chemistry C* **122**, 3780-3785,



- doi:10.1021/acs.jpcc.7b12387 (2018).
- 46 Kim, Y. *et al.* Electrochemical Stability of  $\text{Li}_{6.5}\text{La}_3\text{Zr}_{1.5}\text{M}_{0.5}\text{O}_{12}$  (M = Nb or Ta) against Metallic Lithium. **4**, doi:10.3389/fenrg.2016.00020 (2016).
  - 47 Wolfenstine, J., Allen, J. L., Read, J. & Sakamoto, J. J. J. o. M. S. Chemical stability of cubic  $\text{Li}_7\text{La}_3\text{Zr}_2\text{O}_{12}$  with molten lithium at elevated temperature. **48**, 5846-5851, doi:10.1007/s10853-013-7380-z (2013).
  - 48 Nemori, H. *et al.* Stability of garnet-type solid electrolyte  $\text{Li}_x\text{La}_3\text{A}_{2-y}\text{B}_y\text{O}_{12}$  (A=Nb or Ta, B=Sc or Zr). *Solid State Ionics* **282**, 7-12, doi:https://doi.org/10.1016/j.ssi.2015.09.015 (2015).
  - 49 Thompson, T. *et al.* Tetragonal vs. cubic phase stability in Al – free Ta doped  $\text{Li}_7\text{La}_3\text{Zr}_2\text{O}_{12}$  (LLZO). *Journal of Materials Chemistry A* **2**, 13431-13436, doi:10.1039/C4TA02099E (2014).
  - 50 Botros, M. *et al.* Microstrain and electrochemical performance of garnet solid electrolyte integrated in a hybrid battery cell. *RSC Advances* **9**, 31102-31114, doi:10.1039/C9RA07091E (2019).
  - 51 Chen, Y., Rangasamy, E., Liang, C. & An, K. Origin of High  $\text{Li}^+$  Conduction in Doped  $\text{Li}_7\text{La}_3\text{Zr}_2\text{O}_{12}$  Garnets. *Chemistry of Materials* **27**, 5491-5494, doi:10.1021/acs.chemmater.5b02521 (2015).
  - 52 Wang, C. *et al.* In Situ Neutron Depth Profiling of Lithium Metal–Garnet Interfaces for Solid State Batteries. *Journal of the American Chemical Society* **139**, 14257-14264, doi:10.1021/jacs.7b07904 (2017).
  - 53 Krauskopf, T. *et al.* Lithium-Metal Growth Kinetics on LLZO Garnet-Type Solid Electrolytes. *Joule*, doi:https://doi.org/10.1016/j.joule.2019.06.013 (2019).

- 54 Ong, S. P., Wang, L., Kang, B. & Ceder, G. Li–Fe–P–O<sub>2</sub> Phase Diagram from First Principles Calculations. *Chemistry of Materials* **20**, 1798-1807, doi:10.1021/cm702327g (2008).
- 55 Tippens, J. *et al.* Visualizing Chemomechanical Degradation of a Solid-State Battery Electrolyte. *ACS Energy Letters* **4**, 1475-1483, doi:10.1021/acsenenergylett.9b00816 (2019).
- 56 Echlin, P. Handbook of Sample Preparation for Scanning Electron Microscopy and X-Ray Microanalysis. doi:10.1007/978-0-387-85731-2 (2009).
- 57 Liu, C. *et al.* Reversible ion exchange and structural stability of garnet-type Nb-doped Li<sub>7</sub>La<sub>3</sub>Zr<sub>2</sub>O<sub>12</sub> in water for applications in lithium batteries. *Journal of Power Sources* **282**, 286-293, doi:https://doi.org/10.1016/j.jpowsour.2015.02.050 (2015).
- 58 Persson, K. Materials Data on Li<sub>8</sub>Nb<sub>2</sub>O<sub>9</sub> by Materials Project. doi:10.17188/1202164 (2020).
- 59 Huo, H. *et al.* In-situ formed Li<sub>2</sub>CO<sub>3</sub>-free garnet/Li interface by rapid acid treatment for dendrite-free solid-state batteries. *Nano Energy* **61**, 119-125, doi:https://doi.org/10.1016/j.nanoen.2019.04.058 (2019).
- 60 Riess, I. Review of the limitation of the Hebb-Wagner polarization method for measuring partial conductivities in mixed ionic electronic conductors. *Solid State Ionics* **91**, 221-232, doi:https://doi.org/10.1016/S0167-2738(96)83022-0 (1996).
- 61 Buschmann, H. *et al.* Structure and dynamics of the fast lithium ion conductor “Li<sub>7</sub>La<sub>3</sub>Zr<sub>2</sub>O<sub>12</sub>”. *Physical Chemistry Chemical Physics* **13**,

- 19378-19392, doi:10.1039/C1CP22108F (2011).
- 62 Tu, Q., Barroso-Luque, L., Shi, T. & Ceder, G. Electrodeposition and Mechanical Stability at Lithium-Solid Electrolyte Interface during Plating in Solid-State Batteries. *Cell Reports Physical Science* **1**, 100106, doi:<https://doi.org/10.1016/j.xcrp.2020.100106> (2020).
- 63 Fu, K. *et al.* Three-dimensional bilayer garnet solid electrolyte based high energy density lithium metal–sulfur batteries. *Energy & Environmental Science* **10**, 1568-1575, doi:10.1039/C7EE01004D (2017).
- 64 Fett, T., Rizzi, G., Guin, J. P. & Wiederhorn, S. M. Ring-on-ring strength measurements on rectangular glass slides. *Journal of Materials Science* **42**, 393-395, doi:10.1007/s10853-006-1102-8 (2007).
- 65 Hudson, J. A. Tensile strength and the ring test. *International Journal of Rock Mechanics and Mining Sciences & Geomechanics Abstracts* **6**, 91-97, doi: 10.1016/0148-9062(69)90029-1 (1969).
- 66 Wu, J.-F., Pang, W. K., Peterson, V. K., Wei, L. & Guo, X. Garnet-Type Fast Li-Ion Conductors with High Ionic Conductivities for All-Solid-State Batteries. *ACS Applied Materials & Interfaces* **9**, 12461-12468, doi:10.1021/acsami.7b00614 (2017).
- 67 Wu, J.-F. *et al.* Gallium-Doped  $\text{Li}_7\text{La}_3\text{Zr}_2\text{O}_{12}$  Garnet-Type Electrolytes with High Lithium-Ion Conductivity. *ACS Applied Materials & Interfaces* **9**, 1542-1552, doi:10.1021/acsami.6b13902 (2017).
- 68 Lin, F. *et al.* Synchrotron X-ray Analytical Techniques for Studying Materials Electrochemistry in Rechargeable Batteries. *Chemical Reviews* **117**, 13123-13186, doi:10.1021/acs.chemrev.7b00007 (2017).

- 69 Cheng, L. *et al.* Garnet Electrolyte Surface Degradation and Recovery. *ACS Applied Energy Materials* **1**, 7244-7252, doi:10.1021/acsaem.8b01723 (2018).
- 70 Khanal, G. P. *et al.* Effect of thermal annealing on crystal structures and electrical properties in BaTiO<sub>3</sub> ceramics. *Journal of Applied Physics* **124**, 034102, doi:10.1063/1.5023814 (2018).
- 71 Galven, C., Fourquet, J.-L., Crosnier-Lopez, M.-P. & Le Berre, F. Instability of the Lithium Garnet Li<sub>7</sub>La<sub>3</sub>Sn<sub>2</sub>O<sub>12</sub>: Li<sup>+</sup>/H<sup>+</sup> Exchange and Structural Study. *Chemistry of Materials* **23**, 1892-1900, doi:10.1021/cm103595x (2011).
- 72 Larraz, G., Orera, A. & Sanjuán, M. L. Cubic phases of garnet-type Li<sub>7</sub>La<sub>3</sub>Zr<sub>2</sub>O<sub>12</sub>: the role of hydration. *Journal of Materials Chemistry A* **1**, 11419-11428, doi:10.1039/C3TA11996C (2013).
- 73 Wang, Y. & Lai, W. Phase transition in lithium garnet oxide ionic conductors Li<sub>7</sub>La<sub>3</sub>Zr<sub>2</sub>O<sub>12</sub>: The role of Ta substitution and H<sub>2</sub>O/CO<sub>2</sub> exposure. *Journal of Power Sources* **275**, 612-620, doi: 10.1016/j.jpowsour.2014.11.062 (2015).
- 74 Mote, V. D., Purushotham, Y. & Dole, B. N. Williamson-Hall analysis in estimation of lattice strain in nanometer-sized ZnO particles. *Journal of Theoretical and Applied Physics* **6**, 6, doi:10.1186/2251-7235-6-6 (2012).
- 75 Chevalier, J., Gremillard, L., Virkar, A. & Clarke, D. The Tetragonal-Monoclinic Transformation in Zirconia: Lessons Learned and Future Trends. *Journal of the American Ceramic Society* **92**, 1901-1920, doi:10.1111/j.1551-2916.2009.03278.x (2009).

- 76 Cheng, L. *et al.* The origin of high electrolyte–electrode interfacial resistances in lithium cells containing garnet type solid electrolytes. *Physical Chemistry Chemical Physics* **16**, 18294-18300, doi:10.1039/C4CP02921F (2014).
- 77 Flatscher, F., Philipp, M., Ganschow, S., Wilkening, H. M. R. & Rettenwander, D. The natural critical current density limit for  $\text{Li}_7\text{La}_3\text{Zr}_2\text{O}_{12}$  garnets. *Journal of Materials Chemistry A*, doi:10.1039/C9TA14177D (2020).
- 78 Pesci, Federico M. *et al.* Elucidating the role of dopants in the critical current density for dendrite formation in garnet electrolytes. *Journal of Materials Chemistry A* **6**, 19817-19827, doi:10.1039/C8TA08366E (2018).
- 79 Ulvestad, A. A Brief Review of Current Lithium Ion Battery Technology and Potential Solid State Battery Technologies. 2018, arXiv:1803.04317. (2018).
- 80 Duan, J. *et al.* Building Safe Lithium-Ion Batteries for Electric Vehicles: A Review. *Electrochemical Energy Reviews* **3**, 1-42, doi:10.1007/s41918-019-00060-4 (2020).
- 81 Miao, Y., Hynan, P., von Jouanne, A. & Yokochi, A. Current Li-Ion Battery Technologies in Electric Vehicles and Opportunities for Advancements. **12**, 1074 (2019).
- 82 Yang, C. *et al.* An Electron/Ion Dual-Conductive Alloy Framework for High-Rate and High-Capacity Solid-State Lithium-Metal Batteries. *Advanced Materials* **31**, 1804815, doi: 10.1002/adma.201804815 (2019).
- 83 Taylor, N. J. *et al.* Demonstration of high current densities and extended

- cycling in the garnet  $\text{Li}_7\text{La}_3\text{Zr}_2\text{O}_{12}$  solid electrolyte. *Journal of Power Sources* **396**, 314-318, doi: 10.1016/j.jpowsour.2018.06.055 (2018).
- 84 Wiedemann, D. *et al.* Unravelling Ultraslow Lithium-Ion Diffusion in  $\gamma\text{-LiAlO}_2$ : Experiments with Tracers, Neutrons, and Charge Carriers. *Chemistry of Materials* **28**, 915-924, doi:10.1021/acs.chemmater.5b04608 (2016).
- 85 Birkel, C. R., Roberts, M. R., McTurk, E., Bruce, P. G. & Howey, D. A. Degradation diagnostics for lithium ion cells. *Journal of Power Sources* **341**, 373-386, doi: 10.1016/j.jpowsour.2016.12.011 (2017).
- 86 Krewer, U. *et al.* Review—Dynamic Models of Li-Ion Batteries for Diagnosis and Operation: A Review and Perspective. *Journal of The Electrochemical Society* **165**, A3656-A3673, doi:10.1149/2.1061814jes (2018).
- 87 Watanabe, S., Kinoshita, M., Hosokawa, T., Morigaki, K. & Nakura, K. Capacity fading of  $\text{LiAl}_y\text{Ni}_{1-x-y}\text{Co}_x\text{O}_2$  cathode for lithium-ion batteries during accelerated calendar and cycle life tests (effect of depth of discharge in charge–discharge cycling on the suppression of the micro-crack generation of  $\text{LiAl}_y\text{Ni}_{1-x-y}\text{Co}_x\text{O}_2$  particle). *Journal of Power Sources* **260**, 50-56, doi: 10.1016/j.jpowsour.2014.02.103 (2014).
- 88 Watanabe, S., Kinoshita, M., Hosokawa, T., Morigaki, K. & Nakura, K. Capacity fade of  $\text{LiAl}_y\text{Ni}_{1-x-y}\text{Co}_x\text{O}_2$  cathode for lithium-ion batteries during accelerated calendar and cycle life tests (surface analysis of  $\text{LiAl}_y\text{Ni}_{1-x-y}\text{Co}_x\text{O}_2$  cathode after cycle tests in restricted depth of discharge ranges). *Journal of Power Sources* **258**, 210-217, doi:

- 10.1016/j.jpowsour.2014.02.018 (2014).
- 89 Li, Y. *et al.* Garnet Electrolyte with an Ultralow Interfacial Resistance for Li-Metal Batteries. *Journal of the American Chemical Society* **140**, 6448-6455, doi:10.1021/jacs.8b03106 (2018).
- 90 Ruan, Y. *et al.* Acid Induced Conversion towards Robust and Lithiophilic Interface for Li-  $\text{Li}_7\text{La}_3\text{Zr}_2\text{O}_{12}$  Solid-State Battery. *Journal of Materials Chemistry A* **7**, 14565-14574, doi:10.1039/C9TA01911A (2019).
- 91 Xu, H. *et al.* Li<sub>3</sub>N-Modified Garnet Electrolyte for All-Solid-State Lithium Metal Batteries Operated at 40 °C. *Nano Letters* **18**, 7414-7418, doi:10.1021/acs.nanolett.8b03902 (2018).
- 92 Huo, H. *et al.* Design of a mixed conductive garnet/Li interface for dendrite-free solid lithium metal batteries. *Energy & Environmental Science* **13**, 127-134, doi:10.1039/C9EE01903K (2020).

## Chapter 3. The role of interlayer chemistry in Li-metal growth through a garnet-type solid electrolyte

(The content of this chapter has been published in *Advanced Energy Materials*. Reprinted with permission from [Kim, S., Jung, C., Kim, H. *et al.*, *Adv. Energy Mater.* **2020**, 10, 1903993. <https://doi.org/10.1002/aenm.201903993>]. Copyright 2020 WILEY-VCH Verlag GmbH & Co. KGaA, Weinheim.)

### 3.1. Introduction

Solid-state batteries (SSBs) have attracted intense interest in recent years as next-generation batteries that are safer and potentially capable of providing higher volumetric energy densities than current batteries. Employing a non-flammable solid electrolyte enables batteries that are intrinsically safer under abusing conditions to be fabricated. Moreover, an SSB can feasibly use a lithium-metal electrode, the anode with the highest theoretical capacity (3860 mAh/g), in a lithium cell, since the solid electrolyte is believed to effectively block lithium dendrites, the main obstacles to adopting lithium-metal anodes in conventional battery systems. In this regard, excellent solid electrolytes have been extensively sought after over the past few decades, leading to the discovery of new systems that include sulfides, NASICONs, LiSICONs, perovskites, and garnet-type solid electrolytes that rival conventional liquid electrolytes.<sup>1-7</sup> Among them, the garnet-type solid electrolyte, which is based on the  $\text{Li}_7\text{La}_3\text{Zr}_2\text{O}_{12}$  (LLZO) nominal formula, is considered to be a promising candidate.<sup>8,9</sup> LLZO is chemically stable against lithium metal and also benefits from relatively high ionic conductivity at room temperature ( $\sim 1$  mS/cm), with a lithium-



ion transference number close to unity.<sup>10-17</sup> Moreover, the material stabilities of oxides in ambient air facilitate the practical synthesis of solid electrolytes and the fabrication of SSBs using LLZOs.

Nevertheless, attempts to use LLZO-based solid electrolytes in lithium cells have revealed potential technical challenges, such as unexpectedly premature short circuiting. In contrast to its projected role as a mechanical barrier, short circuiting through the LLZO has frequently been observed during cycling and was found to arise from lithium-metal growth penetrating through the LLZO.<sup>18-21</sup> Several recent studies have suggested that intra-short circuits are likely to be formed because of the localized electrodeposition of lithium in pre-existing flaws due to the build-up of crack-tip stress and the corresponding crack propagation that finally causes the solid electrolyte to mechanically fail.<sup>22-24</sup> Other researchers have also proposed that the interfacial resistance between an electrode and LLZO is not only the source of slow SSB kinetics, but it significantly contributes to short-circuit failure.<sup>20,25-29</sup> Poor contact between lithium metal and LLZO has been reported to cause large interfacial resistance that results in an inhomogeneously distributed current that triggers such failure.<sup>19,26,27,30</sup> In this respect, recent studies have attempted to reduce contact resistance by removing surface impurities or introducing an artificial interlayer between the lithium metal and the LLZO, which have led to some improvements.<sup>26,27,31-37</sup>

While previous research revealed that reduced initial impedance at the interface between the solid electrolyte and the lithium metal may contribute to SSB stability, a mechanistic understanding of this interface remains elusive. Moreover, it is not

clear how the presence of the interlayer at the interface alters the deposition mechanism during electrochemical reactions, and how lithium growth at an interface with a specific defect morphology is influenced by the presence of the interlayer. Direct real-time probing of lithium-growth behavior at the interface would help to elucidate the underlying lithium-deposition mechanism in the presence of morphological defects or an artificial interlayer, and would serve as an important milestone toward the rational tailoring of SSB interfaces.

Herein, we successfully used an *in operando* microscopy technique to probe lithium deposition through the LLZO electrolyte in an anode-free solid-state battery setup. This simple and novel technique facilitates the direct witnessing of lithium-metal-deposition behavior on LLZO surfaces with morphological defects and/or artificial interlayers during battery operation. It is demonstrated that lithium deposition is mainly affected by the geometry of the LLZO surface, where pre-existing surface flaws act as preferred sites for the electrodeposition of lithium. More importantly, we carefully examined the interface with artificial interlayers exploiting various types of metal as model materials, which revealed that lithium plating is strongly dominated by the kinetics of alloying and precipitation through the metal interlayer; the unevenness of the lithium plating due to the geometry of the surface can either be exacerbated or mitigated by the interlayer metal species. Supported by these intriguing observations, we propose the following dynamic roles of the interlayer during battery operation: as a buffer layer for lithium redistribution and as a seed layer for lithium precipitation. Considering the facile nature of the deposition process and the wide applicability of interlayer engineering on the LLZO surface,

our findings are expected to provide useful guidance for achieving ideal SSB interfaces.

## 3.2. Experimental and computational details

### 3.2.1. Material synthesis

Tantalum-doped pristine LLZO powder, with a nominal composition of  $\text{Li}_{6.5}\text{La}_3\text{Zr}_{1.5}\text{Ta}_{0.5}\text{O}_{12}$ , was prepared by solid-state reaction. Precursor powders, namely  $\text{Li}_2\text{CO}_3$  (>99.0%, ChemPoint),  $\text{La}_2\text{O}_3$  (98.6%, MolyCorp),  $\text{ZrO}_2$  (98%, Zircoa Inc.), and  $\text{Ta}_2\text{O}_5$  (99.9%, Plant Material) were mixed in stoichiometric ratios and then subjected to tubular mixing for 30 min, followed by ball-mixing for 24 h with  $\text{ZrO}_2$  beads. The resulting mixture was calcinated at 950 °C for 5 h and then at 1200 °C for 5 h. The calcined powder was ball-milled for 30 h to produce a powder with a D50 value of  $\sim 0.7\ \mu\text{m}$ . A 100-g sample of this LLZO powder was hot pressed at 20.7 MPa and 1080 °C for 2 h to produce a column with a relative density >98%. The column was wire-sawed into  $\sim 350\text{-}\mu\text{m}$ -thick thin pellets that were finally heat treated in dry air at 800 °C for 1 h. During treatment, the pellets changed color from black to white. To prepare a flat and smooth surface, a surface of a prepared pellet was polished carefully with P800-, 1200-, 2400-, and 4000-grit SiC abrasive paper to a thickness of about 300  $\mu\text{m}$ . The last two steps were carried out in an Ar glove box to minimize surface contamination from exposure to air.

After the LLZO electrolyte pellet preparation, metal layers were deposited onto the pellets. Prior to depositing a metal layer, a 100- $\mu\text{m}$ -layer of lithium metal on a 10- $\mu\text{m}$ -thick 11-mm-diameter copper foil (Honjo Metal) was pressed onto one side of a polished LLZO electrolyte pellet at 250 MPa with a cold isostatic press (CIP, Samyang Ceratech, CIP 70/150-3KB) for use as an ideal reversible counter

electrode<sup>38</sup> and to avoid any detrimental effects of the CIP process on the metal layer. The LLZO pellet was then masked with polyimide tape with an 11-mm-diameter hole in order to deposit the metal layer as the working electrode. Each metal layer was deposited using a different method that depended on its processability. The lithium-metal layer was deposited by thermal evaporation using a vacuum evaporator (Korea Vacuum Tech., LTD, 16KVS004). A piece of solid lithium was placed inside the Ta boat of the evaporator under ambient Ar to avoid contaminations of the lithium by oxygen and nitrogen impurities. After the main chamber was evacuated to below  $10^{-5}$  Torr, lithium was evaporated from the heated boat and 1- $\mu$ m-thick lithium was deposited onto the LLZO pellet for 2000 s at a rate of 0.5 nm/s. The gold layer was deposited using a high-resolution sputter coater (Cressington, 208HR) in a dry room where the relative humidity was kept under 1% and the dew point was below -50 °C. A sputtered current of 20 mA was used at an Ar pressure of  $\sim 0.06$  mbar, and the thickness of the sputtered Au layer was determined by the thickness controller connected to the sputter coater. Deposition was performed for 1 min or 6 min to give 5-nm- or 30-nm-thick gold layers. Silicon and silver layers were deposited using an RF-sputter system (SNTEK, 16-SN-055). The sputtering system was connected to an Ar glove box to facilitate transfer of the LLZO solid electrolyte to the sputter chamber without exposure to air. The deposition conditions for each metal depended on the sputtering rate for each material. Both depositions were carried out at a working pressure of 5 mTorr under a 40-sccm flow of high-purity Ar gas (99.9999%) at a constant substrate temperature of 22 °C. An n-type silicon target (99.999%) or a silver target (99.99%) were used for each layer. Each target was pre-sputtered for 10 min at 150 W, and then deposited for 20 min at 150 W for a 100-

nm-thick silicon layer, and for 5 min at the same power for a 100-nm-thick silver layer. The LLZO solid electrolytes were vacuum sealed in an Ar glove box following metal deposition.

### **3.2.2. *In operando* observation and electrochemical test**

We assembled a modified 2032-type coin cell for the in-house cell. We used a casing with an 8-mm-diameter hole in its centre and nickel mesh placed on the top of the metal layer as the current collector, which enabled the metal surface to be observed in real time during lithium deposition. Except for the spring, the other components were used in the same manner as a conventionally structured coin cell. The optical microscope (Micro Support, Axis Pro) was placed in an Ar glove box and the electrical connections of the electrochemical test system (Bio-Logics, Bistat) were also extended into the Ar glove box so that each experiment could be conducted without exposure to air.

Using this system, lithium was electrochemically deposited at 60 °C in order to observe deposition behavior at a higher current density. The deposition area was 0.95 cm<sup>2</sup>, as defined by the size of the metal layer. A constant current of 0.1 mA/cm<sup>2</sup> was applied to the lithium-metal layer and the gold layer (5 nm or 30 nm) for 2 h. To increase the amount of lithium deposited, the current was increased from 0.1 mA/cm<sup>2</sup> to 0.4 mA/cm<sup>2</sup> in steps of 0.1 mA/cm<sup>2</sup> for the cells with a silicon or silver layer deposited on the LLZO.

Galvanostatic lithium plating and stripping experiments were performed on each interlayer using the modified coin cell with the nickel mesh on top of the interlayer

to provide an open surface for lithium deposition. To avoid surface oxidation, all experiments were carried out inside an Ar glove box at 60 °C. The cells were charged at a constant current density of 0.2 mA/cm<sup>2</sup> to an areal capacity of 1 mAh/cm<sup>2</sup>, and then discharged at the same current density to 3.5 V to avoid decomposition of the LLZO. For the full cell test, a typical coin cell was used with a copper foil welded spacer in order to represent the actual battery structure. Ionic liquid (2M LiFSI in Pyr13FSI) wetted NCM111 (LiNi<sub>1/3</sub>Co<sub>1/3</sub>Mn<sub>1/3</sub>O<sub>2</sub>) electrode was applied as a hybrid cathode and metal interlayer as the interlayer at the interface between the solid electrolyte and the current collector for anode. Note that the ionic-liquid is only wetted on the cathode side. The cells were charged to an areal capacity of 1 mAh/cm<sup>2</sup>, and discharged to 2.8 V at different current densities of 0.1 and 0.2 mA/cm<sup>2</sup>.

### **3.2.3. Material characterization**

Surface metal-layer roughness following charging and discharging were observed by atomic force microscopy (AFM, NT-MDT) in tapping mode. A 100-nm-thick silver or gold layer was deposited on the polished LLZO surface in the same manner as described above, and in-house cells were also during electrochemical lithium deposition and stripping. A constant current of 0.2 mA/cm<sup>2</sup> was applied for 15 min and 150 min for the charged state, and a current density of 0.1 mA/cm<sup>2</sup> in reverse direction was applied until the cell voltage reached 4 V, after which the current was decreased to 0.01 mA/cm<sup>2</sup> at 4 V in order to strip the maximum amount of lithium for the discharged state. All cells were sealed after charging and discharging in an Ar glove box and then transferred to the AFM system. In order to prevent oxidation of the metal surface, disassembly and AFM were also conducted in a glove box with

less than < 1 ppm O<sub>2</sub> and H<sub>2</sub>O. A scan rate of 0.5 Hz and an image resolution of 256 × 256 were used.

### 3.2.4. Simulation method

The behavior of lithium ions in the LLZO is described using the Nernst-Planck equation, in which convection is neglected and charge conservation is assumed:

$$\mathbf{N}_i = -D_i \nabla c_i - z_i u_i F c_i \nabla \varphi_i$$

$$\sum_i z_i c_i = 0$$

Here  $\mathbf{N}_i$  is the flux,  $D_i$  is the diffusion coefficient,  $c_i$  is the concentration,  $z_i$  is the valency,  $u_i$  is the mobility,  $\varphi_i$  is the electrolyte potential of the ionic species  $i$ , and  $F$  is the Faraday constant.

The mass balance of the ionic species in the LLZO is treated by the following equation:

$$\frac{\partial c_i}{\partial t} + \nabla \cdot \mathbf{N}_i = R_i$$

Here,  $R_i$  is the total reaction rate, where the reaction kinetics is described using the concentration-dependent Butler–Volmer equation. We set the temperature to 300 K and used the lithium-ion diffusion coefficient of LLZO, namely  $5 \times 10^{-13} \text{ m}^2 \text{ s}^{-1}$ , with a transference number of unity.<sup>39</sup> A bias voltage of 0.1 V was applied to control the lithium-ion direction. The simulation was performed with the electrodeposition module and a tertiary current distribution using the Nernst-Planck interface in COMSOL Multiphysics,<sup>40</sup> as in our previous modelling studies.<sup>41,42</sup>



### 3.3. Results and Discussion

#### 3.3.1. Surface-morphology-dependent lithium plating

The in-house cell and microscope system shown in Figure 3.1 were used for the *in operando* observations of lithium deposition on LLZO. Lithium foil was attached to the bottom of the LLZO pellet and the top surface was pre-coated with the selected interlayer metal. The cell was assembled using a nickel-mesh current collector with a centre hole through which the surface of the LLZO was observed in an Ar-controlled environment. We first investigated electrochemical lithium-deposition behaviour through the LLZO electrolyte in the absence of an interlayer metal. For this purpose, lithium was pre-coated to a thickness of 1  $\mu\text{m}$  on the top surface of the LLZO by thermal evaporation to ensure electrical contact with the current collector and to mimic the practical conditions of the lithium/LLZO interface. Figure 3.2 shows snapshots of lithium metal growth through the LLZO under electrical bias. Even though 1- $\mu\text{m}$ -thick lithium is present between the microscope and the LLZO, defects on the surface of the LLZO, such as scratches and holes that arise during the fabrication of the polycrystalline LLZO pellets, are still visible. Lithium metal begins to appear in island shapes under an applied galvanostatic current ( $0.1 \text{ mA}/\text{cm}^2$ ) and continues to grow over time (Figure 3.2 b-d). The blurred features observed in Figure 3.2 c-d (indicated by arrows) after a 60-min period of deposition correspond to filamentary lithium metal that has grown from the surface; these features are out of focus in the microscopy image due to their heights above the LLZO surface. It is worth noting that all of the small lithium-metal islands first form at pre-existing black dots on the pristine LLZO surface during initial lithiation; these dots are defects on

the LLZO surface. Moreover, during the subsequent deposition process, lithium grows preferably at these islands; consequently, regions that are highly populated with islands end up growing filamentary lithium metal. These observations indicate that lithium deposition occurs nonuniformly at the interface between the lithium electrode and the LLZO electrolyte, and is the result of the preferred growth of lithium at LLZO surface defects.

In order to provide further evidence for the above-mentioned hypothesis, we conducted similar experiments in which the LLZO pellet was prepared by careful polishing and coated with an almost transparent ~5-nm-thin gold layer instead of the relatively thick 1  $\mu\text{m}$  lithium layer. Figure 3.3 shows that morphological defects, such as small scratches, holes, and cracks, are still clearly visible on the surface of the LLZO, despite the LLZO pellet being better polished than in the previous experiment. Lithium metal was consistently observed to begin to grow from holes (indicated by the yellow dotted circles in Figure 3.3a) to form island-shaped metal under an applied current (0.1  $\text{mA}/\text{cm}^2$ ). Moreover, metal-island clusters continued to preferentially grow into filamentary lithium metal (indicated by arrows in Figure 3.3c and d). Considering the relatively low current density of 0.1  $\text{mA}/\text{cm}^2$ , these observations imply that lithium tends to first fill flaws on the LLZO surface rather than be uniformly deposited, even at a low current density, which is consistent with a previous report in which asperity flaws were observed to induce concentrated electric fields as well as low barriers for lithium nucleation;<sup>22,23</sup> they are also consistent with our previous modelling study that suggested that the filamentary lithium-growth mechanism is promoted by local perturbations in the surface current density around uneven lithium depositions.<sup>41</sup> In Figure 3.4, we schematically

propose how lithium-deposition proceeds at the electrode/LLZO interface in the presence of possible processing defects. i) Morphological flaws on the solid electrolyte surface induce local electric fields with lithium-ion flux concentrating at these sites. ii) Accordingly, lithium is preferentially deposited at the defect sites to form lithium-metal islands rather than a uniform film. iii) This inhomogeneity is accelerated by further deposition, and lithium-metal islands continuously grow and merge to form filamentary lithium. This scenario was further validated by continuum mechanics simulations, as detailed in Figure 3.5, which shows that the lithium-ion current density is locally concentrated at asperity flaws. This inhomogeneous lithium deposition acts as a source of mechanical pressure that facilitates the formation of voids and contact loss, leading to cell failure.<sup>22,24,43</sup> Since morphological defects on the LLZO surface are inevitable to some extent during manufacturing, an appropriate approach that mitigates this problem needs to be devised.

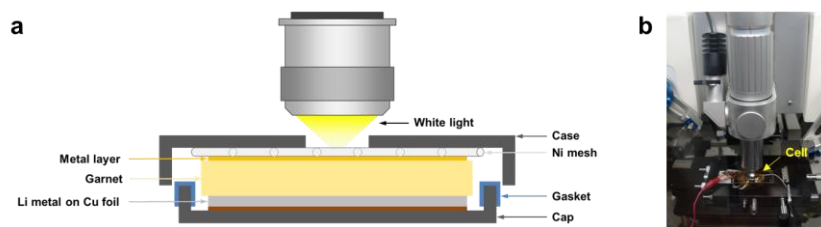


**Figure 3.1.** (a) Side-view schematic and (b) actual images of the *in operando* optical system with a coin-type half-cell.

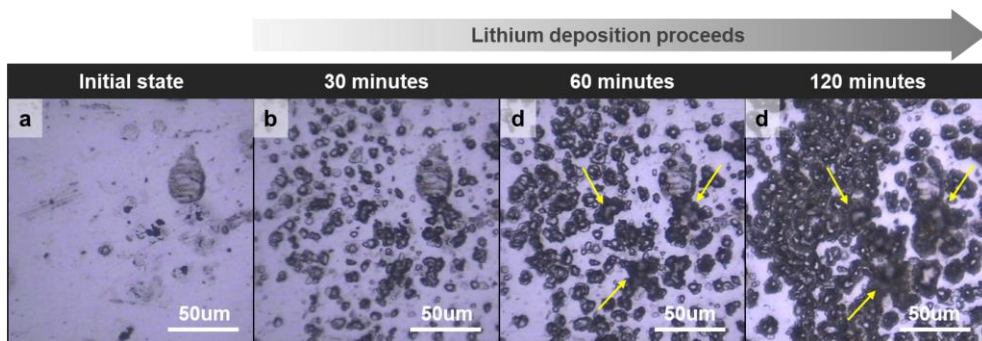


**Figure 3.2.** *In operando* optical microscopy images of lithium deposition on a pre-coated thick ( $\sim 1 \mu\text{m}$ ) lithium layer during the galvanostatic deposition of lithium.

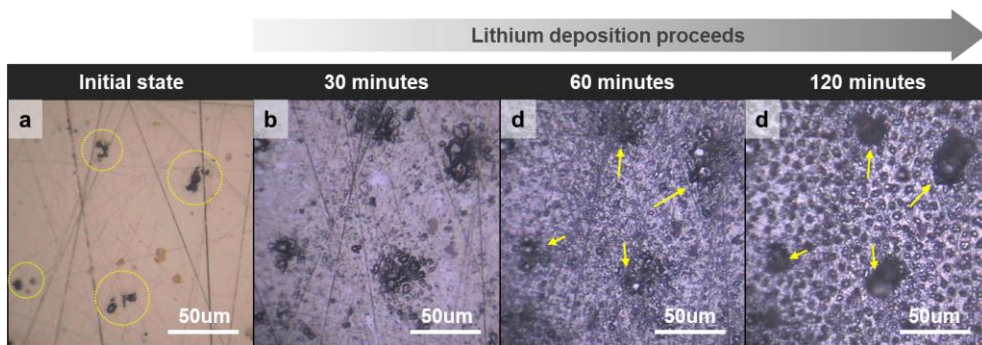


**Figure 3.3.** *In operando* optical microscopy images of lithium deposition on a polished LLZO with a sputtered thin ( $\sim 5$  nm) gold layer during the galvanostatic deposition of lithium.

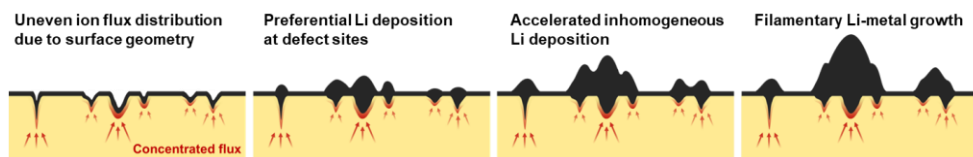


**Figure 3.4.** Schematic descriptions of uneven lithium-ion flux induced by surface morphological fluctuations and the corresponding inhomogeneous lithium deposition.

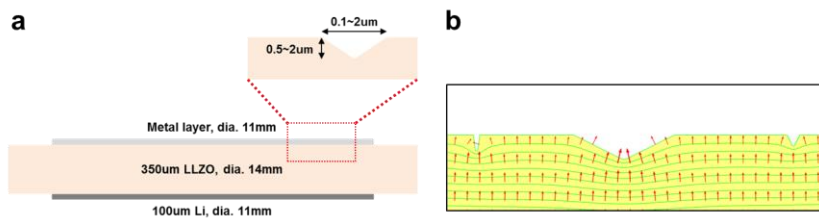


**Figure 3.5.** Demonstrating the local lithium-ion flux dependence on surface geometry (a) Reference model used for simulations. (b) Simulation result. In panel (b), the green lines are equipotential lines, and the red arrows show the intensity and direction of the lithium-ion current density.



### 3.3.2. Lithium redistribution by diffusion through the metal layer

It is noteworthy that regions without apparent defects display relatively uniformly deposited lithium involving many small lithium-metal nuclei when the gold interlayer was used (Figure 3.3c and d). Despite such regions also containing small scratches and holes, lithium metal was far more uniformly nucleated and dispersed in the absence of significant preferential lithium growth, which is in stark contrast to the observations made for bare lithium (Figure 3.2c and d). Moreover, comparing the average nucleus sizes after 60 min of deposition reveals that nucleation with the gold interlayer involves smaller nuclei (Figure 3.3c) than those with bare lithium (Figure 3.2c). We conclude that uniform nucleus dispersion is due to the presence of the thin (~5 nm) gold layer on the LLZO, which alloys with lithium to provide relatively fast lithium transport. As proof of concept, we fabricated a similar electrochemical cell but with a thicker (30 nm) gold layer in order to provide further evidence for the role of the gold during the early stage of the lithium-metal nucleation process. Figure 3.6 shows snapshots along this timeline. We observed that the gold interlayer changed color from reddish-gold (Figure 3.6a) to beige and sequentially bluish grey (Figure 3.6b and c) when an electrochemical bias was applied, which is indicative of the formation of a Li-Au alloy. These color changes are followed by morphological changes in the lithium metal, with the formation of island-type small precipitations observed (Figure 3.6d). Interestingly, closer inspection reveals that the color of the gold layer begins to change from the defect sites, with this change rapidly spreading to other regions. Moreover, after completion of the first color transition (reddish-gold to beige) in the entire region, the next color change (beige to bluish-grey) occurs in the layer in a similar manner, commencing from defect sites and

propagating over the entire region. As Li-Au alloy phases are typically accompanied by specific intrinsic colours,<sup>44,45</sup> the path of observed color changes reflects the alloying route involving lithium diffusion/insertion through the gold layer.<sup>46,47</sup>

Taking the above observations into account, we propose that the gold interlayer serves as an in-plane lithium-transport medium by propagating alloying reactions, which facilitates uniform lithium redistribution within the layer prior to lithium precipitation. In Figure 3.7, we provide a schematic illustration of lithium deposition in the presence of the gold interlayer. i) A locally developed electric field induces a larger lithium-ion flux around a morphological flaw; however, the presence of the gold interlayer leads to the formation of a Li-Au alloy instead of a lithium protrusion. ii) Lithium rapidly diffuses from the defect site (Li-Au alloy) to other regions (pristine gold) due to the chemical potential gradient of lithium within the interlayer, which converts the entire gold interlayer into a lithium-rich alloy. iii) Finally, lithium metal begins to precipitate from the lithium-rich alloy phase when the lithium concentration becomes critical or over-saturated. In this model, the gold interlayer plays the unexpected role of a “buffer layer”, which dynamically functions as a medium for lithium redistribution in addition to its previously reported role of improving the electrical contact between the lithium-metal anode and the LLZO solid electrolyte.<sup>26</sup> Even when lithium ions are unevenly supplied to the LLZO surface due to its irregular morphology, they are readily redistributed by facile interlayer diffusion through alloying reactions, which indicates that the application of an appropriate buffer layer that provides sufficiently fast lithium interdiffusion may become an effective strategy for mitigating lithium-plating inhomogeneity.

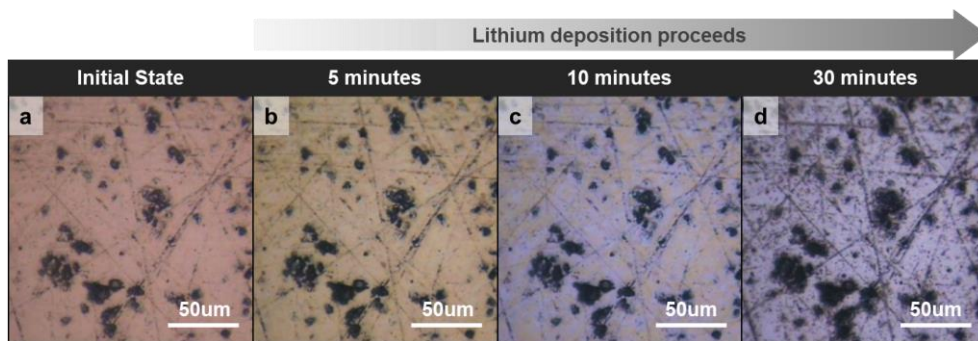


**Figure 3.6.** In operando optical microscopy images of polished LLZO with a sputtered ( $\sim 30$  nm) gold layer during the  $0.1\text{-mA cm}^{-2}$  galvanostatic deposition of lithium metal, which shows the lithium-gold alloying reaction, followed by lithium precipitation.

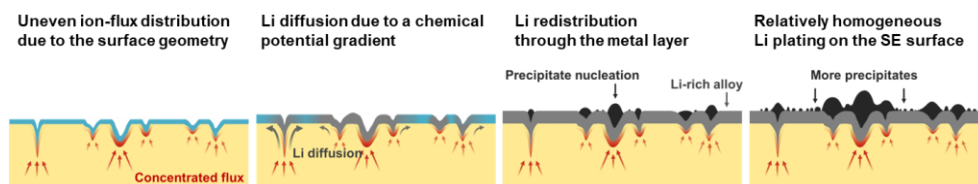


**Figure 3.7.** Schematic description of lithium redistribution through the gold layer and lithium nucleation.

### 3.3.3. Interlayer chemistry impacts on lithium plating/stripping behavior

Given the proposed new role of the interlayer, we expected the lithium-metal deposition behavior to critically depend on the thermodynamic and kinetic properties of the interlayer metal and its alloying nature with lithium. In particular, lithium-metal precipitation eventually takes place after the alloying process; *i.e.*, upon lithium supersaturation in the alloy leading to nucleation and growth within the alloy structure. Hence, various properties of the interlayer species, such as solubility, the diffusivity of lithium in the projected alloy, its crystal structure, and its compatibility with crystalline lithium are important aspects that govern lithium precipitation.<sup>48-51</sup> In this respect, we carried out further experiments using several other interlayers. Among the materials that are known to alloy with lithium, silicon and silver were chosen in this study, considering the availability of various alloys and the appreciable lithium diffusivities in their alloys.<sup>52-55</sup> A 100-nm-thick coating of each interlayer species was pre-coated on a separate LLZO surface, and lithium was electrochemically deposited in similar in-house cells to those described above. The pre-coated LLZO surface still exhibits scratches and small holes (Figure 3.8a and 3.9a for silicon and silver, respectively). The LLZO surface with the silicon interlayer was time-dependently monitored during lithium deposition, the optical micrographs of which are shown in Figure 3.8. As was observed for the gold interlayer, the color changed during the early stages, which is indicative of the alloying reaction between lithium and silicon (Figure 3.8b). However, subsequent lithium-precipitation behavior was observed to noticeably differ from that of the gold interlayer; lithium metal preferentially precipitates at only a few sites (Figure 3.8c), in contrast to the gold case. Moreover, whisker-shaped lithium metal rapidly grows

at these sites, whereas precipitation at other new sites is significantly inhibited (Figure 3.8d). On the other hand, we observed the opposite tendency for the LLZO surface pre-coated with a silver interlayer, as shown in Figure 3.9. The overall process, which involves the electrochemical deposition of lithium, is similar to that observed for the gold interlayer. The alloying reaction occurs first, as evidenced by the colour change of the silver interlayer, followed by the uniform formation of numerous small nuclei. Interestingly, the changes in color (Figure 3.9b) are almost instantaneously accompanied by morphological changes (Figure 3.10a) on the timescale of our observations, indicating that the two reactions occur nearly simultaneously and implying that both the alloying reaction and precipitate nucleation in the alloy are so fast in the case of the silver interlayer that the sequential processes are unable to be distinguished, unlike the gold and silicon systems. It is noteworthy that lithium deposition is not preferred at any defect site on the LLZO surface, even though scratches and small holes are still present under pristine conditions, leading to a far more uniform distribution of island-shaped precipitates on the LLZO surface that are devoid of filamentary lithium growth (Figure 3.9c and d), as was observed for the gold interlayer (Figure 3.6d), or the formation of massive whiskers, as observed for the silicon interlayer (Figure 3.8d).

In order to further confirm the more facile and uniform lithium deposition for the silver interlayer, more careful comparisons were made with the gold interlayer system by employing identical experimental conditions, and by considering the current density and the interlayer thickness, as shown in Figure 3.10. The silver interlayer consistently exhibited more-uniform lithium-precipitate growth, with smaller particle sizes than the gold interlayer. The time-of-flight secondary ion mass

spectrometry (ToF-SIMS) data shown in Figure 3.11 also show that the lithium is far more uniformly spatially distributed on the LLZO with the silver interlayer, while slightly bigger clusters of lithium precipitates are locally observed with the gold interlayer.

Figure 3.12 shows atomic force microscopy (AFM) images that respectively probe the lithium-deposition morphologies on the silver and gold interlayers as functions of deposition time. Even under the same lithium deposition conditions, the degrees of roughness ( $R_{\text{rms}}$ ) of the two systems are evidently different, which demonstrates that a much more uniform distribution of smaller lithium nuclei is achieved with the silver interlayer. Roughness due to uneven deposition becomes more severe as deposition proceeds in the gold system, confirming the results in Figure 3.11. We also note that the silver interlayer is more reversible upon lithium stripping, exhibiting more-efficient lithium stripping with a lower  $R_{\text{rms}}$  value than the gold interlayer, indicating that the silver interlayer has enhanced deposition and stripping kinetics. The better efficacy of the lithium deposition/stripping process with the silver interlayer was further validated by comparative electrochemical testing of solid-state batteries that use the solid electrolyte, as shown in Figure 3.13 and 3.14. Two electrode cells, called half cells, were constructed with 100-nm-thick metal coated on one side of the LLZO, with lithium foil on the other side, and subjected to testing at 60 °C. The results presented in Figure 3.13 show that the coulombic efficiencies of cells using the various interlayers are closely related to the lithium deposition and stripping behavior, as discussed above. The battery with the silver interlayer, which induces the most-uniform and reversible lithium deposition among the tested metals, exhibits the highest efficiency of 71%, while that with the silicon

interlayer, which forms massive lithium whiskers, shows the lowest efficiency of 28%. Taking account of the highest efficiency of the silver interlayer, we expected silver to be possibly applied as the interlayer for anode-free batteries. In order to demonstrate it, the electrochemical tests were conducted on the hybrid solid-state full cells using an ionic-liquid-wetted (2M LiFSI in Pyr13FSI) NCM111 ( $\text{LiNi}_{1/3}\text{Co}_{1/3}\text{Mn}_{1/3}\text{O}_2$ ) electrode as a cathode and the 100-nm-thick metal interlayer as the interlayer at the interface between the solid electrolyte and the current collector for anode. Note that the ionic-liquid is only wetted on the cathode side. Figure 3.14 presents the electrochemical performance of the cell at the different current densities of 0.1 and 0.2  $\text{mA cm}^{-2}$  at 60 °C. The initial coulombic efficiencies are 86.0 and 82.1% at each current density, and the efficiencies for the following cycles increase to 93.4 and 94.5% at 0.1  $\text{mA/cm}^2$ , and to 90.5 and 94.3% at 0.2  $\text{mA/cm}^2$ . Although these values are not sufficient for the requirement of the practical batteries, the performance is notably better than the case of the Si interlayer exhibiting 29.4% of the initial coulombic efficiency as shown in Figure 3.14b, demonstrating its potential applicability to the anode-free solid-state batteries.

With this understanding on the deposition behavior of each interlayer and its effects on the electrochemical performance of the cells, we also tried to elucidate the nature of the interlayers for the reverse reaction of the stripping. Figure 3.15 illustrates the snapshots of the optical microscopic images during lithium stripping until the cell voltage reaches 4V after the lithium deposition. When the reverse current was applied, it was observed that the whisker-shaped lithium metal grown on the silicon interlayer during the deposition process hardly participates in the stripping reaction as if the dead lithium causes the decay of coulombic efficiency in the cells



that employ lithium metal anode.<sup>56</sup> De-lithiation of lithium-silicon alloy was partially observed accompanying the typical pulverization phenomena of silicon alloy anode.<sup>57</sup> In contrast, it was monitored that the lithium was stripped from almost the entire region of the lithium deposited on gold or silver interlayer, and most of the precipitates disappeared or decreased in size particularly for silver interlayer (Figure 3.15b and c). While the protrusions formed during deposition (indicated by the red dotted circles in Figure 3.15b) still remains in some areas for the gold interlayer case, much uniform and homogenous stripping reaction was observed for the silver interlayer. The unreacted precipitates are attributable to the slow kinetics of lithium stripping in the region, which may reduce the coulombic efficiency in the cell. These results are consistent with those previously discussed in AFM study (Figure 3.12) and electrochemical performance testing, confirming that the silver interlayer has enhanced deposition and stripping kinetics compared with gold and silicon interlayer. Nevertheless, it should be noted that the roughened surface of the interlayer does not return to its original state after being stripped even for the silver case, as shown in Figure 3.12a and Figure 3.15c. We speculate that it is due to the morphological change as a result of the alloy formation, and has contributed to the drop of the coulombic efficiency in the cell employing the silver interlayer as well. The irreversibility due to the morphological deformation of the interlayer was further verified by investigating the cross section of the interface at the different charge/discharge states using scanning electron microscopy (SEM). As shown in Figure 3.16, it was revealed that silver layer expands in volume under the lithium metal precipitates during lithium deposition, but it generally recovers its original thickness after the completion of the stripping process, indicating the reversibility.

Nevertheless, the deformed shape of silver interlayer could not completely recover its original state, and there were some non-uniform interlayer area, which might have been caused by the morphological change of the silver during the lithiation. It implies that the morphological alternation of the interlayers due to formation of alloys with lithium can cause the reduction in the coulombic efficiency of the anode-free solid-state battery, which needs to be further studied in the future regarding the long-term stability of the interlayer during the battery operations. So far, our observation indicates that the interlayer can significantly affect the electrochemical performance of anode-free solid-state batteries that employ solid electrolytes by regulating lithiation and de-lithiation behavior at the interface.

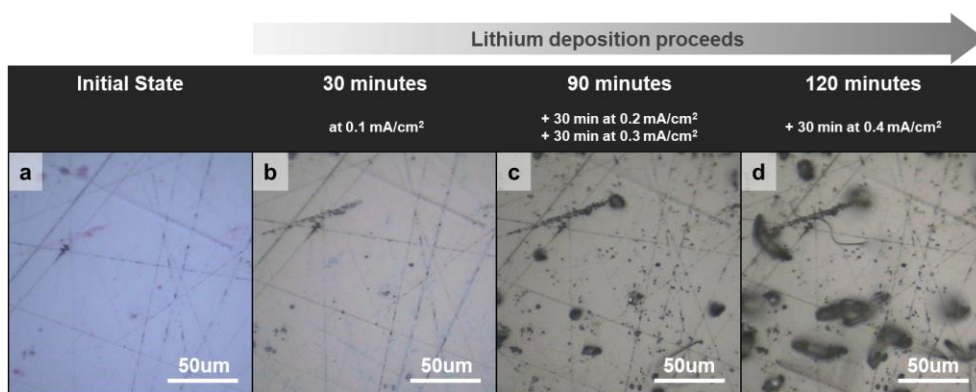


**Figure 3.8.** *In operando* optical microscopy images of sputtered (~100 nm) a silicon layer on polished LLZO surfaces during lithium deposition with stepwise increases in current density (from 0.1 to 0.4 mA cm<sup>-2</sup>).

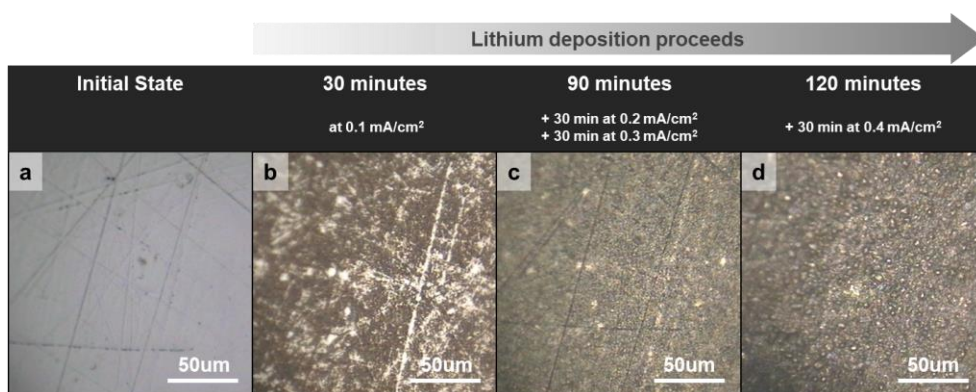


**Figure 3.9.** *In operando* optical microscopy images of sputtered (~100 nm) a silver layer on polished LLZO surfaces during lithium deposition with stepwise increases in current density (from 0.1 to 0.4 mA cm<sup>-2</sup>).

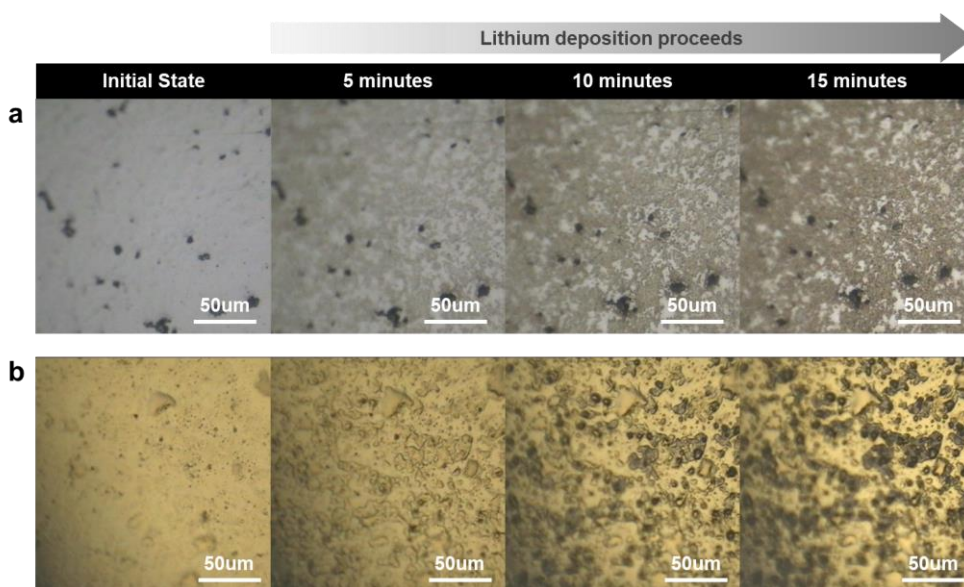


**Figure 3.10.** In operando optical microscopy images of sputtered 100-nm-thick (a) silver and (b) gold layers on polished LLZO surfaces during the  $0.1\text{-mA cm}^{-2}$  galvanostatic deposition of lithium on/through the layer. Although both layers show simultaneous diffusion and nucleation reactions, the resultant lithium deposition behavior is different due to the disparity in the kinetics of the alloying and precipitation reactions. While sufficiently fast diffusion and nucleation reactions through the silver layer induce uniform nucleation through the entire region of the layer, the relatively slow reaction rate of lithium with gold results in a non-uniform distribution of nuclei through the gold layer when compared to the silver layer.

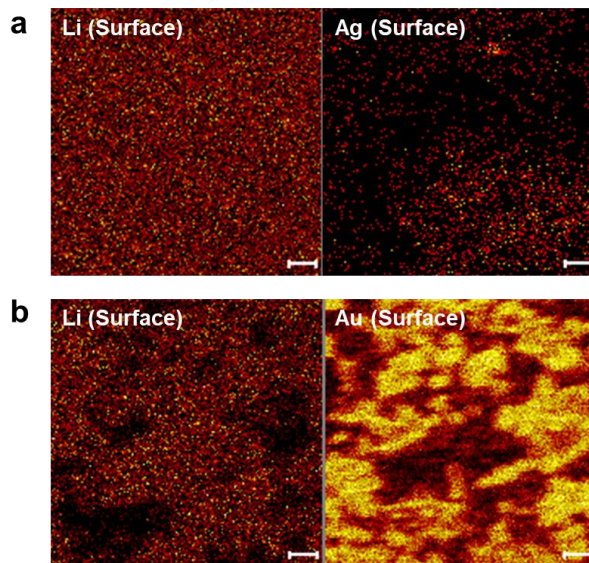


**Figure 3.11.** SIMS analyses of interlayers on polished LLZO surfaces after the galvanostatic deposition of lithium at  $0.1 \text{ mA cm}^{-2}$  for 15 min ( $0.025 \text{ mAh cm}^{-2}$ ) on/through 100-nm-thick (a) silver and (b) gold layers (Scale bars:  $10 \text{ }\mu\text{m}$ ). Lithium is much more uniformly distributed on and through the silver layer in two dimensions, while lithium and gold are locally concentrated in the gold layer. These observations are consistent with the optical microscopy results that show rapid overall changes in colour through the silver layer, but localized colors in the gold layer due to the different kinetics of the alloying reactions (Figure 3.10b).

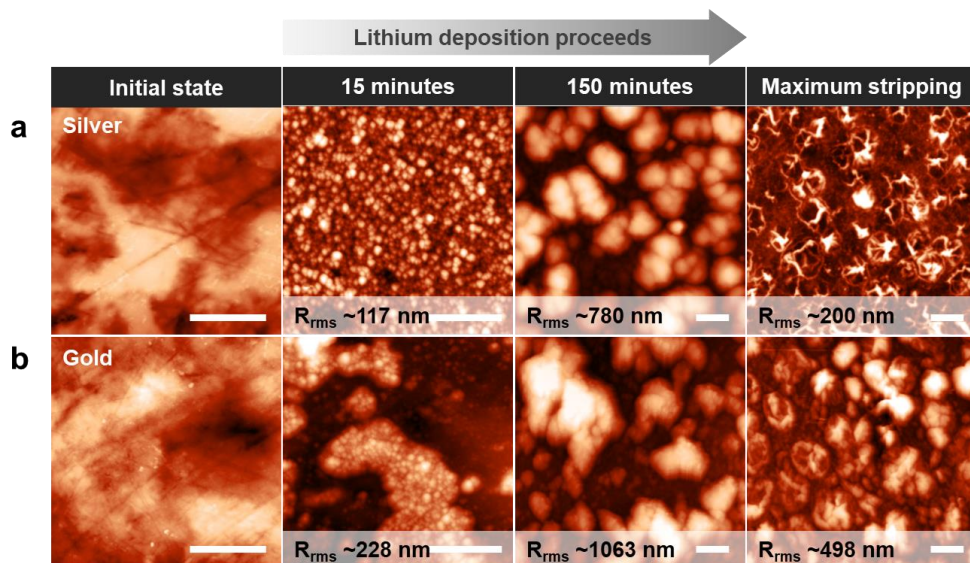


**Figure 3.12.** AFM images of the surface of (a) silver and (b) gold interlayers at various charge/discharge states after  $0.2 \text{ mA cm}^{-2}$  galvanostatic deposition and  $0.1 \text{ mA cm}^{-2}$  galvanostatic stripping of lithium. ( $R_{rms}$  = root mean square roughness, and the scale bar in each the image =  $10 \mu\text{m}$ . The maximum amounts of lithium stripped from each interlayer at  $0.47 \text{ mAh cm}^{-2}$  for silver and  $0.38 \text{ mAh cm}^{-2}$  for gold case differ due to their distinct reversibilities.)

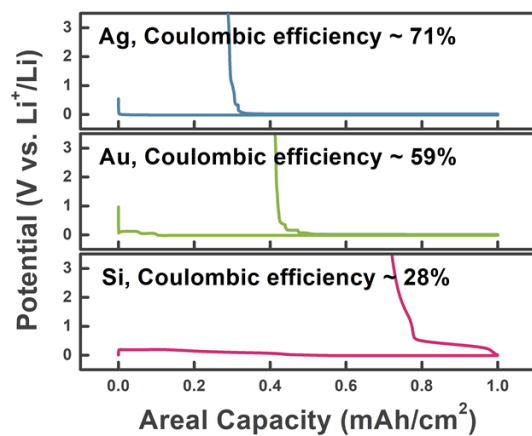


**Figure 3.13.** Electrochemical performance of solid-state batteries employing 100-nm-thick interlayers under the same test conditions of 0.2 mA cm<sup>-2</sup> galvanostatic deposition and stripping of lithium at 60 °C, showing distinct coulombic efficiencies.



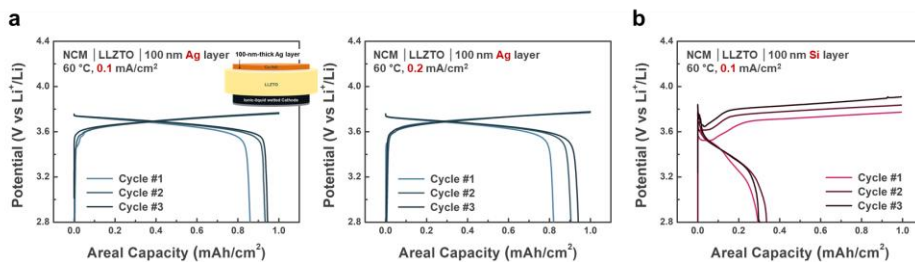


**Figure 3.14.** Electrochemical performance of anode-free hybrid-solid-state batteries.

The hybrid full cells, using ionic liquid wetted NCM111 electrode as a hybrid cathode and 100-nm-thick (a) silver and (b) silicon metal layer as an interlayer at solid electrolyte/anode current collector interface, were tested under the galvanostatic charge/discharge condition with the current densities of 0.1 and 0.2 mA cm<sup>-2</sup> for silver interlayer and 0.1 mA cm<sup>-2</sup> for silicon interlayer at 60 °C.

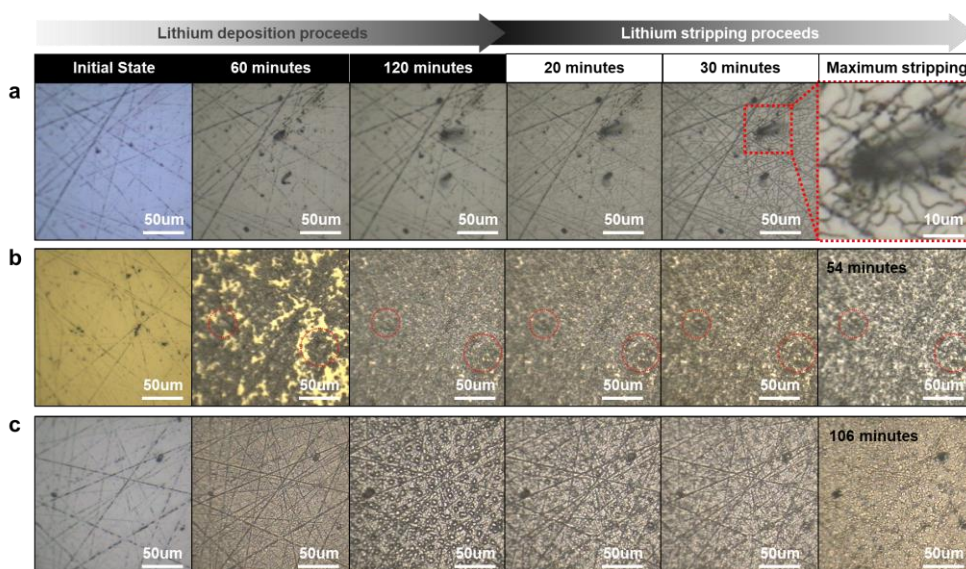


**Figure 3.15.** *In operando* optical microscopy images of the sputtered 100-nm-thick (a) silicon, (b) gold and (c) silver layers on polished LLZO surfaces during 0.1 mA  $\text{cm}^{-2}$  galvanostatic deposition and stripping of lithium through the layer.

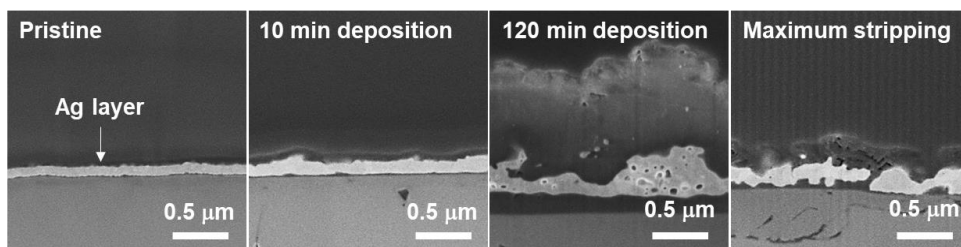


**Figure 3.16.** Cross-sectional SEM image of silver layer at different charge/discharge state after  $0.1 \text{ mA cm}^{-2}$  galvanostatic deposition and stripping of lithium.

### 3.3.4. Possible explanations for different lithium nucleation kinetics depending on interlayer

We propose that the apparent disparities in the lithium precipitation behavior observed for gold, silver, and silicon interlayers originate from the distinct nucleation kinetics and alloying properties of each interlayer medium. According to classical nucleation theory,<sup>58,59</sup> the critical sizes of nuclei and their populations are governed by the nucleation energy barrier, which is determined by the balance between the interfacial energy and the reduction in the free energy, as shown schematically in Figure 3.17. As observed during the initial nucleation steps, the population of lithium metal nuclei is the highest in the Li-Ag alloy, followed by Li-Au and then Li-Si, which implies that the energy barriers for nucleation in these matrix alloys increase in the order:  $\text{Li-Ag} < \text{Li-Au} < \text{Li-Si}$ . Since it is widely accepted that the overpotentials during electrodeposition reflect the nucleation barrier,<sup>60</sup> we also conducted the experiments evaluating the overpotential during the initial stage of the lithium precipitation. According to the previous study by Yan *et al.*, the different lithium nucleation energetics could be estimated by comparing the overpotentials during the lithium deposition.<sup>46</sup> Similar approaches were taken, and new electrochemical tests were comparatively carried out for the three interface layers as presented in Figure 3.18. When calculating the overpotentials from the results presented in the figure, it was observed that the magnitude of the overpotentials systematically increases from silver to gold and silicon interlayers. The overpotential for the silver layer appears to be negligibly small, *i.e.* less than 1 mV, while the silicon interlayer exhibits an appreciable overpotential of 7.4 mV. It implies that the

energy barrier required for the lithium precipitation would be notably higher in the silicon interlayer than the case in the gold or silver interlayer, which is also consistent with our observations by *in operando* microscopy. Given the same free energy for reduction of the lithium precipitate, we believe that distinct interface interactions between each matrix alloy and the lithium precipitates are dominant factors. While we still do not understand why the energetics should differ in the above-mentioned order, we suggest several plausible explanations. Besides, we conducted the same continuum mechanics simulations on the solid electrolyte with the different interlayers in order to examine the possible change in the initial lithium ion flux distribution due to the existence of the interlayer. However, the results showed no differences in the lithium ion flux through the electrolyte with or without interlayer. It infers that the lithium plating behavior is altered by the distinct nucleation kinetics and alloying properties of interlayer materials, which cannot be captured in the simple continuum simulation only taking account of the change of the lithium ion flux at the surface of LLZO. One of the possible reasons involves the different solubilities of the interlayer atoms in the lithium metal. In a previous report, Yan *et al.* studied the behavior of lithium-metal nucleation on a variety of metal substrates with different alloying properties and suggested that the solubility of a metal in the lithium alters the magnitude of the electrochemical overpotential to eventually facilitate nucleation behavior.<sup>46</sup> Metals with high solubilities in the matrix possibly exhibit lower interfacial energies between the precipitate and matrix material by creating a chemically compatible interface as the precipitates nucleate.<sup>61-63</sup> According to phase diagrams,<sup>52</sup> lithium does not exhibit appreciable silicon solubility, whereas the  $\beta$ -Li phase has a high silver solubility limit.<sup>53</sup> Moreover, intermetallic

Li-Si compounds do not show noticeable lithium solubilities in any phase; on the other hand, Li-Ag alloys allow a wide range of composition variations. The significant solubility of each component in the interface supposedly influences precipitation behavior and kinetics favorably. Another possible factor that may affect the interfacial energy is the crystal structure of the final alloy state of the interlayer and its compatibility with crystalline lithium metal, which may create elastic strain energy.<sup>64-69</sup> Ichitsubo *et al.* demonstrated that the strain accommodated by the aluminum matrix during lithium insertion significantly retards lithiation kinetics.<sup>67</sup> While determining the structure of the crystallographic interface between the lithium precipitate and the matrix alloy, as well as the corresponding strain field is not trivial, the strain energy is greatly influenced by the structure of the material; it is therefore likely that changes in the crystal structure of the alloy matrix change the precipitation energy barrier. In a similar vein, the mechanical properties of the alloy may exert distinct external pressure on the lithium precipitates, affecting their nucleation behavior. In a previous study, Motoyama *et al.* showed that external pressure changes nucleation behavior by demonstrating that a higher overpotential was required for lithium precipitation under a greater external pressure generated in a current collector at the interface with a solid-state electrolyte (lithium phosphorous oxynitride, LiPON).<sup>70</sup> Since each lithium alloy has its own elastic modulus, lithium nucleation in each medium experiences a distinct mechanical stress, which influences the energetics of the lithium-precipitation process. The rate of nucleation and growth depends on the thermodynamic and kinetic properties of the lithium-alloy matrix; the overall reaction is determined by these properties, which determine the entire lithium-metal plating behavior. Therefore, exploring suitable interlayers as dynamic

buffer layers for lithium precipitation is important for regulating the lithium-metal anode for stable lithium batteries.

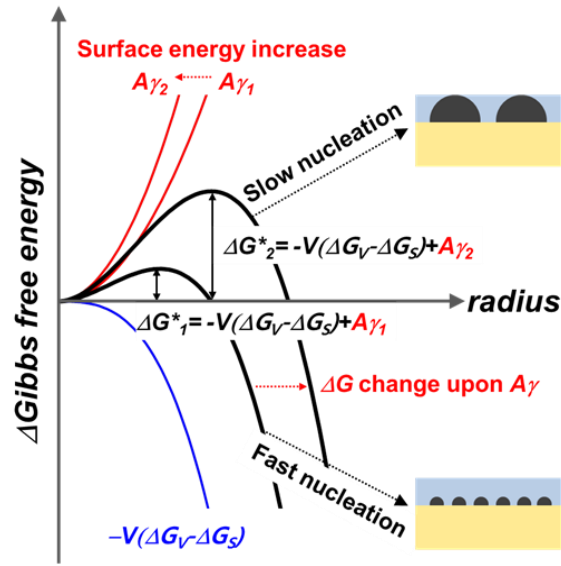


**Figure 3.17.** Classical picture of nucleation and growth, showing the free energy change associated with the surface energy for nucleation. It is well known that an energy barrier ( $\Delta G_{\text{nucleation}} = -V\Delta G_V + V\Delta G_{\text{strain}} + A\gamma$ ) is associated with nucleation due to changes in the volume free energy ( $\Delta G_V$ ), interfacial energy ( $\gamma$ ), and misfit strain energy ( $\Delta G_{\text{strain}}$ ). The activation energy barrier  $\Delta G^*$  increases with surface energy.



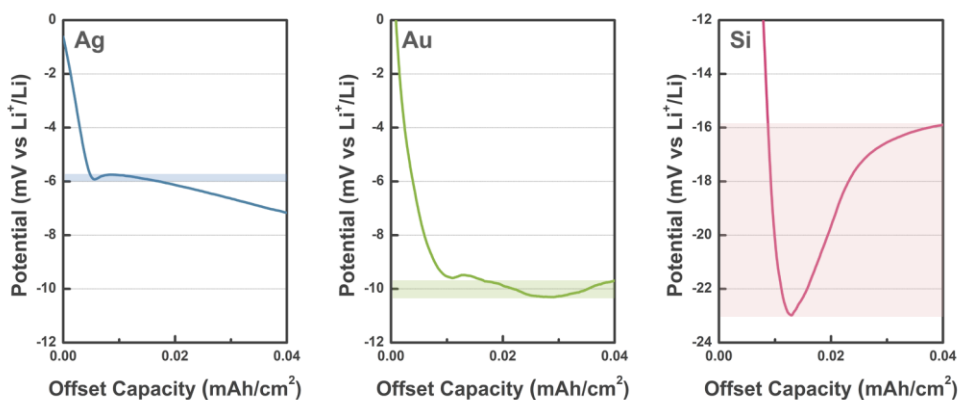


**Figure 3.18.** Voltage profiles of silicon, gold and silver interlayer during lithium deposition at a current density of  $0.1 \text{ mA cm}^{-2}$  showing the differences of the overpotential for precipitation in each interlayer. For the ease of comparison, the curves are shifted horizontally according to the onset of lithium precipitation and the magnitudes of vertical axis are set to 12 mV.

### 3.4. Conclusion

Electrochemical lithium deposition through the LLZO electrolyte was successfully probed using *in operando* experiments in an anode-free solid-state battery. We found that lithium plating is strongly affected by the geometry of the LLZO surface, where non-uniform/filamentary lithium growth is triggered particularly at morphological defects where the electric field and corresponding lithium ion-flux are concentrated. We also demonstrated that lithium-growth behavior is significantly altered when the LLZO surface is modified by an artificial interlayer, and that lithium distribution on the LLZO can be effectively regulated. We revealed that the kinetics of the alloying and precipitation reactions alter lithium distribution and the subsequent deposition morphology, which depends on directly the interlayer species, as observed by microscopy. Supported by these intriguing observations, we proposed various roles for the interlayer during battery operation: as a dynamic buffer layer for lithium redistribution, and as a matrix layer for facile lithium precipitation. In addition, we confirmed that the interlayer not only affects the deposition process, but also the sequential stripping process, influencing the interfacial kinetics and the electrochemical performance of the cell. Considering the ease of interlayer deposition on the LLZO surface and its wide applicability, we expect that our findings will provide useful guidelines for securing optimal interfaces for SSBs.

### 3.5. References

- 1 Manthiram, A., Yu, X. & Wang, S. Lithium battery chemistries enabled by solid-state electrolytes. *Nature Reviews Materials* **2**, 16103, doi:10.1038/natrevmats.2016.103 (2017).
- 2 Janek, J. & Zeier, W. G. A solid future for battery development. *Nature Energy* **1**, 16141, doi:10.1038/nenergy.2016.141 (2016).
- 3 Zheng, F., Kotobuki, M., Song, S., Lai, M. O. & Lu, L. Review on solid electrolytes for all-solid-state lithium-ion batteries. *Journal of Power Sources* **389**, 198-213, doi: 10.1016/j.jpowsour.2018.04.022 (2018).
- 4 Sun, C., Liu, J., Gong, Y., Wilkinson, D. P. & Zhang, J. Recent advances in all-solid-state rechargeable lithium batteries. *Nano Energy* **33**, 363-386, doi: 10.1016/j.nanoen.2017.01.028 (2017).
- 5 Chang, D., Oh, K., Kim, S. J. & Kang, K. Super-Ionic Conduction in Solid-State  $\text{Li}_7\text{P}_3\text{S}_{11}$ -Type Sulfide Electrolytes. *Chemistry of Materials* **30**, 8764-8770, doi:10.1021/acs.chemmater.8b03000 (2018).
- 6 Oh, K. *et al.* Native Defects in  $\text{Li}_{10}\text{GeP}_2\text{S}_{12}$  and Their Effect on Lithium Diffusion. *Chemistry of Materials* **30**, 4995-5004, doi:10.1021/acs.chemmater.8b01163 (2018).
- 7 Yoon, K., Kim, J.-J., Seong, W. M., Lee, M. H. & Kang, K. Investigation on the interface between  $\text{Li}_{10}\text{GeP}_2\text{S}_{12}$  electrolyte and carbon conductive agents in all-solid-state lithium battery. *Scientific Reports* **8**, 8066, doi:10.1038/s41598-018-26101-4 (2018).
- 8 Thangadurai, V., Narayanan, S. & Pinzaru, D. Garnet-type solid-state fast

- Li ion conductors for Li batteries: critical review. *Chemical Society Reviews* **43**, 4714-4727, doi:10.1039/C4CS00020J (2014).
- 9 Cao, S. *et al.* Modeling, Preparation, and Elemental Doping of  $\text{Li}_7\text{La}_3\text{Zr}_2\text{O}_{12}$  Garnet-Type Solid Electrolytes: A Review. *J. Korean Ceram. Soc* **56**, 111-129, doi:10.4191/kcers.2019.56.2.01 (2019).
  - 10 Murugan, R., Thangadurai, V. & Weppner, W. Fast Lithium Ion Conduction in Garnet-Type  $\text{Li}_7\text{La}_3\text{Zr}_2\text{O}_{12}$ . **46**, 7778-7781, doi:10.1002/anie.200701144 (2007).
  - 11 Murugan, R., Ramakumar, S. & Janani, N. High conductive yttrium doped  $\text{Li}_7\text{La}_3\text{Zr}_2\text{O}_{12}$  cubic lithium garnet. *Electrochemistry Communications* **13**, 1373-1375, doi:10.1016/j.elecom.2011.08.014 (2011).
  - 12 Buschmann, H., Berendts, S., Mogwitz, B. & Janek, J. Lithium metal electrode kinetics and ionic conductivity of the solid lithium ion conductors “ $\text{Li}_7\text{La}_3\text{Zr}_2\text{O}_{12}$ ” and  $\text{Li}_{7-x}\text{La}_3\text{Zr}_{2-x}\text{Ta}_x\text{O}_{12}$  with garnet-type structure. *Journal of Power Sources* **206**, 236-244, doi: 10.1016/j.jpowsour.2012.01.094 (2012).
  - 13 Lee, J.-M. *et al.* High lithium ion conductivity of  $\text{Li}_7\text{La}_3\text{Zr}_2\text{O}_{12}$  synthesized by solid state reaction. *Solid State Ionics* **258**, 13-17, doi: 10.1016/j.ssi.2014.01.043 (2014).
  - 14 Zhu, Y., He, X. & Mo, Y. Origin of Outstanding Stability in the Lithium Solid Electrolyte Materials: Insights from Thermodynamic Analyses Based on First-Principles Calculations. *ACS Applied Materials & Interfaces* **7**, 23685-23693, doi:10.1021/acsami.5b07517 (2015).
  - 15 Li, Y., Han, J.-T., Wang, C.-A., Xie, H. & Goodenough, J. B. Optimizing

- Li<sup>+</sup> conductivity in a garnet framework. *Journal of Materials Chemistry* **22**, 15357-15361, doi:10.1039/C2JM31413D (2012).
- 16 Sharafi, A., Haslam, C. G., Kerns, R. D., Wolfenstine, J. & Sakamoto, J. Controlling and correlating the effect of grain size with the mechanical and electrochemical properties of Li<sub>7</sub>La<sub>3</sub>Zr<sub>2</sub>O<sub>12</sub> solid-state electrolyte. *Journal of Materials Chemistry A* **5**, 21491-21504, doi:10.1039/C7TA06790A (2017).
- 17 Shin, D. O. *et al.* Synergistic multi-doping effects on the Li<sub>7</sub>La<sub>3</sub>Zr<sub>2</sub>O<sub>12</sub> solid electrolyte for fast lithium ion conduction. *Scientific Reports* **5**, 18053, doi:10.1038/srep18053 <https://www.nature.com/articles/srep18053#supplementary-information> (2015).
- 18 Cheng, E. J., Sharafi, A. & Sakamoto, J. Intergranular Li metal propagation through polycrystalline Li<sub>6.25</sub>Al<sub>0.25</sub>La<sub>3</sub>Zr<sub>2</sub>O<sub>12</sub> ceramic electrolyte. *Electrochimica Acta* **223**, 85-91, doi: 10.1016/j.electacta.2016.12.018 (2017).
- 19 Aguesse, F. *et al.* Investigating the Dendritic Growth during Full Cell Cycling of Garnet Electrolyte in Direct Contact with Li Metal. *ACS Applied Materials & Interfaces* **9**, 3808-3816, doi:10.1021/acsami.6b13925 (2017).
- 20 Sharafi, A., Meyer, H. M., Nanda, J., Wolfenstine, J. & Sakamoto, J. Characterizing the Li– Li<sub>7</sub>La<sub>3</sub>Zr<sub>2</sub>O<sub>12</sub> interface stability and kinetics as a function of temperature and current density. *Journal of Power Sources* **302**, 135-139, doi: 10.1016/j.jpowsour.2015.10.053 (2016).
- 21 Krauskopf, T. *et al.* Lithium-Metal Growth Kinetics on LLZO Garnet-Type

- Solid Electrolytes. *Joule*, doi: 10.1016/j.joule.2019.06.013 (2019).
- 22 Porz, L. *et al.* Mechanism of lithium metal penetration through inorganic solid electrolytes. *Advanced Energy Materials* **7**, 1701003 (2017).
- 23 Swamy, T. *et al.* Lithium Metal Penetration Induced by Electrodeposition through Solid Electrolytes: Example in Single-Crystal  $\text{Li}_6\text{La}_3\text{ZrTaO}_{12}$  Garnet. *Journal of The Electrochemical Society* **165**, A3648-A3655, doi:10.1149/2.1391814jes (2018).
- 24 Manalastas, W. *et al.* Mechanical failure of garnet electrolytes during Li electrodeposition observed by in-operando microscopy. *Journal of Power Sources* **412**, 287-293, doi: 10.1016/j.jpowsour.2018.11.041 (2019).
- 25 Koshikawa, H. *et al.* Dynamic changes in charge-transfer resistance at Li metal/ $\text{Li}_7\text{La}_3\text{Zr}_2\text{O}_{12}$  interfaces during electrochemical Li dissolution/deposition cycles. *Journal of Power Sources* **376**, 147-151, doi: 10.1016/j.jpowsour.2017.11.082 (2018).
- 26 Tsai, C.-L. *et al.*  $\text{Li}_7\text{La}_3\text{Zr}_2\text{O}_{12}$  Interface Modification for Li Dendrite Prevention. *ACS Applied Materials & Interfaces* **8**, 10617-10626, doi:10.1021/acsami.6b00831 (2016).
- 27 Sharafi, A. *et al.* Surface Chemistry Mechanism of Ultra-Low Interfacial Resistance in the Solid-State Electrolyte  $\text{Li}_7\text{La}_3\text{Zr}_2\text{O}_{12}$ . *Chemistry of Materials* **29**, 7961-7968, doi:10.1021/acs.chemmater.7b03002 (2017).
- 28 Inada, R. *et al.* Formation and Stability of Interface between Garnet-Type Ta-doped  $\text{Li}_7\text{La}_3\text{Zr}_2\text{O}_{12}$  Solid Electrolyte and Lithium Metal Electrode. *Batteries* **4**, 26, doi:10.3390/batteries4020026 (2018).
- 29 Hofstetter, K., Samson, A. J., Narayanan, S. & Thangadurai, V. Present

- understanding of the stability of Li-stuffed garnets with moisture, carbon dioxide, and metallic lithium. *Journal of Power Sources* **390**, 297-312, doi: 10.1016/j.jpowsour.2018.04.016 (2018).
- 30 Wang, M. & Sakamoto, J. Correlating the interface resistance and surface adhesion of the Li metal-solid electrolyte interface. *Journal of Power Sources* **377**, 7-11, doi: 10.1016/j.jpowsour.2017.11.078 (2018).
  - 31 Han, X. *et al.* Negating interfacial impedance in garnet-based solid-state Li metal batteries. *Nature Materials* **16**, 572, doi:10.1038/nmat4821 (2016).
  - 32 Fu, K. *et al.* Toward garnet electrolyte-based Li metal batteries: An ultrathin, highly effective, artificial solid-state electrolyte/metallic Li interface. *Science Advances* **3**, e1601659, doi:10.1126/sciadv.1601659 (2017).
  - 33 Luo, W. *et al.* Transition from Superlithiophobicity to Superlithiophilicity of Garnet Solid-State Electrolyte. *Journal of the American Chemical Society* **138**, 12258-12262, doi:10.1021/jacs.6b06777 (2016).
  - 34 Wang, C. *et al.* Conformal, Nanoscale ZnO Surface Modification of Garnet-Based Solid-State Electrolyte for Lithium Metal Anodes. *Nano Letters* **17**, 565-571, doi:10.1021/acs.nanolett.6b04695 (2017).
  - 35 Fu, K. *et al.* Transient Behavior of the Metal Interface in Lithium Metal–Garnet Batteries. *Angewandte Chemie* **56**, 14942-14947, doi:10.1002/anie.201708637 (2017).
  - 36 Luo, W. *et al.* Reducing Interfacial Resistance between Garnet-Structured Solid-State Electrolyte and Li-Metal Anode by a Germanium Layer. *Advanced Materials* **29**, 1606042, doi:10.1002/adma.201606042 (2017).

- 37 He, M., Cui, Z., Chen, C., Li, Y. & Guo, X. Formation of self-limited, stable and conductive interfaces between garnet electrolytes and lithium anodes for reversible lithium cycling in solid-state batteries. *Journal of Materials Chemistry A* **6**, 11463-11470, doi:10.1039/C8TA02276C (2018).
- 38 Krauskopf, T., Hartmann, H., Zeier, W. G. & Janek, J. Toward a Fundamental Understanding of the Lithium Metal Anode in Solid-State Batteries—An Electrochemo-Mechanical Study on the Garnet-Type Solid Electrolyte  $\text{Li}_{6.25}\text{Al}_{0.25}\text{La}_3\text{Zr}_2\text{O}_{12}$ . *ACS Applied Materials & Interfaces* **11**, 14463-14477, doi:10.1021/acsami.9b02537 (2019).
- 39 Jalem, R. *et al.* Concerted Migration Mechanism in the Li Ion Dynamics of Garnet-Type  $\text{Li}_7\text{La}_3\text{Zr}_2\text{O}_{12}$ . *Chemistry of Materials* **25**, 425-430, doi:10.1021/cm303542x (2013).
- 40 COMSOL Multiphysics® v. 5.6. www.comsol.com. COMSOL AB, Stockholm, Sweden.
- 41 Yoon, G., Moon, S., Ceder, G. & Kang, K. Deposition and Stripping Behavior of Lithium Metal in Electrochemical System: Continuum Mechanics Study. *Chemistry of Materials* **30**, 6769-6776, doi:10.1021/acs.chemmater.8b02623 (2018).
- 42 Moon, S. *et al.* Simple and Effective Gas-Phase Doping for Lithium Metal Protection in Lithium Metal Batteries. *Chemistry of Materials* **29**, 9182-9191, doi:10.1021/acs.chemmater.7b03027 (2017).
- 43 Schmidt, R. D. & Sakamoto, J. In-situ, non-destructive acoustic characterization of solid state electrolyte cells. *Journal of Power Sources* **324**, 126-133, doi: 10.1016/j.jpowsour.2016.05.062 (2016).



- 44 Wang, J., King, P. & Huggins, R. A. Investigations of binary lithium-zinc, lithium-cadmium and lithium-lead alloys as negative electrodes in organic solvent-based electrolyte. *Solid State Ionics* **20**, 185-189, doi: 10.1016/0167-2738(86)90212-2 (1986).
- 45 Cretu, C. & van der Lingen, E. Coloured gold alloys. *Gold Bulletin* **32**, 115-126, doi:10.1007/bf03214796 (1999).
- 46 Yan, K. *et al.* Selective deposition and stable encapsulation of lithium through heterogeneous seeded growth. *Nature Energy* **1**, 16010, doi:10.1038/nenergy.2016.10 (2016).
- 47 Bach, P. *et al.* Electrochemical Lithiation Cycles of Gold Anodes Observed by In Situ High-Energy X-ray Diffraction. *Chemistry of Materials* **28**, 2941-2948, doi:10.1021/acs.chemmater.5b04719 (2016).
- 48 Lifshitz, I. M. & Slyozov, V. V. The kinetics of precipitation from supersaturated solid solutions. *Journal of Physics and Chemistry of Solids* **19**, 35-50, doi: 10.1016/0022-3697(61)90054-3 (1961).
- 49 Epler, M. Vol. 9 (ed George F. Vander Voort) 134-139 (ASM International, 2004).
- 50 Carter, J. R. & Swalin, R. A. On the Kinetics and Mechanism of the Precipitation of Lithium from Germanium. *Journal of Applied Physics* **31**, 1191-1200, doi:10.1063/1.1735801 (1960).
- 51 Dutta, B., Palmiere, E. J. & Sellars, C. M. Modelling the kinetics of strain induced precipitation in Nb microalloyed steels. *Acta Materialia* **49**, 785-794, doi:10.1016/S1359-6454(00)00389-X (2001).
- 52 Okamoto, H. Li-Si (Lithium-Silicon). *Journal of Phase Equilibria and*

- Diffusion* **30**, 118-119, doi:10.1007/s11669-008-9431-8 (2009).
- 53 Pelton, A. D. The Ag–Li (Silver-Lithium) system. *Bulletin of Alloy Phase Diagrams* **7**, 223-228, doi:10.1007/bf02868993 (1986).
- 54 Bucci, G., Nadimpalli, S. P. V., Sethuraman, V. A., Bower, A. F. & Guduru, P. R. Measurement and modeling of the mechanical and electrochemical response of amorphous Si thin film electrodes during cyclic lithiation. *Journal of the Mechanics and Physics of Solids* **62**, 276-294, doi:10.1016/j.jmps.2013.10.005 (2014).
- 55 Xie, J. *et al.* Electrochemical kinetics of nanosized Ag and Ag<sub>2</sub>O thin films prepared by radio frequency magnetron sputtering. *Journal of Solid State Electrochemistry* **15**, 2031-2039, doi:10.1007/s10008-010-1228-0 (2011).
- 56 Chen, K.-H. *et al.* Dead lithium: mass transport effects on voltage, capacity, and failure of lithium metal anodes. *Journal of Materials Chemistry A* **5**, 11671-11681, doi:10.1039/C7TA00371D (2017).
- 57 Sun, Y., Liu, N. & Cui, Y. Promises and challenges of nanomaterials for lithium-based rechargeable batteries. *Nature Energy* **1**, 16071, doi:10.1038/nenergy.2016.71 (2016).
- 58 Plieth, W. *Electrochemistry for Materials Science*. 1 edn, (Elsevier Science, 2007).
- 59 David A. Porter, K. E. E., Mohamed Youssef Abdelraouf Sherif. *Phase Transformations in Metals and Alloys (Revised Reprint)*. (CRC Press, 2009).
- 60 Pei, A., Zheng, G., Shi, F., Li, Y. & Cui, Y. Nanoscale Nucleation and Growth of Electrodeposited Lithium Metal. *Nano Letters* **17**, 1132-1139,

- doi:10.1021/acs.nanolett.6b04755 (2017).
- 61 Ardell, A. J. & Ozolins, V. Trans-interface diffusion-controlled coarsening. *Nature Materials* **4**, 309-316, doi:10.1038/nmat1340 (2005).
- 62 Sluiter, M. & Kawazoe, Y. Prediction of matrix-precipitate interfacial free energies: Application to Al-Al<sub>3</sub>Li. *Physical Review B* **54**, 10381-10384, doi:10.1103/PhysRevB.54.10381 (1996).
- 63 Fu, S.-W. & Lee, C. C. A study on intermetallic compound formation in Ag–Al system and evaluation of its mechanical properties by micro-indentation. *Journal of Materials Science: Materials in Electronics* **29**, 3985-3991, doi:10.1007/s10854-017-8340-1 (2018).
- 64 Kali, R., Badjate, S. & Mukhopadhyay, A. Effects of residual stress on overpotentials and mechanical integrity during electrochemical Li-alloying of Al film electrodes. *Journal of Applied Electrochemistry* **47**, 479-486, doi:10.1007/s10800-017-1054-5 (2017).
- 65 Sheldon, B. W., Soni, S. K., Xiao, X. & Qi, Y. Stress Contributions to Solution Thermodynamics in Li-Si Alloys. *Electrochemical and Solid-State Letters* **15**, A9-A11, doi:10.1149/2.016201esl (2011).
- 66 Mukhopadhyay, A. & Sheldon, B. W. Deformation and stress in electrode materials for Li-ion batteries. *Progress in Materials Science* **63**, 58-116, doi:https://doi.org/10.1016/j.pmatsci.2014.02.001 (2014).
- 67 Ichitsubo, T. *et al.* Influence of Mechanical Strain on the Electrochemical Lithiation of Aluminum-Based Electrode Materials. *Journal of The Electrochemical Society* **159**, A14-A17, doi:10.1149/2.038201jes (2011).
- 68 Chou, C.-Y., Kim, H. & Hwang, G. S. A Comparative First-Principles

- Study of the Structure, Energetics, and Properties of Li–M (M = Si, Ge, Sn) Alloys. *The Journal of Physical Chemistry C* **115**, 20018-20026, doi:10.1021/jp205484v (2011).
- 69 Larché, F. C. & Cahn, J. W. Overview no. 41 The interactions of composition and stress in crystalline solids. *Acta Metallurgica* **33**, 331-357, doi: 10.1016/0001-6160(85)90077-X (1985).
- 70 Motoyama, M., Ejiri, M. & Iriyama, Y. Modeling the Nucleation and Growth of Li at Metal Current Collector/LiPON Interfaces. *Journal of The Electrochemical Society* **162**, A7067-A7071, doi:10.1149/2.0051513jes (2015).

## Chapter 4. High-power solid-state batteries enabled by preferred directional lithium growth mechanism

(The content of this chapter has been published in *ACS Energy Letters*. Reprinted with permission from [Kim, S., Yoon, G., Jung, S.-K. *et al.*, *ACS Energy Letters*, **2023**, 8, 9. <https://doi.org/10.1021/acsenergylett.2c02150>]. Copyright 2022 American Chemical Society.)

### 4.1. Introduction

Solid-state batteries using lithium metal anodes and solid electrolytes are considered promising alternatives to the current lithium-ion batteries because they are safe and can potentially exhibit high energy densities.<sup>1-7</sup> Among the various solid electrolytes proposed so far, garnet-type oxide electrolytes (such as  $\text{Li}_7\text{La}_3\text{Zr}_2\text{O}_{12}$  (LLZO)) are some of the leading candidates for lithium-metal solid-state batteries due to their high ionic conductivities at room temperature ( $\sim 1 \text{ mS cm}^{-1}$ ) and chemical stability with lithium metal.<sup>3,8-11</sup> However, their real-world implementation has been hampered by the premature short-circuiting caused by lithium metal piercing through the LLZO under practical current densities.<sup>12-14</sup> Various mechanisms have been suggested as causes of this phenomenon and currently under extensive investigations<sup>7,15-18</sup>, however, the interfacial inhomogeneity/instability occurring between lithium metal anode and LLZO has been considered as the most crucial attribute.

Many studies have reported that the internal short circuits can be caused by the localized electrodeposition arising from the inhomogeneous interfacial nature, which

is typically induced by the poor contact of lithium metal with LLZO and intrinsically low lattice-lithium diffusivity in dynamic lithium stripping and deposition processes.<sup>5,14,19-21</sup> As illustrated in Figure 4.1a, the ill-defined interface can induce the inhomogeneous current distribution and the localized lithium plating, which trigger a rapid lithium penetration into the electrolyte through the grain boundaries, or by crack propagation.<sup>18,22</sup> It is further aggravated during the lithium stripping process due to the morphological instability at the interface involving the lithium void, which tends to be formed due to the sluggish lattice-lithium diffusion compared with the applied current density, eventually causing lithium metal penetration into the electrolyte.<sup>20,21,23,24</sup> For the past several years, researchers found that introducing an interlayer between the LLZO electrolyte and lithium metal anode could improve the interfacial homogeneity and stability.<sup>19,23,25-30</sup> Various compounds such as metallic alloys, oxides, nitrides and halides were proposed as promising interlayers on the LLZO with the enhanced wettability with lithium metal and the high lithium ionic conduction that allows the homogeneous lithium flux.<sup>5,25-28,31-43</sup> In particular, metallic interlayers that can alloy with lithium were demonstrated to be markedly effective; it promotes not only the wettability with the LLZO but also the lattice-lithium diffusion in the alloying matrix, successfully homogenizing the lithium-ion flux distribution even during the high-rate stripping process.<sup>31,34,44,45</sup>

Nevertheless, it has been arduous to achieve acceptable long-term performance for practical applications due to the limitations of the interlayers proposed so far. It is typically attributable to degradation of the interlayer itself during long-term operation of batteries, depending on its working mechanism, as schematically illustrated in Figure 4.1b. The widely reported alloying interlayers (*e.g.*, gold, silver,

germanium, and silicon) are often accompanied with significant volume change during alloying/dealloying, and the repeated deposition/stripping of lithium constantly degenerates the original morphology of the interlayer.<sup>5,26,28,30-33</sup> It ultimately causes the rupture of the interlayer coated on LLZO, exposing the naked LLZO interface to the lithium metal, failing in the role of the interlayer. Similar degradations are also expected for oxide-based or nitride-based interlayers, which can undergo conversion reaction with lithium metal.<sup>35,36,39,46,47</sup> Such conversion reactions generally yield a significant morphological change upon repeated lithium uptake, continuously deteriorating the interlayer stability. Moreover, the alloys that can homogenize the lithium-ion flux such as gold and silver are vulnerable to the chemical diffusion into the lithium matrix upon its contact.<sup>48,49</sup> The alloying element is likely to diffuse out from the interface into the lithium bulk region over time, gradually losing its interlayer role during long-term operation of the battery. Another aspect that has been often overlooked is the lack of the selectivity in the lithium deposition with respect to the interlayer position. While lithium is supposed to be deposited between the current collector and the interlayer, some electrically conductive interlayers may allow the lithium deposition between the interlayer and the LLZO, as schematically illustrated in right panel of Figure 4.1b. Even slight electrical leakage through the thin interlayer may induce the lithium nucleation underneath the interlayer, inducing the detachment of the interlayer from the LLZO surface and its deterioration.

In this study, we focus on how to design an optimal interlayer rationally considering these degradation mechanisms of the interlayer upon the lithium plating and stripping. Based on the thermodynamic properties of the candidate materials

estimated by density functional theory (DFT) calculations, a carbon-based material is selected as the core component of interlayer, which can preferentially induce lithium plating between the current collector (copper) and the interlayer. In this consideration, it is also unveiled that the crystalline orientations of the carbon domains are important in homogenizing the lithium-ion flux through the interlayer, indicating the necessity in the crystalline engineering of carbon. Additionally, it is shown that the high kinetic energy barrier for lithium nucleation can be effectively lowered with the aid of the pre-lithium deposits, which further facilitate the preferred lithium growth without destructing the original interlayer/electrolyte interface. Through the series of in-depth characterizations, we demonstrate that this rational selection is quite effective, which allows the long-term stability of the interlayer not only in the morphology but also in securing the reversible lithium stripping/deposition. We fabricate a high-capacity solid-state cell with an NCA811 ( $\text{LiNi}_{0.8}\text{Co}_{0.1}\text{Al}_{0.1}\text{O}_2$ ) cathode, employing the optimized carbon interlayer between an LLZO electrolyte and lithium metal anode, and validate that it exhibits remarkable room-temperature cycling performance over 250 cycles with 99.6 % capacity retention, delivering  $4.0 \text{ mAh cm}^{-2}$  at  $2.5 \text{ mA cm}^{-2}$  with a cumulative capacity of over  $1,000 \text{ mAh cm}^{-2}$ . The successful long-term operation at record-high  $2.5 \text{ mA cm}^{-2}$  at room temperature paves a new pathway toward the development of practical all-solid-state lithium metal batteries.



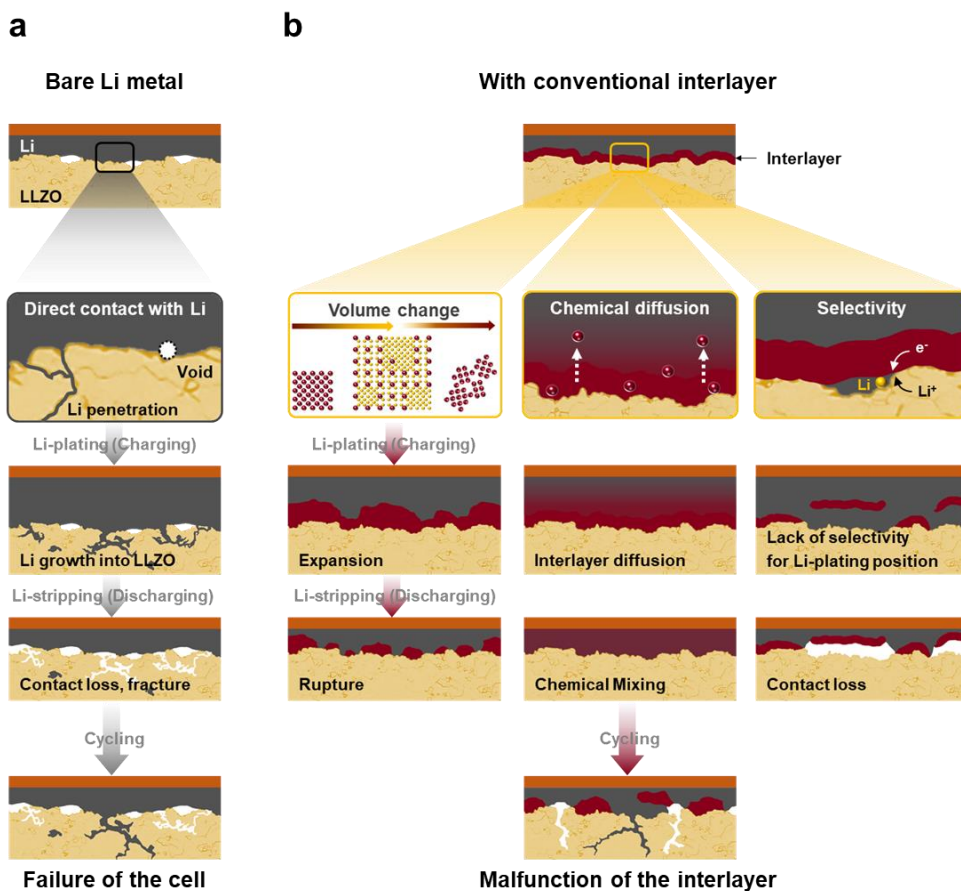


**Figure 4.1.** Schematic illustrations of the degradation mechanism at the interface of a solid electrolyte and a lithium-metal anode during repetitive lithium plating and stripping. (a) The failure of the cell on using bare lithium metal anode. (b) The failure of the cell on using conventional interlayers at the interface of LLZO electrolyte/lithium metal anode due to the (electro)chemical/physical instability of the interlayer.

## 4.2. Experimental and computational details

### 4.2.1. Material synthesis

Solid electrolyte pellets of  $\text{Li}_{6.5}\text{La}_3\text{Zr}_{1.5}\text{Ta}_{0.5}\text{O}_{12}$  (LLZO, 14 mm diameter and 500  $\mu\text{m}$  thickness) were purchased from Toshima. Acid treatment and protonation of the LLZO-pellet surface were carried out for all the experiments to ensure chemical/physical stability against lithium metal.<sup>6</sup> The pellets were immersed in 1 M HCl solution (in distilled water) at a weight ratio of 1:10 (pellet:acid solution) at room temperature for 30 min. The container was rotated at approximately 60 rpm during protonation to prevent local variation in acid concentration (due to the released lithium) and close contact of the electrolyte with the container. Subsequently, the solution was removed, then the pellets were immediately washed with ethanol, and dried (in a dry room).

The interlayers were prepared using slurry casting, a conventional method to fabricate electrodes for lithium-ion batteries. Carbon powder (graphite or amorphous carbon) and Polyvinylidene fluoride (PVDF) binder (93:7 w/w) were mixed and dispersed in N-Methyl-2-pyrrolidone (NMP) to prepare a slurry. For the carbon layer using another amorphous carbon with different particle (10~20 nm) and crystallite size ( $\sim 0.7$  nm), 25% of the total amount of carbon powder was replaced by the smaller amorphous carbon. It was then homogenized using a Thinky planetary mixer, coated on a copper foil, and dried in a vacuum oven for 12 h. The loading level and the thickness of the interlayer was approximately  $0.3\text{--}0.4\text{ mg cm}^{-2}$  and 2–3 (Figure 4.2)  $\mu\text{m}$ , respectively.

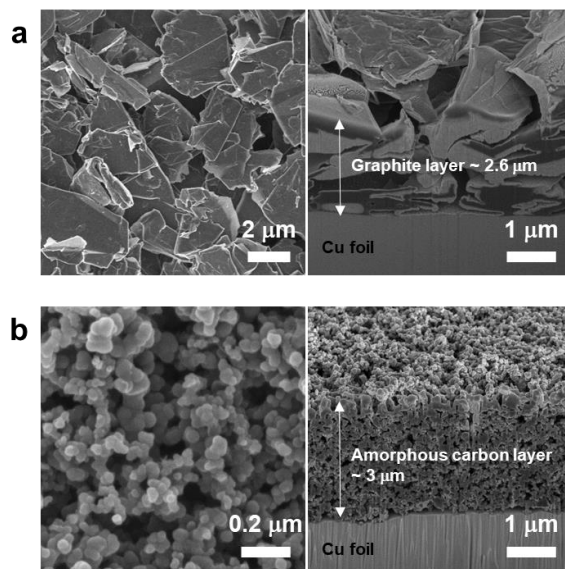


**Figure 4.2.** Carbon interlayers coated on copper foil. SEM images of (left) surface and (right) cross-section of as-prepared (a) graphite and (b) amorphous carbon interlayer. Although these as-prepared interlayers seem porous, they become dense after assembling with LLZO pellet under 250 MPa using cold isostatic press (CIP).

#### 4.2.2. Cell assembly and electrochemical test

Two types of asymmetric (Figure 4.3) cells were fabricated using LLZO pellets in a dry room, where the dew point was maintained under  $-50\text{ }^{\circ}\text{C}$ . One type of asymmetric cells (Cell#1), used to examine lithium plating behavior through carbon interlayers, consists of a lithium-metal electrode (20- $\mu\text{m}$ -thick lithium metal on 10- $\mu\text{m}$ -thick copper foil (Honjo Metal Co. Ltd.) with a diameter of 11 mm) as a counter electrode and a carbon layer with a diameter of 11mm as a working electrode. Each electrode was placed onto each side of the pellet, and both were attached by applying a pressure of 250 MPa for 3 min using a cold isostatic press (CIP). The other type of asymmetric cells (Cell#2) consisted of the same configuration, but pre-existing lithium-metal layer was added to the carbon interlayer so that the working electrode was lithium-metal with the carbon interlayer. To prepare the lithium-metal electrode with carbon interlayers, the carbon interlayers were transferred to lithium metal. The coated interlayer and lithium metal were positioned to face each other and compressed using the CIP as described above. After pressing, the copper foil substrate was detached from the assembly. Finally, the prepared working electrode (lithium-metal electrode with the interlayer) and the counter electrode, lithium metal, were attached onto each side of the LLZO pellet using CIP. The cells were assembled using a modified 2032-type coin cell configuration<sup>5</sup> to prevent air exposure and apply a constant atmospheric pressure by maintaining the vacuum state.

These cells were used for galvanostatic lithium plating/stripping tests, electrochemical impedance spectroscopy (EIS)/ galvanostatic electrochemical impedance spectroscopy (GEIS) measurements, and galvanostatic intermittent

titration technique (GITT) analyses. Galvanostatic lithium plating/stripping tests were conducted on the asymmetric cells (Cell#1 and #2, see Figure 4.3 for details) at a current density of 0.1 or 0.3 mA cm<sup>-2</sup> at 25 and 100 °C. The EIS measurements were conducted at 25 °C at an open-circuit voltage over a frequency range of 0.1–10 kHz using an alternating current (AC) perturbation of 10 mV, utilizing a frequency response analyzer (Solartron, SI 1255 FRA) in conjunction with a potentiostat (Solartron, SI 1287 ECI). GEIS was used to track the evolution of impedance over time; the same equipment was used for measurement under a direct current (DC) of density 0.3 mA cm<sup>-2</sup> with 10% AC amplitude of the applied current. For GITT measurements, asymmetric cell #1 with graphite layer or amorphous carbon layer was used;<sup>50,51</sup> after fully charging (lithiation) the electrode according to its active material weight, constant anodic current pulses (0.3 mA cm<sup>-2</sup>) were applied for 3 min, alternating with open-circuit voltage periods of 177 min at 25 °C.

A hybrid solid-state lithium cells using an ionic liquid electrolyte as catholyte was used to evaluate the electrochemical performance of the LLZO solid electrolyte in a battery full cell employing the lithium metal anode with the interlayer. Here, an NCA electrode (loading capacity: 5.1 mAh cm<sup>-2</sup>; Samsung SDI) coated on Al foil was used as the cathode, and an ionic liquid, 2 M lithium bis(fluorosulfonyl)imide (LiFSI) in N-methyl-N-propyl pyrrolidinium bis(fluorosulfonyl)imide (Pyr13FSI, Kanto Chemical Co. INC.), was used as the catholyte. The catholyte was dropped onto the cathode and then infiltrated into it in vacuum for 2 h; the infiltrated amount of ionic liquid was 20 wt% relative to the cathode weight. The ionic-liquid-infiltrated cathode was then placed on the other side of the LLZO pellet in a 2032-type coin cell. To eliminate the possibility of direct contact between the ionic liquid and lithium metal,

a relatively small cathode (diameter 0.4 cm) was used for the cell. The anodes (bare lithium-metal electrode or lithium metal electrode with the carbon interlayer) were assembled in the same way as for the asymmetric cells. Finally, the cell was sealed under vacuum using a polymer coated Al film. The charge/discharge characteristics of the hybrid electrolyte cells were examined using a battery cycler (TOSCAT-3100, Toyo System). The cells were charged/discharged with current densities of 0.5 mA cm<sup>-2</sup> for the first three cycles, 0.8 mA cm<sup>-2</sup> for the next two cycles, 1.0 mA cm<sup>-2</sup> for the subsequent two cycles, 1.6 mA cm<sup>-2</sup> for the 8<sup>th</sup> to the 10<sup>th</sup> cycle, 2 mA cm<sup>-2</sup> for the 11<sup>th</sup> to the 13<sup>th</sup> cycle, and 2.5 mA cm<sup>-2</sup> for subsequent long-term cycling using a conventional constant current (CC)-constant voltage (CV) protocol, and discharged in the CC mode in the potential range of 2.8–4.3 V (vs. Li<sup>+</sup>/Li).

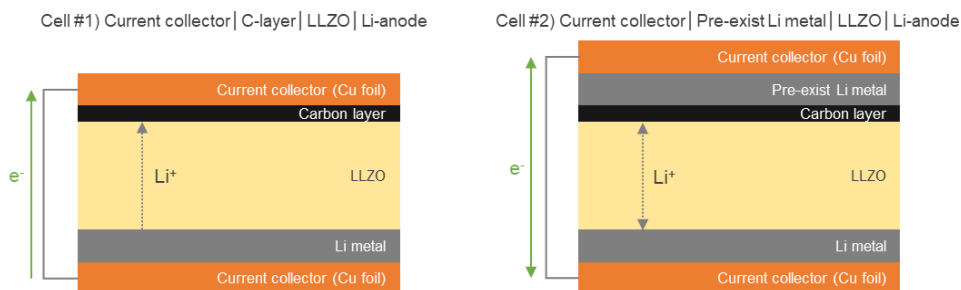


**Figure 4.3.** Schematic of cells used for lithium plating experiments. Cell #1 uses lithium metal as a counter electrode and a carbon layer as a working electrode. It was used for lithium plating experiments described in Figure 4.7 and 4.8, and for GITT test presented in Figure 4.22. Cell#2 uses lithium metal as a counter electrode and a carbon layer with lithium metal as a working electrode. It was used for lithium plating experiments described in Figure 4.10 and lithium stripping experiments described in Figure 4.15, 4.17 and 4.19.

### 4.2.3. Material characterization

The cross-sections of the interface between LLZO electrolyte and anodes after lithium plating/stripping experiments were prepared by cross-section polisher (JEOL, IB-19520CCP) equipped with a specific air-isolation system. To prevent the contamination and reaction from air exposure, all the specimens were prepared in an Ar-purged glove box and transferred to cross-section polisher using an air-tight transfer vessel. The cross section was polished using Ar-ion beam with 6 kV acceleration voltage at -70 °C in vacuum state. Processed cross section of the cells was examined using a field-emission scanning electron microscope (SU-8030, Hitachi) coupled with an EDS spectrometer (X-max 80, Oxford). 5 kV accelerating voltage and an 8 mm working distance were applied for SEM image analysis, and 15 kV accelerating voltage and an 16 mm working distance were applied for EDS mapping.

### 4.2.4. Simulation methods

Density functional theory (DFT) calculations were used to investigate the interfacial adhesion energies ( $W_{ad}$ ) and predict the location of thermodynamically stable Li plating sites for the interlayers.  $W_{ad}$  is defined as the energy difference between the combined interface and the isolated slabs.

$$W_{ad} = \frac{1}{A} (E_{interface} - E_{substrate} - E_{film})$$

Here, A indicates the interfacial area between two slabs, and  $E_{interface}$ ,  $E_{substrate}$ , and  $E_{film}$  are the calculated energies of the optimized model structures. To build the interface models, surface slabs were constructed for each interface material,



followed by the application of lattice transformations to combine two surface slabs into a single interface model. A slight modification of lattice parameters was allowed (e.g. an elongation or shrinkage of less than 5% and/or angle distortion of less than 3°) to accommodate the differences in lattice parameters of the surface slabs. Thicknesses of the surface slabs were determined by conducting energy convergence tests with increasing values of slab thickness and inserting a 15-Å-thick vacuum slab into the interface model; the *Pymatgen*<sup>52</sup> interface builder was used for model construction. All calculations were performed using the Vienna Ab initio Simulation Package (VASP); a projector-augmented wave pseudopotential with a plane-wave basis set<sup>53</sup> was used, as provided by VASP, and the Perdew-Burke-Ernzerhof version of the generalized gradient approximation<sup>54</sup> was used for the exchange-correlation functional. The semi-empirical DFT-D3 correction of Grimme et al.<sup>55</sup> was applied (when required) to describe the van der Waals interaction. Structure optimizations were performed until all the forces converged within 0.02 eV Å<sup>-1</sup>, using a cutoff energy of 400 eV.

As shown in Figure 4.4, the  $W_{ad}$  values for the two assumed cases were calculated using different interlayer materials. The interface between the interlayer and the lithium metal (interlayer/Li) was generated in both cases; thus, its value was not taken into account while comparing interfacial energies.

Continuum mechanics simulation with COMSOL was used to investigate the influence of carbon morphology on electrochemical behavior.<sup>56</sup> The geometry of the model structure mimicking the experimental cell configuration is illustrated in the left panel of Figure 4.5. The dimensions of all the components were selected in

agreement with the experimental design. Two separate simulations with modified interface condition were used to analyze the influence of carbon morphology on electrochemistry: one with a perfect interface representing carbon black, and the other with a partially active interface representing graphite (which has directional particle morphology and limited lithiation spots).

Simulations were performed using the secondary current distribution interface in COMSOL, where the interface reaction kinetics were described with the Butler-Volmer equation. To isolate the effect on the anode interface, the kinetic parameters of the cathode part (e.g. Li-ion diffusivity in the cathode and the cathode-electrolyte interfacial resistance) were set to ensure that the cathode reaction would not be a rate-limiting factor. All the other parameters were selected from experimental results (of this study or from previous publications), as shown in **Table 4.1**.

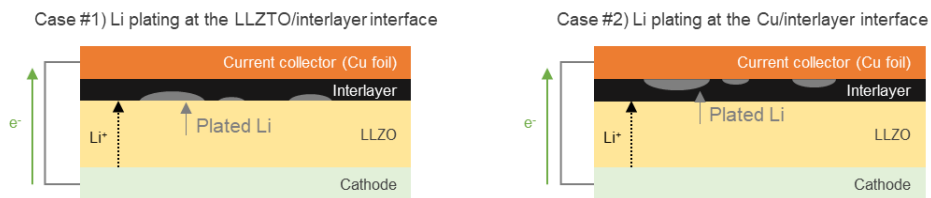


**Figure 4.4.** Schematic of lithium plating positions and the corresponding interfaces used for interfacial energy calculations. Case #1 describes lithium plating at the interlayer/solid-electrolyte interface. Lithium-metal plating between the solid electrolyte and the interlayer, which are in direct contact, does not prevent lithium-metal penetration into the electrolyte. In contrast, when lithium is plated between the current collector and the interlayer, as shown in Case #2, the interlayer effectively prevents direct contact of the lithium metal and the solid electrolyte.

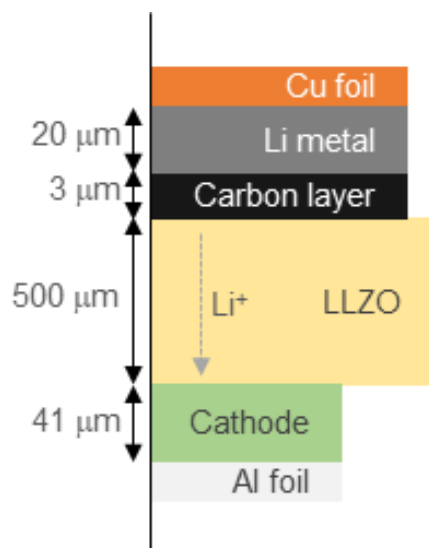


**Figure 4.5.** The geometry of the model structure mimicking the experimental cell configuration.

Parameter	Value	Description
$i_{app}$	2 mA cm <sup>-2</sup>	Current density for charge and discharge
$\sigma_{SE}$	0.8 mS cm <sup>-1</sup>	Li ion conductivity of the solid electrolyte
$D_{Li,C}$	10 <sup>-10</sup> cm <sup>2</sup> s <sup>-1</sup>	Li ion diffusivity in carbon
$D_{Li,self}$	5.79·10 <sup>-11</sup> cm <sup>2</sup> s <sup>-1</sup>	Self-diffusivity of Li in Li metal
$R_{anode}$	15 $\Omega$ cm <sup>2</sup>	Interfacial resistance at the anode
$V_{cutoff}$	2.8–4.3 V	Cutoff voltage for charge and discharge

**Table 4.1.** Parameters related to the electrochemical reaction simulation

## 4.3. Results and Discussion

### 4.3.1. Material selection through thermodynamic calculations

In designing the optimal interlayer, several criteria were established considering the underlying mechanisms of short-circuit formation in the cell, as illustrated in Figure 4.1. We reasoned that the interlayer should be able to (1) provide an intimate contact both with the LLZO electrolyte and lithium metal, (2) act as a buffer layer for lithium redistribution to mitigate current inhomogeneity at the interface, and (3) sustain its physical and chemical stability guiding the lithium deposition during the long-term cycling. Given with these criteria, the suitability of several candidate materials was first screened based on their thermodynamic preferences with respect to the position of lithium plating at the interface (*i.e.*, between current collector (copper) and LLZO (case #1) vs. between interlayer and LLZO (case #2)), as illustrated in Table 4.2. The preferential position of lithium was determined by comparing the interfacial energies of respective copper/interlayer/LLZO systems from DFT calculations (see section 4.2.4 and Figure 4.4 for details). Table 4.2 compares the interfacial energies of candidate interlayer materials in these two cases. It indicates that the lithium metal plating can occur preferentially either at the interlayer/current collector or interlayer/LLZO interface depending on the interlayer species. With a tungsten interlayer applied, lithium metal was predicted to be plated between the electrolyte and the interlayer, which infers the likelihood of the detachment of the tungsten interlayer from the LLZO. On the other hand, interlayer candidates such as LiF, Ag, Au, Si, and carbon could help on the preferential lithium plating toward the current collector, indicating the morphological stability.

Metallic interlayers such as Ag, Au and Si were, however, found to undergo substantially large volume change upon contact with lithium metal along with the potential risk of the dilution in the lithium matrix, indicating that they would not retain their original morphology after repetitive lithium plating and stripping (Figure 4.6).<sup>5,57,58</sup> Furthermore, LiF, which could be applied as a viable interlayer material to passivate the LLZO electrolyte<sup>13,59-61</sup>, exhibit substantially lower lithium-ion conductivity ( $\sim 10^{-11}$  S/cm) than that of LLZOs<sup>3,62,63</sup>. It implies that LiF interlayer may exacerbate the imbalance of the lithium-ion flux distribution at the interface, thus was excluded. On the other hand, carbon-based material preliminarily satisfies all the criteria mentioned above, and was considered as one of the most suitable candidates. It was predicted that it would induce the lithium metal to plate preferentially between the interlayer and current collector, and provide sufficiently high ionic conductivities to enable fast redistribution of lithium ions through interlayers.<sup>64</sup> Additionally, unlike alloying compounds, the morphology of interlayers is not likely to change significantly as the lithium uptake by carbon involves intercalation/de-intercalation or adsorption/desorption,<sup>65</sup> which accompanies only marginal volume change. Indeed, recent investigations have shown the promise of several carbonaceous materials as a stable interlayer between lithium metal anodes and solid electrolytes,<sup>27,66</sup> while the underlying mechanism has not been fully elucidated, and its application to the full-cell employing commercial-level cathodes has yet to be examined.

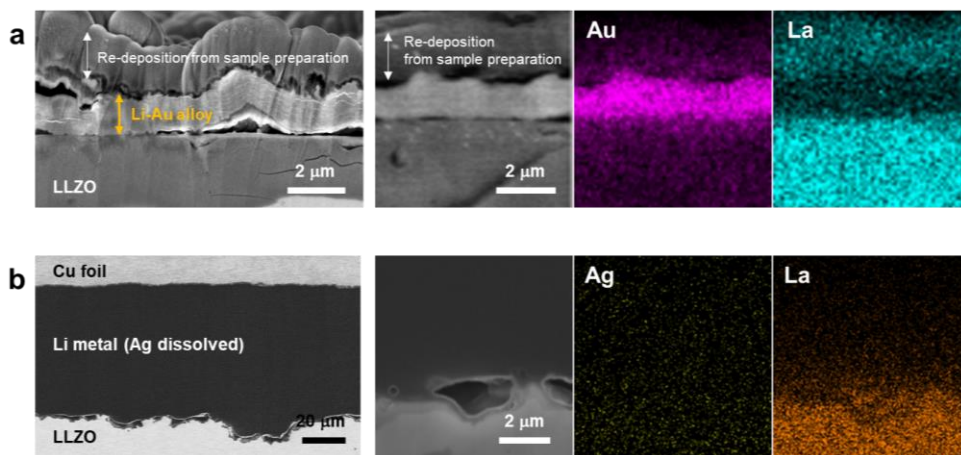
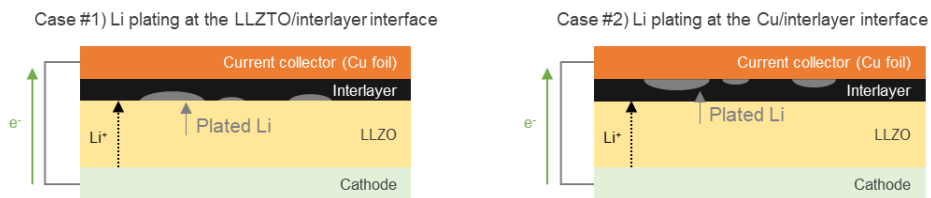


**Figure 4.6.** Cross-sectional SEM and EDS images of anode/LLZO electrolyte interfaces showing the instability of metal interlayers. (a) Volume expansion of gold interlayer after the lithium plating with alloying reaction. Initially 100 nm-thick gold layer was deposited by RF sputtering<sup>5</sup> on the one side of LLZO electrolyte, and lithium of  $0.5 \text{ mAh cm}^{-2}$  was electrochemically deposited to gold layer. It is shown that the thickness of lithiated gold interlayer increased to over  $1 \text{ }\mu\text{m}$  due to the volume expansion accompanying the alloying reaction, causing the interlayer detachment from LLZO electrolyte. (b) Dissolution of silver interlayer into lithium metal. The images show the cross section of LLZO electrolyte/lithium metal interface of a hybrid solid-state lithium cell employing NCA111 cathode ( $3.2 \text{ mAh cm}^{-2}$ ), which initially included a 30 nm-thick silver interlayer at the interface, after 20 cycles at  $0.6 \text{ mA cm}^{-2}$  at  $25 \text{ }^{\circ}\text{C}$ . Due to the chemical interdiffusion of silver and lithium, causing a dilution of silver into lithium metal, silver is barely detected at the interface. Beside, voids are observed at the interface as anticipated in the interface of LLZO/bare lithium metal, which indicates the loss of the silver interlayer role.





Interlayer material	Calculated interface energy		Preferential behavior	Volume expansion
	Case #1 <sup>i)</sup>	Case #2 <sup>ii)</sup>		
	(Collector/interlayer) + (Li/LLZO)	(Collector/Li) + (interlayer/LLZO)		
LiC <sub>6</sub> (001)	(-0.554) + (-0.708) = -1.362 J m <sup>-2</sup>	(-1.485) + (-0.354) = -1.839 J m <sup>-2</sup>	Case #2	+11 %
W (110)	(-3.363) + (-0.708) = -4.071 J m <sup>-2</sup>	(-1.485) + (-2.002) = -3.487 J m <sup>-2</sup>	Case #1	
LiF (001)	(-0.716) + (-0.708) = -1.424 J m <sup>-2</sup>	(-1.485) + (-0.781) = -2.266 J m <sup>-2</sup>	Case #2	0 %
Li <sub>3</sub> Au (001)	(-1.555) + (-0.708) = -2.263 J m <sup>-2</sup>	(-1.485) + (-1.296) = -2.781 J m <sup>-2</sup>	Case #2	+245 %
Li <sub>9</sub> Ag <sub>4</sub> (001)	(-1.373) + (-0.708) = -2.081 J m <sup>-2</sup>	(-1.485) + (-1.353) = -2.838 J m <sup>-2</sup>	Case #2	+211 %
Li <sub>5</sub> Si <sub>2</sub> (001)	(-1.319) + (-0.708) = -2.027 J m <sup>-2</sup>	(-1.485) + (-1.286) = -2.771 J m <sup>-2</sup>	Case #2	+133 %

i) Case #1) Li plating between LLZO and the interlayer

ii) Case #2) Li plating between the current collector and the interlayer

**Table 4.2.** Calculated interfacial energies according to the lithium plating position and interlayer materials (see section 4.2.4 and Figure 4.4 for details).

### 4.3.2. Kinetics of lithium precipitation and the strategy to guide lithium plating

Among various carbonaceous materials, graphitic and amorphous carbon types were investigated as model systems in this study. These two types of carbon were particularly selected as they can help unravel the relationships among carbon crystallinity, lithium transport property and plating behavior.<sup>65,67</sup> The carbon interlayers were prepared by casting/drying of the slurry of carbon powder and polyvinylidene fluoride binder (93:7 w/w) dispersed in N-Methyl-2-pyrrolidone (NMP) with approximately 3  $\mu\text{m}$  of thickness (Figure 4.2). In order to examine the lithium plating behavior through the carbon layer, an asymmetric half-cell was first prepared using lithium metal, LLZO pellet and the current collector coated with the carbon interlayer assembled under 250 MPa using cold isostatic press. In this electrochemical system, lithium was electrochemically stripped out from the lithium metal electrode and re-deposited onto the opposite lithium-free electrode with the interlayer (Figure 4.3). Figure 4.7 illustrates the cross-sectional scanning electron microscopy (SEM) images of the interfaces with the energy dispersive X-ray spectroscopy (EDS) mapping after the lithium deposition on the interlayer-coated electrode. The electrochemical deposition was conducted at an elevated temperature (100 °C), a temperature at which the kinetic barrier can become sufficiently low, thereby enabling to verify the preferential lithium deposition positions as suggested from the interfacial energy calculations in Table 4.2. The figure clearly depicts that lithium was plated preferentially between the carbon interlayer and the current collector regardless of the type of carbon, as indicated by the arrows and dashed lines on the left and right panel, respectively. This is in agreement with our theoretical

predictions from DFT calculations, and supports the validity of selecting the interlayer materials based on the preferential lithium deposition position.

However, we found that lowering the operation temperature can significantly randomize the preferential lithium deposition positions. As presented in Figure 4.8, the lithium metal was plated not only between the carbon and the current collector but also between the LLZO electrolyte and the carbon, notably deteriorating the original morphology of the carbon interlayer. This tendency was more pronounced for the graphite layer than the amorphous carbon layer. The discrepancy of the results at the low temperature strongly suggests that there is a competition between the thermodynamic-driven deposition preference and the lithium transport kinetics through the carbon interlayer. Since the lithium transport through the interlayer can become sluggish at lower temperatures (25 °C), the lithium plating at the remote positions may be kinetically hindered despite the energetic preference, making a randomized lithium deposition behavior. This speculation could be further supported by the similar experiment at 60 °C, at which the kinetics of lithium transport can be slightly more facile, as shown in Figure 4.9. At 60 °C, it was observed that the lithium metal could be readily precipitated at the carbon interlayer/current-collector interface particularly for the amorphous carbon interlayer as in the case of 100 °C, confirming that the irregular lithium deposition was caused by the low temperature. Nevertheless, it was also noted that the lithium plating still partially occurred at the interlayer/LLZO electrolyte interface with the graphite case even at 60 °C, inferring that the intrinsic lithium diffusion property of the carbon may have a substantial influence. The aligned graphitic interlayer along the interface would not be favorable for the vertical lithium transport through the interlayer owing to the two-dimensional

nature of lithium diffusion in graphite, which contrasts to the amorphous carbon with the non-directional lithium diffusion property. This difference in the lithium transport would be also reflected in the high-current operation performance of the electrochemical system, as will be discussed further in detail later. Additionally, we could verify that the sluggish lithium nucleation kinetics was partly responsible for the randomized lithium deposition at the low temperature. In our comparative experiment, it was found that the preferential lithium deposition can be noticeably promoted even at the low temperature if a thin seed layer of lithium metal is simply added between the current collector and the interlayer (see Experimental section and Figure 4.3 for details). Figure 4.10 illustrates the cross-sectional SEM images of the sample with the thin seed layer inserted for the two cases of carbon interlayers. It evidently demonstrates that the lithium plating takes place onto the pre-existing lithium metal upon the electrochemical bias even at 25 °C regardless of the type of carbon, indicating that the absence of the nucleation step kinetically helps on the lithium precipitation at the thermodynamically favorable sites.<sup>68</sup>

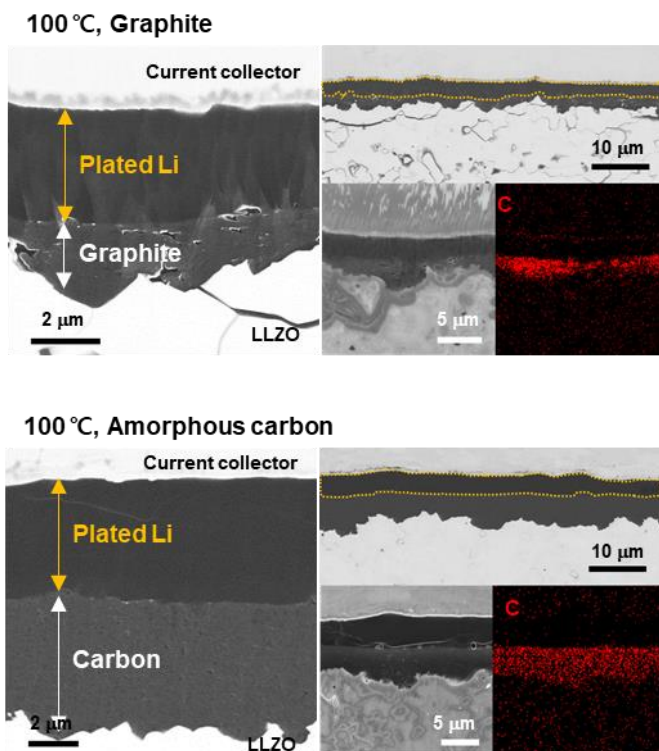


**Figure 4.7.** Cross-sectional SEM and EDS images of the LLZO solid electrolyte/anode interfaces after electrodeposition of lithium at various magnification scales to the (top) graphite layer and (bottom) amorphous carbon layer at 100 °C.

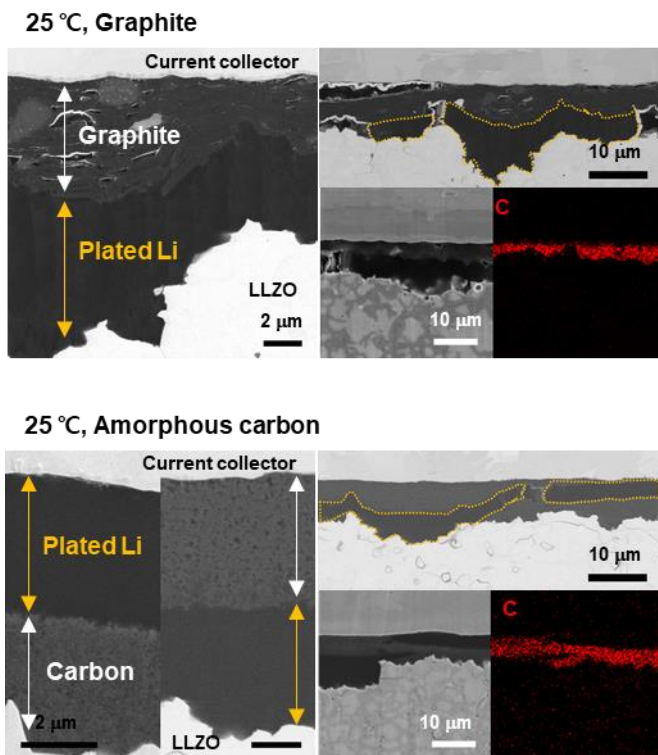
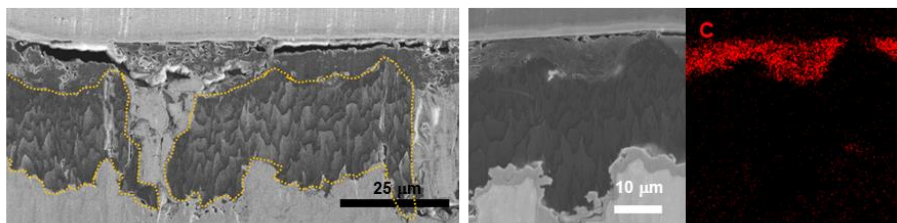


**Figure 4.8.** Cross-sectional SEM and EDS images of the LLZO solid electrolyte/anode interfaces after electrodeposition of lithium at various magnification scales to the (top) graphite layer and (bottom) amorphous carbon layer at 25 °C.

60 °C, Graphite



60 °C, Amorphous carbon

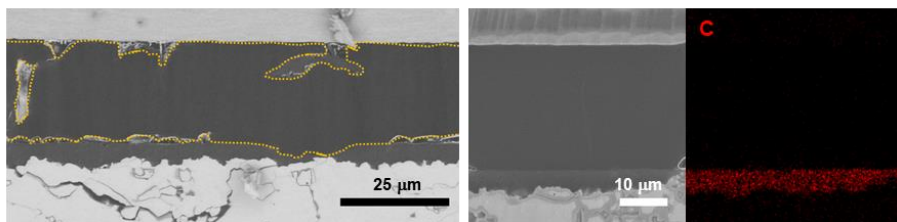


**Figure 4.9.** Cross-sectional SEM and EDS images of the LLZO solid electrolyte/anode interfaces after electrodeposition of lithium at various magnification scales to the (top) graphite layer and (bottom) amorphous carbon layer at 60 °C.

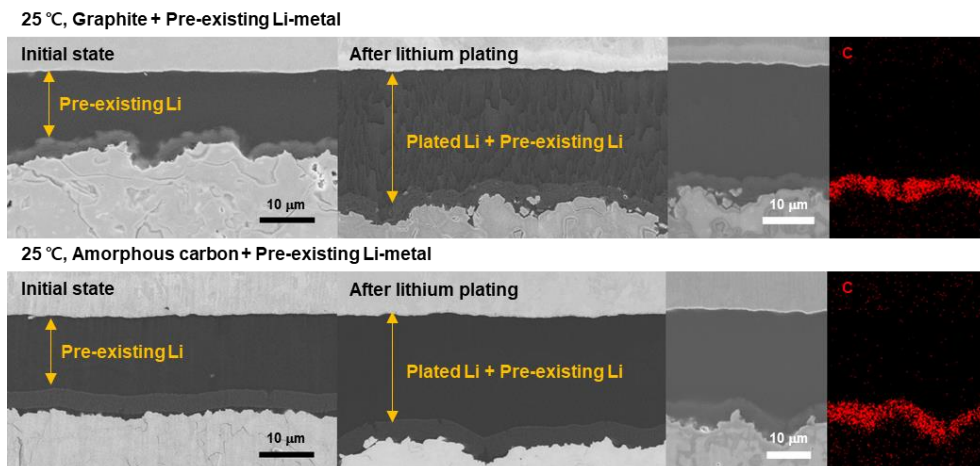


**Figure 4.10.** Cross-sectional SEM and EDS images of the LLZO solid electrolyte/anode interfaces after electrodeposition of lithium at various magnification scales through the (top) graphite interlayer or (bottom) amorphous carbon interlayer with the pre-existing lithium metal at 25 °C.



### 4.3.3. Influence of the carbon interlayer on cell performance

Inspired by the stability of the carbon-interlayer at the interface, a series of lithium cells were assembled using NCA811 ( $\text{LiNi}_{0.8}\text{Co}_{0.1}\text{Al}_{0.1}\text{O}_2$ ) cathodes (with a capacity of  $5.1 \text{ mAh cm}^{-2}$  at  $25^\circ\text{C}$ ) and lithium metal anodes with graphite or amorphous carbon interlayer placed on LLZO electrolyte in comparisons to a bare lithium metal anode. The NCA811 cathode was soaked with a drop of liquid electrolyte for the cathode interface, whereas the lithium metal anode was interfaced only with the LLZO solid electrolyte with or without carbon interlayer. Figure 4.11 comparatively presents the charge/discharge curves of the hybrid solid-state cells without and with interlayer, respectively, cycled at increasing current densities from  $0.5$  to  $2.5 \text{ mA cm}^{-2}$ . It is observed that the NCA811/LLZO/Li cell without the interlayer exhibits a characteristic voltage profile of NCA811 at a relatively low current density ( $0.5 \text{ mA cm}^{-2}$ ), however, the polarization gets notably greater with a higher current density of  $0.8 \text{ mA cm}^{-2}$ , and it short-circuits at  $1.0 \text{ mA cm}^{-2}$ , which agrees with the previous observations.<sup>44,45</sup> On the other hand, the presence of the carbon interlayer allows a successful operation of the cell at considerably higher current densities. The cell with the graphite interlayer (green lines in Figure 4.11b) could sustain the current density of  $1.6 \text{ mA cm}^{-2}$ , delivering a reversible capacity of approximately  $4 \text{ mAh cm}^{-2}$ , while a higher current operation at  $2 \text{ mA cm}^{-2}$  caused a cell failure. More remarkable is that the employment of the amorphous carbon interlayer in the NCA811/LLZO/Li cell could further improve the cell stability. As presented with the blue lines in Figure 4.11b, the cells were capable of delivering appreciable capacities without cell failure at increasing rates from  $0.5$  to  $2.5 \text{ mA cm}^{-2}$ . Short-circuit signals such as voltage noise and/or sudden drop were not observable at a current density of as high as  $2.5$

mA cm<sup>-2</sup>, exhibiting 70 % retention of the initial capacity (5.2 mAh cm<sup>-2</sup>) at 0.5 mA cm<sup>-2</sup>. The cell could also display the extended cycle stability, as shown in Figure 4.12, at 2.5 mA cm<sup>-2</sup>, which did not exhibit any noticeable capacity degradations over 80 cycles.

It is noteworthy that the cells with the interlayer exhibited slightly different capacities and stabilities depending on the carbon types, *e.g.*, the graphite interlayer cell delivered lower capacities (4.4 mAh cm<sup>-2</sup> at 0.8 mA cm<sup>-2</sup>, 4.2 mAh cm<sup>-2</sup> at 1.0 mA cm<sup>-2</sup>, and 3.3 mAh cm<sup>-2</sup> at 1.6 mA cm<sup>-2</sup>) than the cell with the amorphous interlayer (5.0 mAh cm<sup>-2</sup> at 0.8 mA cm<sup>-2</sup>, 4.9 mAh cm<sup>-2</sup> at 1.0 mA cm<sup>-2</sup>, and 4.3 mAh cm<sup>-2</sup> at 1.6 mA cm<sup>-2</sup>), and, more importantly, showed the earlier short-circuit formation at 2.0 mA cm<sup>-2</sup>. We found that the difference in the performance was primarily caused by the durability of the carbon interlayer upon the repeated lithium stripping and deposition processes, similar to the observations in the half-cell experiments in Figure 4.7-4.10. Figure 4.13 illustrates a series of cross-sectional images of the NCA811/LLZO/Li cell with the graphite interlayer after the shortage, probing the interfacial region of LLZO/Li. Figure 4.13a clearly depicts that the lithium metal has penetrated through the LLZO electrolyte (as indicated with a black arrow), causing the breakdown of the LLZO pellet. A closer view of this region (dotted line box) in Figure 4.13b reveals that the lithium metal penetration into the electrolyte was linked with the lithium plating between the graphite interlayer and the LLZO electrolyte, which caused the direct contact between the lithium deposits and the LLZO electrolyte. It suggests that the insufficient lithium transport property at this high current density could not guarantee the preferential lithium deposition at the interface of LLZO/interlayer, which is consistent with the observations of the

kinetic limitations at the low temperature in Figure 4.8. It was further observed that voids were formed at the graphite interlayer/lithium metal interface as shown in Figure 4.13c and Figure 4.14, confirming the sluggish lithium transport through the graphite interlayer. Since the void formation is known to be related to the lithium stripping behavior<sup>20,21</sup>, it infers that the lithium transport through the interlayer, depending on the type of carbon, also influences the lithium stripping behavior as well as the lithium plating behavior, and eventually affects the cell performances.

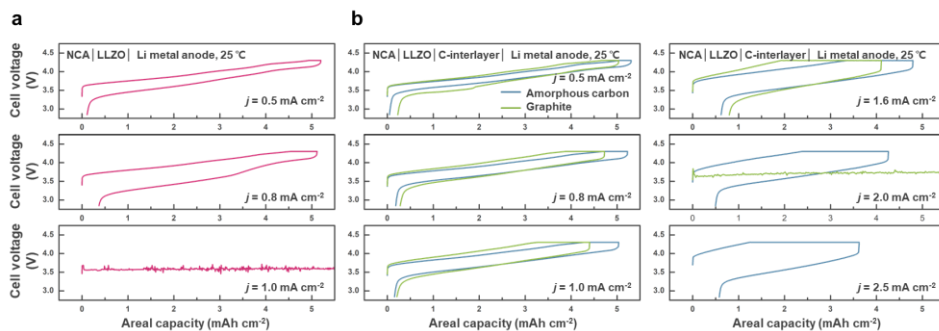


**Figure 4.11.** Electrochemical performance of hybrid solid-state battery cells using garnet-type solid electrolytes and lithium-metal anodes (a) without and (b) with carbon interlayers, showing the significant differences in results due to the presence of the interlayer and the type of carbon.

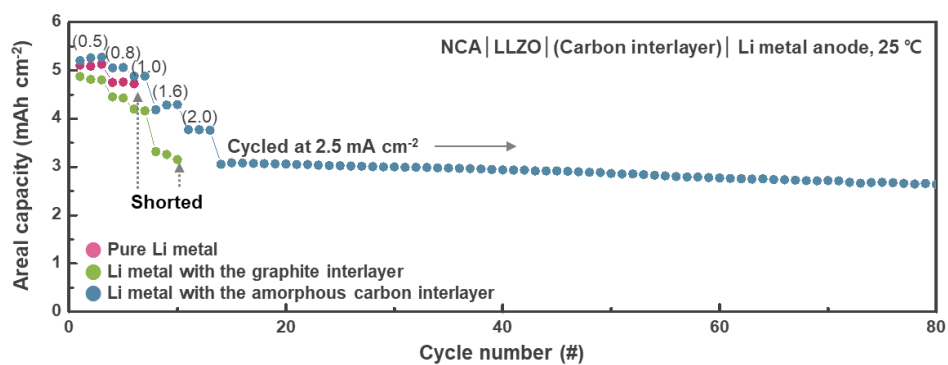


**Figure 4.12.** Rate and cycle performances of hybrid solid-state battery cells using garnet-type solid electrolytes and lithium-metal anodes without and with carbon interlayers, showing the significant differences in results due to the presence of the interlayer and the type of carbon.

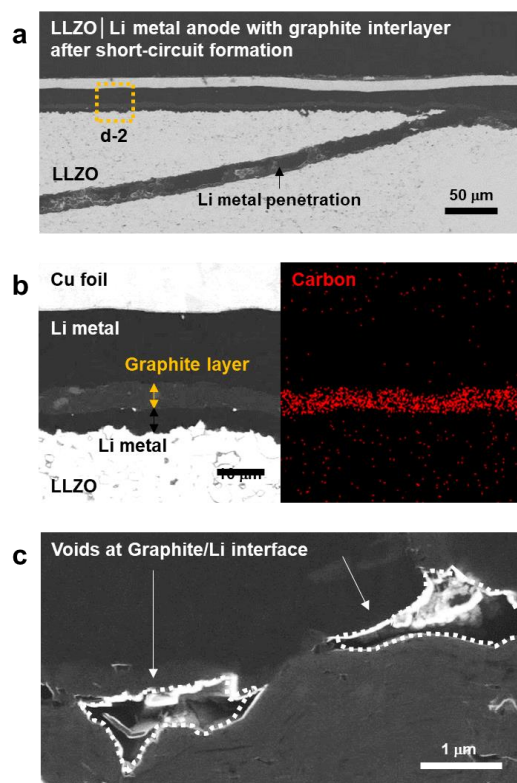


**Figure 4.13.** Cross-sectional SEM and EDS images recorded after the failure of a cell with a graphite interlayer. Lithium metal was plated between the interlayer and the solid electrolyte causing lithium penetration; voids were observed at the graphite layer/lithium metal interface.

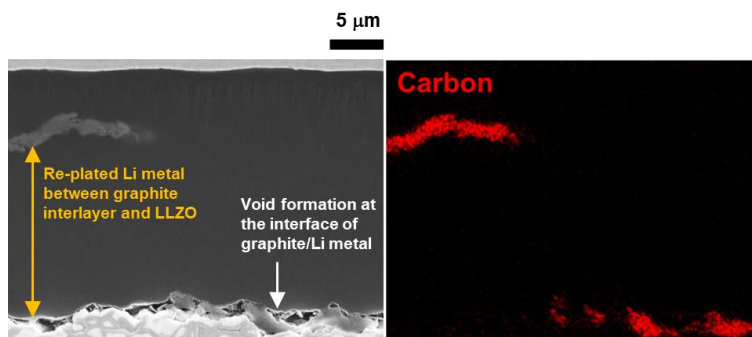


**Figure 4.14.** Cross-sectional SEM and EDS images recorded after the failure of the cell with a graphite interlayer shown in Figure 4.13c. Lithium metal was plated between the interlayer and the solid electrolyte, causing the rupture of the interlayer, and voids were observed at the graphite layer/lithium metal interface.

#### 4.3.4. Lithium stripping through the interlayer and the orientation of lithium transport pathways

In order to further elucidate the influence of the type of carbon in the interlayer, the kinetics of lithium transport through each interlayer was investigated regarding the lithium stripping process in the asymmetric half-cell (Figure 4.3). Figure 4.15 shows the overall voltage response curves of the lithium metal electrodes with the graphite or amorphous interlayer during lithium stripping under the same conditions ( $0.3 \text{ mA cm}^{-2}$  at  $25^\circ\text{C}$ ) as a function of the amount of lithium stripped. Each curve was recorded over a series of current pulses (5 minutes each) and rest periods (115 minutes); the magnitude of the vertical line in cell voltage is the overpotential measured during the rest, which accounts for the resistance increase of the cell.<sup>50</sup> Notably, the cell with the graphite interlayer showed a significant increase in overpotential after  $\sim 0.5 \text{ mAh cm}^{-2}$  of lithium stripping, whereas the cell with the amorphous carbon interlayer showed a stable profile with a constantly low overpotential. A comparison of the electrochemical impedance spectroscopy (EIS) results before and after lithium stripping (Figure 4.15 right and Figure 4.16) indicated the increase is mainly attributed to the change in the interfacial resistance, and it is particularly greater in the cell with the graphite interlayer (from  $0.4 \text{ } \Omega \text{ cm}^2$  to  $60.8 \text{ } \Omega \text{ cm}^2$ ) than the case with the amorphous carbon, suggesting the deterioration of the graphite interface. The change in the impedance could be more clearly visualized from the galvanostatic electrochemical impedance spectroscopy (GEIS), which displays the real-time development of the interfacial resistance with the progress of stripping.<sup>44</sup> As shown in Figure 4.17 and Figure 4.18, the interfacial



resistance gets gradually larger in the cell containing the graphite interlayer with the progress of lithium stripping (Figure 4.15), and almost divulges at a higher degree of the stripping. It contrasts to a negligible change detected in the cell with the amorphous carbon interlayer.

The increase in the electrochemical impedance was observed to be coupled with the delamination of the interlayer, as validated with an SEM analysis in Figure 4.19. The figures illustrate the cross-sectional images of the interfaces of the solid electrolyte and the lithium metal anode with the graphite (Figure 4.19a) or the amorphous carbon (Figure 4.19b) interlayers after the stripping (left-hand-side images) and the subsequent lithium plating (right-hand-side images). We found that a large gap was generated after the lithium stripping at the graphite interlayer/lithium metal interface, which was extensively observed throughout the sample. It is generally known to be detrimental, inhibiting the effective lithium transport, and substantially increases the cell resistance, in a remarkable consistency with the observations in the EIS analysis. On the other hand, the interfaces formed by the amorphous carbon interlayer at LLZO/interlayer/lithium maintained the intimate physical contact throughout the stripping process. Moreover, it was observed that the subsequent lithium plating could be considerably affected by the distinct stripping behaviors of the two cases. The right-hand-side image of Figure 4.19a shows that the redeposition of lithium takes place primarily at the interface between the LLZO and the graphite layer due to the presence of the gap that disconnects the current collector, which further aggravates the delamination of the interlayer from the LLZO. On the contrary, in the cell with amorphous carbon interlayer, lithium could be re-plated on the pre-existing lithium metal through the interlayer, which continues to aid in the

preferential plating after lithium stripping due to its morphological stability.

We suppose that the distinct behaviors of the two interlayers are attributable to the different lithium transport pathways arising from the crystallographic characteristics of each material (Figure 4.20). Graphite is constructed by stackings of graphene basal planes, within which lithium ions diffuse *via* intercalation/de-intercalation mechanism.<sup>69</sup> This two-dimensional lithium transport behavior provides anisotropic pathways of lithium ions in the interlayer containing graphite platelets with the preferred orientations, as schematically illustrated in Figure 4.21. It may cause non-uniform current distribution at the graphite interlayer/lithium metal interface under kinetically challenging conditions such as at low temperature and high current-rates, which eventually leads to localized lithium stripping. On the other hand, amorphous carbon can offer the isotropic lithium transport pathways due to its highly disordered structure and the transport mechanisms involving surface adsorption/desorption and lithium cluster storage in nano-pores.<sup>65,67</sup> The three-dimensional lithium transport (without preference for a specific direction) would lead to a uniform current distribution through the amorphous carbon interlayer and at the interlayer/lithium metal interface. We could also confirm that this inhomogeneity of lithium transport is consistently observable in the measurements of apparent lithium diffusivities through each carbon interlayer. In Figure 4.22, the diffusion coefficients of lithium were estimated for each carbon layer during de-lithiation using a galvanostatic intermittent titration technique (GITT).<sup>50,51</sup> It presents that the lithium diffusivity in the graphite interlayer remains lower than that in the amorphous interlayer, contradictory to the higher intrinsic lithium diffusivity in graphite than in soft carbons or hard carbons.<sup>64</sup> It is because of the geometric texture of the graphite

interlayer with the preferred orientations of graphite platelets, and implies that the directionality of lithium transport in the interlayer can have a considerable effect on the overall performance. The influence of anisotropic lithium transport could be further validated by computational simulations, as shown in Figure 4.23 and 4.24. The continuum mechanics simulations (see section 4.2.4 and Figure 4.24) could analyze the spatial distribution of lithium concentration near the region of the interlayer and lithium-metal electrode during stripping process.<sup>70</sup> Considering the textured basal planes of the graphite,<sup>69</sup> the interfaces formed with the lithium metal or LLZO electrolyte were set to be partially activated/available for lithium transport. It illustrates that the lithium concentration evolves uniformly with the amorphous carbon interlayer, delivering a desired discharge capacity of  $5 \text{ mAh cm}^{-2}$  at  $2 \text{ mA cm}^{-2}$ , whereas inhomogeneous lithium distributions developed in the cell using the graphite interlayer with a limited capacity lower than  $1 \text{ mAh cm}^{-2}$  at the same current density. This result confirms that the non-uniform current distribution that arises from the anisotropic lithium transport in the interlayer can cause a detrimental effect on the cell performance.

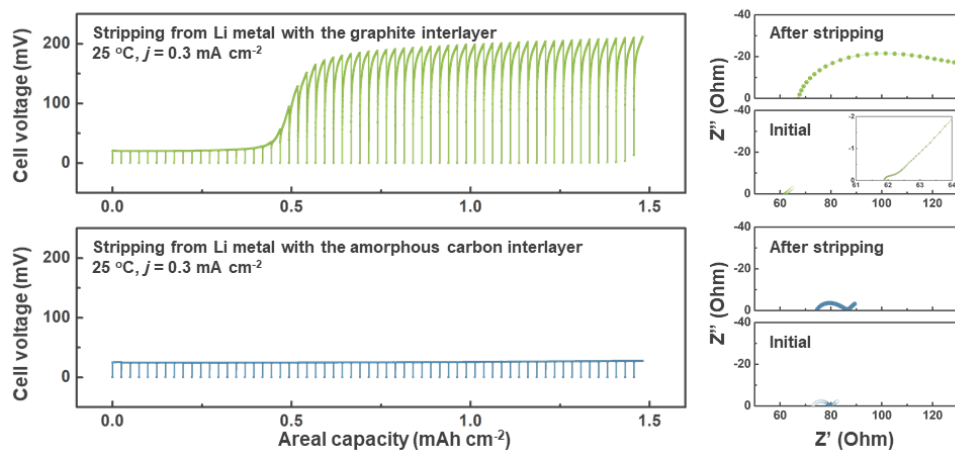


**Figure 4.15.** Voltage responses to the pulse currents as a function of the capacity during lithium stripping from the cell with (top) the graphite interlayer and (bottom) the amorphous carbon interlayer, and the EIS result of each cell before and after stripping.

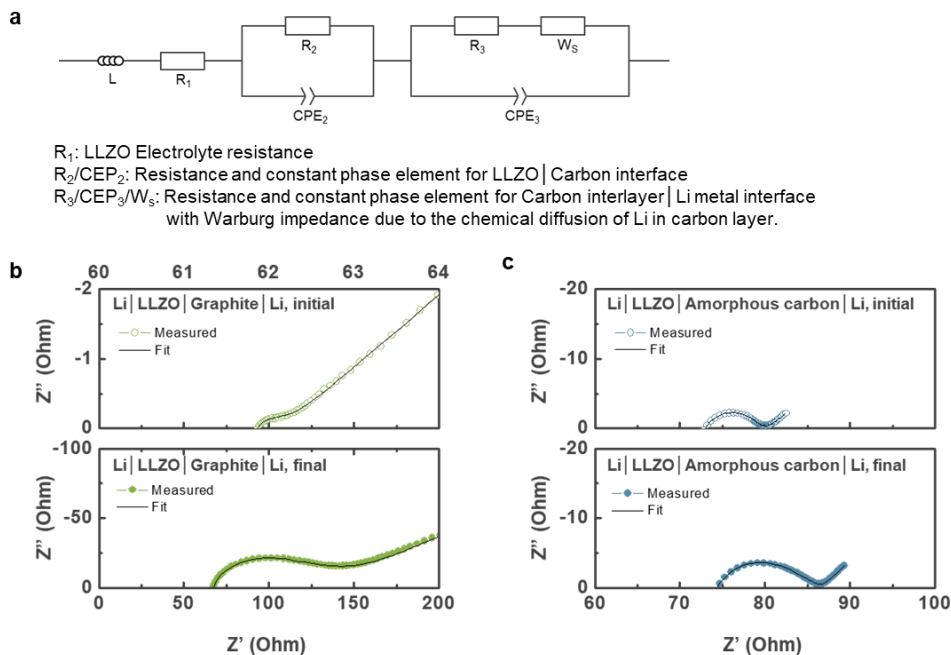


**Figure 4.16. Fitting results of EIS featured in Figure 4.15.** (a) Equivalent circuit used for fitting the EIS results shown in Figure 4.15.  $R_1$  at high frequency represents the resistance of LLZO solid electrolyte.  $R_2$ - $CPE_2$  and  $R_3$ - $CPE_3$ - $W_s$  circuits can be attributed to the interfacial responses.<sup>71-73</sup> Meanwhile, as Li metal counter electrode was attached by a high pressure of 250 MPa, the interfacial resistance at LLZO/Li metal interface was considered negligible as reported.<sup>44</sup> (b-c) Enlarged Nyquist plots of Figure 4.15 and the fitting results (the resistance and capacitance data in table) of cells using (b) the graphite interlayer and (c) the amorphous carbon interlayer before and after lithium stripping. The interfacial resistance at working electrode with the graphite interlayer increase notably (from 0.4  $\Omega$  to 64.0  $\Omega$ ), indicating the decrease in the contact area due to the lithium delamination from the graphite interlayer<sup>44</sup>, whereas the interfacial resistances and the capacitances from the cell with the amorphous carbon interlayer show the similar values.

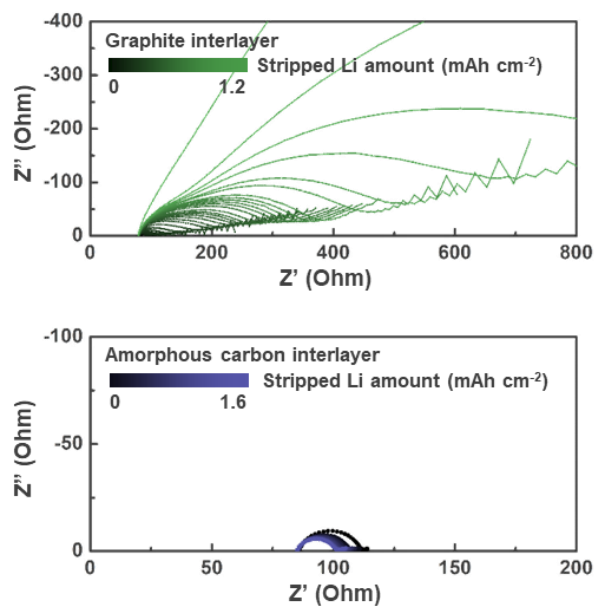


**Figure 4.17.** Nyquist representations of the impedance-spectra evolutions on lithium stripping from the lithium metal anode with (a) the graphite interlayer and (b) the amorphous carbon interlayer.

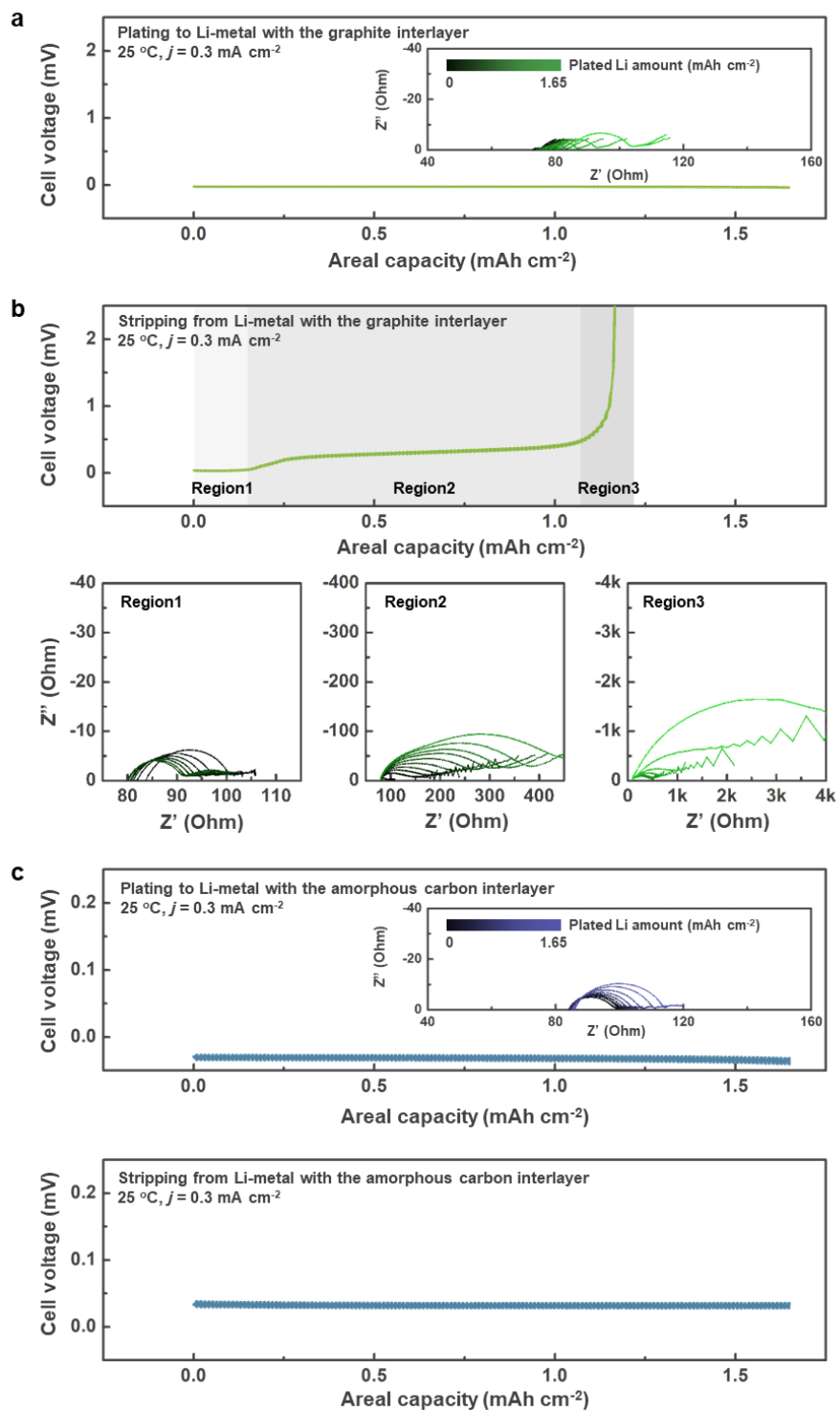


**Figure 4.18.** Detailed results of GEIS measurements using cells with graphite and amorphous-carbon interlayers. (a) Voltage profile of the cell with the graphite interlayer during lithium plating at  $0.3 \text{ mA cm}^{-2}$  and (inset graph) the evolution of EIS according to the amount of plated lithium amount (b) Voltage profile of the cell with the graphite interlayer during lithium stripping at  $0.3 \text{ mA cm}^{-2}$  and comparison of EIS (section-wise) according to the voltage change. (c) Voltage profile of the cell with the amorphous carbon interlayer during (upper) lithium plating and (lower) stripping at  $0.3 \text{ mA cm}^{-2}$ .



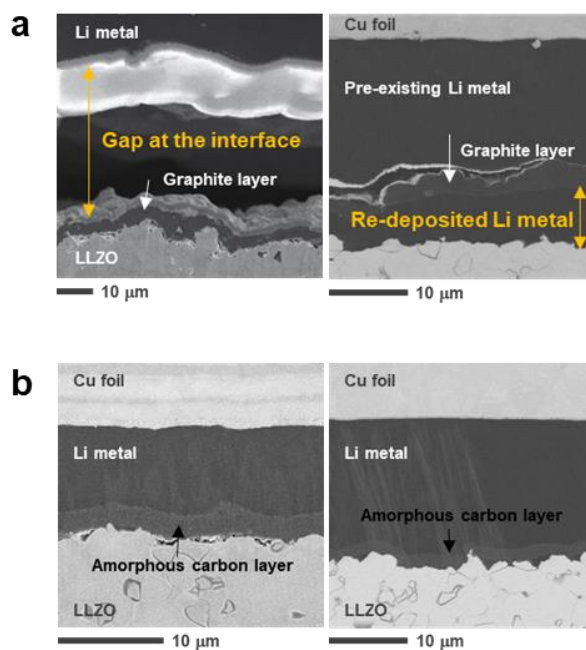


**Figure 4.19.** Cross-sectional SEM images of the LLZO solid electrolyte/lithium metal anode interface with (a) the graphite interlayer and (b) the amorphous carbon interlayer after lithium stripping and subsequent lithium plating.

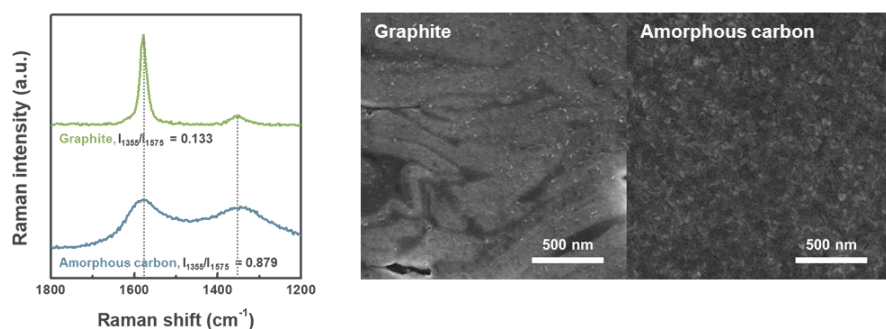


**Figure 4.20.** Crystallinities and morphologies of graphite and amorphous carbon. (a) Raman spectra. Raman spectra were collected using a Renishaw inVia<sup>TM</sup> Raman microscope with a 514 nm laser. The ratio of intensities at 1355 cm<sup>-1</sup> and 1575 cm<sup>-1</sup> Raman shift ( $I_{1355}/I_{1575}$ ), an indicator of the crystallinity of carbon materials,<sup>74</sup> indicates that the graphite used here has a higher crystallinity than the amorphous carbon. (b) Cross-sectional SEM images of the graphite and amorphous layers. Graphite particles have a plate-like shape and are aligned in the horizontal direction, whereas amorphous carbon contains very small spherical particles with no preferential orientation.

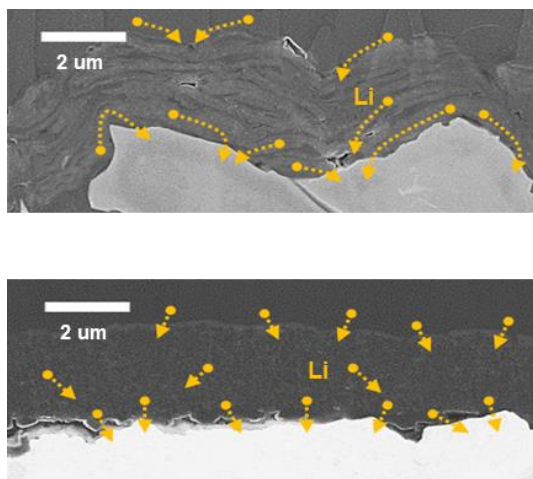


**Figure 4.21.** SEM images of the particles in each interlayer indicating the dependence of the local lithium transport pathway on the orientation of particle alignment and crystallites of carbon (top: graphite, bottom: amorphous carbon).

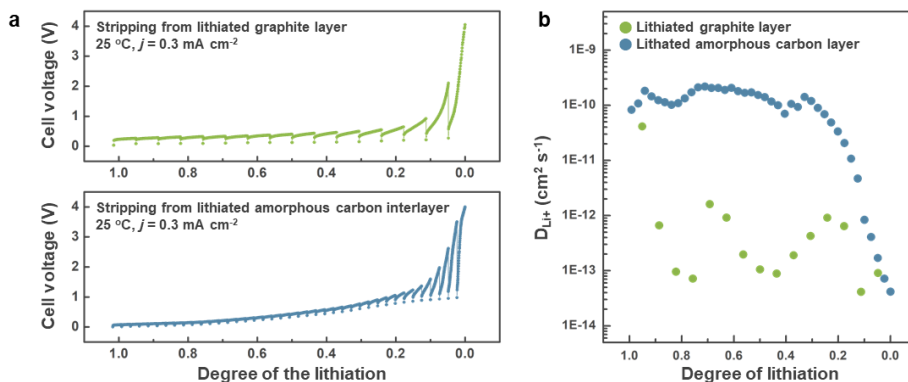


**Figure 4.22.** Apparent lithium diffusivities of the graphite and amorphous-carbon interlayers. (a) GITT profiles and (b) Calculated diffusion coefficients. (a) GITT profiles during de-lithiation of the lithiated graphite and amorphous carbon, along with their lithium contents. The cells with configuration of Cell#1 described in Figure 4.3 were prepared using graphite and amorphous carbon interlayer, and fully lithiated at 0.1 C-rate considering the amount and the capacity of each carbon interlayer. Then, GITT measurements with a de-lithiation current pulse at  $0.3 \text{ mA cm}^{-2}$  for 3 minutes and the rest period for 177 minutes were conducted. (b) The calculated lithium diffusivities from the graphite and amorphous-carbon layers. The lithium diffusivity in the amorphous carbon layer is higher than in the graphite interlayer, which is contradictory to the higher intrinsic lithium diffusivity in graphite than in soft carbons or hard carbons.<sup>64</sup>

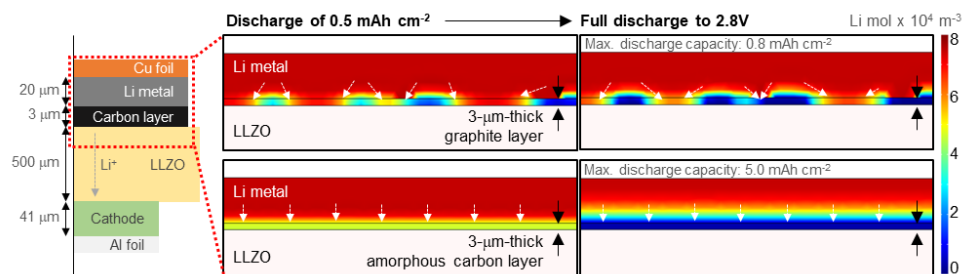


**Figure 4.23.** Simulation of the consequent lithium concentration distribution with the lithium diffusion pathways (white arrows) in the anode with (top) the graphite interlayer and (bottom) the amorphous carbon interlayer during lithium stripping (*e.g.*, discharging of the full cell with the configuration at the left side) at  $2 \text{ mA cm}^{-2}$ .

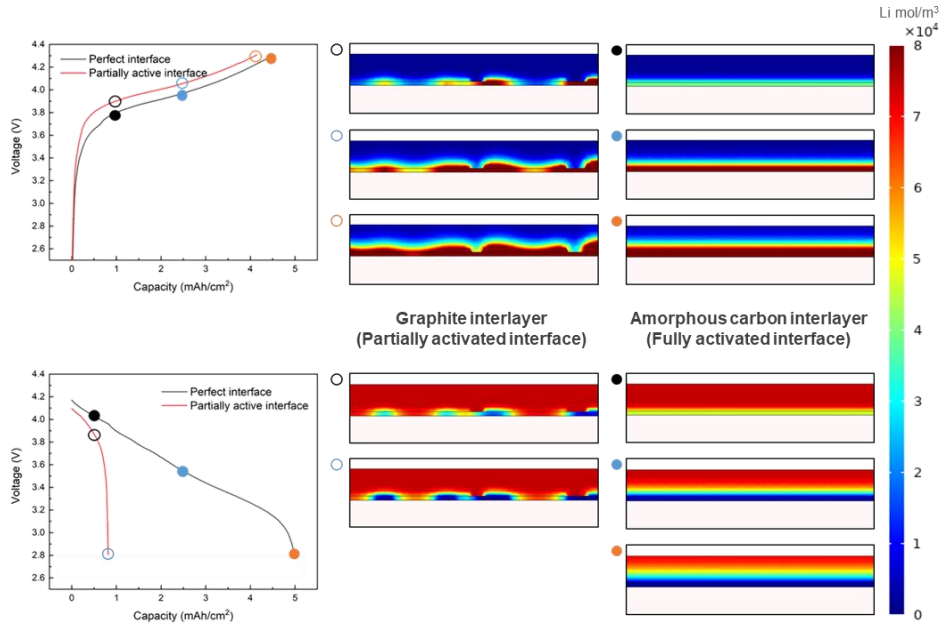


**Figure 4.24.** Simulation results of the lithium-concentration distribution in the lithium metal anode with graphite or amorphous carbon interlayer of cell with different state of (top) charging and (bottom) discharging.

#### **4.3.5. Optimization of amorphous carbon interlayer for LLZO electrolyte**

Based on the understandings of the lithium plating/stripping behaviors depending on carbon types, we further optimized the amorphous carbon interlayer for the enhanced lithium transport, and tested its applicability in the following. As the isotropic lithium transport in the carbon interlayer is important in the uniform current distribution, we adopted the amorphous carbon, of which the particle and crystallite size is smaller (Figure 4.25). Considering that lithium transport in amorphous carbon occurs through the surface interactions<sup>65,67</sup>, this small-sized amorphous carbon was expected to provide more effective lithium transport pathways. Accordingly, a portion of the small-sized carbon particles was added to the original amorphous carbon interlayer with the weight fraction of 25%, and a hybrid solid-state lithium cell was assembled employing NCA811 cathode. Figure 4.26 presents the electrochemical performance of the cell tested in the practical battery conditions of high current density ( $2.5 \text{ mA cm}^{-2}$ ) and areal capacity ( $5.1 \text{ mAh cm}^{-2}$ ) at CCCV (constant current and constant voltage) mode within 2.8-4.3 V region at 25°C (see Experimental section for details). The cell exhibits a remarkable cycling performance over 250 cycles at  $2.5 \text{ mA cm}^{-2}$  without significant capacity degradation or short-circuit failure, after the initial pre-cycles. The capacity retention is as high as 99.6 % after 250 cycles, presenting an extraordinarily high cycle stability. Moreover, the change in the electrochemical profiles was markedly small throughout the cycles, indicating the robustness of the cell. For comparisons with other solid-state cells employing LLZO electrolyte that have been reported, we plotted

performance map of solid-state lithium metal cells in terms of important practical parameters of current density and areal capacity in Figure 4.27. Notably, the state-of-the-art cell reported till date implements a cathode with an areal capacity less than  $1.0 \text{ mAh cm}^{-2}$ , which is not applicable for practical battery systems. On the other hand, our system adopts the cathode of  $5.1 \text{ mAh cm}^{-2}$  areal capacity, which meets the industrial standard. The cumulative lithium capacities were calculated and depicted in the inset of the graph, summing up the delivered capacity of the lithium metal anodes through the cycles in the full cells. It records  $1005 \text{ mAh cm}^{-2}$ , which are significantly higher than other reported values.<sup>26,27,29,37,45,75-82</sup> To the best of our knowledge, these are the highest values reported for solid-state lithium metal cells that were operated at  $25^\circ\text{C}$  employing garnet-type oxide electrolytes and lithium metal anodes. This outstanding performance demonstration is expected to pave a new pathway toward the development of practical-level all-solid-state-batteries, and highlights the importance of the interlayer design/stability not only ensuring the intimate contact but also regulating the lithium transport path in relation with the crystalline domain orientations for current re-distribution, thus warrants further future research.



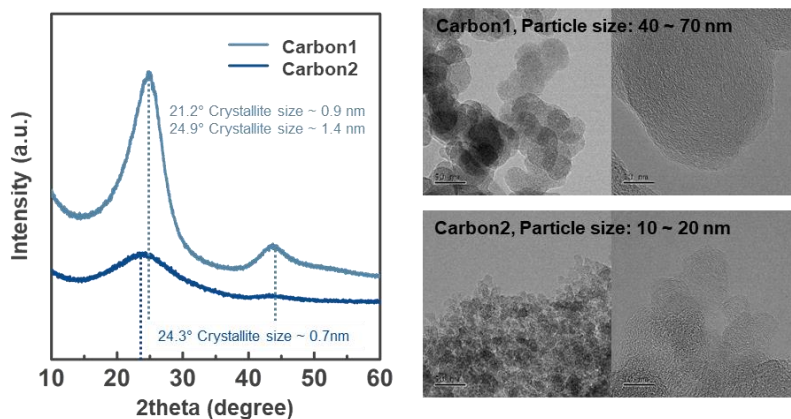


**Figure 4.25.** XRD patterns and TEM images of the amorphous carbon powder used for the optimal interlayer. The second carbon exhibits small crystallites ( $\sim 0.7$  nm) and particle size (10–20 nm), facilitating more isotropic lithium transport through the interlayer.

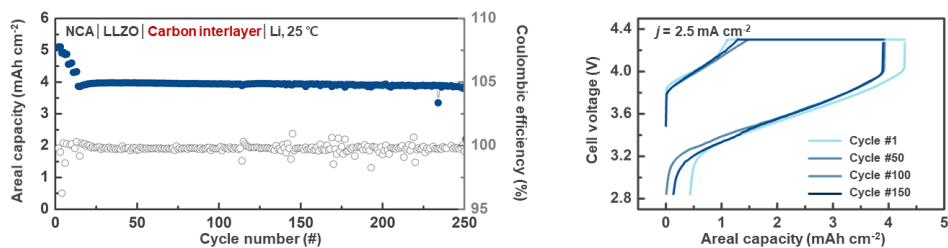


**Figure 4.26.** Long-term cycling performance of the NCA811/LLZO/amorphous carbon interlayer/lithium-metal cell. The cell maintained stable cycling performance over 250 cycles, generating  $4.0 \text{ mAh cm}^{-2}$  at  $2.5 \text{ mA cm}^{-2}$  without significant degradation of the capacity. Initial 13 pre-cycles were conducted at 0.5, 0.8, 1.0, 1.6 and  $2 \text{ mA cm}^{-2}$ , respectively, before cycling at  $2.5 \text{ mA cm}^{-2}$ .

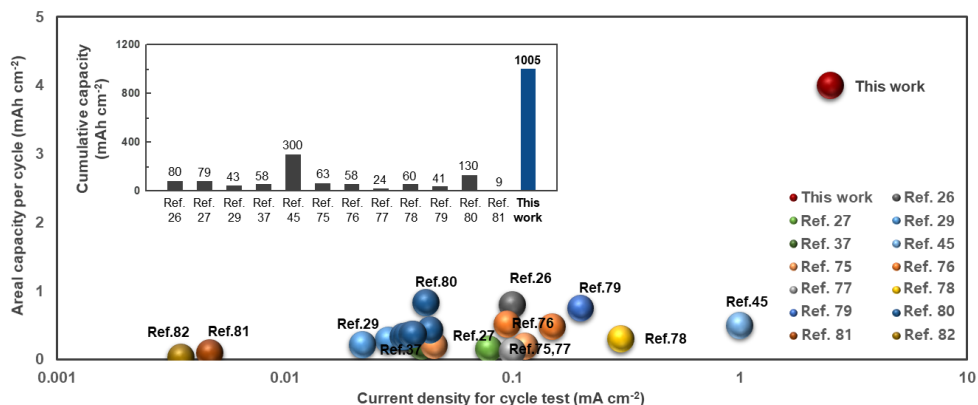


**Figure 4.27.** A performance comparison of solid-state batteries using garnet-type solid electrolytes and lithium-metal anodes. The plot summarizes the current densities ( $x$ -axis) and areal plating capacities of cathodes ( $y$ -axis) reported previously.<sup>26,27,29,37,45,75-82</sup> The inset graph compares the cumulative areal capacities of lithium plating (the number at the top of each bar) of full cells.

## 4.4. Conclusion

An optimal interlayer was introduced at the interface of a lithium metal anode and an LLZO solid electrolyte to construct a high-power solid-state lithium metal battery capable of stable room temperature operation. This interlayer was designed through a systematic investigation of the role of the interlayer on lithium plating/stripping behavior using theoretical and experimental analyses. Based on the thermodynamic properties of the candidate materials, a carbon-based material was selected as the most suitable material for an ideal interlayer, which can induce lithium plating between the current collector (copper) and the interlayer without significant physical/chemical changes. It was also shown that preferential lithium plating between the interlayer and the current collector can be effectively facilitated by the introduction of a thin seed layer of lithium metal, which can effectively lower the high kinetic energy barrier for lithium nucleation. Moreover, the critical impact of the crystalline orientation of the graphitic carbon on the stability of interlayer was elucidated by showing that the amorphous carbon interlayer, which can provide isotropic lithium transport (without preference for a specific direction), could maintain its original interlayer/lithium metal interface after the repeated lithium plating/stripping, in contrast to the case of the graphite interlayer. A full cell utilizing an optimal amorphous carbon interlayer presented excellent performance, with a cumulative lithium metal capacity of over  $1000 \text{ mAh cm}^{-2}$  at  $2.5 \text{ mA cm}^{-2}$  at room temperature. This is the first report of a potential high-power solid-state lithium metal battery at a commercial-level, successfully operating without short-circuiting, and validates the efficacy of the interlayer designing strategy described here.

Although other requirements such as fast and/or low-temperature charging should be further examined in the future, the findings in this study are expected to open new frontiers in the development of solid-state batteries by providing the critical keys to ensure the stable interface between lithium anode and the oxide-based electrolyte.

## 4.5. References

- 1 Janek, J. & Zeier, W. G. A solid future for battery development. *Nature Energy* **1**, 16141, doi:10.1038/nenergy.2016.141 (2016).
- 2 Manthiram, A., Yu, X. & Wang, S. Lithium battery chemistries enabled by solid-state electrolytes. *Nature Reviews Materials* **2**, 16103, doi:10.1038/natrevmats.2016.103 (2017).
- 3 Samson, A. J., Hofstetter, K., Bag, S. & Thangadurai, V. A bird's-eye view of Li-stuffed garnet-type  $\text{Li}_7\text{La}_3\text{Zr}_2\text{O}_{12}$  ceramic electrolytes for advanced all-solid-state Li batteries. *Energy & Environmental Science* **12**, 2957-2975, doi:10.1039/C9EE01548E (2019).
- 4 Sun, C., Liu, J., Gong, Y., Wilkinson, D. P. & Zhang, J. Recent advances in all-solid-state rechargeable lithium batteries. *Nano Energy* **33**, 363-386, doi:https://doi.org/10.1016/j.nanoen.2017.01.028 (2017).
- 5 Kim, S. *et al.* The Role of Interlayer Chemistry in Li-Metal Growth through a Garnet-Type Solid Electrolyte. **10**, 1903993, doi:https://doi.org/10.1002/aenm.201903993 (2020).
- 6 Kim, S. *et al.* High-energy and durable lithium metal batteries using garnet-type solid electrolytes with tailored lithium-metal compatibility. *Nature Communications* **13**, 1883, doi:10.1038/s41467-022-29531-x (2022).
- 7 Sharafi, A. *et al.* Surface Chemistry Mechanism of Ultra-Low Interfacial Resistance in the Solid-State Electrolyte  $\text{Li}_7\text{La}_3\text{Zr}_2\text{O}_{12}$ . *Chemistry of Materials* **29**, 7961-7968, doi:10.1021/acs.chemmater.7b03002 (2017).

- 8 Miara, L. J. *et al.* Effect of Rb and Ta Doping on the Ionic Conductivity and Stability of the Garnet  $\text{Li}_{7+2x-y}(\text{La}_{3-x}\text{Rb}_x)(\text{Zr}_{2-y}\text{Ta}_y)\text{O}_{12}$  ( $0 \leq x \leq 0.375$ ,  $0 \leq y \leq 1$ ) Superionic Conductor: A First Principles Investigation. *Chemistry of Materials* **25**, 3048-3055, doi:10.1021/cm401232r (2013).
- 9 Li, Y., Han, J.-T., Wang, C.-A., Xie, H. & Goodenough, J. B. Optimizing  $\text{Li}^+$  conductivity in a garnet framework. *Journal of Materials Chemistry* **22**, 15357-15361, doi:10.1039/C2JM31413D (2012).
- 10 Murugan, R., Thangadurai, V. & Weppner, W. Fast Lithium Ion Conduction in Garnet-Type  $\text{Li}_7\text{La}_3\text{Zr}_2\text{O}_{12}$ . **46**, 7778-7781, doi:10.1002/anie.200701144 (2007).
- 11 Zhu, Y., He, X. & Mo, Y. Origin of Outstanding Stability in the Lithium Solid Electrolyte Materials: Insights from Thermodynamic Analyses Based on First-Principles Calculations. *ACS Applied Materials & Interfaces* **7**, 23685-23693, doi:10.1021/acsami.5b07517 (2015).
- 12 Cheng, E. J., Sharafi, A. & Sakamoto, J. Intergranular Li metal propagation through polycrystalline  $\text{Li}_{6.25}\text{Al}_{0.25}\text{La}_3\text{Zr}_2\text{O}_{12}$  ceramic electrolyte. *Electrochimica Acta* **223**, 85-91, doi:https://doi.org/10.1016/j.electacta.2016.12.018 (2017).
- 13 Aguesse, F. *et al.* Investigating the Dendritic Growth during Full Cell Cycling of Garnet Electrolyte in Direct Contact with Li Metal. *ACS Applied Materials & Interfaces* **9**, 3808-3816, doi:10.1021/acsami.6b13925 (2017).
- 14 Sharafi, A., Meyer, H. M., Nanda, J., Wolfenstine, J. & Sakamoto, J. Characterizing the Li– $\text{Li}_7\text{La}_3\text{Zr}_2\text{O}_{12}$  interface stability and kinetics as a

- function of temperature and current density. *Journal of Power Sources* **302**, 135-139, doi:<https://doi.org/10.1016/j.jpowsour.2015.10.053> (2016).
- 15 Swamy, T. *et al.* Lithium Metal Penetration Induced by Electrodeposition through Solid Electrolytes: Example in Single-Crystal  $\text{Li}_6\text{La}_3\text{ZrTaO}_{12}$  Garnet. *Journal of The Electrochemical Society* **165**, A3648-A3655, doi:10.1149/2.1391814jes (2018).
  - 16 Porz, L. *et al.* Mechanism of lithium metal penetration through inorganic solid electrolytes. *Advanced Energy Materials* **7**, 1701003 (2017).
  - 17 Han, F. *et al.* High electronic conductivity as the origin of lithium dendrite formation within solid electrolytes. *Nature Energy* **4**, 187-196, doi:10.1038/s41560-018-0312-z (2019).
  - 18 Liu, X. *et al.* Local electronic structure variation resulting in Li ‘filament’ formation within solid electrolytes. *Nature Materials*, doi:10.1038/s41563-021-01019-x (2021).
  - 19 Tsai, C.-L. *et al.*  $\text{Li}_7\text{La}_3\text{Zr}_2\text{O}_{12}$  Interface Modification for Li Dendrite Prevention. *ACS Applied Materials & Interfaces* **8**, 10617-10626, doi:10.1021/acsami.6b00831 (2016).
  - 20 Krauskopf, T., Hartmann, H., Zeier, W. G. & Janek, J. Toward a Fundamental Understanding of the Lithium Metal Anode in Solid-State Batteries—An Electrochemo-Mechanical Study on the Garnet-Type Solid Electrolyte  $\text{Li}_{6.25}\text{Al}_{0.25}\text{La}_3\text{Zr}_2\text{O}_{12}$ . *ACS Applied Materials & Interfaces* **11**, 14463-14477, doi:10.1021/acsami.9b02537 (2019).
  - 21 Kasemchainan, J. *et al.* Critical stripping current leads to dendrite formation on plating in lithium anode solid electrolyte cells. *Nature*



- Materials* **18**, 1105-1111, doi:10.1038/s41563-019-0438-9 (2019).
- 22 Ning, Z. *et al.* Visualizing plating-induced cracking in lithium-anode solid-electrolyte cells. *Nature Materials*, doi:10.1038/s41563-021-00967-8 (2021).
- 23 Krauskopf, T., Richter, F. H., Zeier, W. G. & Janek, J. Physicochemical Concepts of the Lithium Metal Anode in Solid-State Batteries. *Chemical Reviews* **120**, 7745-7794, doi:10.1021/acs.chemrev.0c00431 (2020).
- 24 Koshikawa, H. *et al.* Dynamic changes in charge-transfer resistance at Li metal/  $\text{Li}_7\text{La}_3\text{Zr}_2\text{O}_{12}$  interfaces during electrochemical Li dissolution/deposition cycles. *Journal of Power Sources* **376**, 147-151, doi:https://doi.org/10.1016/j.jpowsour.2017.11.082 (2018).
- 25 Han, X. *et al.* Negating interfacial impedance in garnet-based solid-state Li metal batteries. *Nature Materials* **16**, 572, doi:10.1038/nmat4821 (2016).
- 26 Luo, W. *et al.* Reducing Interfacial Resistance between Garnet-Structured Solid-State Electrolyte and Li-Metal Anode by a Germanium Layer. *Advanced Materials* **29**, 1606042, doi:doi:10.1002/adma.201606042 (2017).
- 27 Shao, Y. *et al.* Drawing a Soft Interface: An Effective Interfacial Modification Strategy for Garnet-Type Solid-State Li Batteries. *ACS Energy Letters* **3**, 1212-1218, doi:10.1021/acsenenergylett.8b00453 (2018).
- 28 Luo, W. *et al.* Transition from Superlithiophobicity to Superlithiophilicity of Garnet Solid-State Electrolyte. *Journal of the American Chemical Society* **138**, 12258-12262, doi:10.1021/jacs.6b06777 (2016).
- 29 Huo, H. *et al.* In-situ formed  $\text{Li}_2\text{CO}_3$ -free garnet/Li interface by rapid acid

- treatment for dendrite-free solid-state batteries. *Nano Energy* **61**, 119-125, doi:https://doi.org/10.1016/j.nanoen.2019.04.058 (2019).
- 30 Ferraresi, G., Uhlenbruck, S., Tsai, C.-L., Novák, P. & Villevieille, C. Engineering of Sn and Pre-Lithiated Sn as Negative Electrode Materials Coupled to Garnet Ta-LLZO Solid Electrolyte for All-Solid-State Li Batteries. *Batteries & Supercaps* **3**, 557-565, doi: 10.1002/batt.201900173 (2020).
  - 31 Feng, W., Dong, X., Li, P., Wang, Y. & Xia, Y. Interfacial modification of Li/Garnet electrolyte by a lithiophilic and breathing interlayer. *Journal of Power Sources* **419**, 91-98, doi: 10.1016/j.jpowsour.2019.02.066 (2019).
  - 32 Feng, W. *et al.* Building an Interfacial Framework: Li/Garnet Interface Stabilization through a Cu<sub>6</sub>Sn<sub>5</sub> Layer. *ACS Energy Letters* **4**, 1725-1731, doi:10.1021/acsenerylett.9b01158 (2019).
  - 33 He, M., Cui, Z., Chen, C., Li, Y. & Guo, X. Formation of self-limited, stable and conductive interfaces between garnet electrolytes and lithium anodes for reversible lithium cycling in solid-state batteries. *Journal of Materials Chemistry A* **6**, 11463-11470, doi:10.1039/C8TA02276C (2018).
  - 34 Meng, J., Zhang, Y., Zhou, X., Lei, M. & Li, C. Li<sub>2</sub>CO<sub>3</sub>-affiliative mechanism for air-accessible interface engineering of garnet electrolyte via facile liquid metal painting. *Nature Communications* **11**, 3716, doi:10.1038/s41467-020-17493-x (2020).
  - 35 Wang, C. *et al.* Conformal, Nanoscale ZnO Surface Modification of Garnet-Based Solid-State Electrolyte for Lithium Metal Anodes. *Nano Letters* **17**, 565-571, doi:10.1021/acs.nanolett.6b04695 (2017).

- 36 Lou, J. *et al.* Achieving efficient and stable interface between metallic lithium and garnet-type solid electrolyte through a thin indium tin oxide interlayer. *Journal of Power Sources* **448**, 227440, doi: 10.1016/j.jpowsour.2019.227440 (2020).
- 37 Huo, H. *et al.* Design of a mixed conductive garnet/Li interface for dendrite-free solid lithium metal batteries. *Energy & Environmental Science* **13**, 127-134, doi:10.1039/C9EE01903K (2020).
- 38 Zhong, Y. *et al.* A Highly Efficient All-Solid-State Lithium/Electrolyte Interface Induced by an Energetic Reaction. *Angewandte Chemie International Edition* **59**, 14003-14008, doi: 10.1002/anie.202004477 (2020).
- 39 Baniya, A. *et al.* Mitigating Interfacial Mismatch between Lithium Metal and Garnet-Type Solid Electrolyte by Depositing Metal Nitride Lithiophilic Interlayer. *ACS Applied Energy Materials* **5**, 648-657, doi:10.1021/acsaem.1c03157 (2022).
- 40 Ruan, Y. *et al.* A 3D Cross-Linking Lithiophilic and Electronically Insulating Interfacial Engineering for Garnet-Type Solid-State Lithium Batteries. *Advanced Functional Materials* **31**, 2007815, doi:https://doi.org/10.1002/adfm.202007815 (2021).
- 41 Tang, S. *et al.* Modifying an ultrathin insulating layer to suppress lithium dendrite formation within garnet solid electrolytes. *Journal of Materials Chemistry A* **9**, 3576-3583, doi:10.1039/D0TA11311E (2021).
- 42 Cui, C. *et al.* One-step fabrication of garnet solid electrolyte with integrated lithiophilic surface. *Energy Storage Materials* **45**, 814-820,

- doi:<https://doi.org/10.1016/j.ensm.2021.12.027> (2022).
- 43 Huang, Y. *et al.* Graphitic Carbon Nitride (g-C<sub>3</sub>N<sub>4</sub>): An Interface Enabler for Solid-State Lithium Metal Batteries. *Angewandte Chemie International Edition* **59**, 3699-3704, doi:<https://doi.org/10.1002/anie.201914417> (2020).
- 44 Krauskopf, T., Mogwitz, B., Rosenbach, C., Zeier, W. G. & Janek, J. Diffusion Limitation of Lithium Metal and Li–Mg Alloy Anodes on LLZO Type Solid Electrolytes as a Function of Temperature and Pressure. *Advanced Energy Materials* **9**, 1902568, doi: 10.1002/aenm.201902568 (2019).
- 45 Lee, K. *et al.* Multifunctional Interface for High-Rate and Long-Durable Garnet-Type Solid Electrolyte in Lithium Metal Batteries. *ACS Energy Letters* **7**, 381-389, doi:10.1021/acsenerylett.1c02332 (2022).
- 46 Huggins, R. A. *Advanced Batteries: Materials Science Aspects*. (Springer New York, NY, 2009).
- 47 Chou, C.-Y., Kim, H. & Hwang, G. S. A Comparative First-Principles Study of the Structure, Energetics, and Properties of Li–M (M = Si, Ge, Sn) Alloys. *The Journal of Physical Chemistry C* **115**, 20018-20026, doi:10.1021/jp205484v (2011).
- 48 Yan, K. *et al.* Selective deposition and stable encapsulation of lithium through heterogeneous seeded growth. *Nature Energy* **1**, 16010, doi:10.1038/nenergy.2016.10 (2016).
- 49 Kim, S. Y. & Li, J. Porous Mixed Ionic Electronic Conductor Interlayers for Solid-State Batteries. *Energy Material Advances* **2021**, 1519569, doi:10.34133/2021/1519569 (2021).

- 50 Weppner, W. & Huggins, R. A. Determination of the Kinetic Parameters of Mixed-Conducting Electrodes and Application to the System  $\text{Li}_3\text{Sb}$ . *Journal of The Electrochemical Society* **124**, 1569-1578, doi:10.1149/1.2133112 (1977).
- 51 Wen, C. J., Boukamp, B. A., Huggins, R. A. & Weppner, W. Thermodynamic and Mass Transport Properties of “LiAl”. *Journal of The Electrochemical Society* **126**, 2258-2266, doi:10.1149/1.2128939 (1979).
- 52 Ong, S. P. *et al.* Python Materials Genomics (pymatgen): A robust, open-source python library for materials analysis. *Computational Materials Science* **68**, 314-319, doi: 10.1016/j.commatsci.2012.10.028 (2013).
- 53 Blöchl, P. E. Projector augmented-wave method. *Physical Review B* **50**, 17953-17979, doi:10.1103/PhysRevB.50.17953 (1994).
- 54 Perdew, J. P., Burke, K. & Ernzerhof, M. Generalized Gradient Approximation Made Simple. *Physical Review Letters* **77**, 3865-3868, doi:10.1103/PhysRevLett.77.3865 (1996).
- 55 Grimme, S., Ehrlich, S. & Goerigk, L. Effect of the damping function in dispersion corrected density functional theory. *Journal of Computational Chemistry* **32**, 1456-1465, doi:https://doi.org/10.1002/jcc.21759 (2011).
- 56 COMSOL Multiphysics® v. 5.6. www.comsol.com. COMSOL AB, Stockholm, Sweden.
- 57 Li, H. *et al.* Circumventing huge volume strain in alloy anodes of lithium batteries. *Nature Communications* **11**, 1584, doi:10.1038/s41467-020-15452-0 (2020).
- 58 Jin, S. *et al.* Solid–Solution-Based Metal Alloy Phase for Highly

- Reversible Lithium Metal Anode. *Journal of the American Chemical Society* **142**, 8818-8826, doi:10.1021/jacs.0c01811 (2020).
- 59 Tian, H.-K., Xu, B. & Qi, Y. Computational study of lithium nucleation tendency in  $\text{Li}_7\text{La}_3\text{Zr}_2\text{O}_{12}$  (LLZO) and rational design of interlayer materials to prevent lithium dendrites. *Journal of Power Sources* **392**, 79-86, doi:https://doi.org/10.1016/j.jpowsour.2018.04.098 (2018).
- 60 Song, Y. *et al.* Revealing the Short-Circuiting Mechanism of Garnet-Based Solid-State Electrolyte. **9**, 1900671, doi: 10.1002/aenm.201900671 (2019).
- 61 Song, Y. *et al.* Probing into the origin of an electronic conductivity surge in a garnet solid-state electrolyte. *Journal of Materials Chemistry A* **7**, 22898-22902, doi:10.1039/C9TA10269H (2019).
- 62 Pan, J., Cheng, Y.-T. & Qi, Y. General method to predict voltage-dependent ionic conduction in a solid electrolyte coating on electrodes. *Physical Review B* **91**, 134116, doi:10.1103/PhysRevB.91.134116 (2015).
- 63 Oi, T. Ionic conductivity of LiF thin films containing Di- or trivalent metal fluorides. *Materials Research Bulletin* **19**, 451-457, doi: 10.1016/0025-5408(84)90105-3 (1984).
- 64 Guo, H.-j. *et al.* Diffusion coefficient of lithium in artificial graphite, mesocarbon microbeads, and disordered carbon. *New Carbon Materials* **22**, 7-10, doi: 10.1016/S1872-5805(07)60006-7 (2007).
- 65 Dahn, J. R., Zheng, T., Liu, Y. & Xue, J. S. Mechanisms for Lithium Insertion in Carbonaceous Materials. *Science* **270**, 590, doi:10.1126/science.270.5236.590 (1995).

- 66 Suzuki, N. *et al.* Highly Cyclable All-Solid-State Battery with Deposition-Type Lithium Metal Anode Based on Thin Carbon Black Layer. *Advanced Energy and Sustainability Research* **2**, 2100066, doi: 10.1002/aesr.202100066 (2021).
- 67 Buiel, E. & Dahn, J. R. Li-insertion in hard carbon anode materials for Li-ion batteries. *Electrochimica Acta* **45**, 121-130, doi: 10.1016/S0013-4686(99)00198-X (1999).
- 68 David A. Porter, K. E. E., Mohamed Youssef Abdelraouf Sherif. *Phase Transformations in Metals and Alloys (Revised Reprint)*. (CRC Press, 2009).
- 69 Persson, K. *et al.* Lithium Diffusion in Graphitic Carbon. *The Journal of Physical Chemistry Letters* **1**, 1176-1180, doi:10.1021/jz100188d (2010).
- 70 Yoon, G., Moon, S., Ceder, G. & Kang, K. Deposition and Stripping Behavior of Lithium Metal in Electrochemical System: Continuum Mechanics Study. *Chemistry of Materials* **30**, 6769-6776, doi:10.1021/acs.chemmater.8b02623 (2018).
- 71 Zhang, W. *et al.* Degradation Mechanisms at the  $\text{Li}_{10}\text{GeP}_2\text{S}_{12}/\text{LiCoO}_2$  Cathode Interface in an All-Solid-State Lithium-Ion Battery. *ACS Applied Materials & Interfaces* **10**, 22226-22236, doi:10.1021/acsami.8b05132 (2018).
- 72 Fuchs, T. *et al.* Working Principle of an Ionic Liquid Interlayer During Pressureless Lithium Stripping on  $\text{Li}_{6.25}\text{Al}_{0.25}\text{La}_3\text{Zr}_2\text{O}_{12}$  (LLZO) Garnet-Type Solid Electrolyte. *Batteries & Supercaps* **4**, 1145-1155, doi:10.1002/batt.202100015 (2021).

- 73 Zuo, T.-T. *et al.* A mechanistic investigation of the  $\text{Li}_{10}\text{GeP}_2\text{S}_{12}|\text{LiNi}_{1-x-y}\text{Co}_x\text{Mn}_y\text{O}_2$  interface stability in all-solid-state lithium batteries. *Nature Communications* **12**, 6669, doi:10.1038/s41467-021-26895-4 (2021).
- 74 Tuinstra, F. & Koenig, J. L. Raman Spectrum of Graphite. *Journal of Chemical Physics* **53**, 1126-1130, doi:10.1063/1.1674108 (1970).
- 75 Huo, H. *et al.* A flexible electron-blocking interfacial shield for dendrite-free solid lithium metal batteries. *Nature Communications* **12**, 176, doi:10.1038/s41467-020-20463-y (2021).
- 76 Ruan, Y. *et al.* Acid induced conversion towards a robust and lithiophilic interface for Li–  $\text{Li}_7\text{La}_3\text{Zr}_2\text{O}_{12}$  solid-state batteries. *Journal of Materials Chemistry A* **7**, 14565-14574, doi:10.1039/C9TA01911A (2019).
- 77 Xu, H. *et al.*  $\text{Li}_3\text{N}$ -Modified Garnet Electrolyte for All-Solid-State Lithium Metal Batteries Operated at 40 °C. *Nano Letters* **18**, 7414-7418, doi:10.1021/acs.nanolett.8b03902 (2018).
- 78 Chen, H. *et al.* Improved Interface Stability and Room-Temperature Performance of Solid-State Lithium Batteries by Integrating Cathode/Electrolyte and Graphite Coating. *ACS Applied Materials & Interfaces* **12**, 15120-15127, doi:10.1021/acsami.9b22690 (2020).
- 79 Su, J. *et al.* Overcoming the abnormal grain growth in Ga-doped  $\text{Li}_7\text{La}_3\text{Zr}_2\text{O}_{12}$  to enhance the electrochemical stability against Li metal. *Ceramics International* **45**, 14991-14996, doi: 10.1016/j.ceramint.2019.04.236 (2019).
- 80 Chen, S. *et al.* All-Solid-State Batteries with a Limited Lithium Metal Anode at Room Temperature using a Garnet-Based Electrolyte. *Advanced*



- Materials* **33**, 2002325, doi: 10.1002/adma.202002325 (2021).
- 81 Han, F. *et al.* Interphase Engineering Enabled All-Ceramic Lithium Battery. *Joule* **2**, 497-508, doi: 10.1016/j.joule.2018.02.007 (2018).
- 82 Ohta, S., Kobayashi, T., Seki, J. & Asaoka, T. Electrochemical performance of an all-solid-state lithium ion battery with garnet-type oxide electrolyte. *Journal of Power Sources* **202**, 332-335, doi: 10.1016/j.jpowsour.2011.10.064 (2012).

## Chapter 5. Summary

In this thesis, I comprehensively investigated the lithium metal batteries using solid electrolytes (Solid-state lithium metal batteries, SLMBs) and suggested the strategies to implement the high performance SLMBs. The content include (i) the solid electrolyte surface/interface tailoring by selecting suitable dopants for the grain boundary and bulk to stabilize the interface with lithium metal, (ii) the real-time observation of lithium plating/stripping behavior depending on the electrolyte surface/interface chemistry, and (iii) an interlayer design strategy to achieve the stable solid-state lithium metal batteries for long-term operation.

In the first part, I focused on exploring the composition impacts of the solid electrolyte on the stability of the interface between solid electrolyte and lithium metal, which is a critical factor to secure the stable SLMBs. Using garnet-type  $\text{Li}_7\text{La}_3\text{Zr}_2\text{O}_{12}$ -based oxide electrolytes (LLZOs), chemical/electrochemical instabilities of the doped-LLZO against Li metal were investigated. I focused on the potential by-product formation along grain boundaries, which could lead the lithium propagation through the electrolyte, due to the decomposition of LLZOs in contact with lithium metal upon dopants of LLZOs. Through the theoretical and experimental investigation, it was revealed that electrolyte doping with inappropriate species could provoke the electrolyte decomposition that led to the short-circuit formation. Subsequently, proton was rationally selected as an appropriate secondary dopant for grain boundaries and surface, as it was expected to passivate the interface of garnet electrolyte and the lithium metal by forming desirable by-products that are ionically conductive and electronically insulating. Via protonation of LLZO

electrolytes using solution-based etching process, the LLZO surface was not only (electro) chemically passivated, but also physically tailored. After the surface tailoring, the residual stress in LLZO was effectively released, leading to the mechanical strength enhancement, and the intact contact with lithium metal was achieved accompanied by the surface contamination removal and the enlargement of surface area. This approach was validated by showing the considerable enhancement of performance in a full cell comprising the protonated Ta-LLZO electrolyte, Li-metal, and conventional NCM111 cathode. These findings indicate that a coupled approach to designing the bulk and grain boundaries of the solid electrolyte plays a key role in achieving the long-term stability of solid-state batteries.

In the following part, I directly investigated the lithium plating/stripping behavior through the solid electrolyte via *in operando* optical microscopy technique. This real-time observation aided in understanding the interfacial stability during battery operation, from the perspective of lithium metal anode. I found that lithium plating is strongly affected by the geometry of the LLZO surface, where non-uniform/filamentary lithium growth is triggered particularly at morphological defects where the electric field and corresponding lithium ion-flux are concentrated. Also, it was observed that lithium plating behavior significantly altered depending on the electrolyte surface chemistry, which can be readily modified by an artificial interlayer. This finding indicates that the kinetics of the alloying and precipitation reactions with lithium metal in the interlayers dominantly affect lithium distribution and the subsequent deposition morphology. Supported by these intriguing observations, I proposed various roles for the interlayer during battery operation: as a dynamic buffer layer for lithium redistribution, and as a matrix layer for facile

lithium precipitation. In addition, it was confirmed that the interlayer not only affects the deposition process, but also the sequential stripping process, influencing the interfacial stabilities and the electrochemical performance of the cell.

Given with these findings, in the last part, I tried to provide the design strategy for optimal interlayer at the lithium metal/LLZO electrolyte interface, considering the ease of interlayer introduction on the LLZO surface and its wide applicability. Based on the thermodynamic properties of the candidate materials, a carbon-based material was selected as the suitable material for the interlayer, which can induce lithium plating between the current collector and the interlayer without significant degradation. It was also shown that preferential lithium plating between the interlayer and the current collector can be effectively facilitated with a thin seed layer of lithium metal, which can effectively lower the high kinetic energy barrier for lithium nucleation. Moreover, the critical impact of the crystalline orientation of the graphitic carbon on the stability of interlayer was elucidated by showing that the amorphous carbon interlayer, providing isotropic lithium transport (without preference for a specific direction), could maintain its original interlayer/lithium metal interface after the repeated lithium plating/stripping, in contrast to the case of the graphite interlayer. Finally, I fabricated the optimal interlayer using a mixture of amorphous carbons, and validated its efficacy by demonstrating a high-power solid-state lithium metal battery capable of stable room temperature operation.

I hope this work provides strong research insight for scientific understanding of SLMBs and useful guidelines for implementing the high-performance and stable SLMBs.

## Abstract in Korean

### 초록

환경 문제로 인해 지속 가능한 에너지 자원에 대한 수요가 지속적으로 증가함에 따라, 재생 가능한 자원으로부터 생성된 에너지를 효율적으로 저장하고 재분배할 수 있는 에너지 저장 시스템에 대한 세계적인 관심이 증하하고 있다. 리튬 이온 전지는 높은 에너지 밀도, 출력 및 우수한 수명 특성으로 인해 가장 효율적인 에너지 저장 시스템 중 하나로 간주되어 왔다. 그러나, 높은 에너지 밀도에 대한 요구는 현 리튬 이온 전지의 한계를 넘어서고 있다. 리튬 금속을 음극으로 사용하는 리튬 금속 전지가 높은 가능성을 보였지만, 실질적인 구현은 지연되고 있다. 이는 액체 전해질을 사용하는 전지에 리튬 금속 음극이 도입되면, 셀을 관통하는 리튬 금속 수지 성장으로 인한 단락이 형성때문이다. 이는 전지의 안전성을 크게 위협한다. 이와 관련하여, 고체 전해질을 사용한 고체 리튬 금속 전지는 높은 에너지 밀도를 제공하는 안전한 전지를 구현할 수 있는 유망한 해결책으로 평가되고 있다. 그러나, 리튬 금속 음극과 고체 전해질 사이에 발생하는 계면 불안정성과 그로 인한 전해질 내 리튬 관통 현상은 고체 리튬 금속 전지 개발에 걸림돌이 되고 있다. 따라서, 상용화 가능한 수준의 고체 리튬 금속 전지 성능 확보를 위해서는 고체 전해질/리튬 금속 음극의 계면 안정성이 보장되어야 한다. 본 논문에서는 가넷형 고체전해질을 사용하여 리튬 금속 전극과 고체

전해질의 계면에 대해 체계적으로 조사를 제시하고, 고체 전해질과 리튬 금속 전극의 양쪽 관점에서 안정적인 계면을 설계하고 실제 고성능 고체 리튬 금속 전지 구현을 위한 전략을 제시한다.

제2장에서는 가넷형 고체전해질에 리튬 금속 음극을 적용할 경우 계면에서 발생하는 열화 현상을 고체전해질에 집중하여 관찰하고, 전해질 표면을 최적화함으로써 가넷형 고체전해질과 리튬 금속의 계면을 안정화할 수 있는 실현 가능한 방법을 제시한다. 전해질 내 리튬 성장 현상이 고체전해질 분해로부터 촉발될 수 있다는 가정하에, 다양한 도펀트가 도핑된 가넷형 고체전해질의 리튬 금속에 대한 안정성을 탐색한다. 이론적 계산과 실험에 의해, 전해질 조성에 따라 리튬 금속에 대한 가넷형 고체전해질의 화학적/전기화학적 안정성이 크게 달라질 수 있음을 입증하여, 적절한 도펀트 선택의 중요성을 시사한다. 추가적인 계산을 통해, 2차 도펀트의 도입, 즉 양성자화에 의한 전해질 입계면 및 표면 조성 제어는 전해질의 전자전도성 부산물의 형성을 억제할 수 있는 효율적인 방법임을 제안하고, 가넷형 고체전해질의 리튬 금속과의 호환성을 효과적으로 향상시킬 수 있음이 실험적으로 검증한다. 동시에, 용액 기반 산 처리인 고체전해질을 양성자화하는 데 사용한 방법이 전해질 표면의 다른 특성도 조절할 수 있음을 발견한다. 수용성 산 용액을 이용한 고체전해질 표면처리는 고체전해질의 표면의 잔류응력을 효과적으로 방출하고, 전해질과 리튬 금속 음극과의 긴밀한 접촉을 유지하게 하여 계면 안정성을 향상시키는 데 도움이 됨을 밝힌다.

최종적으로 얇은 리튬 금속 음극과 고체 전해질, 그리고 상업화 양극을 사용한 전지 성능이 크게 향상된 것을 보여주어, 제시된 고체전해질 표면 처리법의 효과를 입증한다. 이 연구결과는 고체전해질의 벌크 및 입계면을 함께 설계하는 접근법이, 고체전지의 장기적인 안정성을 달성하는 데 핵심적인 역할을 한다는 것을 강조한다.

한편으로, 리튬 금속 전극은 반복적인 리튬 도금 및 박리를 통해 그 상태가 계속 변화하므로, 고체 리튬 금속 전지의 안정적인 성능을 확보하기 위해서는 리튬 금속의 관점에서 계면 안정성을 이해하는 것이 중요하다. 제3장에서는 리튬 석출 거동을 실시간으로 관찰하여 전기화학 반응 중 고체전해질/리튬 금속 계면의 동적 변화를 설명한다. 리튬 도금은 고체전해질 표면 형상에 강하게 영향을 받으며, 표면의 굽힘 자국이나 구멍과 같은 형태학적 결함에서 불균일한 기둥 형태의 리튬 금속 성장이 시작되는 것을 밝힌다. 중요하게는, 리튬 성장 동역학이 고체전해질 표면 개질을 위해 의도적으로 삽입된 중간층이 존재하면, 중간층의 종류와 그 특성에 따라 리튬 성장/박리 거동이 크게 변화함을 밝힌다. 즉, 중간층의 리튬과 반응 특성에 따라 석출/박리 균일도가 크게 달라짐을 보인다. 이에 근거하여 전지 작동 중 중간층의 동적 역할, 즉 리튬 재분배를 위한 완충층 및 석출 매개층 역할이 논의된다. 이러한 연구결과는 고체전해질/리튬 금속 계면에서의 전기화학적 리튬 도금/박리 공정에 대한 이해를 넓히고, 고체 리튬 금속 전지 성능을 향상시키기 위한 방법으로서 다양한 중간층 탐색의 중요성을 강조하며,

또한 리튬 금속이 없는 (충전 중 양극의 리튬을 음극으로 석출시켜 사용하는) 전고체 전지의 리튬 성장 특성에 대한 통찰을 제공한다.

제4장에서는 반복적인 리튬 석출/박리에 대한 고체전해질/리튬 금속 계면의 장기적 안정성을 보장하고, 상용화 수준의 전지 성능을 제공할 수 있는 고체 리튬 금속 전지를 구현하기 위한 중간 설계 전략을 제안한다. 그 전략으로, (i) 등방성 리튬 수송을 제공하는 결정 방향 제어 탄소 재료를 사용하고, (ii) 리튬 핵 생성 방향을 집전체로 안내하는 리튬 기 증착된 리튬층을 사용하는 최적의 중간층을 소개한다. 이는 초기 상태의 중간층/고체전해질 계면을 유지하면서 집전체 방향으로의 바람직한 리튬 성장을 유도함으로써, 계면의 내구성을 현저히 향상시킬 수 있음을 보인다. 추가적으로 중간층의 재료/기하학적 최적화가 열역학 특성 고려하에 어떠한 과정으로 수행되는지 설명하며, 표면이 개질된 가넷형 고체전해질과 상용화 양극을 적용한 전지에 적용하여 우수한 성능을 보임으로써 그 성능을 입증한다.

이러한 일련의 연구결과는 전해질 관점과 리튬 금속 전극 관점에서 모두에서 고려한 안정적인 계면 확보 및 중간층 설계가 궁극적으로 고체 리튬 금속 전지의 실질적인 구현에 중요한 요소임을 입증한다.

**주요어:** 에너지 저장, 리튬 금속 전지, 고체 전지, 가넷형 고체전해질, 실시간 분석, 중간층

**학번:** 2017-38966